

# NAVAL POSTGRADUATE SCHOOL

## Monterey, California



## THESIS

**THE ROLE OF THE PLANETARY BETA EFFECT ON  
CURRENTS AND EDDIES IN THE LEEUWIN CURRENT  
SYSTEM**

by

Troy J. Tworek

September 2000

Thesis Advisor:  
Second Reader:

Mary L. Batteen  
Curtis A. Collins

Approved for public release; distribution is unlimited.

**DTIC QUALITY INSPECTED 4**

**20001026 151**

# REPORT DOCUMENTATION PAGE

Form Approved  
OMB No. 0704-0188

Public reporting burden for this collection of information is estimated to average 1 hour per response, including the time for reviewing instruction, searching existing data sources, gathering and maintaining the data needed, and completing and reviewing the collection of information. Send comments regarding this burden estimate or any other aspect of this collection of information, including suggestions for reducing this burden, to Washington headquarters Services, Directorate for Information Operations and Reports, 1215 Jefferson Davis Highway, Suite 1204, Arlington, VA 22202-4302, and to the Office of Management and Budget, Paperwork Reduction Project (0704-0188) Washington DC 20503.

1. AGENCY USE ONLY  
(Leave blank)

2. REPORT DATE  
September 2000

3. REPORT TYPE AND DATES COVERED  
Master's Thesis

4. TITLE AND SUBTITLE

The Role of the Planetary Beta Effect on Currents and Eddies in the Leeuwin Current System

5. FUNDING NUMBERS

6. AUTHOR(S)

Tworek, Troy J.

7. PERFORMING ORGANIZATION NAME(S) AND ADDRESS(ES)

Naval Postgraduate School  
Monterey, CA 93943-5000

8. PERFORMING ORGANIZATION  
REPORT NUMBER

9. SPONSORING / MONITORING AGENCY NAME(S) AND ADDRESS(ES)

10. SPONSORING / MONITORING  
AGENCY REPORT NUMBER

11. SUPPLEMENTARY NOTES

The views expressed in this thesis are those of the author and do not reflect the official policy or position of the Department of Defense or the U.S. Government.

12a. DISTRIBUTION / AVAILABILITY STATEMENT

Approved for public release; distribution is unlimited.

12b. DISTRIBUTION CODE

13. ABSTRACT (maximum 200 words)

To investigate the effect of the role played by planetary beta in the generation and maintenance of the Leeuwin Current System (LCS), several numerical experiments are conducted with varying Coriolis parameterizations ( $f$ -plane or  $\beta$ -plane). The seasonal effects of thermal gradients, wind forcing and North West Shelf (NWS) waters are also systematically explored in the numerical experiments. Additionally, the generation mechanisms for undercurrents along both the western and southern coasts of Australia are investigated.

Although surface currents, undercurrents, and mesoscale activity are present in both the  $f$ -plane and  $\beta$ -plane experiments, those run on a  $\beta$ -plane show a more realistic depiction of these features due to the significant role played by the planetary beta effect in the LCS. The combination of thermal forcing, wind forcing, and NWS waters were found to be essential to maintain the highly seasonally varying LCS. Alongshore temperature gradients, which are generated at deeper levels by the strong flow of the Leeuwin Current, are sufficient to establish and maintain an equatorward (westward) undercurrent along western (southern) Australia.

14. SUBJECT TERMS

Primitive equation model, Leeuwin Current System, currents, meanders, eddies, filaments

15. NUMBER OF  
PAGES  
186

16. PRICE CODE

17. SECURITY  
CLASSIFICATION  
OF REPORT  
Unclassified

18. SECURITY CLASSIFICATION OF  
THIS PAGE  
Unclassified

19. SECURITY CLASSIFICATION  
OF ABSTRACT  
Unclassified

20. LIMITATION OF  
ABSTRACT  
UL

NSN 7540-01-280-5500

Standard Form 298 (Rev. 2-89)  
Prescribed by ANSI Std. Z39-18



Approved for public release; distribution is unlimited

**THE ROLE OF THE PLANETARY BETA EFFECT ON CURRENTS AND  
EDDIES IN THE LEEUWIN CURRENT SYSTEM**

Troy J. Tworek  
Lieutenant Commander, United States Navy  
B.S., University of Nebraska-Lincoln, 1991

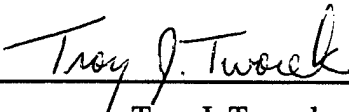
Submitted in partial fulfillment of the  
requirements for the degree of

**MASTER OF SCIENCE IN METEOROLOGY AND PHYSICAL  
OCEANOGRAPHY**

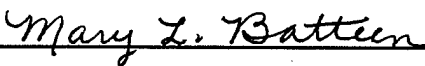
from the


**NAVAL POSTGRADUATE SCHOOL  
September 2000**

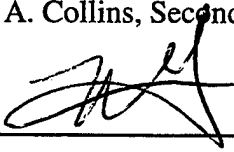
Author:

  
Troy J. Tworek

Approved by:

  
Mary L. Batteen, Thesis Advisor

  
Curtis A. Collins, Second Reader

  
Roland W. Garwood, Chairman  
Department of Oceanography



## ABSTRACT

To investigate the effect of the role played by planetary beta in the generation and maintenance of the Leeuwin Current System (LCS), several numerical experiments are conducted with varying Coriolis parameterizations ( $f$ -plane or  $\beta$ -plane). The seasonal effects of thermal gradients, wind forcing and North West Shelf (NWS) waters are also systematically explored in the numerical experiments. Additionally, the generation mechanisms for undercurrents along both the western and southern coasts of Australia are investigated.

Although surface currents, undercurrents, and mesoscale activity are present in both the  $f$ -plane and  $\beta$ -plane experiments, those run on a  $\beta$ -plane show a more realistic depiction of these features due to the significant role played by the planetary beta effect in the LCS. The combination of thermal forcing, wind forcing, and NWS waters were found to be essential to maintain the highly seasonally varying LCS. Alongshore temperature gradients, which are generated at deeper levels by the strong flow of the Leeuwin Current, are sufficient to establish and maintain an equatorward (westward) undercurrent along western (southern) Australia.



## TABLE OF CONTENTS

I. INTRODUCTION.....	1
II. MODEL DESCRIPTION .....	5
A. MODEL EQUATIONS .....	5
B. FORCING CONDITIONS AND EXPERIMENTAL DESIGN.....	8
III. RESULTS FROM MODEL SIMULATIONS.....	13
A. EXPERIMENTS 1 AND 2.....	13
B. EXPERIMENTS 3 AND 4 .....	15
1. Spin-up Phase.....	15
2. Analysis of Undercurrent Generation Mechanisms .....	16
C. EXPERIMENT 5.....	20
D. EXPERIMENT 6.....	22
E. EXPERIMENT 7 .....	25
F. EXPERIMENT 8 .....	27
G. EXPERIMENT 9.....	30
1. Spin-up Phase.....	30
2. Quasi-equilibrium Phase .....	32
3. Analyses of Mean and Eddy Kinetic Energy.....	34
IV. SUMMARY .....	39
LIST OF REFERENCES .....	159
INITIAL DISTRIBUTION LIST.....	163





## LIST OF FIGURES

1. Annual cycle of net forcing for the Leeuwin Current between 22°S and 32°S: Dashed line is observed pressure gradient forcing; dotted line is observed wind stress; solid line is net forcing. Positive is southward (from Godfrey and Ridgway).....45
2. The model domain for the Leeuwin Current System (LCS) is bounded by 22.5°S to 40°S, 107.5°E to 122.5°E. The cross-shore (alongshore) resolution is 11 km (14 km). Geographical locations and prominent features are labeled.....46
3. Climatological (1980-1989) ECMWF winds in m/s for: (a) February, (b) May, (c) July, and (d) November. Maximum wind vector is 10 m/s.....47
4. Plots of (a) actual and (b) slightly adjusted Levitus climatological temperature fields used as seasonal forcing along the western boundary (107.5°E) at 22.5°S (top) and 40°S (bottom).....51
5. Temperature contours and velocity vectors at 10 m depth at days (a) 9, (b) 27, (c) 60, (d) 87, and (e) 117 of Experiment 1. The contour interval is 1°C. To avoid clutter, the velocity vectors are plotted every third grid point in the east-west direction and every fourth grid point in the north-south direction. Maximum velocity is 100 cm/s.....53
6. Temperature contours and velocity vectors at 10 m depth at days (a) 51 and (b) 159 of Experiment 2. The contour interval is 1°C. To avoid clutter, velocity vectors are plotted every third grid point in the east-west direction and every fourth grid point in the north-south direction. Maximum velocity is 100 cm/s.....58
7. Cross-shore section of meridional velocity ( $v$ ) at ~32°S for Experiment 2 on day 33. Contour interval is 10 cm/s for poleward flow (dashed lines) and 5 cm/s for equatorward flow (solid lines).....60
8. Temperature contours and velocity vectors at 10 m depth at days (a) 87 and (b) 117 of Experiment 3. The contour interval is 1°C. To avoid clutter, the velocity vectors are plotted every third grid point in the east-west direction and every fourth grid point in the north-south direction. Maximum velocity is 100 cm/s.....61
9. Cross-shore section of meridional velocity ( $v$ ) at (a) ~32°S and (b) ~26°S for Experiment 3 on day 15. Contour interval is 10 cm/s for poleward flow (dashed lines) and 5 cm/s for equatorward flow (solid lines).....63

10. Cross-shore section of meridional velocity ( $v$ ) at (a)  $\sim 32^\circ\text{S}$  and (b)  $\sim 26^\circ\text{S}$  for Experiment 1 on day 15. Contour interval is 10 cm/s for poleward flow (dashed lines) and 5 cm/s for equatorward flow (solid lines).....65
11. Velocity vectors at 600 m depth for (a) Experiment 3 and (b) Experiment 4 at day 15. To avoid clutter, the velocity vectors are plotted every third grid point in the east-west direction and every fourth grid point in the north-south direction. Maximum velocity is 30 cm/s.....67
12. Cross-shore section of meridional velocity ( $v$ ) at (a and c)  $\sim 32^\circ\text{S}$  and (b and d)  $\sim 26^\circ\text{S}$  for Experiment 4 on day (a and b) 3 and (c and d) 9. Contour interval is 5 cm/s for poleward flow (dashed lines) and (a and c) 2.5 cm/s and (b and d) 1 cm/s for equatorward flow (solid lines).....69
13. Cross-shore section of zonal velocity ( $u$ ) at (a and b)  $117^\circ\text{E}$  and (c)  $122^\circ\text{E}$  for (a) Experiment 3 and (b and c) Experiment 4 on day 15. The contour interval is (a and b) 5 cm/s and (c) 2.5 cm/s for westward flow (dashed lines) and 10 cm/s for eastward flow (solid lines).....73
14. Cross-shore section of temperature at (a)  $117^\circ\text{E}$  and (b)  $122^\circ\text{E}$  for Experiment 4 on day 15. The contour interval is  $1^\circ\text{C}$ .....76
15. Temperature contours and velocity vectors at 10 m depth at days (a) 33, (b) 195, (c) 231, (d) 297, and (e) 363 of Experiment 5. The contour interval is  $1^\circ\text{C}$ . To avoid clutter, the velocity vectors are plotted every third grid point in the east-west direction and every fourth grid point in the north-south direction. Maximum velocity is 100 cm/s.....78
16. Cross-shore section of meridional velocity ( $v$ ) at (a)  $\sim 32^\circ\text{S}$  and (b)  $\sim 26^\circ\text{S}$  for Experiment 5 on day 33. Contour interval is 1 cm/s for poleward flow (dashed lines) and 5 cm/s for equatorward flow (solid lines).....83
17. Cross-shore section of zonal velocity ( $u$ ) at  $117^\circ\text{E}$  for Experiment 5 on days (a) 243 and (b) 363. Contour interval is 5 cm/s for westward flow (dashed lines) and 2 cm/s for eastward flow (solid lines).....85
18. Temperature contours and velocity vectors at 10 m depth at days (a) 33, (b) 90, and (c) 165 of Experiment 6. The contour interval is  $1^\circ\text{C}$ . Maximum velocity for (a) and (b) is 100 cm/s and for (c) is 50 cm/s.....87
19. Cross-shore section of meridional velocity ( $v$ ) at (a)  $\sim 32^\circ\text{S}$  and (b)  $\sim 26^\circ\text{S}$  for Experiment 6 on day 33. Contour interval is 1 cm/s for poleward flow (dashed lines) and 5 cm/s for equatorward flow (solid lines).....90

20. Cross-shore section of meridional velocity ( $v$ ) at  $34^{\circ}\text{S}$  at days (a) 33 and (b) 165 and at  $\sim 26^{\circ}\text{S}$  at day (c) 315 for Experiment 6. Contour interval is (a) 1 cm/s, (b) 2.5 cm/s, and (c) 5 cm/s for poleward flow (dashed lines) and (a and c) 5 cm/s and (b) 2.5 cm/s for equatorward flow (solid lines).....92
21. Temperature contours and velocity vectors at 10 m depth at days (a) 15, (b) 30, (c) 63, (d) 123, and (e) 363 of Experiment 7. The contour interval is  $1^{\circ}\text{C}$  for (a) – (d) and  $2^{\circ}\text{C}$  for (e). Maximum velocity is 100 cm/s.....95
22. Cross-shore section of meridional velocity ( $v$ ) at (a)  $\sim 32^{\circ}\text{S}$  and (b)  $\sim 26^{\circ}\text{S}$  for Experiment 7 on day 30. Contour interval is (a) 10 cm/s and (b) 1 cm/s for poleward flow (dashed lines) and 5 cm/s for equatorward flow (solid lines).....100
23. Cross-shore section of zonal velocity ( $u$ ) at  $117^{\circ}\text{E}$  for Experiment 7 on day 30. Contour interval is 5 cm/s for westward flow (dashed lines) and 10 cm/s for eastward flow (solid lines).....102
24. Cross-shore section of meridional velocity ( $v$ ) at (a)  $\sim 26^{\circ}\text{S}$  for Experiment 7 on day 345 and (b)  $\sim 32^{\circ}\text{S}$  for Experiment 8 on day 165. Contour interval is (a) 1 cm/s and (b) 5 cm/s for poleward flow (dashed lines) and 5 cm/s for equatorward flow (solid lines).....103
25. Temperature contours and velocity vectors at 10 m depth at days (a) 30, (b) 63, (c) 123, (d) 165, and (e) 363 of Experiment 8. The contour interval is  $1^{\circ}\text{C}$  for (a) – (d) and  $2^{\circ}\text{C}$  for (e). Maximum velocity is 100 cm/s. Note: In (e), temperature contours intersecting coast north of  $28^{\circ}\text{S}$  are  $16^{\circ}\text{C}$ .....105
26. Cross-shore section of meridional velocity ( $v$ ) at (a)  $\sim 32^{\circ}\text{S}$  and (b)  $\sim 26^{\circ}\text{S}$  for Experiment 8 on day 30. Contour interval is (a) 5 cm/s and (b) 2.5 cm/s for poleward flow (dashed lines) and (a) 5 cm/s and (b) 2.5 cm/s for equatorward flow (solid lines).....110
27. Cross-shore section of meridional velocity ( $v$ ) at (a)  $\sim 32^{\circ}\text{S}$  and (b)  $\sim 26^{\circ}\text{S}$  for Experiment 8 on day 363. Contour interval is 2.5 cm/s for poleward flow (dashed lines) and 5 cm/s for equatorward flow (solid lines).....112
28. Temperature contours and velocity vectors at 10 m depth at days (a) 78, (b) 102, (c) 165, and (d) 363 of Experiment 9. The contour interval is  $1^{\circ}\text{C}$  for (a), (b), and (d) and  $2^{\circ}\text{C}$  for (c). Maximum velocity is 100 cm/s.....114
29. Cross-shore section of meridional velocity ( $v$ ) at  $\sim 26^{\circ}\text{S}$  for Experiment 9 on day 102. Contour interval is 10 cm/s for poleward flow (dashed lines) and 1 cm/s for equatorward flow (solid lines).....118

30. Cross-shore section of meridional velocity ( $v$ ) at  $30^{\circ}\text{S}$  for (a) Experiment 9 and (b) Experiment 8 at day 165. Contour interval is (a) 10 cm/s and (b) 5 cm/s for poleward flow (dashed lines) and 5 cm/s for equatorward flow (solid lines).....119
31. Cross-shore section of zonal velocity ( $u$ ) at  $117^{\circ}\text{E}$  for (a) Experiment 9 and (b) Experiment 8 at day 165. Contour interval is 5 cm/s for westward flow (dashed lines) and 10 cm/s for eastward flow (solid lines).....121
32. Cross-shore section of meridional velocity ( $v$ ) at (a)  $\sim 32^{\circ}\text{S}$  and (b)  $\sim 26^{\circ}\text{S}$  for Experiment 9 on day 363. Contour interval is 2.5 cm/s for poleward flow (dashed lines) and (a) 2.5 cm/s and (b) 5 cm/s for equatorward flow (solid lines).....123
33. Temperature contours and velocity vectors at 10 m depth at days (a) 870, (b) 915, (c) 1026, and (d) 1092 of Experiment 9. The contour interval is  $2^{\circ}\text{C}$  for (a),  $3^{\circ}\text{C}$  for (b), and  $1^{\circ}\text{C}$  for (c) and (d). Maximum velocity is 100 cm/s.....125
34. Cross-shore section of meridional velocity ( $v$ ) at  $30^{\circ}\text{S}$  on day 948 for Experiment 9. Contour interval is 5 cm/s for poleward flow (dashed lines) and 5 cm/s for equatorward flow (solid lines).....129
35. Cross-shore section of zonal velocity ( $u$ ) at  $\sim 117^{\circ}\text{E}$  for Experiment 9 on day (a) 930, (b) 990, and (c) 1074. Contour interval for velocities greater than (less than) 10 cm/s is 10 cm/s (5 cm/s) for westward flow (dashed lines). For eastward flow (solid lines), the contour interval is 10 cm/s in (a) and (c) and 5 cm/s in (b).....130
36. Cross-shore section of meridional velocity ( $v$ ) at  $30^{\circ}\text{S}$  for (a) Experiment 9 and (b) Experiment 6 at day 1074. Contour interval is (a) 2 cm/s and (b) 5 cm/s for poleward flow (dashed lines) and 10 cm/s for equatorward flow (solid lines).....133
37. Cross-shore section of zonal velocity ( $u$ ) at  $117^{\circ}\text{E}$  on day 1074 for Experiment 6. Contour interval is 10 cm/s for westward flow (dashed lines) and 2.5 cm/s for eastward flow (solid lines).....135
38. Horizontal map at 10 m depth of average (a) mean kinetic energy (MKE) and (b) eddy kinetic energy (EKE) for Experiment 9 in model year 3, time averaged for April through September, when the Leeuwin Current is strongest. Contour interval for kinetic energy  $((\text{cm/s})^2)$  greater than 1000 is 500 and less than 1000 is 250.....136
39. Temperature contours and velocity vectors at 10 m depth for Experiment (a) 9, (b) 3, (c) 6, and (d) 8 in model year 3, time averaged for April through September, when the Leeuwin Current is strongest. The contour interval is  $1^{\circ}\text{C}$ . Maximum velocity is 100 cm/s.....138

40. Cross-shore section of (a) meridional velocity ( $v$ ) at  $30^{\circ}\text{S}$  on day 930 and (b) zonal velocity ( $u$ ) at  $117^{\circ}\text{E}$  on day 918 for Experiment 3. Contour interval is 5 cm/s for (a) poleward and (b) westward flow (dashed lines) and 5 cm/s for (a) equatorward and (b) eastward flow (solid lines).....142
41. Horizontal map at 10 m depth of average (a) mean kinetic energy (MKE) and (b) eddy kinetic energy (EKE) for Experiment 3 in model year 3, time averaged for April through September, when the Leeuwin Current is strongest. Contour interval for kinetic energy  $((\text{cm/s})^2)$  greater than 1000 is 500 and less than 1000 is 250.....144
42. Cross-shore section of (a) meridional velocity ( $v$ ) at  $30^{\circ}\text{S}$  on day 912 and (b) zonal velocity ( $u$ ) at  $117^{\circ}\text{E}$  on day 924 for Experiment 6. Contour interval is (a) 5 cm/s and (b) 10 cm/s for (a) poleward and (b) westward flow (dashed lines) and (a) 10 cm/s and (b) 2 cm/s for (a) equatorward and (b) eastward flow (solid lines).....146
43. Horizontal map at 10 m depth of average (a) mean kinetic energy (MKE) and (b) eddy kinetic energy (EKE) for Experiment 6 in model year 3, time averaged for April through September, when the Leeuwin Current is strongest. Contour interval for kinetic energy  $((\text{cm/s})^2)$  greater than 1000 is 500 and less than 1000 is (a) 250 and (b) 125.....148
44. Cross-shore section of (a) meridional velocity ( $v$ ) at  $30^{\circ}\text{S}$  on day 915 and (b) zonal velocity ( $u$ ) at  $117^{\circ}\text{E}$  on day 930 for Experiment 8. Contour interval is (a) 2.5 cm/s and (b) 10 cm/s for (a) poleward and (b) westward flow (dashed lines) and (a) 2.5 cm/s and (b) 10 cm/s for (a) equatorward and (b) eastward flow (solid lines).....150
45. Horizontal map at 10 m depth of average (a) mean kinetic energy (MKE) and (b) eddy kinetic energy (EKE) for Experiment 8 in model year 3, time averaged for April through September, when the Leeuwin Current is strongest. Contour interval for kinetic energy  $((\text{cm/s})^2)$  greater than 1000 is 500 and greater than 1000 is 250.....152



## LIST OF TABLES

1. Values of constants used in the model.....	155
2. Temperature profile for North West Shelf Waters.....	156
3. Summary of specific experimental design.....	157





## ACKNOWLEDGEMENT

I would like to thank Dr. Mary Batteen, my advisor, for her extraordinary professional advice, patience, and guidance. Her willingness to spend countless hours setting up model runs and discussing the results enabled me to complete this study and is much appreciated. Additionally, the constructive advice provided by Dr. Curtis Collins, as second reader, was greatly appreciated.

This study would have not been accomplished without the effort and technical expertise of several individuals including, Pat Murray, Frank Schenk, Donna Burych, and Eldor Magat. I am thankful for their support and assistance with the numerous technical, and even the not so technical, issues surrounding the accomplishment of this study.

Above all, I would like to thank my family. The patience, flexibility, and encouragement displayed by my wife Lisa and children (David, Laura, and Matthew) were a wonderful comfort. I could not have done it without their love and understanding. Thanks to all!



## I. INTRODUCTION

The Leeuwin Current is a thermally driven, anomalous, surface eastern boundary current (EBC). It flows poleward over the continental shelf break off the western Australian coast, down to Cape Leeuwin, and then eastward into the Great Australian Bight (e.g., Cresswell and Golding, 1980). There is general agreement (e.g., Godfrey and Ridgway, 1985) that the Leeuwin Current is generated by a meridional pressure gradient resulting from the large amount of heating in the equatorial region and excessive cooling near the poleward region, which overwhelms the equatorward wind stress. The source for the Leeuwin Current is predominantly geostrophic inflow from the west (e.g., McCreary *et al.*, 1986; Thompson, 1987) and is augmented by a source from the North West Shelf (e.g., Gentili, 1972), possibly having its origin in the Pacific Ocean (e.g., Hirst and Godfrey, 1993). As a result of this strong inflow of subtropical water towards the coast, the Leeuwin Current intensifies poleward (e.g., Batteen *et al.*, 1992). The Leeuwin Current flows mainly but not exclusively in the austral autumn and austral winter (Church *et al.*, 1989). The surface poleward current along the western Australian coast is weakest and shallowest between November and January, followed by the period of strongest and deepest flow between March and May.

The Leeuwin Current is unlike any other subtropical EBC. The major subtropical EBCs such as the California, Canary, Peru, and Benguela currents are characterized by climatologically weak ( $<10$  cm/s), broad ( $\sim 1000$  km wide), cold surface flow towards the equator in the direction of the prevailing winds, a poleward undercurrent, a shallow ( $<30$

m depth) thermocline, and high biological production due to vast regional upwelling (Parrish *et al.*, 1983). Observational studies along the coast of Western Australia have shown that the Leeuwin Current is characterized by a strong ( $>150$  cm/s at times), narrow ( $<100$  km wide), poleward surface current that flows opposite the prevailing wind direction (e.g., Cresswell and Golding, 1980; Godfrey *et al.*, 1986), anomalous warm water at the surface, a deep ( $>50$  m depth) thermocline (Thompson, 1984), and lower biological production due to vast regions of downwelling (Batteen *et al.*, 1992).

Godfrey and Ridgway (1985) have examined the observed seasonal signals of the forcing mechanisms between  $22^{\circ}\text{S}$  and  $32^{\circ}\text{S}$ . They discuss for this region, the relative strengths of the equatorward wind forcing and the opposing pressure gradient (Figure 1), noting that the individual seasonal cycle of one forcing mechanism reinforces the seasonal trends of the other. Specifically, the pressure gradient term, which experiences a larger seasonal amplitude than wind forcing, reaches its strongest poleward forcing when the opposing wind stress reaches its weakest forcing. This combination of the two similar phases could explain the observed seasonal trends in the Leeuwin Current System (LCS). Added to this seasonal forcing is a surge of warm, less saline water which flows poleward from the North West Shelf (NWS) region during the austral autumn (i.e., March through May) (Smith *et al.*, 1991). This surge of warmer water coincides with the period in which Godfrey and Ridgway (1985) found the strongest poleward pressure gradient forcing and weakest equatorward wind stress, resulting in a strong poleward driving function.

Below the Leeuwin Current, there is an equally significant anomalous equatorward undercurrent off western Australia (e.g., Church *et al.*, 1989). Smith *et al.*, (1991) stated that the speed of the undercurrent can reach ~30 cm/s between ~250 m and 350 m and observed that current meter data from the LUCIE experiment showed the equatorward current to be narrow and situated on the continental shelf slope between ~250 m and 450 m. Although there is evidence of a westward flow of ~20 cm/s centered between ~400 m and 700 m depth at Clifly Head off the southern coast of Australia (Cresswell and Peterson, 1993), no studies to date have clearly resolved whether there is a westward undercurrent in this region.

Previous numerical modeling studies by Batteen *et al.* (1992) investigated the effects of annual climatological wind forcing and initialized thermohaline gradients on the LCS, but the study was limited to the coast off western Australia, during the period when the LCS is observed to be strongest. Batteen and Butler (1998) examined the effects of continuously forced annual Indian Ocean thermohaline gradients on the LCS off both the western and southwestern coasts of Australia.

This study extends prior efforts through the addition of seasonal (rather than annual) wind forcing and thermal gradients, permitting a more representative forcing of the highly seasonal LCS. In particular, a full primitive equation (PE) ocean model is used to investigate the individual and combined roles of seasonal wind stress and thermal gradients, including NWS forcing, in the generation of currents and eddies off the western and southern coasts of Australia. One particular focus of this study will be to examine the development and variation of the equatorward undercurrent along the

western coast of Australia. The nature of the subsurface flow off the southwestern coast of Australia will also be investigated, with particular focus on whether there is a westward undercurrent. Additionally, the dependence of Coriolis parameterization ( $\beta$ -plane vs.  $f$ -plane) on the generation, evolution, and maintenance of currents and eddies off the western and southern coasts of Australia will be investigated.

This study is organized as follows. In Chapter II we describe the numerical model and the specific experimental conditions. The results and energy analyses of the model experiments are presented in Chapter III. A summary is presented in section IV.

## II. MODEL DESCRIPTION

### A. MODEL EQUATIONS

This study uses the eddy-resolving, limited-area EBC model of Batteen (1997) with open northern, western, and southern boundaries. Additionally, it has been modified by Batteen and Butler (1998) to have an open eastern boundary to account for interaction with the waters of the Great Australian Bight (GAB).

The model is multi-level, uses non-adiabatic primitive equations on a  $\beta$ -plane or  $f$ -plane, and has both baroclinic and barotropic velocity components. It is based on the hydrostatic, Boussinesq, and rigid lid approximations. Equations governing the model are as follows:

$$\frac{du}{dt} = \frac{-1}{\rho_0} \frac{\partial p}{\partial x} + fv - A_M \nabla^4 u + K_M \frac{\partial^2 u}{\partial z^2} \quad (1)$$

$$\frac{dv}{dt} = \frac{-1}{\rho_0} \frac{\partial p}{\partial y} - fu - A_M \nabla^4 v + K_M \frac{\partial^2 v}{\partial z^2} \quad (2)$$

$$\frac{\partial u}{\partial x} + \frac{\partial v}{\partial y} + \frac{\partial w}{\partial z} = 0 \quad (3)$$

$$\frac{\partial p}{\partial z} = -\rho g \quad (4)$$

$$\rho = \rho_0 [1 - \alpha(T - T_0) + \beta(S - S_0)] \quad (5)$$

$$\frac{dT}{dt} = -A_H \nabla^4 T + K_H \frac{\partial^2 T}{\partial z^2} \quad (6)$$

$$\frac{dS}{dt} = -A_H \nabla^4 S + K_H \frac{\partial^2 S}{\partial z^2} \quad (7)$$



In the above equations,  $t$  is time,  $T$  is temperature,  $S$  is salinity,  $p$  is pressure, and  $\rho$  is density. A right-handed Cartesian coordinate system  $(x,y,z)$  is used where  $x$  points onshore,  $y$  alongshore, and  $z$  upward. The corresponding velocity components are  $(u,v,w)$ . The variation of  $f$  with latitude is taken as  $f = (f_o + \beta y)$ , where  $f_o$  is the value of  $f$  at the mid-latitude of the region and  $\beta$  (or beta, the variation of the coriolis parameter with latitude)  $= \partial f / \partial y$  is given the value at the mid-latitude of the model domain. Table 1 provides a complete list of symbols found in the model equations, as well as values of constants used throughout the study.

A space-staggered B-scheme (Arakawa and Lamb, 1977) is used for the horizontal finite differencing. Batteen and Han (1981) have shown this scheme to be appropriate when the grid spacing is approximately on the same order as, or less than, the Rossby radius of deformation. The horizontal grid spacing is 11 km in the east-west direction and 14 km in the north-south direction, while the internal Rossby radius of deformation is  $\sim 30$  km, as determined by Feliks (1985). The model uses ten vertical layers, with constant  $z$ -levels, at depths of 10, 30, 75, 150, 250, 400, 600, 1226, 2283, and 3656 m. This vertical spacing scheme concentrates more layers above the thermocline, which is in the dynamically active portion of the ocean.

The model domain (Figure 2) encompasses the western and southwestern coasts of Australia, from 22.5°S to 40°S (1792 km alongshore), and from 107.5°E to 122.5°E (1408 km cross-shore). The coastal boundaries of the model domain are closed, and have both the tangential and normal components of velocity set to zero. Bottom topography has been omitted to focus on the roles of climatological wind forcing, thermal gradients,

and Coriolis parameterization. The coastal boundary is modeled as a vertical wall and the constant depth used in the model is 4500 m.

A modified version of the radiation boundary conditions of Camerlengo and O'Brien (1980) is used for the open boundaries to the north, south, east, and west with some spatial smoothing applied within five grid points (~60 km) of these boundaries (Batteen, 1997). Biharmonic lateral heat and momentum diffusion is used in the model with the same choice of coefficients (i.e.,  $2.0 \times 10^{17} \text{ cm}^4/\text{s}$ ) as in Batteen (1997). Holland (1978) showed that highly scale-selective biharmonic diffusion acts predominantly on submesoscales, while Holland and Batteen (1986) found that baroclinic mesoscale processes could be damped by Laplacian lateral heat diffusion. As a result, the use of biharmonic lateral diffusion should allow mesoscale eddy generation via barotropic (horizontal shear) and/or baroclinic (vertical shear) instability mechanisms. Weak ( $0.5 \text{ cm}^2/\text{s}$ ) vertical eddy viscosities and conductivities are also used. Bottom stress is parameterized by a simplified quadratic drag law (Weatherly, 1972), as in Batteen (1997).

The method of solution is straightforward with the rigid lid and flat bottom assumptions because the vertically integrated horizontal velocity is subsequently nondivergent. The vertical mean flow can be described by a streamfunction which can be predicted from the vorticity equation, while the vertical shear currents can be predicted after the vertical mean flow is subtracted from the original equations. The other variables, i.e. temperature, salinity, density, vertical velocity, and pressure, can be explicitly obtained from the thermodynamic energy equation (6), salinity equation (7),

equation of state (5), continuity equation (3), and hydrostatic equation (4), respectively (For more complete details on the method of solution, see Batteen, 1997).

## **B. FORCING CONDITIONS AND EXPERIMENTAL DESIGN**

The model is forced from rest with climatological wind fields from a  $2.5^\circ$  by  $2.5^\circ$  grid of the European Centre for Medium Range Weather Forecasts (ECMWF) near-surface wind analyses (Trenberth *et al.*, 1990). The monthly mean stresses based on twice daily wind analyses from 1980-1989 have been interpolated spatially to the 11 by 14 km model resolution and temporally to daily wind values. Examples of the wind fields are shown in Figure 3, which illustrates the seasonal influence and migration of flow around the Southern Indian Ocean Subtropical High over the area encompassed by the model domain. In February (Figure 3a), the winds circulate anticyclonically around the Subtropical High positioned west-southwest of Cape Leeuwin. This flow produces upwelling favorable winds along both the western and southern coasts of Australia. By May (Figure 3b), the Subtropical High has migrated equatorward to  $\sim 30^\circ\text{S}$ . The equatorward flow has weakened off western Australia and the wind has shifted to downwelling favorable westerlies off the southern coast of Australia. The Subtropical High reaches its maximum equatorward extent by July (Figure 3c), resulting in weak and variable flow off Western Australia. Strong westerlies and northwesterlies continue to dominate along the southern coast. By November (Figure 3d), the Subtropical High has migrated poleward, producing upwelling favorable winds with a strong equatorward

component along the western coast of Australia. The winds off southern Australia have shifted from downwelling favorable westerlies to weak upwelling favorable easterlies.

The effects of thermal gradients on the Leeuwin Current are incorporated by using the monthly temperature climatology from Levitus and Boyer (1994) to initialize the model, and every third day, to force the model at the western boundary (107.5°E). The seasonal temperature forcing conditions from Levitus and Boyer, which are initially assumed to be homogeneous, are shown for the seven levels in Figure 4a for the equatorward (22.5°S) and poleward (40°S) boundaries of the model domain. Note that at the poleward end of the western boundary, there are times (e.g., see months 4, 6, and 10 in Figure 4a), when cooler water overlies warmer water in the upper layers. Before inserting such temperatures in the model, the temperatures have been slightly adjusted (e.g., Figure 4b) so that warm water always overlies the cool water. This is an initialization requirement in the model, since at a boundary there is only forcing, and no convective adjustment. As a result, the western boundary temperature forcing used in the model is that depicted in Figure 4b.

Since the lower three levels of temperature from Levitus and Boyer (1994) do not exhibit much horizontal variation, they are assumed to be constant for each level. The temperature values used for levels 8-10 are 3.88°C, 2.20°C, and 2.00°C. To focus on the role played by thermal forcing, salinity variations are omitted in this study. The constant salinity used is 34.7.

While the temperatures to the north are warmer than those to the south, only the upper layer (e.g., Figure 4) temperature forcing conditions show significant seasonal

variability with a temperature maximum in late summer to early fall and minimum in late winter to early spring throughout the region. Below ~75m depth (not shown), both the seasonal temperature fluctuations and the temperature gradient weaken, as expected.

The NWS waters provide a significant influx of warm tropical water to the Leeuwin Current and are used as an additional thermal forcing source. The climatology of Levitus and Boyer (1994) provides a representative temperature profile for the NWS waters, which is used in this study (Table 2). The NWS waters are modeled as a horizontal homogeneous raft of warm water simulating a “dam breaking” applied to the northeastern ocean boundary of the model domain once during each model year (see Figure 28b, for example). This model approach is consistent with the hypothesis of flow reversals as a function of monsoonal winds isolating water on the NWS, which subsequently flow poleward (Gentili, 1972).

Table 3 summarizes the design of the seven basic experiments and two sensitivity experiments. In Experiment 1, the effects of seasonal thermal gradients on the generation of the Leeuwin Current when the model is run on a  $f$ -plane is investigated. With the use of a numerical model, we examine in an idealized way, the development of flow from rest when the temperatures are initially assigned the offshore alongshore gradient. The system is then forced every third day at the western boundary ( $107.5^{\circ}\text{E}$ ) with seasonally-varying climatological temperature fields from Levitus and Boyer (1994). Experiment 2, a sensitivity experiment, is the same as Experiment 1 except an ideal (straightened) west and south coast are employed (e.g., see Figure 6a). To isolate the effects of planetary beta, Experiment 3 is run using the same initialization and forcing parameters as in

Experiment 1, but on a  $\beta$ -plane. Experiment 4, a sensitivity experiment, is the same as Experiment 3 except only the top five layers are forced. Experiment 5 examines the role of seasonal wind forcing in the absence of thermal gradients on a  $f$ -plane. The model is initialized using a horizontally homogeneous temperature field and is then forced daily with seasonal ECMWF winds. Experiment 6 is the same as Experiment 5 except it is run on a  $\beta$ -plane. Experiment 7 investigates the combined effects of seasonal wind forcing and thermal gradients on a  $f$ -plane. Model initialization and forcing is a combination of Experiments 1 and 5. To isolate the effects of planetary beta, Experiment 8 is run using the same initialization and forcing parameters as in Experiment 7, but on a  $\beta$ -plane. Lastly, Experiment 9 examines the additional impact of the NWS waters (Table 2), along with seasonal wind forcing and thermal gradients. The model is run on a  $\beta$ -plane as in Experiment 8 with the release of NWS waters each year on model day 75 (which corresponds to mid-March, the timing of which is based on observations by Cresswell and Peterson, 1993). Note that in all of the experiments, the model is allowed to reach a quasi-equilibrium state by running each experiment for three years.

**THIS PAGE INTENTIONALLY LEFT BLANK**

### III. RESULTS FROM MODEL SIMULATIONS

#### A. EXPERIMENTS 1 AND 2 – RESULTS OF $f$ -PLANE THERMAL FORCING EXPERIMENTS

Due to the initial alongshore temperature field, the resulting pressure gradient establishes an onshore geostrophic inflow from the interior of the ocean. The onshore flow varies between  $\sim 2$  and  $10$  cm/s. As the flow approaches the coast, it turns and forms a narrow poleward boundary current, which subsequently enters the Great Australian Bight (Figure 5a). Additional onshore flow augments the coastal current causing the magnitude of the current to increase in both the poleward and eastward directions (not shown). By day 27 (Figure 5b), maximum velocities of the order of  $\sim 65$  cm/s are observed off Western Australia near Cape Leeuwin (see Figure 2 for geographical locations), and maximum velocities of  $\sim 100$  cm/s are observed off southern Australia.

The initial temperature field changes, as warm water is advected poleward and eastward throughout the domain. By day 27 (Figure 5b),  $22^{\circ}\text{C}$  water has moved as far south as Freemantle while  $20^{\circ}\text{C}$  water has been advected around Cape Leeuwin and reached the Great Australian Bight. Additionally, anticyclonic meanders develop along the coastal promontories, mesoscale features in the current intensify and grow, and by day 60 (see Figure 5c), eddies have formed off Freemantle, Cape Naturaliste and southwest of Clifffy Head.



Since this experiment was conducted on an  $f$ -plane, it was not clear that eddies would develop. In Batteen (1997), several experiments were run on an  $f$ -plane for the California Current System (CCS), the classical eastern boundary current system. In all experiments straight coastline geometry was used, while the model was forced using different types of wind stress. Under these conditions, eddies did not develop due to the undercurrent being too deep and weak, resulting in no near-surface baroclinic (vertical shear) or barotropic (horizontal shear) instability. Why did the eddies develop in this experiment?

Since the eddies are generated at preferred locations (coastal promontories), is irregular coastline geometry the dominant mechanism for eddy formation? Experiment 2, which used a straightened coast (e.g., see Figure 6a), was conducted to ascertain whether eddy generation could occur when no irregular coastline geometry is used. As expected, eddies did form at the coastal promontory (see Figure 6a). In time (e.g., see day 159 in Figure 6b), there was additional eddy generation with no apparent geographical preference, which showed that eddies could occur regardless of the coastline geometry used.

A meridional cross-section at  $\sim 32^\circ\text{S}$  (see Figure 7) reveals a poleward surface current with a core velocity of  $\sim 50$  cm/s overlying an equatorward undercurrent below  $\sim 200$  m depth with a core velocity of  $\sim 25$  cm/s centered at  $\sim 500$  m depth. The presence of a surface poleward current overlying a relatively shallow undercurrent results in both baroclinic and barotropic shear, which could lead to the subsequent generation of eddies.

What is the reason for the relatively shallow undercurrent in this case, since previous studies of the CCS did not show this feature?

The formation of the equatorward undercurrent could possibly be attributed to a temperature gradient reversal with depth, i.e., Figure 4 shows that below ~400 m depth the temperature in the poleward end of the model domain is warmer than the temperature in the equatorward end of the model domain. This reversal in temperature gradient with depth offers a plausible explanation for the formation of the undercurrent (This topic will be addressed in more detail in section III.B.2).

## **B. EXPERIMENTS 3 AND 4 – RESULTS OF $\beta$ -PLANE THERMAL FORCING EXPERIMENTS**

### **1. Spin-up Phase**

The  $\beta$ -plane model simulations of the Leeuwin Current are quite similar to the  $f$ -plane runs, with anticyclonic meander and eddy formations at coastal promontories. As expected, the significant difference is the westward propagation of the eddies in the  $\beta$ -plane cases. For example, a comparison of Experiments 1 and 3 on day 87 (Figure 5d and Figure 8a, respectively) and on day 117 (Figure 5e and Figure 8b, respectively) shows the core of the eddy moving to the south at ~29°S in Experiment 1 (compare Figures 5d and 5e), while Experiment 3 shows the eddy west of Freemantle (originally at ~111°E) propagating to the northwest at ~7 km/day (compare Figures 8a and 8b).

Additionally, westward propagation occurs along the southern coast of Australia in the  $\beta$ -plane experiment but not in the  $f$ -plane run (not shown).

For the same reason that the Leeuwin Current intensifies as it flows poleward (geostrophic inflow), one would expect the undercurrent to intensify as it flows equatorward. Closer examination of cross-sections along the west coast however, reveals the opposite. For example, a comparison of day 15 for Experiment 3 at  $\sim 32^\circ\text{S}$  (see Figure 9a) and at  $\sim 26^\circ\text{S}$  (see Figure 9b) shows core velocities for the undercurrent decreasing equatorward from  $\sim 25$  cm/s at  $\sim 32^\circ\text{S}$  to 15 cm/s at  $\sim 26^\circ\text{S}$ . A comparison for day 15 at the same latitudes for the  $f$ -plane Experiment 1 also shows the same trend (e.g., see Figures 10a and 10b). Why is this?

## 2. Analysis of Undercurrent Generation Mechanisms

Previous modeling studies (Weaver and Middleton, 1988; Batteen *et al.*, 1992; Batteen and Butler, 1998) have generated an equatorward undercurrent off the western coast of Australia, consistent with observations of LUCIE (Boland *et al.*, 1988). Off the southern coast of Australia, although Cresswell and Peterson (1993) have found evidence of a westward flow at Cliffy Head between 400 and 700 m depth with a speed of  $\sim 20$  cm/s, a lack of observations off this coast, particularly east of Cliffy Head, leaves some question as to the nature of the subsurface flow in that region, including its generation mechanism if present.

It is not clear what the mechanism for the generation of undercurrents is in the LCS. One possible mechanism for the development of the equatorward undercurrent off western Australia could be the pressure gradient forcing at depth. As discussed earlier, the Indian Ocean seasonal thermal gradients experience a reversal between ~400 m and 700 m depth (see Figure 4b), such that warmer waters are present in the poleward end of the model domain and cooler waters in the equatorward end.

Another possible mechanism for the generation of the equatorward undercurrent is the following: When the system is in equilibrium, the strong flow of the surface current generates alongshore temperature gradients at deeper levels, with warm waters at the poleward end of the model domain off Cape Leeuwin and cooler waters at the equatorward end of the model domain. These gradients are sufficient to establish and maintain an equatorward undercurrent along Western Australia.

An examination of the subsurface flow off the western coast of Australia in Experiment 3 shows that an equatorward undercurrent at ~ 400 to 600 m depth develops in the opposite direction of the surface current in this region. For example, Figure 11a shows the equatorward flow at ~600 m depth.

Of the two proposed mechanisms, the alongshore pressure gradient at depth cannot explain the equatorward undercurrent. In particular, the geostrophic velocity in response to the pressure gradient at depth would be in the offshore direction rather than onshore. Therefore we hypothesize that the second proposed mechanism, the generation of deeper alongshore thermal gradients by the surface flow, may explain the equatorward undercurrent.

To examine this further, we conducted a special experiment (Experiment 4 in Table 3) that removes the thermal gradient below 400 m depth. The model is initialized as in Experiment 3; however, the thermal forcing is only applied at the upper five levels. Level 6 (400 m) is given a constant temperature of  $\sim 10.5^{\circ}\text{C}$ , while level 7 (600 m) is given the constant temperature of  $\sim 8.7^{\circ}\text{C}$ .

Figures 12a and 12b show cross-shore velocity sections for Experiment 4 at  $\sim 32^{\circ}\text{S}$  and at  $\sim 26^{\circ}\text{S}$  for model day 3. At this time, the shallowest equatorward undercurrent with a core velocity of  $\sim 4$  cm/s at  $\sim 600$  m depth has developed near  $\sim 26^{\circ}\text{S}$ . The undercurrent continues to intensify so that by day 9 (Figure 12c and 12d), equatorward undercurrents are well developed at both latitudes. The core of the deepest and strongest undercurrent (Figure 12c), however, is located near the poleward end of the model domain. The progression of development of this undercurrent in the absence of an initial pressure gradient, with the deepest and strongest current in the poleward region of the model domain, is consistent with our second proposed mechanism. In particular, the strengthening poleward surface flow generates alongshore temperature gradients at deeper levels. These temperature gradients, which are most pronounced in the region near Cape Leeuwin, are sufficient to establish and maintain an equatorward undercurrent off western Australia.

We now examine the nature of the subsurface flow off the southern coast of Australia. Analysis of Figure 11a shows that a continuous westward undercurrent develops in the opposite direction of the surface flow off southern Australia in

Experiment 3. A cross-shore velocity section at 117°E (Figure 13a) shows that the westward undercurrent has its core centered at ~600 m depth and has speeds of ~20 cm/s.

Analysis of Figure 11b shows that there is also a continuous westward undercurrent off southern Australia in Experiment 4. A cross-shore velocity section at the same location (i.e., 117°E) for Experiment 4 (e.g., Figure 13b) also shows similar core depths and speeds as in Experiment 3.

In Experiment 4, even with the absence of forcing of a deep thermal gradient, a westward undercurrent still develops. Can we attribute the development of this westward undercurrent along the southern coast of Australia to the generation of alongshore temperature gradients at deeper levels, as was seen in the development of the equatorward undercurrent along the western coast of Australia?

Cross-shore velocity sections for Experiment 4 at 117°E (Figure 13b) and at 122°E (Figure 13c) show core velocities for the undercurrent decreasing eastward from ~15 cm/s at 117°E to ~7.5 cm/s at 122°E. Additionally, the core of the undercurrent deepens eastward from ~600 m depth at 117°E to ~1300 m depth at 122°E. Note that the deepest and strongest undercurrent in the westward region off southern Australia coincides with the region of the strongest surface eastward flow, i.e., Figure 13b (Figure 13c) shows surface flows of ~60 cm/s (~40 cm/s). A comparison of velocity (Figures 13b and 13c) and temperature (Figures 14a and 14b) cross-sections shows that the core of the surface current (undercurrent) at each location coincides with the downward (upward) bending of isotherms. These results are consistent with the proposed generation mechanism that alongshore temperature gradients, which are generated at deeper levels

by the strong flow of the Leeuwin Current, are sufficient to drive an alongshore flow and set up a westward undercurrent below ~400 m depth off southern Australia.

### **C. EXPERIMENT 5 – RESULTS OF $f$ -PLANE WIND FORCING EXPERIMENT**

In this  $f$ -plane experiment the model was run using seasonal wind forcing only (see Table 3), so that no thermal gradients were incorporated. While wind forcing only is an unlikely scenario for the LCS, it could still play an important role in the seasonal cycle of the LCS.

As expected, the initially strong upwelling favorable wind stress results in an equatorward surface current off western Australia and a westward surface current off southern Australia (e.g., Figure 15a). A comparison of cross-sections of meridional velocity at ~32°S (Figure 16a) and ~26°S (Figure 16b) shows a shallow equatorward surface current above ~200 m depth with velocities decreasing equatorward from ~20 cm/s at ~32°S, to ~10 cm/s at ~26°S. Beneath the surface current lies a much weaker poleward undercurrent with an average core depth of ~400 to 600 m and a speed of ~1 cm/s, which is more developed near the equatorward end of the model domain (e.g., compare Figures 16a and 16b). Additionally, during the period of strong equatorward winds (for example, see Figure 3a), offshore Ekman transport has resulted in coastal upwelling off the western coast (e.g., Figure 15a). The weak easterlies off the southern coast have also produced colder water consistent with upwelling along with a westward

current (e.g., Figure 15a), which attains a maximum velocity of  $\sim 50$  cm/s near Clifty Head (not shown).

As the westward surface current off the southern coast flows around Cape Leeuwin, turns equatorward, and flows along the western Australia coast, it encounters the coastline northwest of Dongara, which deflects the surface flow to the northwest. This deflection of the flow sets up an anticyclonic meander (e.g., Figure 15b), and subsequently develops into a warm core, anticyclonic eddy at  $\sim 29^\circ\text{S}$  (e.g., see Figure 15c). Concurrently, a cold core, cyclonic eddy forms to the south of the warm core eddy, resulting in the formation of an eddy pair (e.g., see Figure 15c).

Another interesting development, similar to a study conducted by Batteen and Murray (2000) in which anticyclonic mesoscale activity occurred in an embayment, i.e., the Gulf of Cadiz, occurs in this case. By day 297 (see Figure 15d) an anticyclonic eddy has formed inshore of the equatorward surface current in the embayment area to the north of Cape Naturaliste and persists throughout the remainder of the year. The strong equatorward surface current just offshore and the lack of the planetary  $\beta$ -effect (which would result in westward propagation of the eddy) essentially traps the eddy, preventing any offshore movement. With the exception of the eddy formations just discussed, there was no other mesoscale activity during the first year of the model run.

It is interesting to note that only a relatively weak subsurface current below  $\sim 1000$  m depth develops off the southern coast. For example, Figure 17a shows that the subsurface flow on day 243 is found below the westward surface current of  $\sim 30$  cm/s at  $\sim 1200$  m depth, and is relatively weak, with a typical eastward speed of  $\sim 4$  cm/s. By the



end of the year (e.g., Figure 17b), the equatorward flow below the deep surface current of ~65 cm/s has attained a maximum speed of ~8 cm/s, which is relatively weak compared to the intense surface current.

By the end of the year (e.g., Figure 15e), due to the return of strong equatorward winds, upwelling occurs everywhere inshore of the coastal current off western Australia with the most intense upwelling occurring equatorward of ~31°S. Additionally, the equatorward surface current has intensified to speeds as strong as ~80 cm/s.

#### **D. EXPERIMENT 6 – RESULTS OF $\beta$ -PLANE WIND FORCING EXPERIMENT**

As discussed earlier, results from previous sensitivity studies along eastern ocean boundaries (e.g., Batteen, 1997) have produced various results depending on the type of wind forcing, coastline geometry and Coriolis parameterization used. For the CCS, Batteen (1997) forced the model from rest using seasonal climatological winds along a straight California coast on both an  $f$ -plane and  $\beta$ -plane. Her study also included seasonal climatological wind forcing on an irregular coastline using  $\beta$ -plane only and focused on the role of the beta effect in generating, evolving and maintaining classical mesoscale features in the CCS. The results of her study showed that a surface equatorward current, upwelling of cooler water along the coast, and a poleward undercurrent develop. In addition, both baroclinic and barotropic instability develop due to the vertical and horizontal shear between the equatorward surface current and poleward flow, resulting in the generation of meanders near the coast, upwelling

filaments extending offshore, and the subsequent development of seasonal or semi-permanent cyclonic and anticyclonic eddies farther offshore. While the meridional variability of  $f$  ( $\beta$ -plane) and variability in the equatorward component of wind stress were shown to be necessary ingredients for generating realistic vertical and horizontal structures for the cores of the surface equatorward and subsurface poleward currents, irregularities in the coastline geometry were shown to be important for “anchoring” upwelling and filaments, and for enhancing the growth of meanders and eddies. The results from several numerical experiments in this process-oriented study supported the hypothesis that wind forcing and coastline irregularities on a  $\beta$ -plane are important mechanisms for generation of observed mesoscale features of the CCS (Batteen, 1997).

The expected outcome of wind forcing only on a  $\beta$ -plane in our experiment in the LCS would be similar to what Batteen (1997) found in the CCS. Additionally, one would not expect to see the development of as strong of an equatorward surface current (which formed in the  $f$ -plane run) along the western coast of Australia, due to the westward dispersion of energy associated with the planetary beta effect.

As expected, in response to the strong upwelling favorable wind stress, an equatorward surface current off western Australia and a westward surface current off southern Australia (e.g., Figure 18a) develop, similar to the  $f$ -plane case. A comparison of meridional cross-sections for day 33 at  $\sim 32^\circ\text{S}$  and  $\sim 26^\circ\text{S}$  (see Figures 19a and 19b, respectively) reveals weaker equatorward surface current and stronger poleward undercurrent speeds than in the previous experiment (e.g., see Figures 16a and 16b). This is due to the beta effect, which results in weaker surface currents and stronger

undercurrents. Other differences from the  $f$ -plane are seen with the development of cyclonic meanders off Cape Leeuwin, off the promontory northwest of Freemantle, and off the promontory northwest of Dongara (e.g., Figure 18b).

By day 165 (see Figure 18c), during the period of weakest winds off western Australia (e.g., see Figure 3c), the equatorward flow has weakened significantly from  $\sim 15$  cm/s to  $\sim 7.5$  cm/s (e.g., compare Figures 20a and 20b). While the westward surface current off the southern coast has also weakened, the onshore Ekman transport produced by the stronger westerlies in that region (e.g., see Figure 3c) continues to augment the westward flow, extending the current west of Cape Leeuwin (e.g., Figure 18c). As a result, a large ( $\sim 250$  km diameter) cyclonic eddy has formed off Cape Leeuwin and the surface flow “jets” westward and equatorward around this feature. Additionally, anticyclonic eddies develop resulting in the formation of eddy pairs (e.g., see eddy pairs at  $\sim 28^\circ\text{S}$  and at  $\sim 30^\circ\text{S}$  in Figure 18c).

With the return of upwelling favorable equatorward winds (e.g., see Figure 3d) during the latter part of the year along the western Australia coast, a strong equatorward surface current and a poleward undercurrent re-develop. For example, cross-shore velocity sections at  $\sim 26^\circ\text{S}$  (e.g., Figure 20c) show a relatively strong ( $\sim 30$  cm/s) equatorward surface current overlying a weaker ( $\sim 15$  cm/s) poleward undercurrent centered at  $\sim 400$  m depth.

The structure of the westward surface current and eastward undercurrent along the southern coast of Australia are similar to that of the  $f$ -plane experiment, i.e., a moderate

surface current continues to overly a weaker undercurrent. This is expected since the planetary beta effect should have no effect on a southern coast, which acts like an  $f$ -plane.

## **E. EXPERIMENT 7 – RESULTS OF $f$ -PLANE THERMAL AND WIND FORCING EXPERIMENT**

In previous experiments, the presence of seasonal thermal gradients only caused geostrophic inflow to dominate throughout the domain. The presence of wind forcing only, due to the seasonally varying alongshore and cross-shore components of wind velocity (Figure 3), produces a more complex flow regime. In particular, at the equatorward end of the model domain, since the winds have offshore and equatorward components, Ekman theory predicts poleward and offshore transport of mass, respectively. At the poleward end of the model domain off Western Australia, since the winds have onshore and equatorward components, there should be equatorward and offshore transport, respectively. Off the southern coast, the change from upwelling favorable to downwelling favorable winds as the seasons change should produce offshore and then onshore mass transport.

The combination of seasonal Indian Ocean temperature forcing at the western boundary with seasonal wind forcing is expected to produce results similar to available observations. Based on the results of the previous experiments, it is speculated that the seasonally-varying strengths of the thermal gradients and wind forcing mechanisms (see Figure 1) will result in an unstable poleward flow that adjusts to seasonal variations.

As expected, the initial thermal gradient, with temperature decreasing polewards, establishes a predominantly onshore geostrophic inflow in the interior ocean. On approaching the coast, the onshore flow turns and forms a poleward boundary current (e.g., Figure 21a), which advects warmer water from the equatorward end of the model domain. Offshore to the west, the equatorward wind stress dominates and drives offshore flow. Along the southwest coast, the poleward surface current rounds Cape Leeuwin and flows eastward towards the Great Australian Bight. The upwelling favorable winds east of Albany (see Figure 3a), initially drive an offshore flow, while the westerlies poleward of 38°S drive an onshore flow.

By day 30 (Figure 21b), the poleward flow is well established and intensifies poleward. For example, a cross-shore section of meridional velocity near Freemantle (Figure 22a), depicts the relatively narrow (~20 km) structure of the poleward current extending to ~250 m depth with a core surface velocity of ~40 cm/s. There is also a weaker (~25 cm/s) equatorward undercurrent centered at ~500 m depth. A comparison of this cross-section with one at ~26°S (Figure 22b) reveals a weaker poleward surface current (~4 cm/s) to the north, as expected when thermal forcing dominates.

The current “jets” around Cliffy Head, accelerating toward the Great Australian Bight region (e.g., Figure 21b). Warm (20°C) water has been advected around Cape Leeuwin and reached Albany. A cross-shore section off the southern coast (Figure 23) depicts an eastward surface current, which has a core velocity of ~60 cm/s, overlying a westward undercurrent, which has a core velocity of ~15 cm/s.

By day 30 (Figure 21b), anticyclonic meanders appear, near Freemantle, and in the vicinity of Cape Naturaliste, Cape Leeuwin, and Clifffy Head. In time, the anticyclonic meanders develop into eddies (e.g., see eddy at  $\sim 31^\circ\text{S}$  in Figure 21c) and propagate slightly offshore (e.g., see eddy at  $\sim 31^\circ\text{S}$  in Figure 21d), to a similar offshore extent as was seen in Experiment 1, which had thermal forcing only.

By the end of the year, wind forcing has become the dominant forcing mechanism over the entire model domain. A cold, westward "jet" has formed and rounded Cape Leeuwin (e.g., Figure 21e), similar to Experiment 5 (see Table 3), and extends up the coast to Freemantle. A cross-shore section of meridional velocity at  $\sim 26^\circ\text{S}$  (see Figure 24a) reveals that the flows have reversed (e.g., compare with Figure 22b), resulting in an intense ( $\sim 55$  cm/s) and deep (extends to  $\sim 1100$  m depth) equatorward surface current overlying a weaker ( $\sim 6$  cm/s) poleward undercurrent. Once established, the intense equatorward "jet" that forms in the  $f$ -plane experiment due to the wind forcing dominates over any poleward surface flow that could be due to the effects of thermal forcing (e.g., years 2 and 3, not shown).

## **F. EXPERIMENT 8 - RESULTS OF $\beta$ -PLANE THERMAL AND WIND FORCING EXPERIMENT**

In time, the addition of the planetary beta effect should result in a more realistic depiction of eddies and coastal upwelling off the western coast of Australia due to the westward dispersion of energy. Initially, however, the  $\beta$ -plane model simulation is quite

similar to the  $f$ -plane run of Experiment 7 (see Table 3), with anticyclonic meander and eddy formations (e.g., compare Figures 21b and 25a of Experiments 7 and 8, respectively) at similar geographical locations (for example, off coastal promontories). A comparison of meridional cross-sections at  $\sim 32^\circ\text{S}$  and  $\sim 26^\circ\text{S}$  (e.g., compare Figures 26a and 26b, respectively) also reveals comparable poleward surface current and equatorward undercurrent speeds and core depths as seen at both locations in the previous experiment (e.g., see Figures 22a and 22b).

Similar to the thermal forcing results of Experiments 3 and 4, a significant difference from the  $f$ -plane run is the westward propagation of the eddies in the  $\beta$ -plane case. For example, a comparison of Experiments 7 and 8 on day 63 (Figure 21c and Figure 25b, respectively) and on day 123 (Figure 21d and Figure 25c) shows the core of an eddy at  $\sim 31^\circ\text{S}$  meandering slightly to the north in Experiment 7 (e.g., compare Figures 21c and 21d), while Experiment 8 shows a similarly located eddy propagating to the west-northwest at  $\sim 5$  km/day (e.g., compare Figures 25b and 25c).

By day 165 (Figure 25d), during the period when the Leeuwin Current is observed to be the strongest, a poleward flow is maintained at  $\sim 25$ – $45$  cm/s off the western coast. A cross-shore velocity section near Fremantle (Figure 24b) depicts the typical nature of the Leeuwin Current. A shallow ( $< 250$  m depth) poleward surface current with a speed of  $\sim 25$  cm/s, which is confined to within 50 km of the coast, overlies a weaker equatorward undercurrent with a speed of  $\sim 15$  cm/s at  $\sim 500$  m depth.

By the end of the model year (e.g., Figure 25e), when the winds have become strongly equatorward off the western coast, the signature of the surface poleward

Leeuwin Current is lost, and equatorward currents dominate the coastal region. A comparison of meridional cross-sections at  $\sim 32^{\circ}\text{S}$  and  $\sim 26^{\circ}\text{S}$  (see Figures 27a and 27b, respectively) depicts the dominance of the wind forcing. At  $\sim 32^{\circ}\text{S}$ , a shallow ( $< 200$  m depth) equatorward surface flow of  $\sim 15$  cm/s, overlying a poleward undercurrent with a core speed of  $\sim 10$  cm/s at  $\sim 400$  m depth is evident, while at  $\sim 26^{\circ}\text{S}$  a poleward undercurrent with a core speed of  $\sim 7.5$  cm/s has shoaled inshore of a broad equatorward surface flow of  $\sim 15$  cm/s (Figure 27b). This is due to the planetary beta effect, which has acted to move water offshore along the west coast of Australia. In conjunction with the equatorward surface current, coastal upwelling along the northwest coast (e.g., north of  $\sim 27^{\circ}\text{S}$ ) is more prevalent in this case than in the  $f$ -plane experiment (e.g., compare Figures 21e and 25e).

Further examination of years 2 and 3 (not shown) reveal a very weak Leeuwin Current signature for only a short period of time during the austral winter, a period when it should be most pronounced. Otherwise, wind forcing dominates, resulting in an unrealistic depiction of the LCS similar to the results of the previous experiment. Based on these results, we speculate that there must be another forcing mechanism that, in conjunction with thermal forcing, acts on the LCS and overcomes the dominant equatorward currents due to the wind forcing.



## G. EXPERIMENT 9 – RESULTS OF $\beta$ -PLANE THERMAL, WIND, AND NORTHWEST SHELF WATERS FORCING EXPERIMENT

### 1. Spin-up Phase

The introduction of warm NWS waters, in conjunction with wind forcing and thermal gradient forcing, is expected to generate the most realistic depiction of the Leeuwin Current System. The release of the NWS waters during mid-March of each model year is expected to introduce baroclinicity into the Leeuwin Current (e.g., Batteen *et al.*, 1992), although the effects should diminish away from the source region. Batteen and Butler (1998) demonstrated that the addition of warmer NWS waters could intensify the current velocity and temperature fronts, and act to produce a more unstable flow regime.

Before the onset of NWS waters, the flow is, as expected, the same as in Experiment 8 (e.g., see Figure 25a), with onshore geostrophic flow driving a poleward surface current along the western coast (not shown). Off southern Australia, the current “jets” around Cape Leeuwin and flows into the Great Australian Bight. By day 75 (not shown), anticyclonic meanders and instabilities have developed at coastal promontories, anticyclonic eddies have propagated westward advecting warm water to the offshore regions, and the flow around the southern coast has weakened in response to easterly winds.

The release of the NWS waters in the coastal region north of Carnarvon at day 78 (Figure 28a) introduces a strong thermal front in the region and augments the poleward flow. By day 102 (Figure 28b), the "raft" of NWS water has been advected poleward and has reached Dongara. A cross-shore section of velocity at  $\sim 26^{\circ}\text{S}$  (e.g., Figure 29) depicts the well-developed surface current with speeds of  $\sim 60$  cm/s overlying a weak ( $\sim 6$  cm/s) undercurrent centered at  $\sim 250$  m depth. The flow near Cape Leeuwin has become stronger than in Experiment 8, attaining a speed of  $\sim 60$  cm/s (e.g., see Figure 28b), consistent with the increased thermal forcing and the weakening equatorward winds during this time.

The effects of the NWS waters have reached their farthest extent by day 165 (Figure 28c). A comparison of Experiments 8 and 9 depicts a more well-developed Leeuwin Current along the western and southern coasts of Australia in Experiment 9 than in Experiment 8 (e.g., compare Figures 28c and 25d, respectively). In Experiment 9 (Figure 28c), the warm surge of NWS water is contained close to the coast with  $24^{\circ}\text{C}$  water extending south of Dongara and a pocket of  $22^{\circ}\text{C}$  water approaching Clifty Head, while Experiment 8 (Figure 25d) results show  $20^{\circ}\text{C}$  water at both of these locations. Cross-sections of meridional velocity (Figure 30) at  $30^{\circ}\text{S}$  show a poleward surface flow of  $\sim 60$  cm/s for Experiment 9 (Figure 30a) while the cross-section for Experiment 8 (Figure 30b) depicts a weaker ( $\sim 25$  cm/s) poleward flow. Cross-sections of zonal velocity (Figure 31) at  $117^{\circ}\text{E}$  show an easterly surface flow of  $\sim 120$  cm/s and a westerly undercurrent of  $\sim 30$ - $40$  cm/s for Experiment 9 (Figure 31a), while the cross-section for

Experiment 8 (Figure 31b) shows a weaker ( $\sim 70$  cm/s) easterly surface flow overlying a stronger westerly undercurrent of  $\sim 30$ – $40$  cm/s.

By day 363 (Figure 28d), when the opposing wind forcing (see Figure 3) has returned, the effects of the NWS waters diminish and the poleward surface current off the western coast is no longer discernible. A comparison of meridional cross-sections at  $\sim 32^\circ\text{S}$  (Figure 32a) and  $\sim 26^\circ\text{S}$  (Figure 32b) depicts the equatorward surface flow along the western coast of Australia with a stronger ( $\sim 30$  cm/s) equatorward surface current near Shark Bay (Figure 32a) than at Freemantle ( $\sim 10$  cm/s) (Figure 32b) due to stronger equatorward wind forcing (e.g., see Figure 3d). The opposing wind off the southern coast also results in the weakening and subsequent reversal of the surface flow from eastward to westward (e.g., Figure 28d).

## **2. Quasi-equilibrium Phase**

A continuation of the model run shows that a quasi-steady state has been reached by year 3, and reveals that most features recur on a seasonal basis. Specifically, the release of NWS waters on day 807 (day 78 of year 3, not shown) tends to augment the thermal forcing, which results in the development of a relatively strong surface poleward current. Anticyclonic meanders form near Shark Bay and Dongara and subsequently develop into eddies (e.g., Figure 33a). By day 915 (day 185 of year 3, Figure 33b), during the period when the Leeuwin Current is observed to be the strongest, the water off the coast of Dongara is  $22^\circ\text{C}$ , consistent with observations by Cresswell and Peterson

(1993), while 19°C water has been advected around Cape Leeuwin, extending to the east of Clifty Head. In addition, a typical meridional cross-section during the same period at ~30°S (e.g., see Figure 34) depicts a 25 cm/s poleward surface current inshore of a 15 cm/s core equatorward undercurrent centered at ~250 m depth along the western coast, comparable to results from the LUCIE experiment which measured 38.5 cm/s for the poleward surface current and 5.9 cm/s for the undercurrent with a core located at ~300 m depth during the austral winter (e.g., Church et al., 1989; Boland et al., 1988; Smith et al., 1991). A typical zonal cross-section along the southern coast at 117°E (e.g., see Figure 35a) reveals an ~80 cm/s eastward surface current, consistent with observations reported by Cresswell and Peterson (1993), overlying a deeper, 10 cm/s westward undercurrent.

In time, as expected, the effects of the NWS water begin to diminish and by late spring-early summer, the return of opposing winds (to the flow of the Leeuwin Current) diminishes the poleward and eastward flow. Subsequently, the flow reverses and eddy generation decreases (e.g., Figure 33c), pre-existing eddies propagate offshore (see eddy at 34°S in Figures 33c and 33d), and upwelling occurs along the entire coast (e.g., Figures 33c and 33d), and is strongest north of 28°S. This scenario completes the seasonal cycle of the Leeuwin Current System, as the wind forcing causes the Leeuwin current to weaken and retreat equatorward. The strengthening of the thermal gradient the following year, in conjunction with the release of NWS waters in mid-March, causes the Leeuwin Current to re-intensify and advance poleward during the austral autumn and summer.

Cross-sections of meridional velocity (Figure 36) at 30°S show a weak poleward undercurrent of ~4 cm/s for Experiment 9 (e.g., Figure 36a) while the cross-section for

Experiment 6 (e.g., Figure 36b) depicts a stronger ( $\sim 15$  cm/s) poleward undercurrent. During this period when wind forcing is, once again, dominant along the west coast of Australia, the influence of the opposing surface forcing mechanisms due to thermal forcing and NWS waters is still apparent, resulting in a weaker poleward undercurrent on the west coast in Experiment 9.

Cross-sections of zonal velocity at  $117^{\circ}\text{E}$  show a relatively strong eastward undercurrent of  $\sim 40$  cm/s for Experiment 9 (e.g., Figure 35c), while the cross-section (e.g., Figure 37) for Experiment 6 depicts a much weaker ( $\sim 10$  cm/s) and deeper eastward undercurrent. Along the southern Australia coast, the westward surface flow in both Experiments 6 and 9 has developed in response to strong westward winds, accompanied by an opposing eastward undercurrent which develops below the westward flow.

### **3. Analyses of Mean and Eddy Kinetic Energy**

Typical cross-sections for the surface poleward and subsurface equatorward currents along the west coast (e.g., Figure 34) show considerable horizontal and vertical shear in the upper layer currents. To determine the type of instability that could generate the meander and eddy features, more detailed analysis was performed. Barotropic instability can result from horizontal shear in the currents, while vertical shear in the currents can cause baroclinic instability.

To indicate locations of barotropic and baroclinic instability, horizontal maps of the upper layer mean kinetic energy (MKE), eddy kinetic energy (EKE), and temperature

contours with velocity vectors were time-averaged for the six month period when the Leeuwin Current was the strongest (April–September). MKE and EKE results for this period (e.g., Figures 38a and 38b) show that high values of MKE and EKE are found along the jet axis of the surface current off the western and southern coasts of Australia, particularly in the regions of eddy development (e.g., compare Figures 38a and 38b to Figure 39a). High values of EKE are also indicated offshore, where eddies propagate. A comparison of Figures 38a and 38b shows that maximum values of MKE and EKE occur in the same general region. This is consistent with the results of Batteen (1997), which showed that eddies in the CCS are generated from instabilities of the mean surface current and the undercurrent via barotropic and/or baroclinic instability processes. Additionally, the NWS waters have added greater horizontal and vertical shear, resulting in greater barotropic and baroclinic instability processes, all along the west coast.

To help elucidate the forcing mechanism(s) responsible for the MKE and EKE areas (Figure 38) depicted in Experiment 9, horizontal maps of the upper layer MKE, EKE, and temperature contours with velocity vectors, time averaged for the six month period from April – September, were also obtained for Experiments 3, 6, and 8. In the thermal forcing only case (Experiment 3), typical cross-sections of meridional velocity (e.g., Figure 40a) at  $\sim 30^{\circ}\text{S}$  and zonal velocity (e.g., Figure 40b) at  $\sim 117^{\circ}\text{E}$  both show horizontal and vertical shear in the upper layers near the coast. The MKE and EKE results (e.g., Figure 41) show that the highest MKE and EKE values are found along the jet axis of the eastward surface current (e.g., see Figure 39b) along the southwest and

southern coasts of Australia, particularly in the regions near Cape Leeuwin and Clifly Head.

In the wind forcing only case (Experiment 6), a typical cross-section of meridional velocity (e.g., Figure 42a) at  $\sim 30^{\circ}\text{S}$  shows horizontal shear in the upper layers, while a typical cross-section (e.g., Figure 42b) of zonal velocity at  $\sim 117^{\circ}\text{E}$  shows no near-surface horizontal or vertical shear. The MKE results (e.g., Figure 43a) show that the highest values are found along the jet axis of the westward surface current off the south coast of Australia, with another, less intense maximum near Dongara (e.g., see Figure 39c). The highest values of EKE (e.g., Figure 43b) are located off the western coast of Australia between  $\sim 29^{\circ}\text{S}$  to  $\sim 27^{\circ}\text{S}$  and offshore of Capes Leeuwin and Naturaliste (e.g., Figure 39c). The absence of EKE (i.e., see Figure 43b), in conjunction with no near-surface shear (e.g., Figure 42b), along the southern coast of Australia in Experiment 6 indicates that the eddy development along the southern coast of Australia in Experiment 9 must be due to thermal rather than to wind forcing.

In Experiment 8 (thermal and wind forcing), typical cross-sections of meridional velocity (e.g., Figure 44a) at  $\sim 30^{\circ}\text{S}$  and zonal velocity (e.g., Figure 44b) at  $\sim 117^{\circ}\text{E}$  show both horizontal and vertical shear in the upper layers. The MKE results (e.g., Figure 45a) show that the highest values are found along the jet axis of the eastward surface current along the south coast of Australia and along the jet axis of the equatorward surface current offshore of Shark Bay and between  $\sim 33^{\circ}\text{S}$  to  $\sim 25^{\circ}\text{S}$  west of  $\sim 112^{\circ}\text{E}$  (e.g., compare Figure 45a to Figure 39d). The EKE results (e.g., Figure 45b) show highest values in the same regions as the MKE results, but depict an eddy development region all along

western Australia. Comparison of EKE results from Experiment 8 (e.g., Figure 45b) and Experiment 9 (e.g., Figure 38b) reveal higher values of EKE all along the west coast in Experiment 9, due to the addition of NWS waters. The NWS waters have added greater horizontal and vertical shear, resulting in greater barotropic and baroclinic instability processes, all along the west coast.



**THIS PAGE INTENTIONALLY LEFT BLANK**

#### IV. SUMMARY

The objective of this study was to use a multilevel PE model to investigate the effect of seasonal thermal gradients and wind forcing and the role played by planetary beta in the generation and maintenance of the LCS. Toward this end, several numerical experiments were run with varying Coriolis parameterizations ( $f$ -plane or  $\beta$ -plane) using either thermal gradients only, wind forcing only, or a combination of both. Additionally, the seasonal effects of the NWS waters were included in another experiment, yielding insight into the importance of this secondary forcing mechanism. A final goal of this research was to investigate the development of undercurrents along the western and southern coast of Australia.

The results of Experiment 1 revealed how seasonal thermal gradients on an  $f$ -plane generate and maintain a poleward and eastward surface current overlying a westward and equatorward undercurrent. Additionally, eddies were generated at preferred locations (coastal promontories) but did not migrate westward. To determine whether irregular coastline geometry was the dominant mechanism for eddy formation, Experiment 2 was run using a straightened coast. Eddy generation still occurred, but with no apparent geographical preference. The formation of eddies was attributed to the baroclinic and barotropic shear between the thermally forced poleward surface current and equatorward undercurrent.

In Experiment 3, the beta effect, as expected, did not yield any major differences from Experiment 1, other than the westward propagation of eddies. Examination of

meridional cross-sections along the west coast revealed that the undercurrent weakened equatorward (opposite of the poleward intensifying surface current due to geostrophic inflow) when one would have expected the undercurrent to intensify due to geostrophic inflow. This result led to an investigation of possible generation mechanisms for the coastal undercurrent. A comparison of model results from Experiment 4, which, after initialization used no thermal forcing below the upper five levels, with Experiment 3 showed that along the western and southern coasts of Australia, the strong flow of the surface current generated alongshore temperature gradients at deeper levels, which were sufficient to establish and maintain an equatorward (westward) undercurrent along western (southern) Australia.

The results from Experiment 6, the beta plane, wind forcing only case, demonstrated the importance of spatially and temporally varying wind in the seasonal nature of the LCS. The strong equatorward winds of the austral spring and summer generated significant upwelling along the entire coastline, particularly in the equatorward region of the model domain. This upwelling became weak and somewhat suppressed with the weaker winds of the austral fall and winter, which corresponds to the period when the Leeuwin Current is observed to be the strongest. Cyclonic meander formation and subsequent eddy formation off Cape Leeuwin and the major promontories were consistent with previous EBC studies (e.g., Batteen, 1997).

To isolate the role of the beta effect, the results of Experiment 5 ( $f$ -plane) were compared to Experiment 6. The  $f$ -plane case also generated a westward flow along the southern coast and equatorward flow along the west coast. Closer examination, however,

revealed a stronger equatorward surface current and a weaker poleward undercurrent than the  $\beta$ -plane case. This was attributed to the beta effect, which results in weaker surface currents and stronger undercurrents due to offshore transport at the surface and the resultant inflow at depth. As the model year progressed, an intense equatorward "jet" developed, which was stronger and farther offshore than in Experiment 6. An interesting feature of the  $f$ -plane case was the development and continued presence of an anticyclonic eddy inshore of the "jet" in the embayment north of Cape Naturaliste. With the exception of the eddy just discussed and an eddy pair that generated off the promontory northwest of Dongara, mesoscale activity was non-existent in the  $f$ -plane case.

The results of Experiment 7 explored the combined role of seasonal thermal gradients and wind forcing, on an  $f$ -plane, in the LCS. The relative strength of the combined forcing mechanism initially varied with the seasonal fluctuations of thermal gradients and wind forcing. The poleward and eastward Leeuwin Current strengthened and weakened in response to these seasonal variations. Anticyclonic meanders were generated and, in time, developed into eddies which propagated to a similar offshore extent as was seen in Experiment 1, the thermal forcing only,  $f$ -plane case. By the end of the year, when wind forcing became dominant over the entire model domain, a cold, westward "jet" developed along the south coast and moved around the cape, extending up the coast to Fremantle. Once this "jet" formed, it did not allow for the establishment of any sustained poleward surface flow, even when thermal forcing was the dominant forcing mechanism.

The addition of the beta effect in Experiment 8 provided improved results over Experiment 7. The early spin-up phase was quite similar to the  $f$ -plane case, with the exception of the westward propagation of eddies. A cold, coastal “jet” did not form and the addition of the beta effect allowed for more realistic upwelling to occur at the end of the year, when surface flow became equatorward along the west coast due to the dominance of the wind forcing. In the austral fall and winter of years 2 and 3, however, the Leeuwin Current was only weakly depicted and of short duration when it should have been most pronounced.

The added annual contribution of NWS waters in Experiment 9 augmented the onshore geostrophic inflow, strengthening the poleward flow and advecting warmer waters along the coastal region. The warmer waters along the coast resulted in advection of warmer waters offshore by anticyclonic eddies. The steadily increasing forcing from stronger thermal gradients and the poleward surge of NWS waters combined to extend the duration of the strong poleward and eastward surface flow of the Leeuwin Current through the austral winter, which recurred annually, resulting in the most realistic depiction of the LCS. Analysis of the surface current and undercurrent revealed realistic speeds and a similar core depth for the undercurrent when compared to actual observations. Additionally, the development of the undercurrent along the west and south Australia coasts was consistent with the generation mechanisms investigated in Experiment 4. Specifically, alongshore temperature gradients, which are generated at deeper levels by the strong flow of the Leeuwin Current, are sufficient to establish and maintain an equatorward (westward) undercurrent along western (southern) Australia.

Analyses of MKE and EKE was performed to determine the type of instability that could generate the meander and eddy features in the various experiments. In Experiment 9, a comparison of MKE and EKE revealed that the highest values of both occurred in the same general region, mainly along the jet axis of the surface current off the western and southern coast of Australia. The eddies were found to be generated from instabilities of the mean surface current and the undercurrent via barotropic and/or baroclinic instability processes, consistent with the results of Batteen (1997).

This study provided insight into the interaction of seasonal thermal gradients and wind forcing in the LCS off the western and southwestern coast of Australia, as well as the role of planetary beta in the generation and maintenance of the LCS. The model qualitatively reproduced the complex circulation of this region, while yielding insight into the role of each forcing mechanism as well as identifying the important seasonal effects in the LCS.

THIS PAGE INTENTIONALLY LEFT BLANK

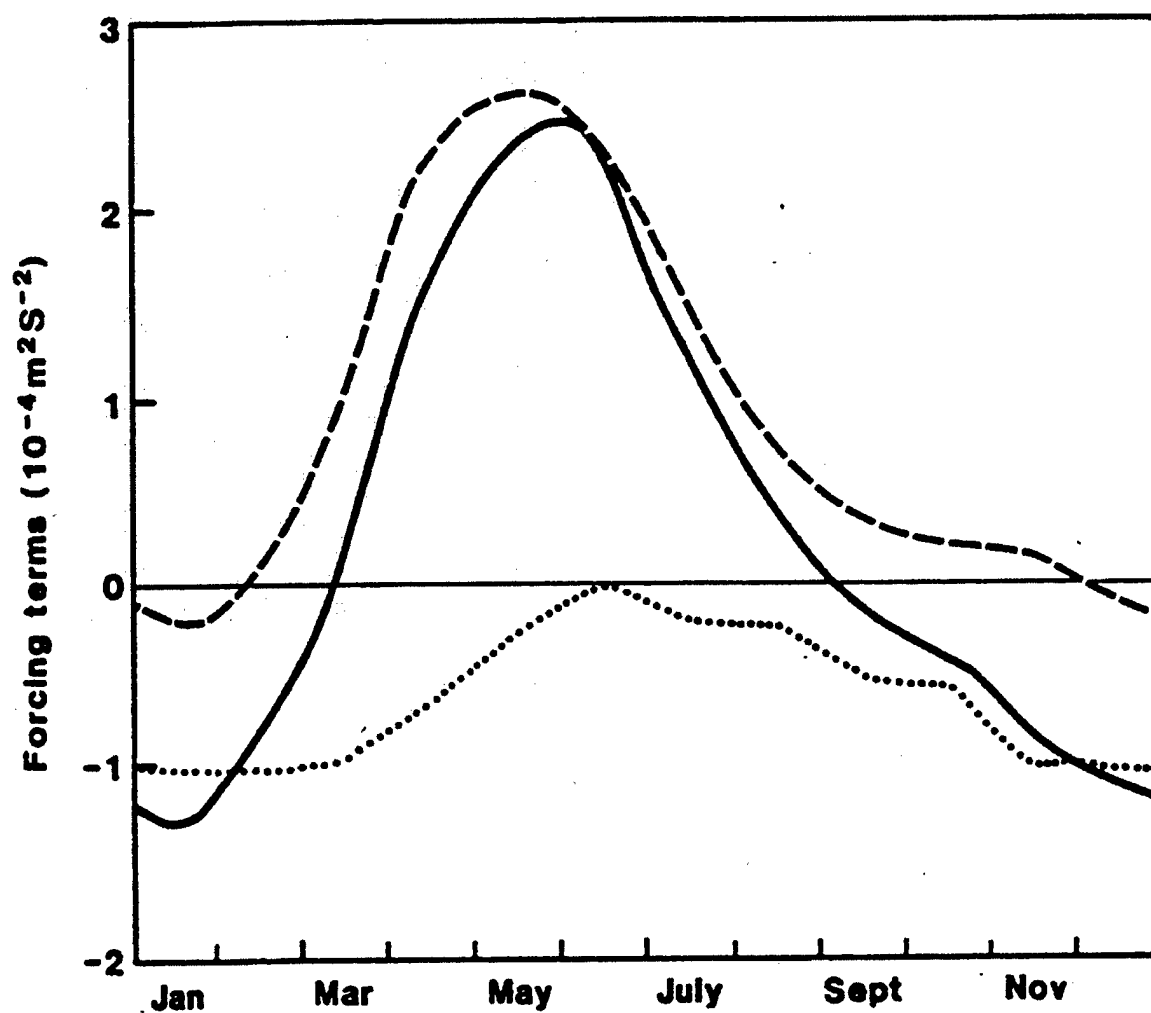


**Figure 1.** Annual cycle of net forcing for the Leeuwin Current between 22°S and 32°S: Dashed line is observed pressure gradient forcing; dotted line is observed wind stress; solid line is net forcing. Positive is southward (from Godfrey and Ridgway).



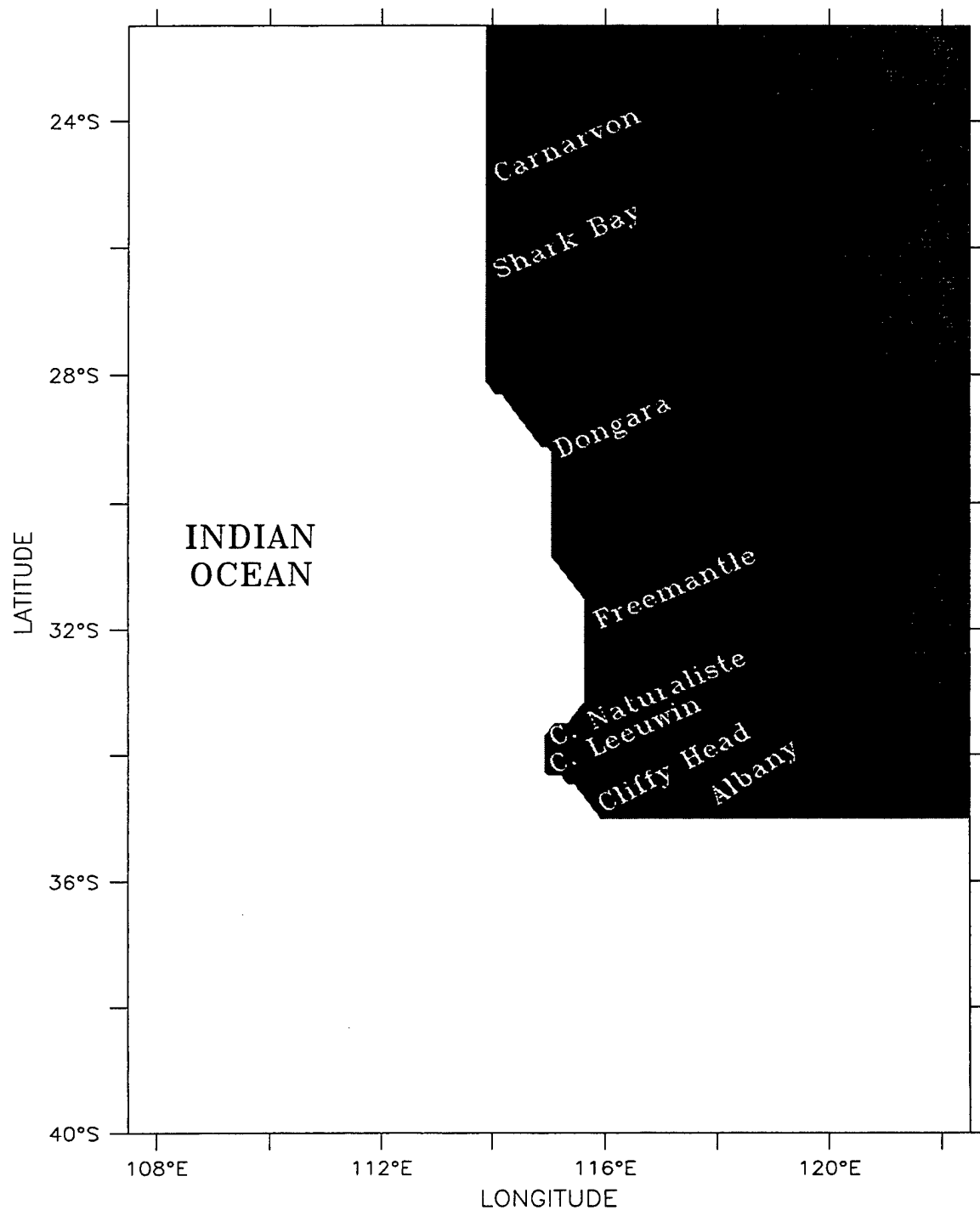


**Figure 2.** The model domain for the Leeuwin Current System (LCS) is bounded by 22.5°S to 40°S, 107.5°E to 122.5°E. The cross-shore (alongshore) resolution is 11 km (14 km). Geographical locations and prominent features are labeled.

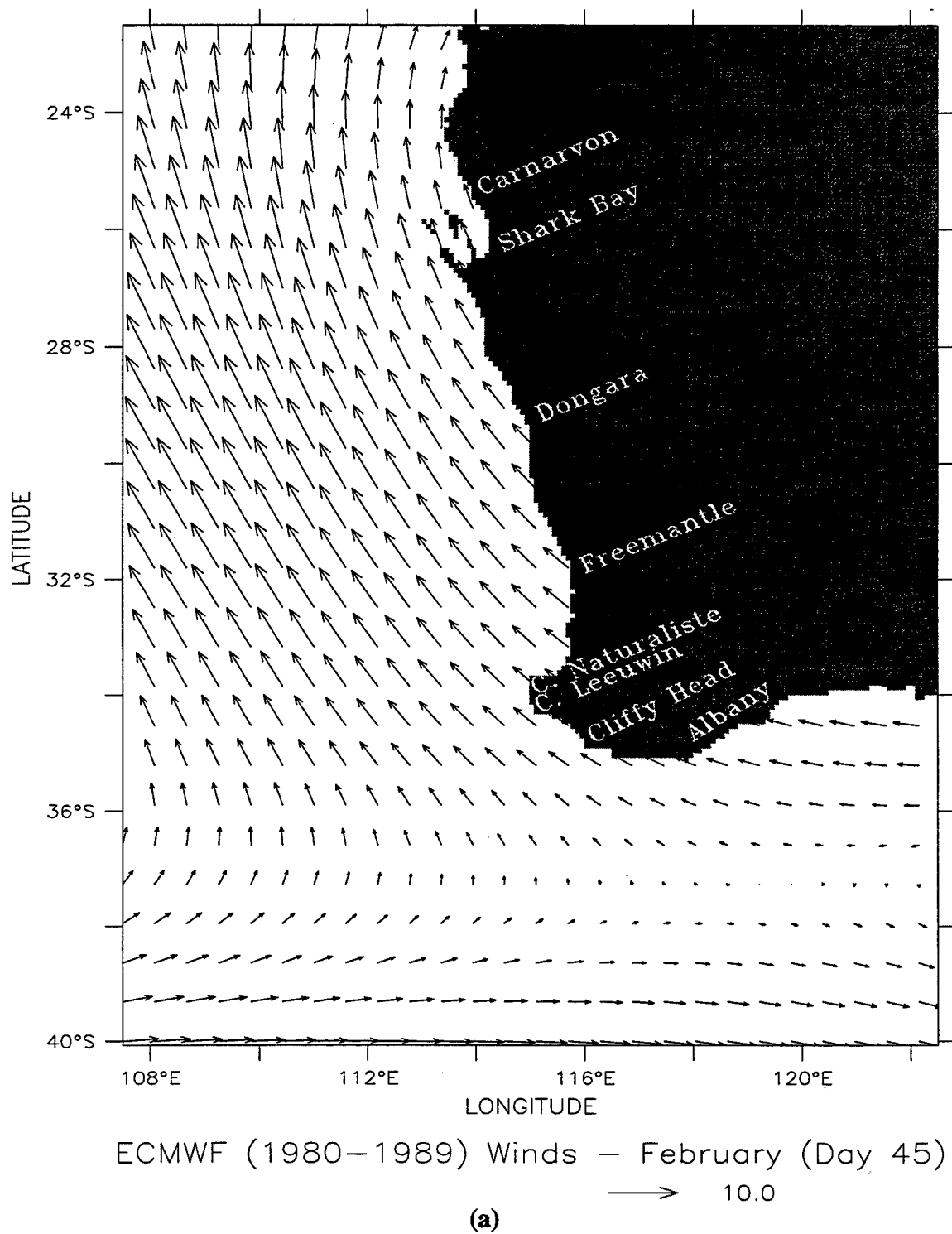
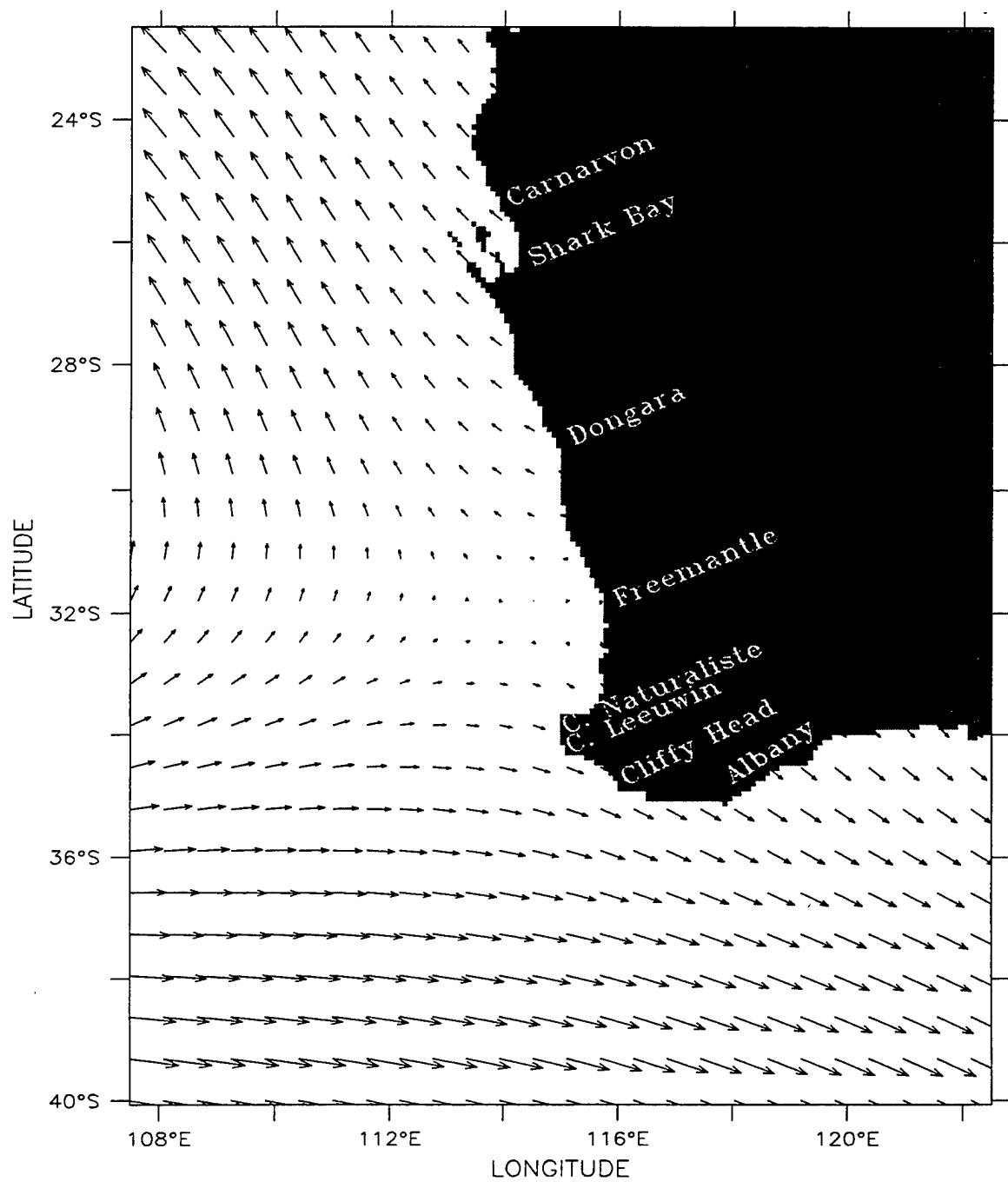


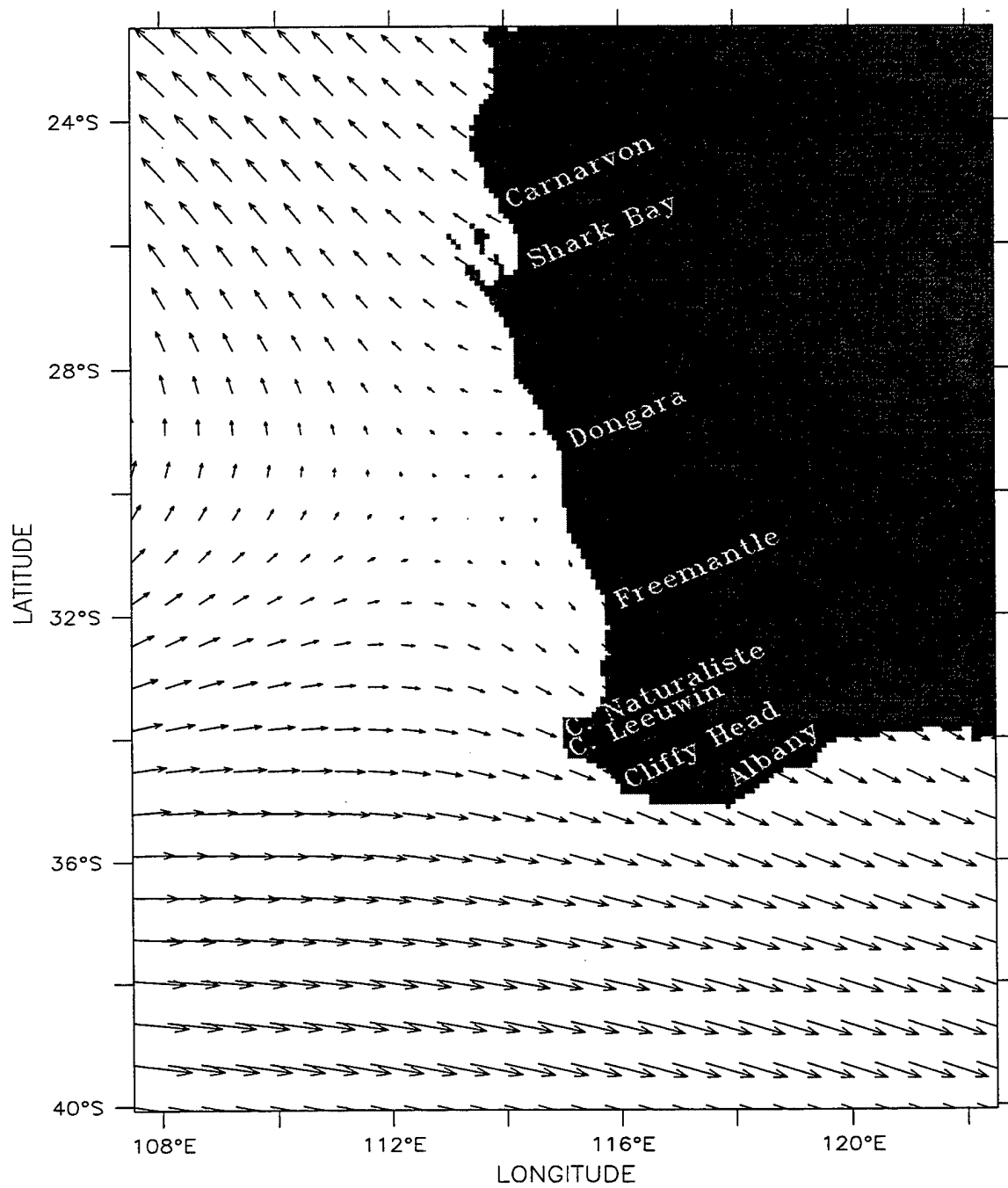
**Figure 3.** Climatological (1980–1989) ECMWF winds in m/s for: (a) February, (b) May, (c) July, and (d) November. Maximum wind vector is 10 m/s.



ECMWF (1980–1989) Winds – May (Day 135)

→ 10.0

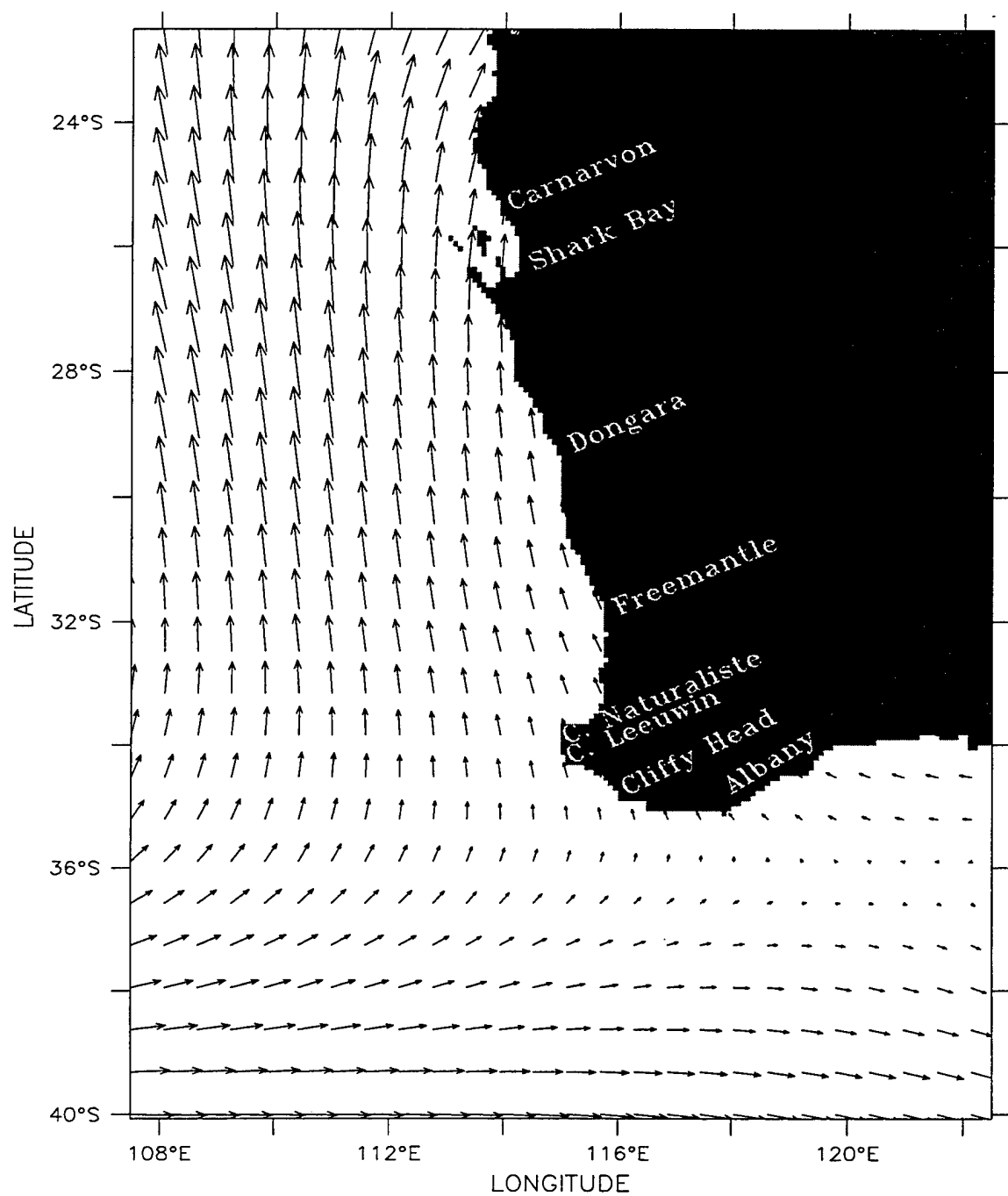
(b)



ECMWF (1980–1989) Winds – July (Day 195)

→ 10.0

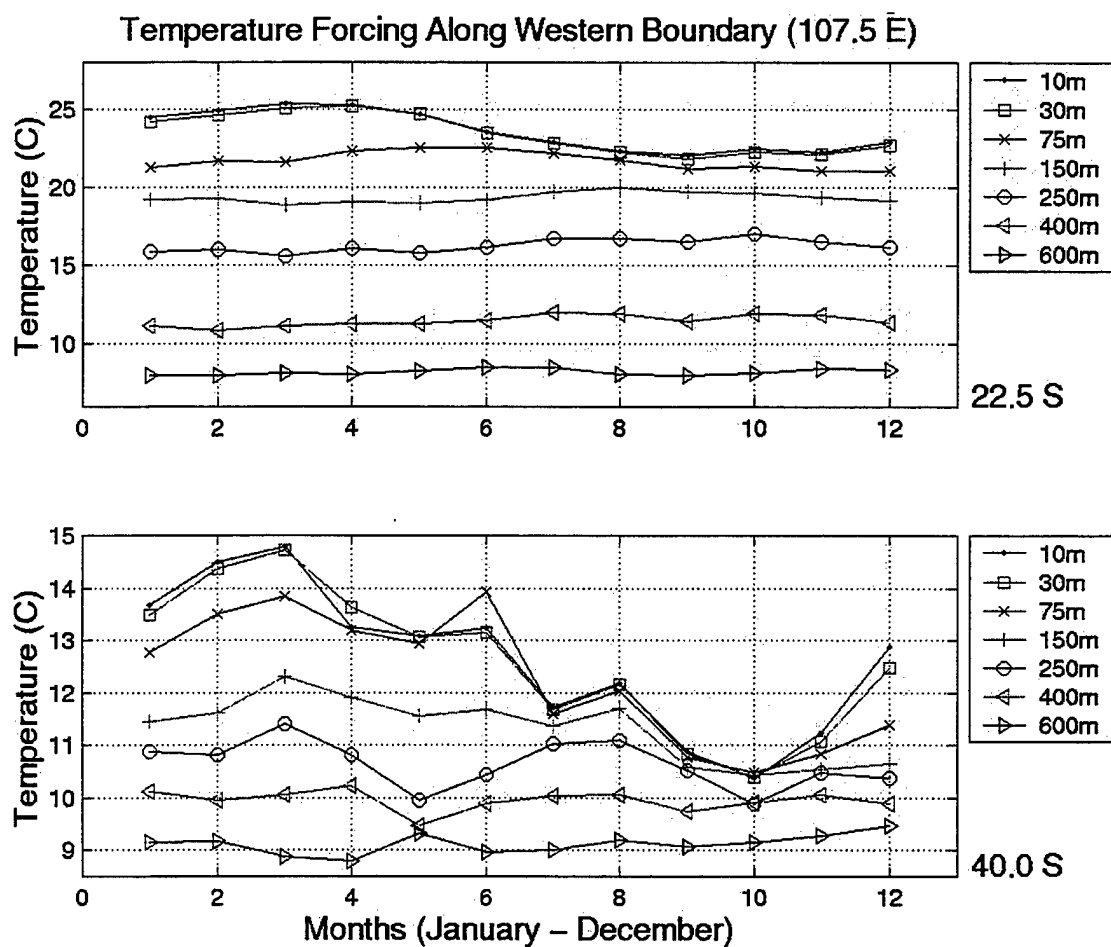
(c)



ECMWF (1980-1989) Winds — November (Day 315)

→ 10.0

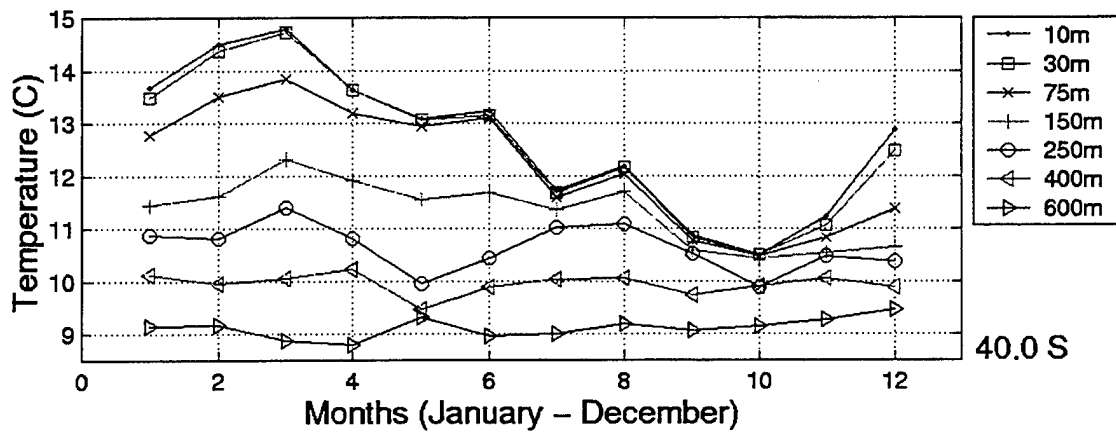
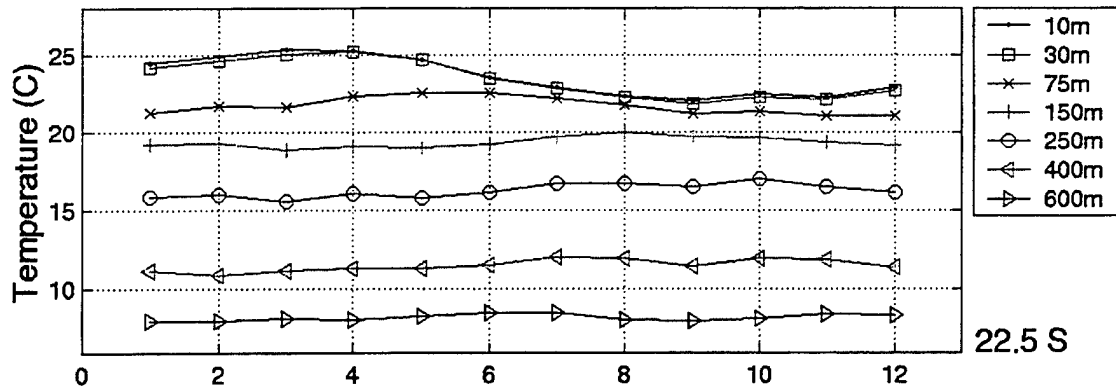
(d)



(a)

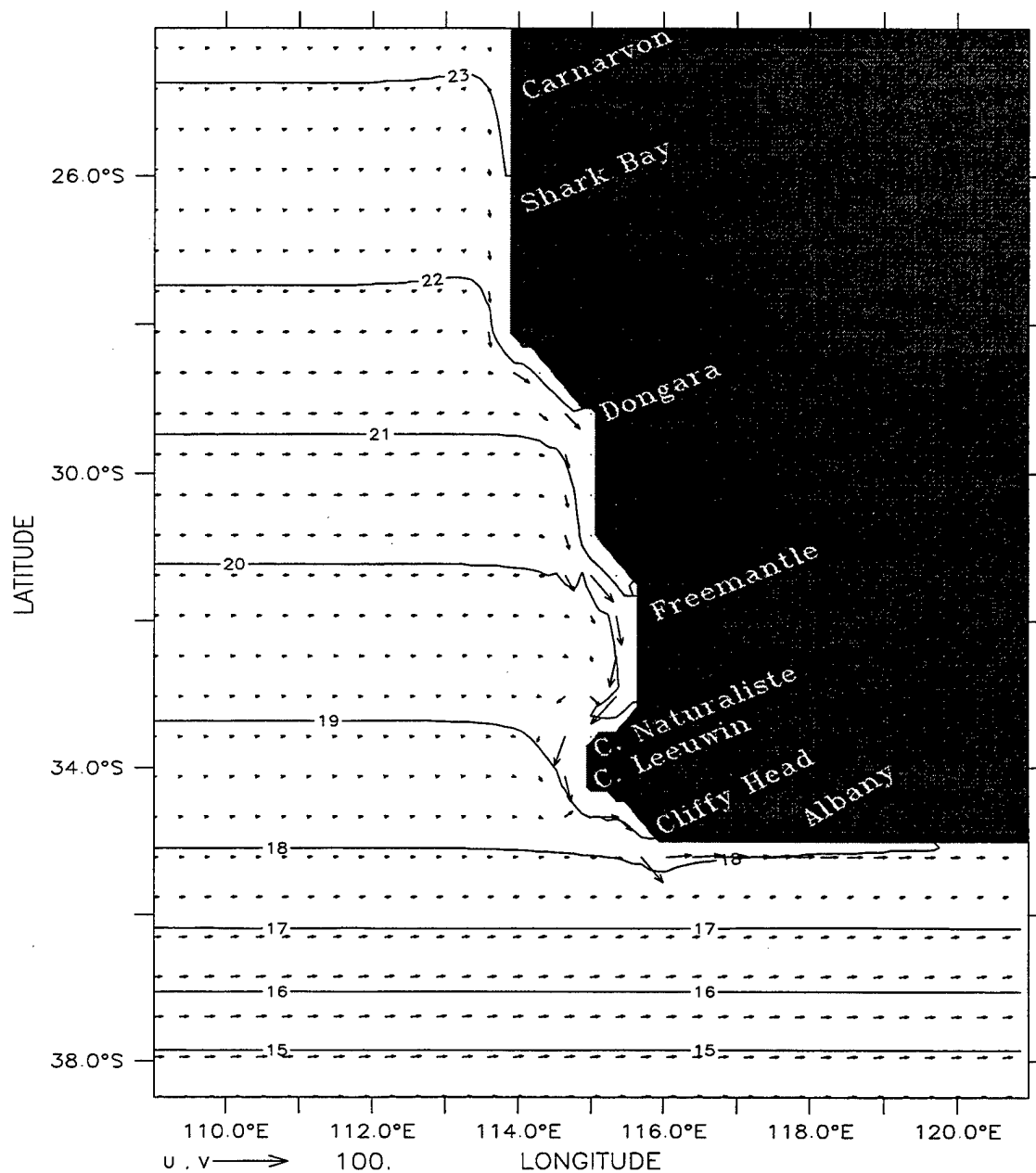
**Figure 4.** Plots of (a) actual and (b) slightly adjusted Levitus climatological temperature fields used as seasonal forcing along the western boundary (107.5°E) at 22.5°S (top) and 40°S (bottom).

Temperature Forcing Along Western Boundary (107.5 E)



(b)

DEPTH (m) : 10  
T (DAY) : 9

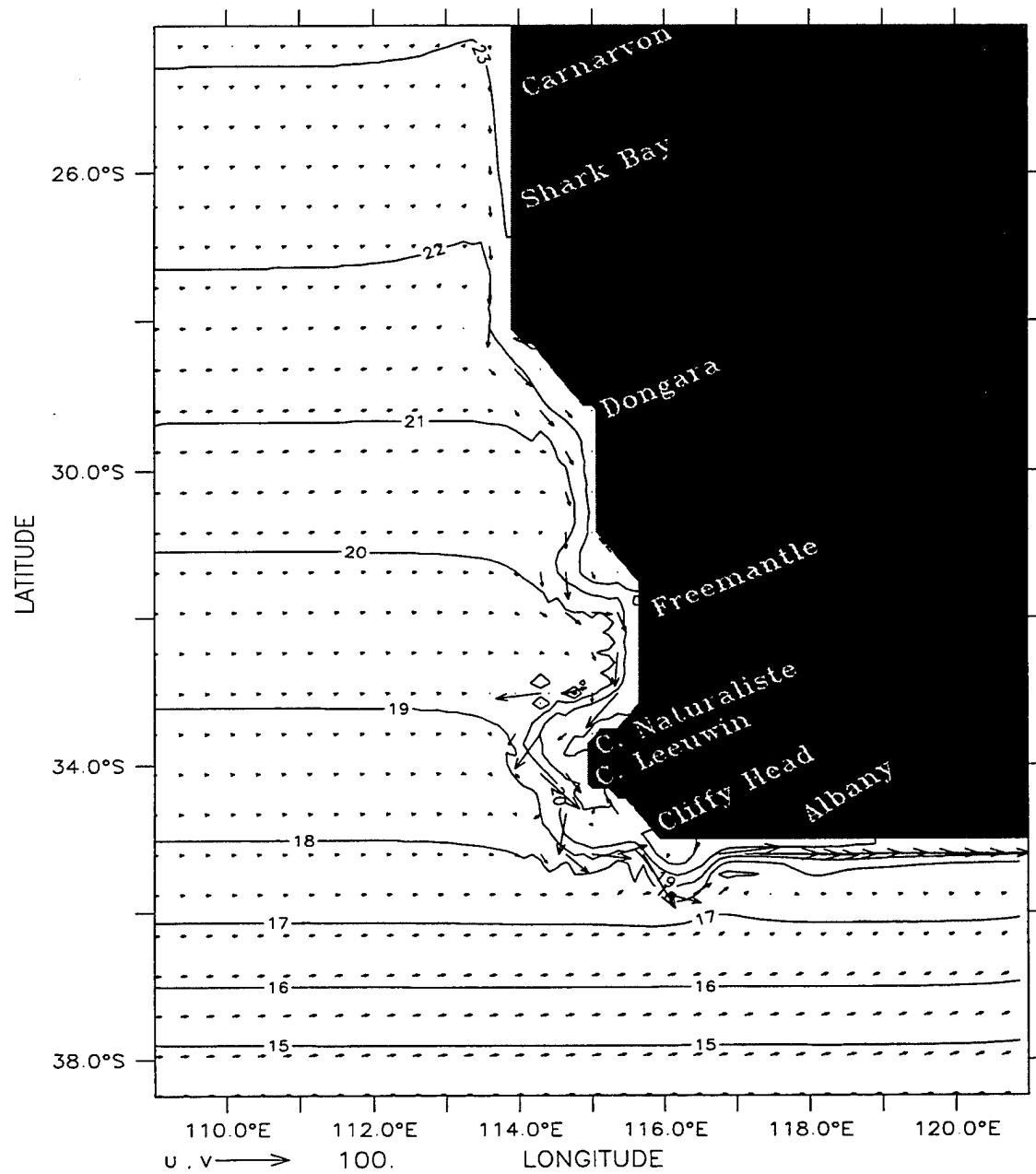


Temperature (deg C) and Velocity (cm/s)  
(a)

**Figure 5.** Temperature contours and velocity vectors at 10 m depth at days (a) 9, (b) 27, (c) 60, (d) 87, and (e) 117 of experiment 1. The contour interval is 1°C. To avoid clutter, the velocity vectors are plotted every third grid point in the east-west direction and every fourth grid point in the north-south direction. Maximum velocity is 100 cm/s.

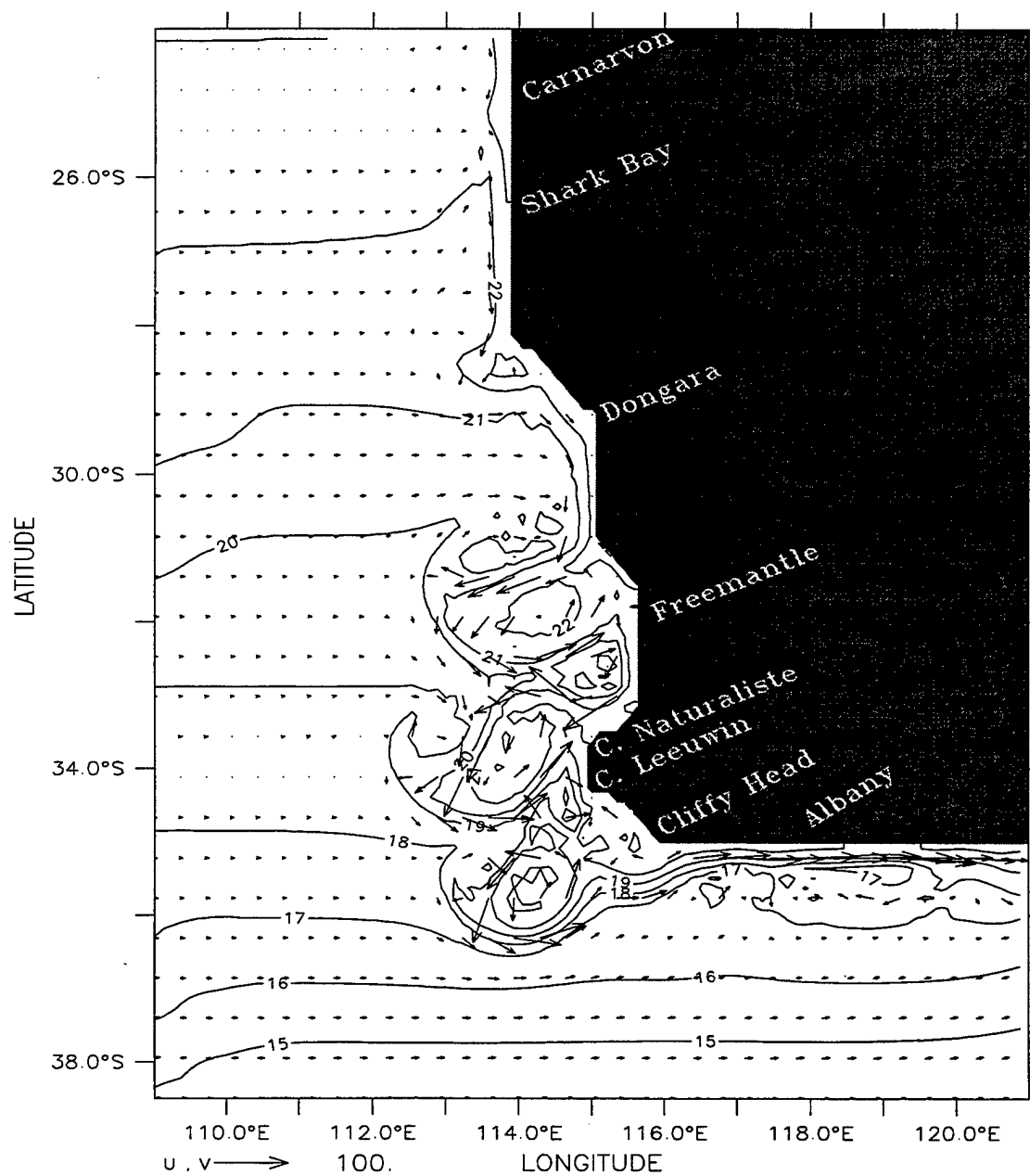


DEPTH (m) : 10  
T (DAY) : 27



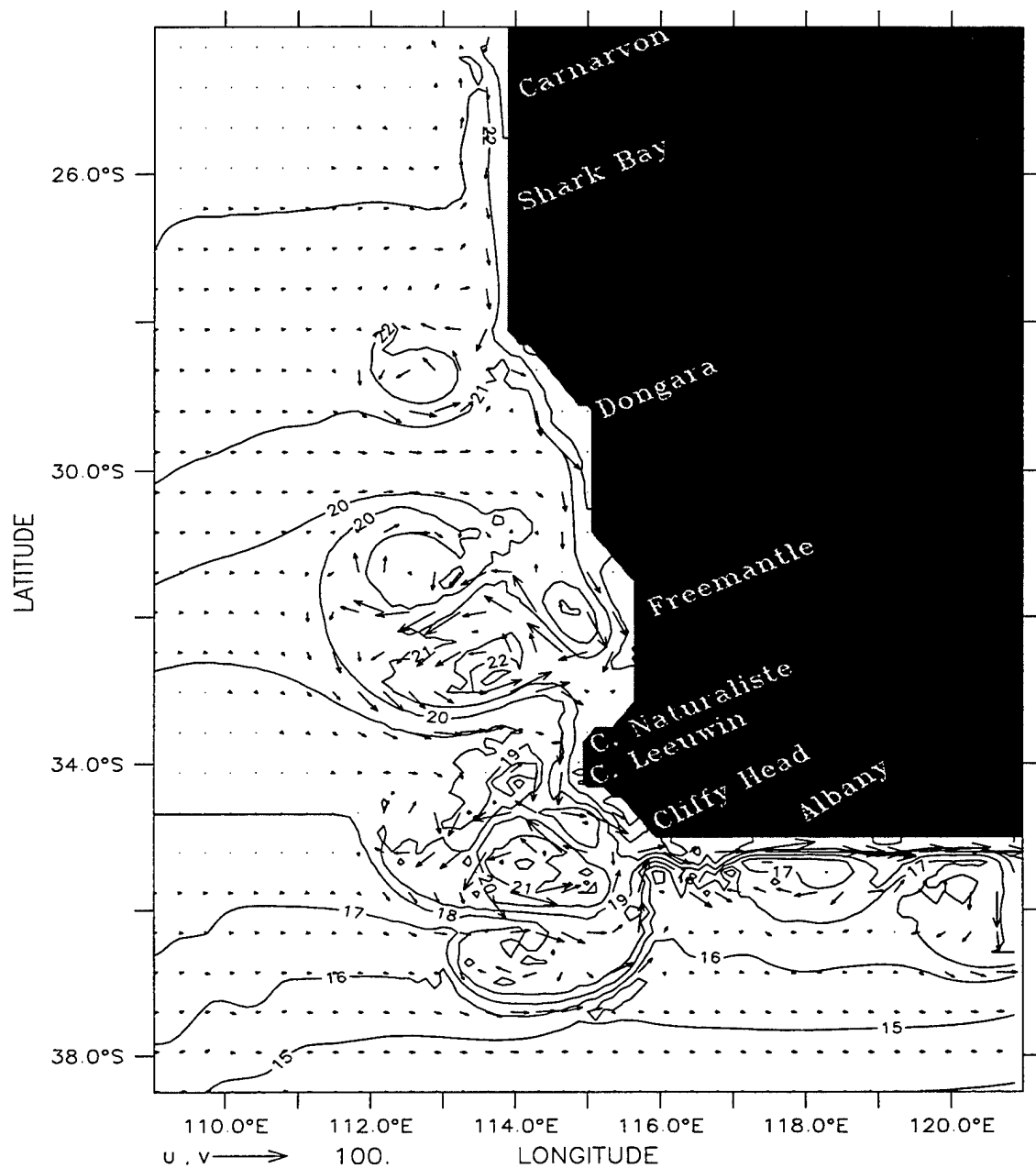
Temperature (deg C) and Velocity (cm/s)  
(b)

DEPTH (m) : 10  
T (DAY) : 60



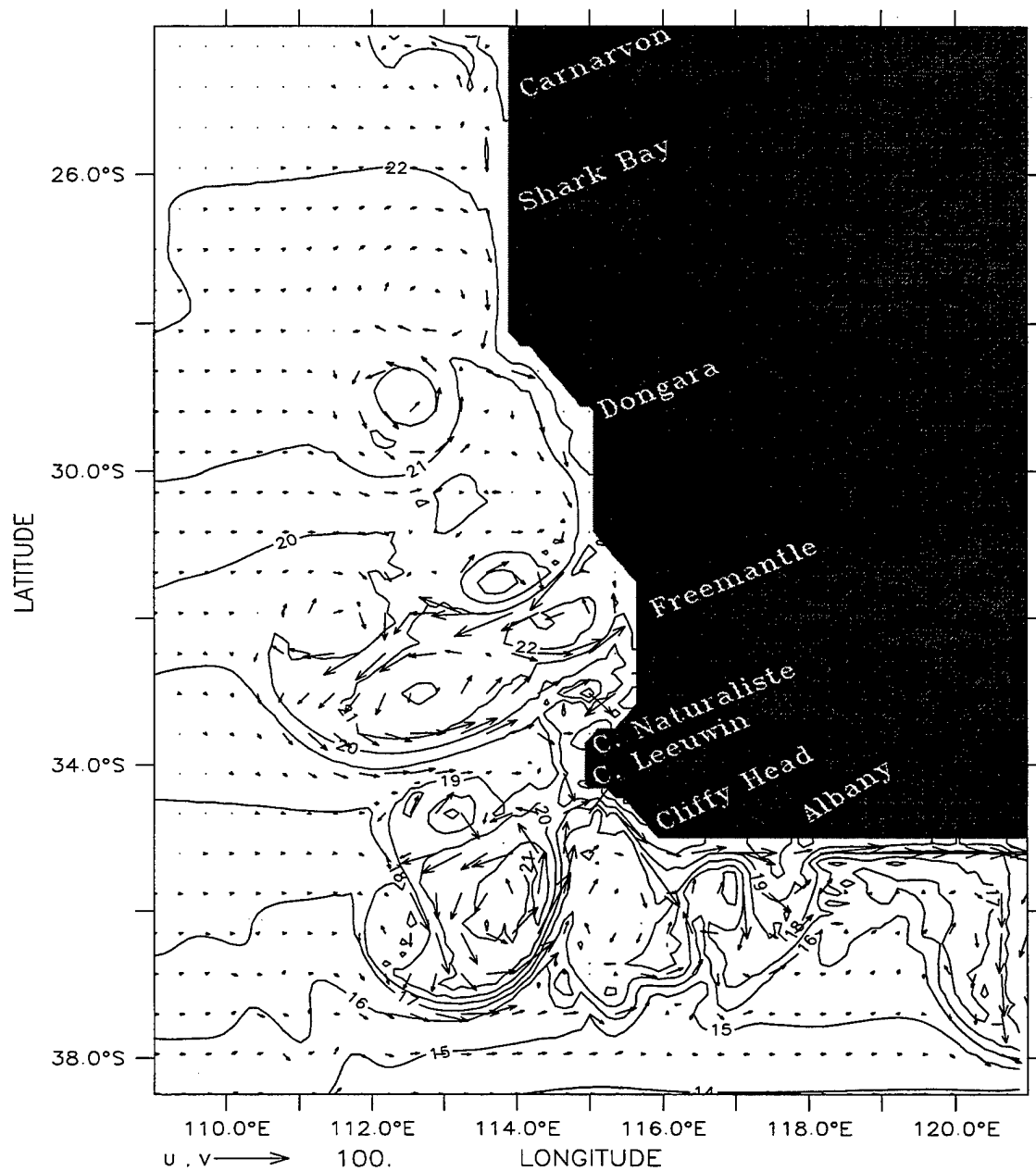
Temperature (deg C) and Velocity (cm/s)  
(c)

DEPTH (m) : 10  
T (DAY) : 87



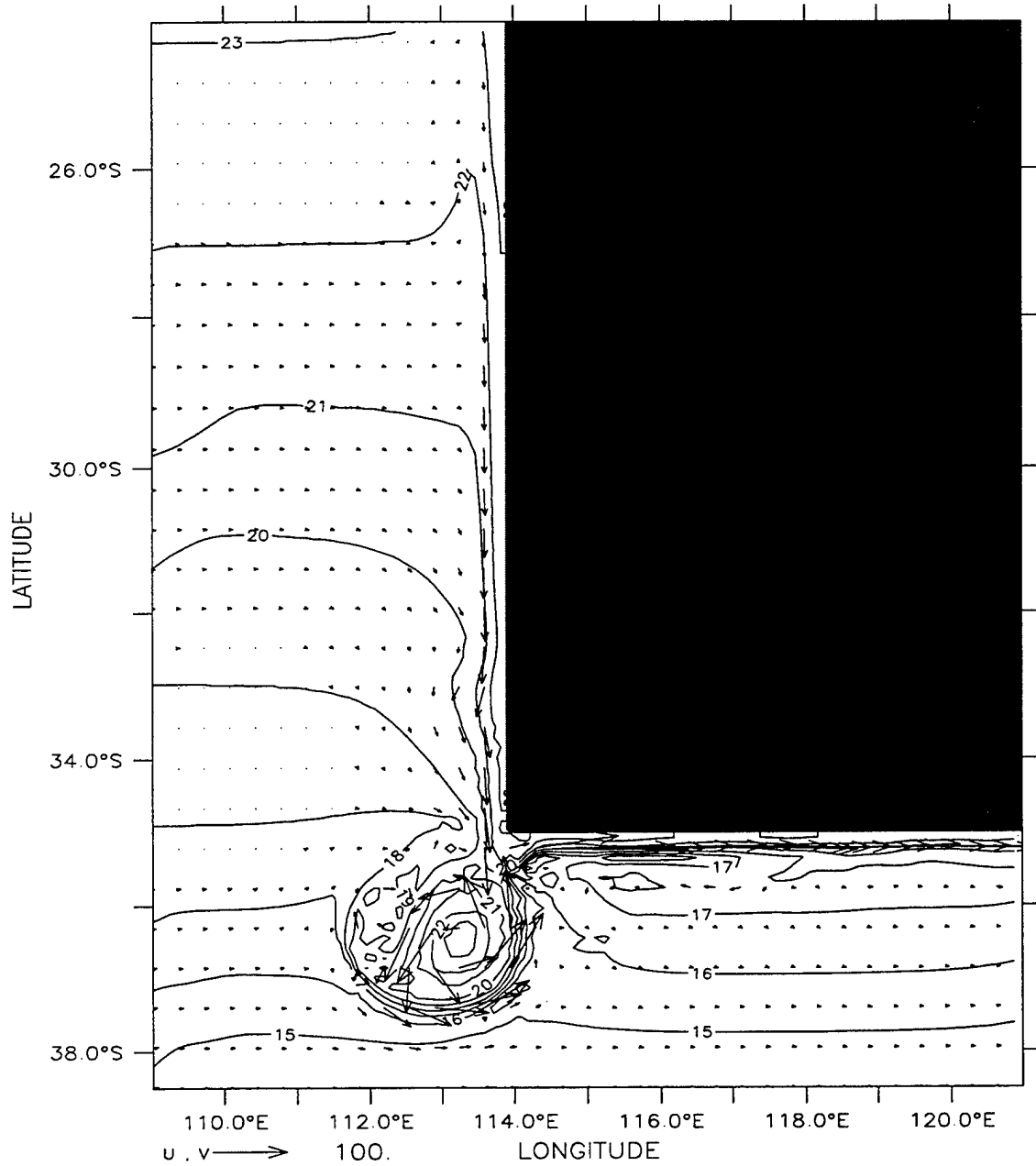
Temperature (deg C) and Velocity (cm/s)  
(d)

DEPTH (m) : 10  
T (DAY) : 117



Temperature (deg C) and Velocity (cm/s)  
(e)

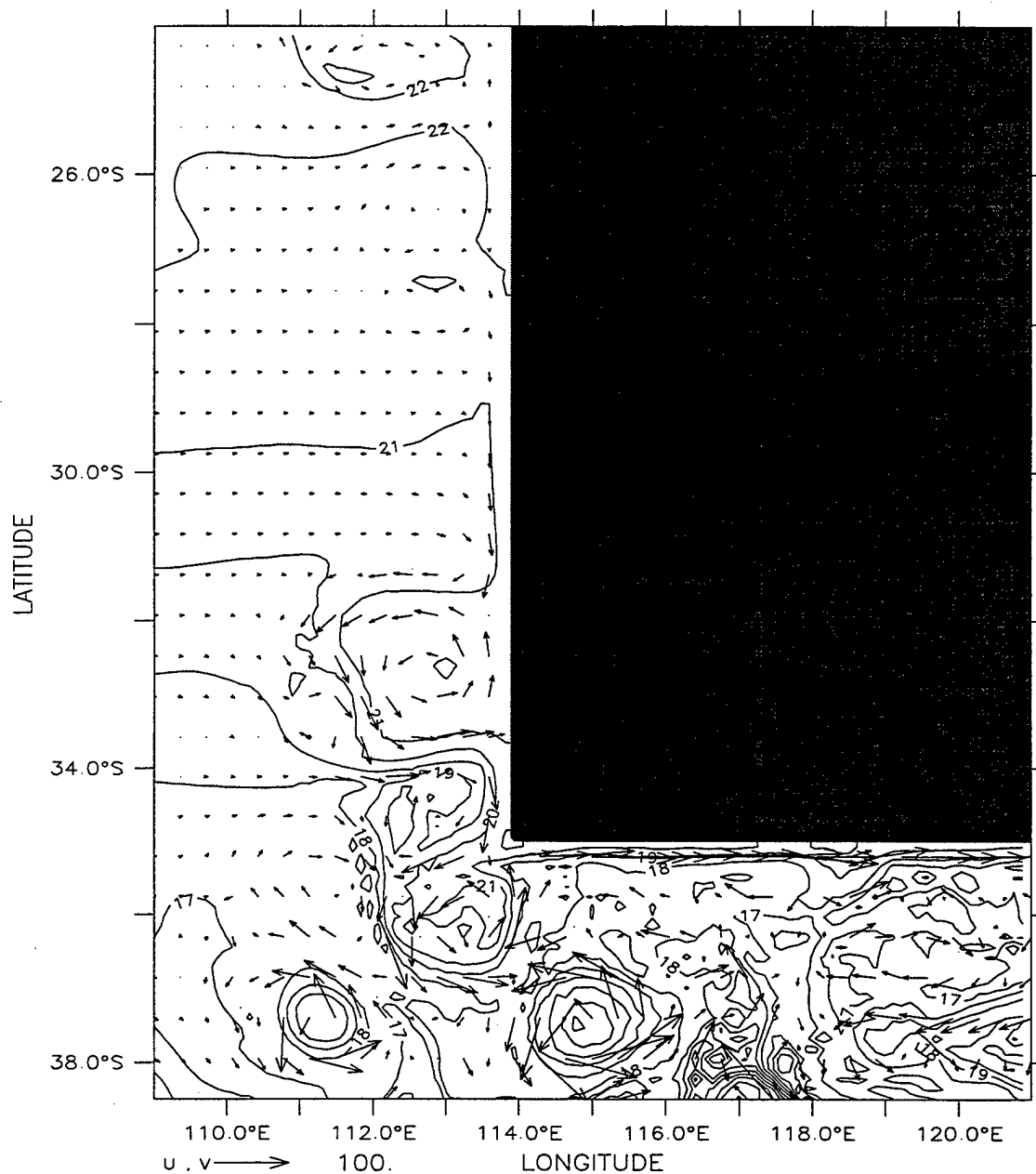
DEPTH (m) : 10  
T (DAY) : 51



Temperature (deg C) and Velocity (cm/s)  
(a)

**Figure 6.** Temperature contours and velocity vectors at 10 m depth at days (a) 51 and (b) 159 of Experiment 2. The contour interval is  $1^{\circ}\text{C}$ . To avoid clutter, velocity vectors are plotted every third grid point in the east-west direction and every fourth grid point in the north-south direction. Maximum velocity is 100 cm/s.

DEPTH (m) : 10  
T (DAY) : 159



Temperature (deg C) and Velocity (cm/s)  
(b)

LATITUDE : 31.9S  
T (DAY) : 33

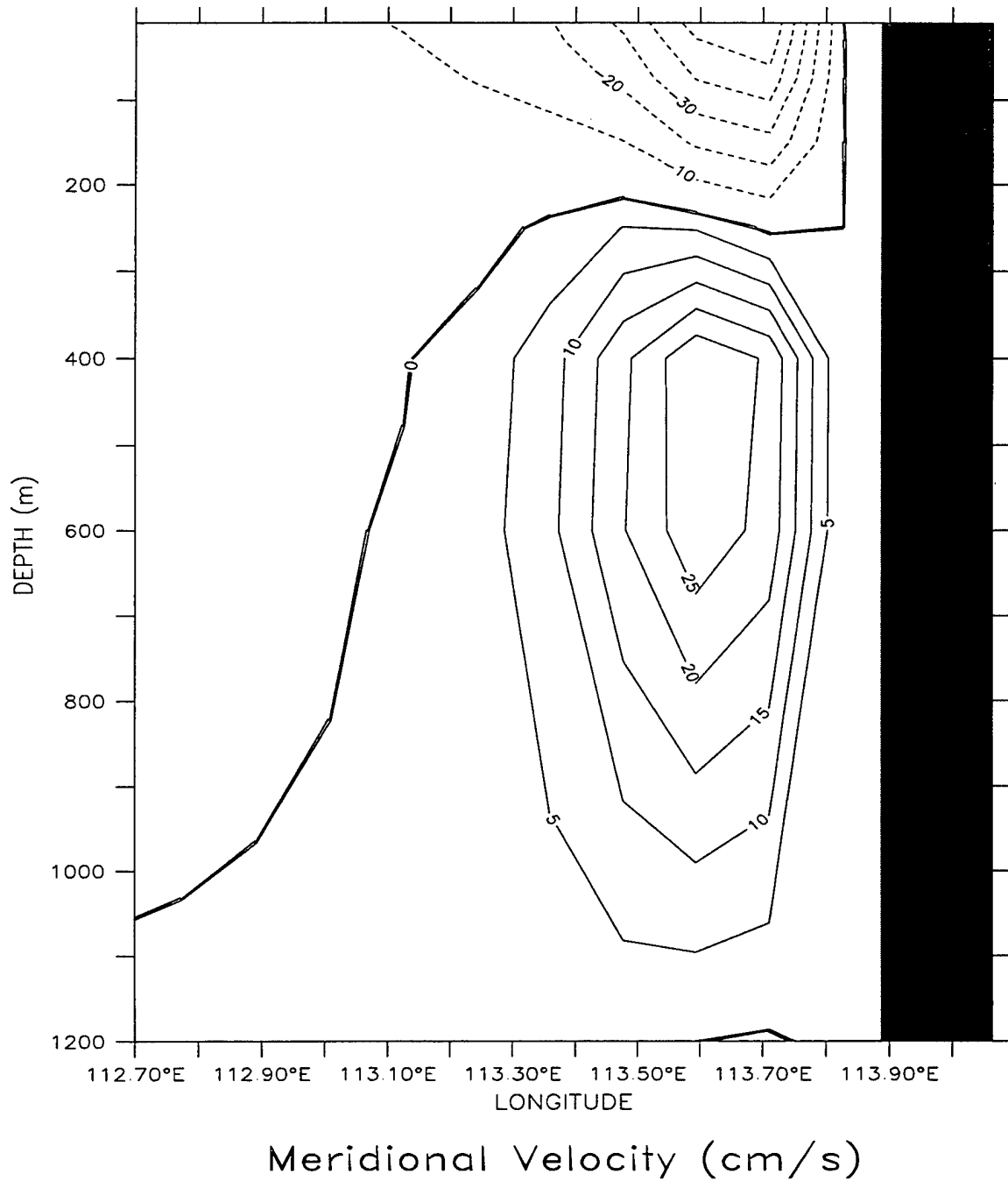
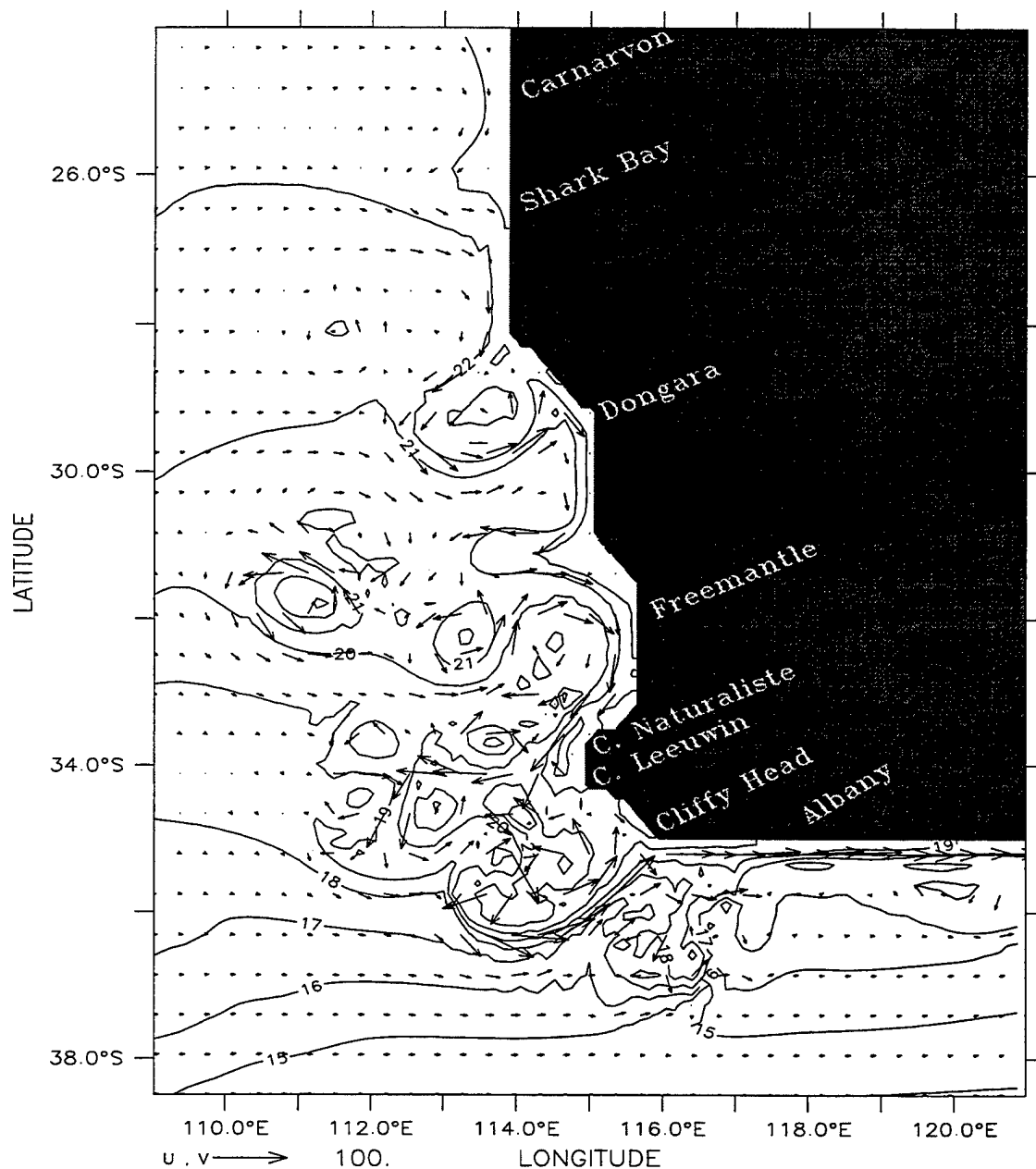


**Figure 7.** Cross-shore section of meridional velocity ( $v$ ) at  $\sim 32^\circ\text{S}$  for Experiment 2 on day 33. Contour interval is 10 cm/s for poleward flow (dashed lines) and 5 cm/s for equatorward flow (solid lines).

DEPTH (m) : 10  
T (DAY) : 87

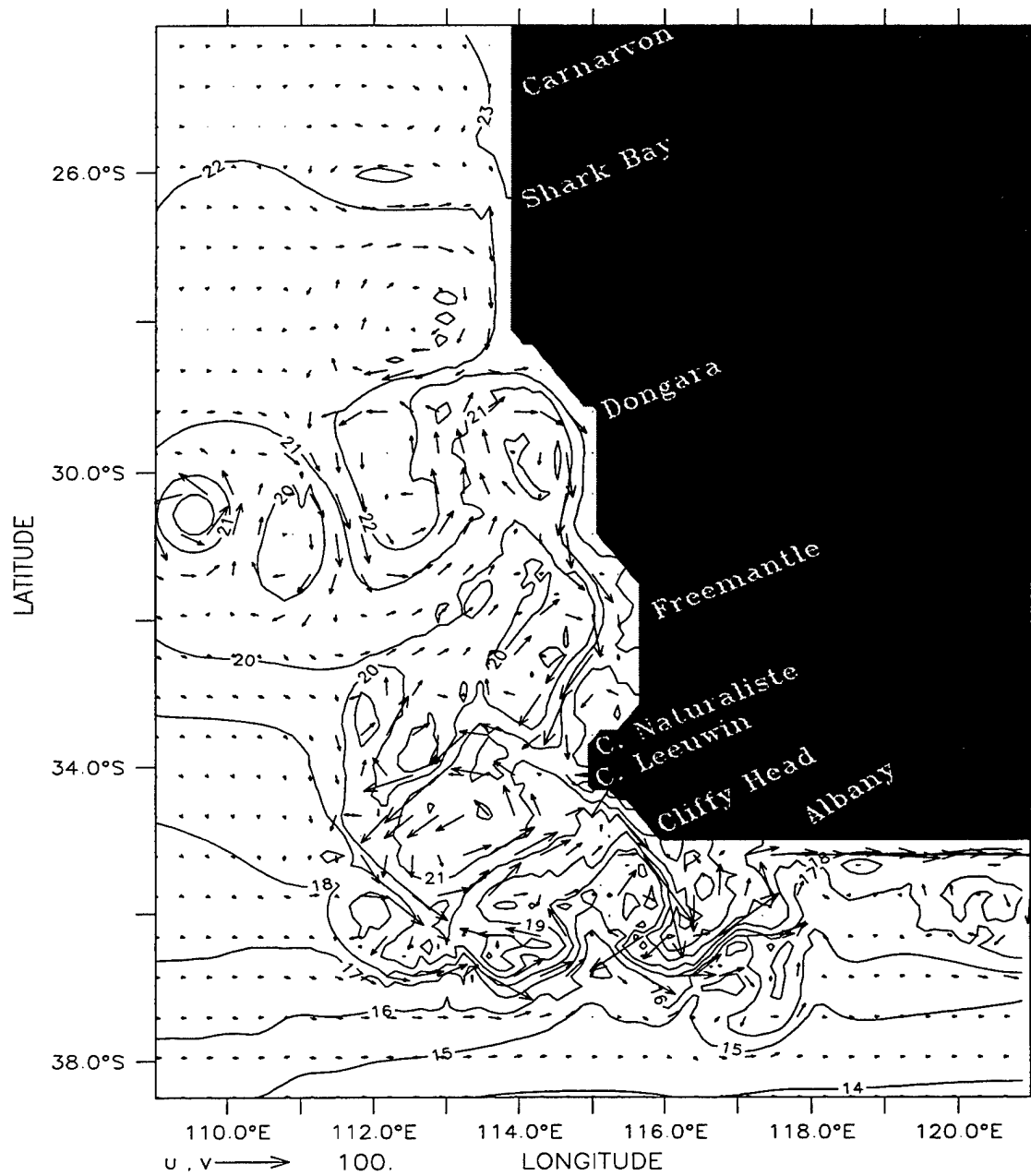


Temperature (deg C) and Velocity (cm/s)  
(a)

**Figure 8.** Temperature contours and velocity vectors at 10 m depth at days (a) 87 and (b) 117 of Experiment 3. The contour interval is 1°C. To avoid clutter, the velocity vectors are plotted every third grid point in the east-west direction and every fourth grid point in the north-south direction. Maximum velocity is 100 cm/s.

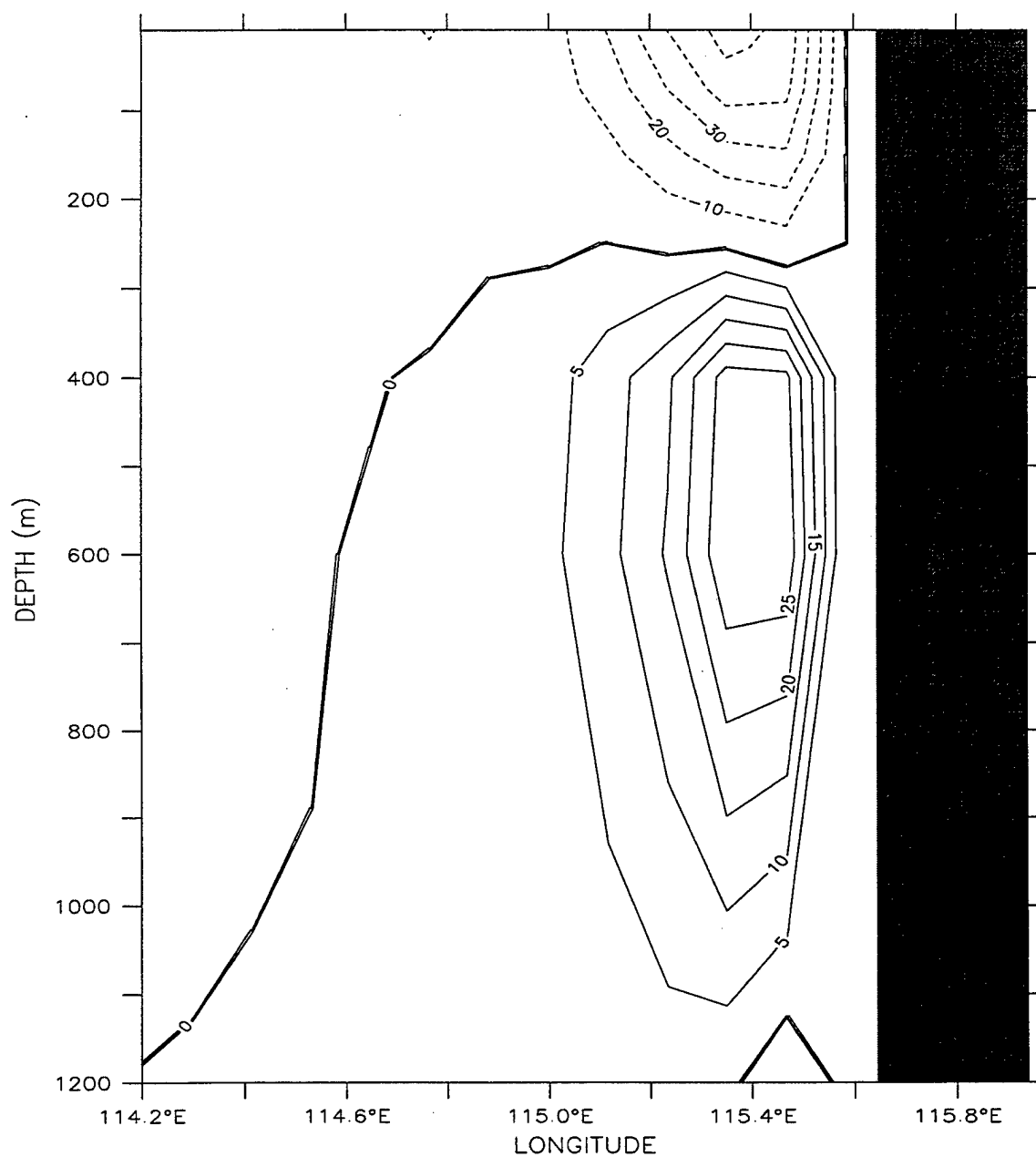


DEPTH (m) : 10  
T (DAY) : 117



Temperature (deg C) and Velocity (cm/s)  
(b)

LATITUDE : 31.9S  
T (DAY) : 15

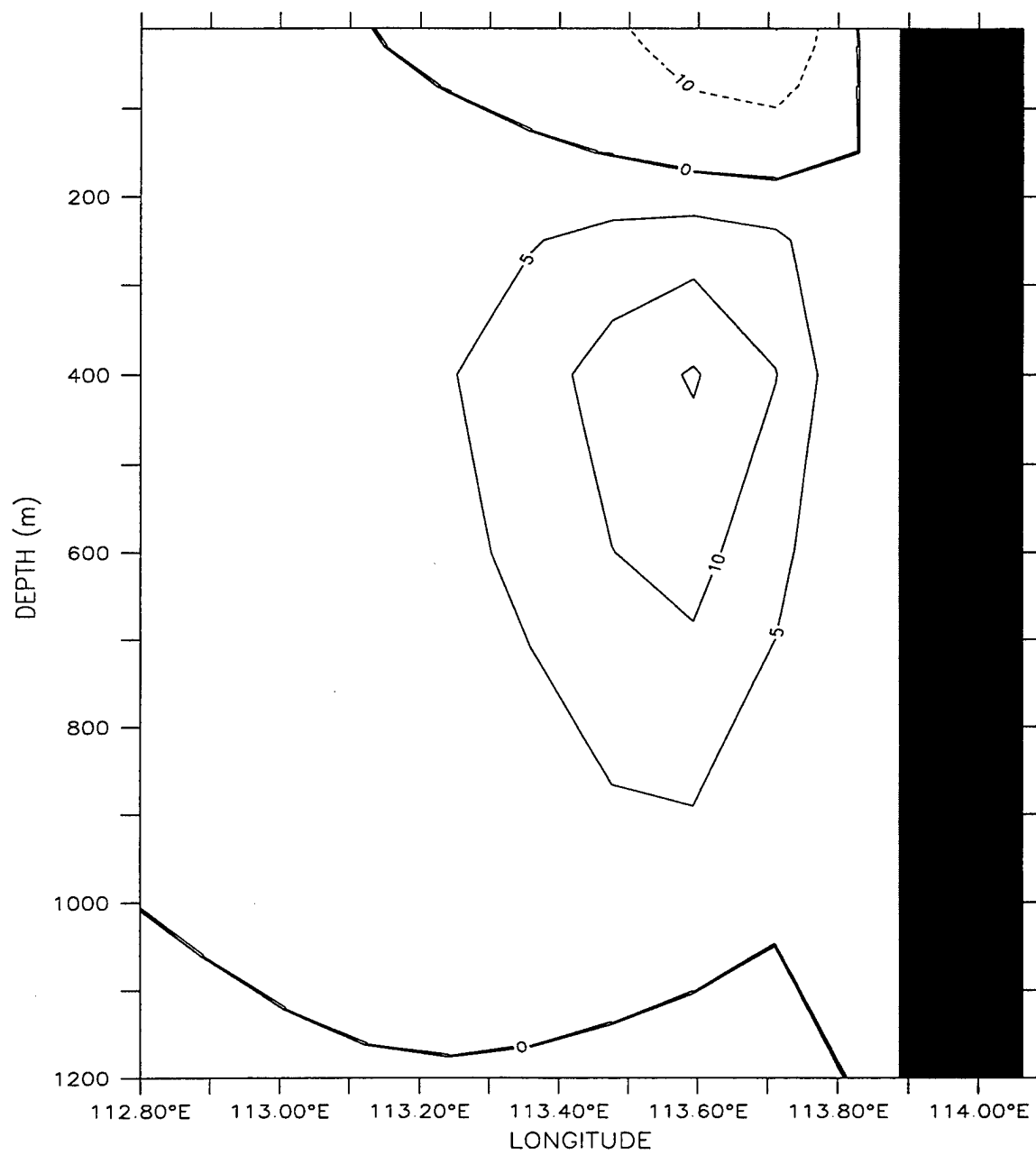


Meridional Velocity (cm/s)

(a)

**Figure 9.** Cross-shore section of meridional velocity ( $v$ ) at (a)  $\sim 32^\circ\text{S}$  and (b)  $\sim 26^\circ\text{S}$  for Experiment 3 on day 15. Contour interval is 10 cm/s for poleward flow (dashed lines) and 5 cm/s for equatorward flow (solid lines).

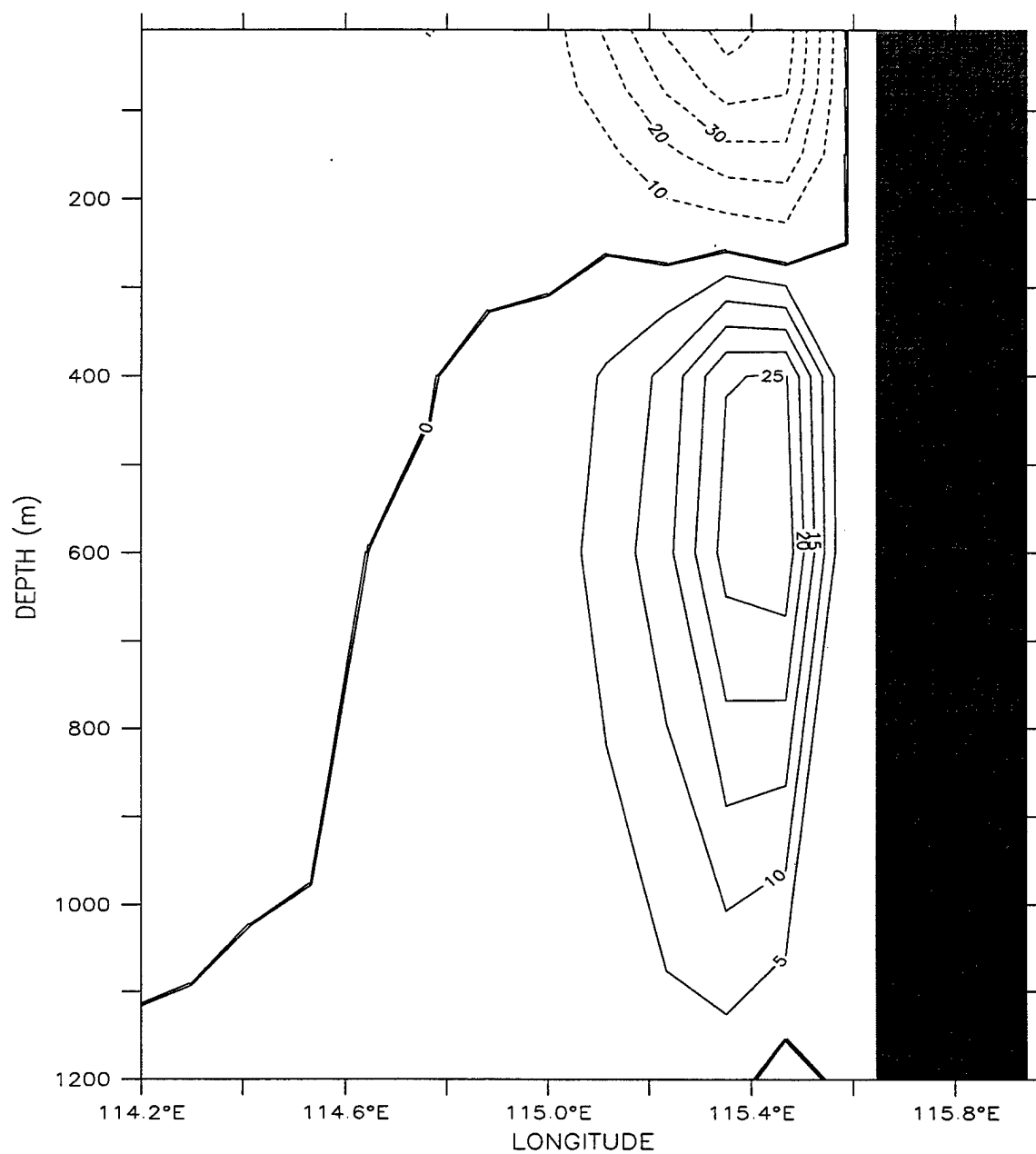
LATITUDE : 26.1S  
T (DAY) : 15



Meridional Velocity (cm/s)

(b)

LATITUDE : 31.9S  
T (DAY) : 15

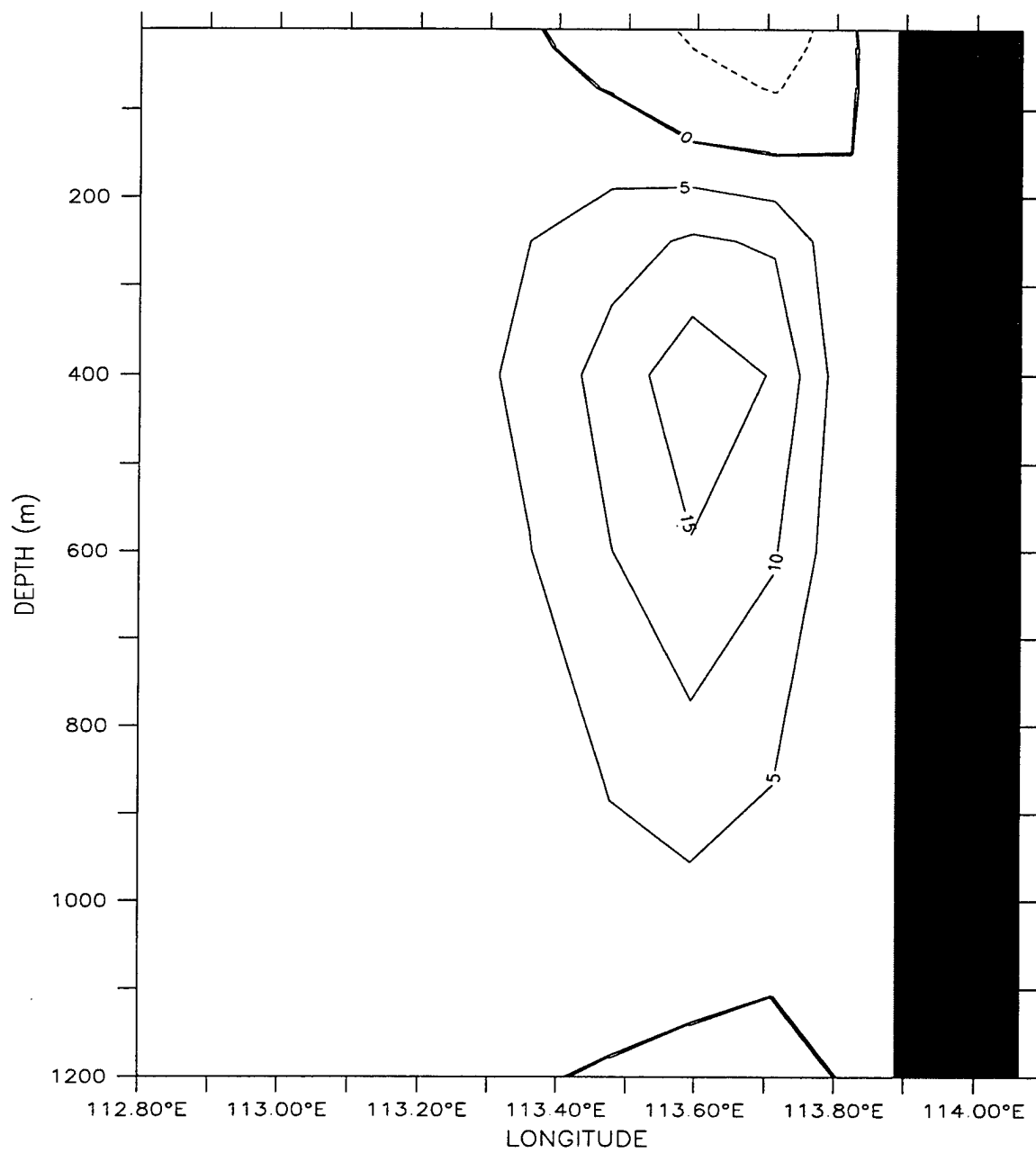


Meridional Velocity (cm/s)

(a)

**Figure 10.** Cross-shore section of meridional velocity (v) at (a) ~32°S and (b) ~26°S for Experiment 1 on day 15. Contour interval is 10 cm/s for poleward flow (dashed lines) and 5 cm/s for equatorward flow (solid lines).

LATITUDE : 26.1S  
T (DAY) : 15



Meridional Velocity (cm/s)  
(b)

DEPTH (m) : 600  
T (DAY) : 15

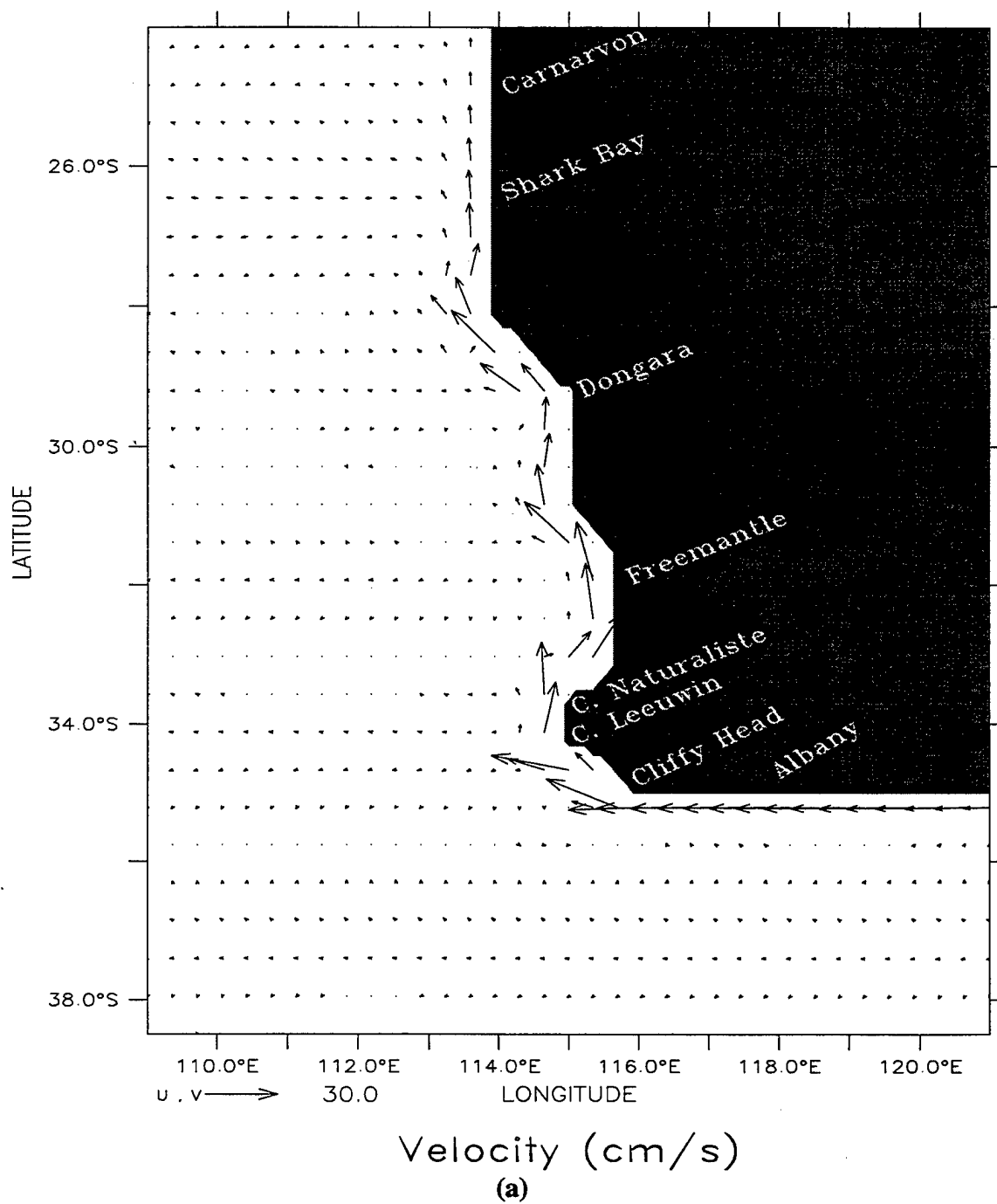
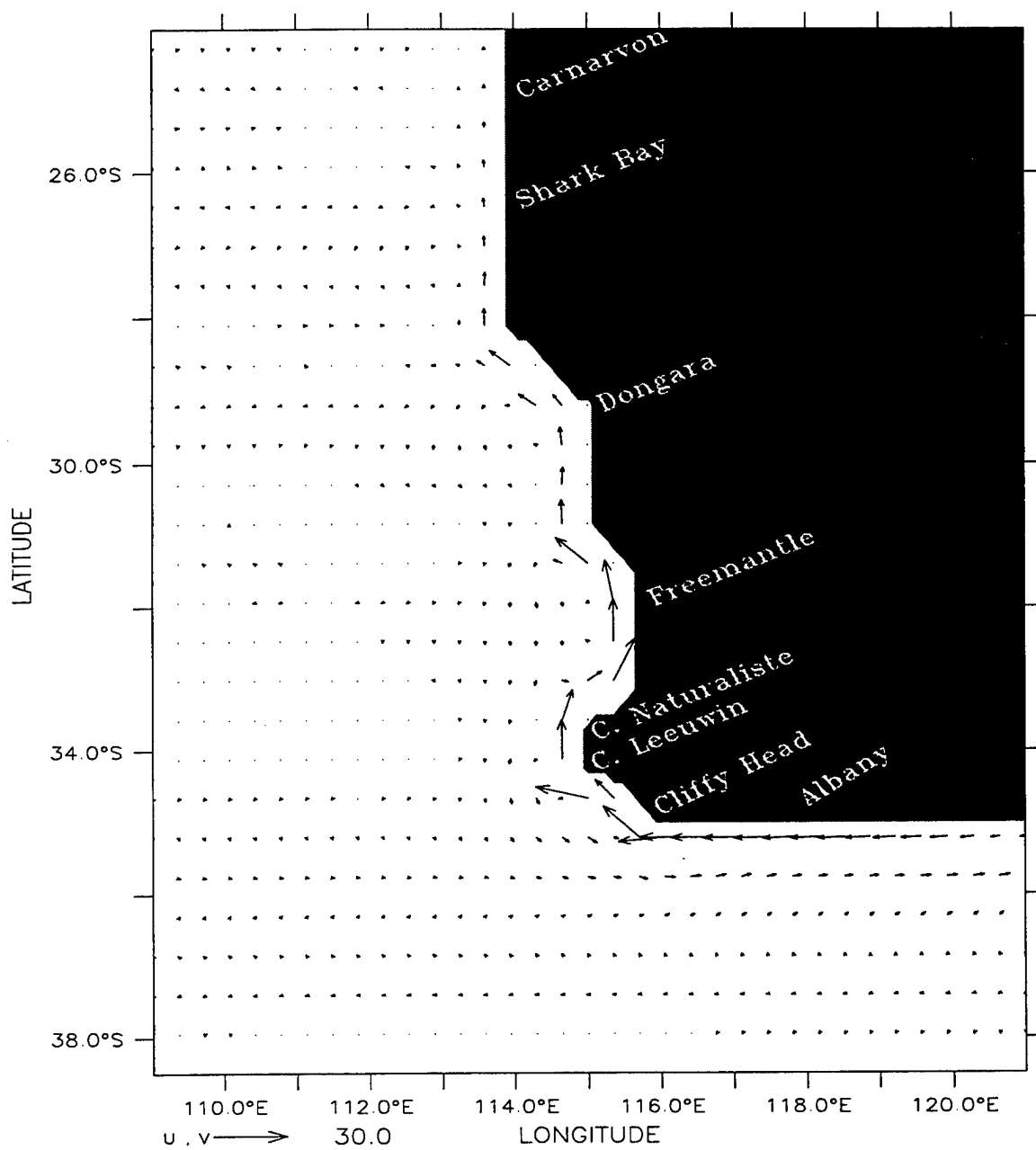


**Figure 11.** Velocity vectors at 600 m depth for (a) Experiment 3 and (b) Experiment 4 at day 15. To avoid clutter, the velocity vectors are plotted every third grid point in the east-west direction and every fourth grid point in the north-south direction. Maximum velocity is 30 cm/s.

DEPTH (m) : 600  
T (DAY) : 15



Velocity (cm/s)  
(b)

LATITUDE : 31.9S  
T (DAY) : 3

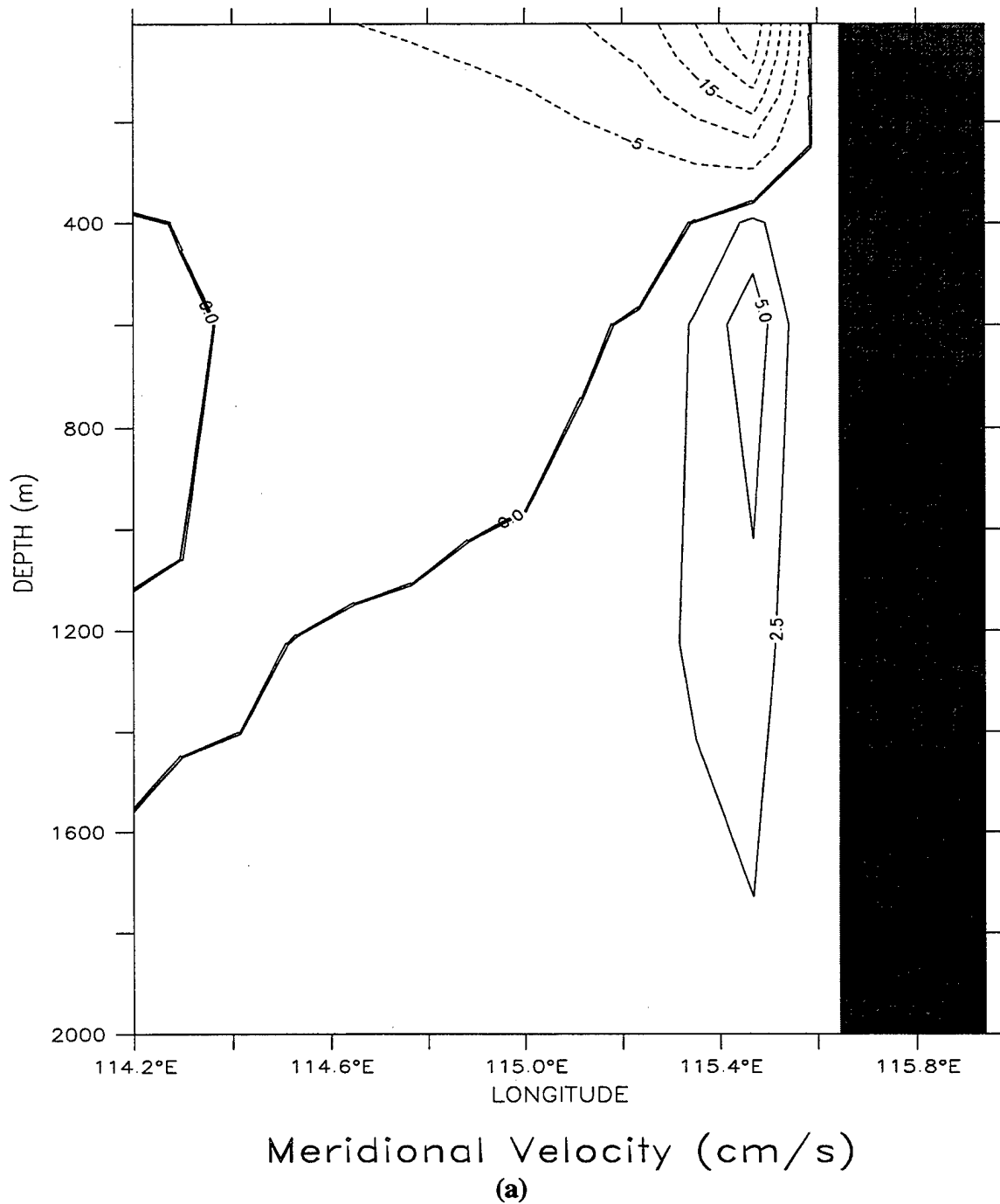
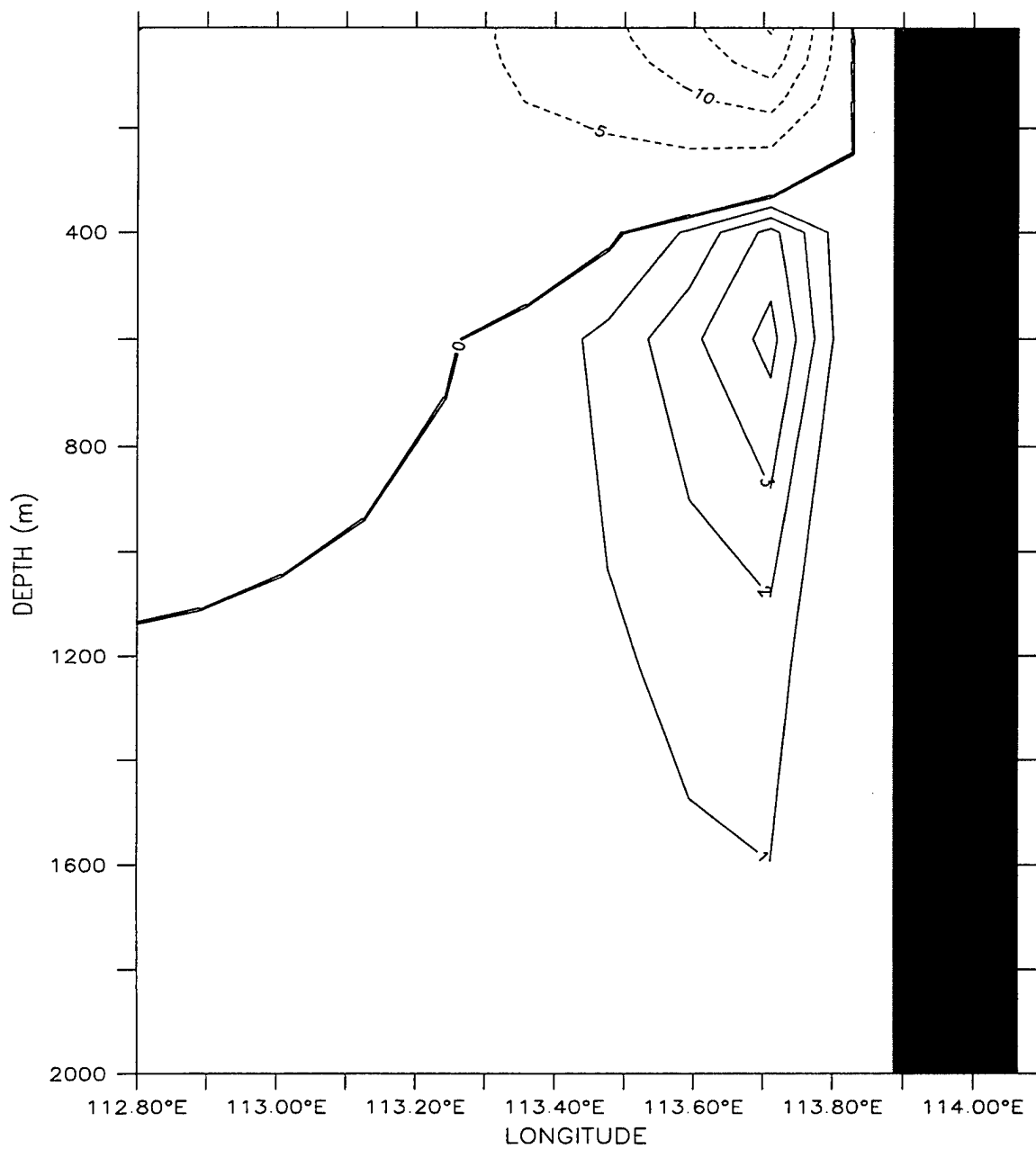


**Figure 12.** Cross-shore section of meridional velocity ( $v$ ) at (a and c) ~32°S and (b and d) ~26°S for Experiment 4 on day (a and b) 3 and (c and d) 9. Contour interval is 5 cm/s for poleward flow (dashed lines) and (a and c) 2.5 cm/s and (b and d) 1 cm/s for equatorward flow (solid lines).

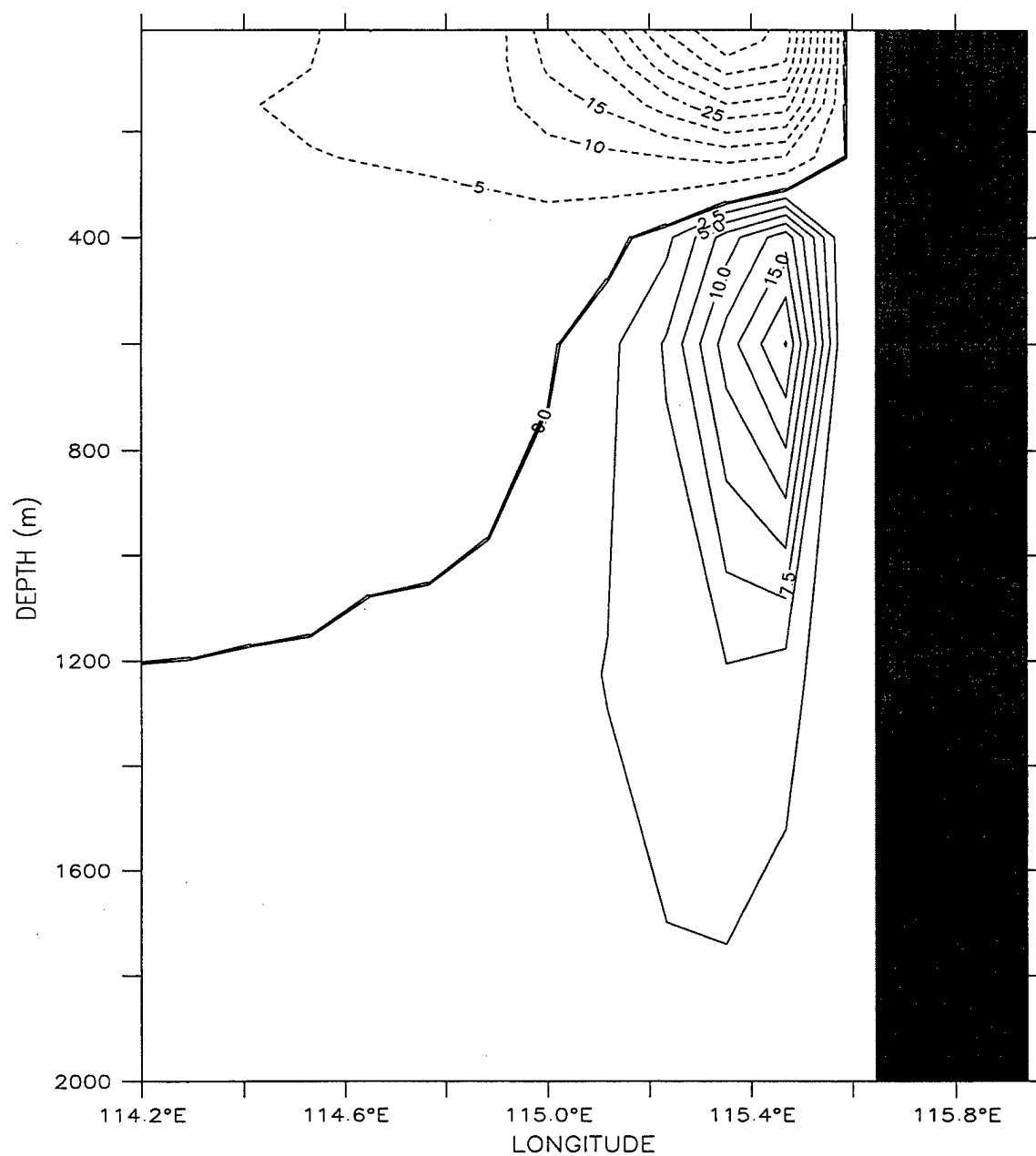


LATITUDE : 26.1S  
T (DAY) : 3



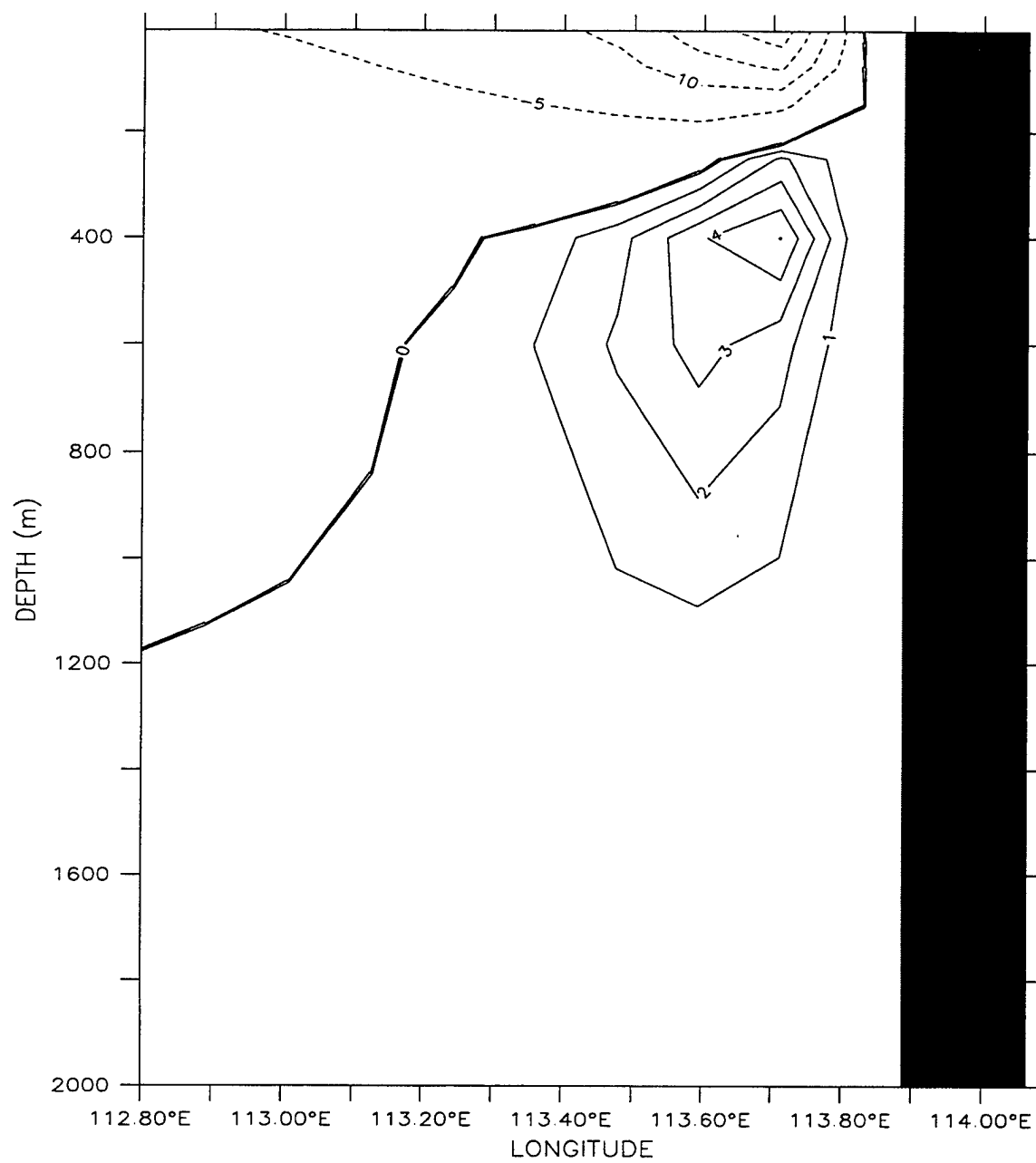
Meridional Velocity (cm/s)  
(b)

LATITUDE : 31.9S  
T (DAY) : 9



Meridional Velocity (cm/s)  
(c)

LATITUDE : 26.1S  
T (DAY) : 9



Meridional Velocity (cm/s)  
(d)

LONGITUDE : 117E(117)  
T (DAY) : 15

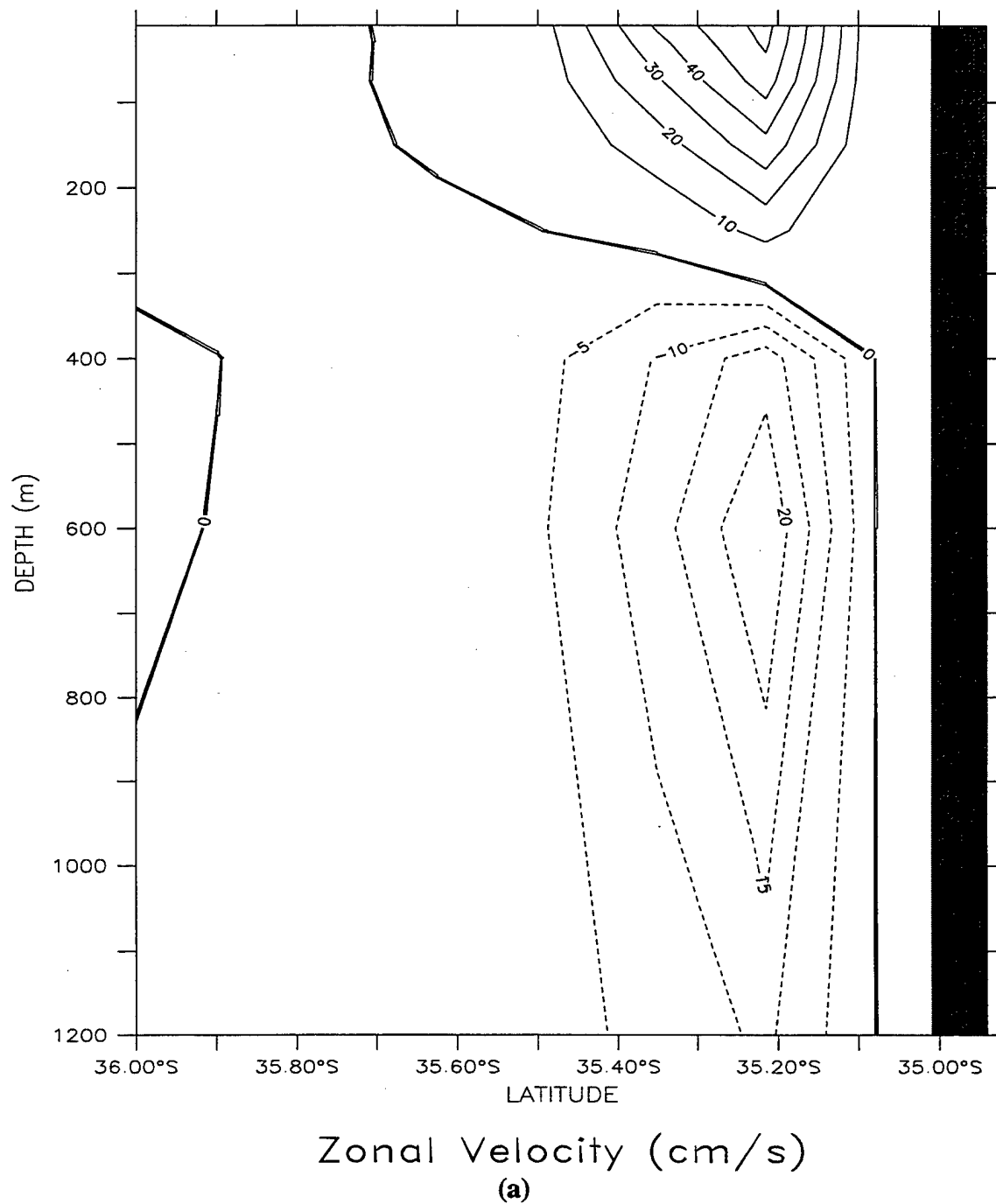
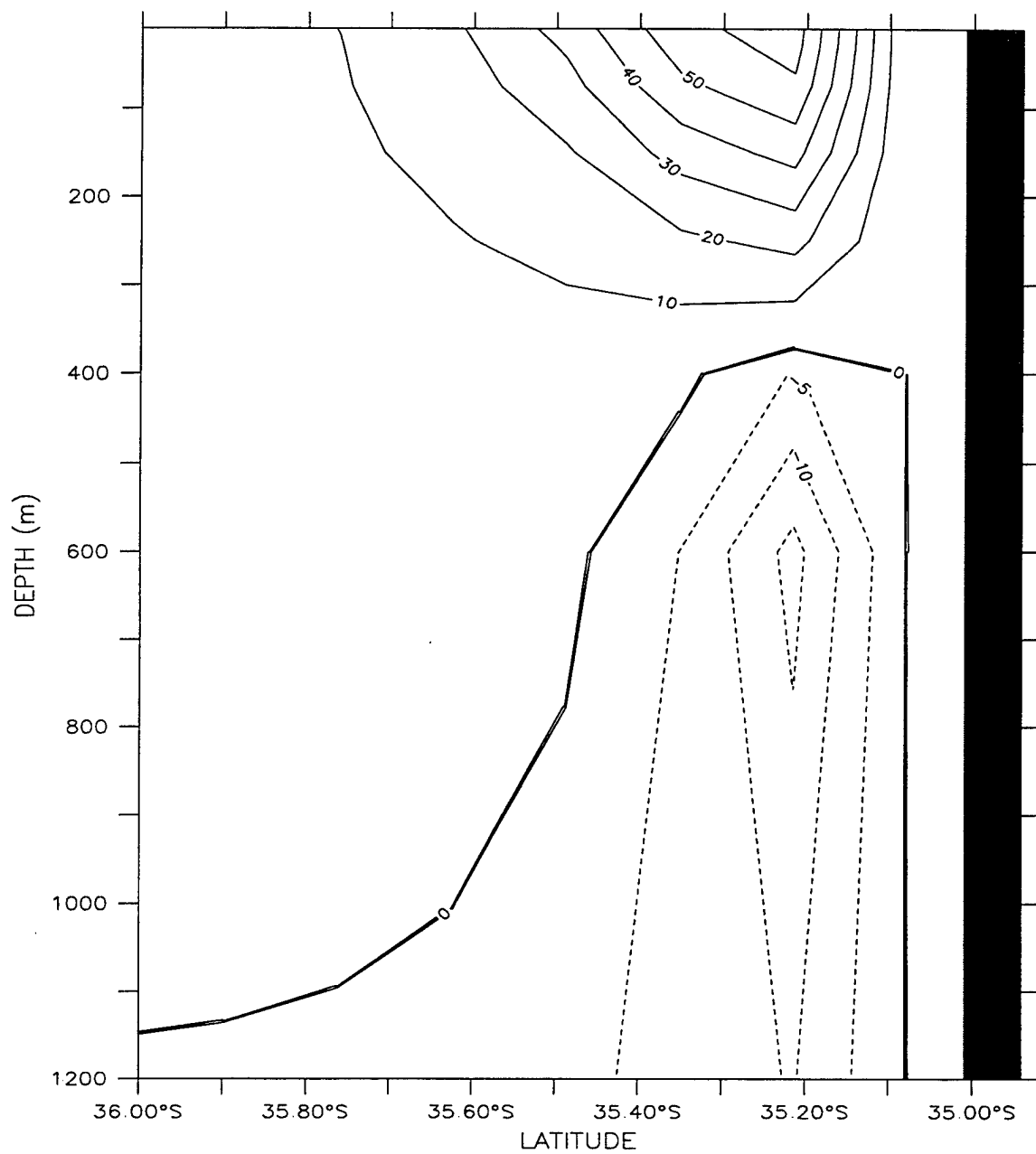


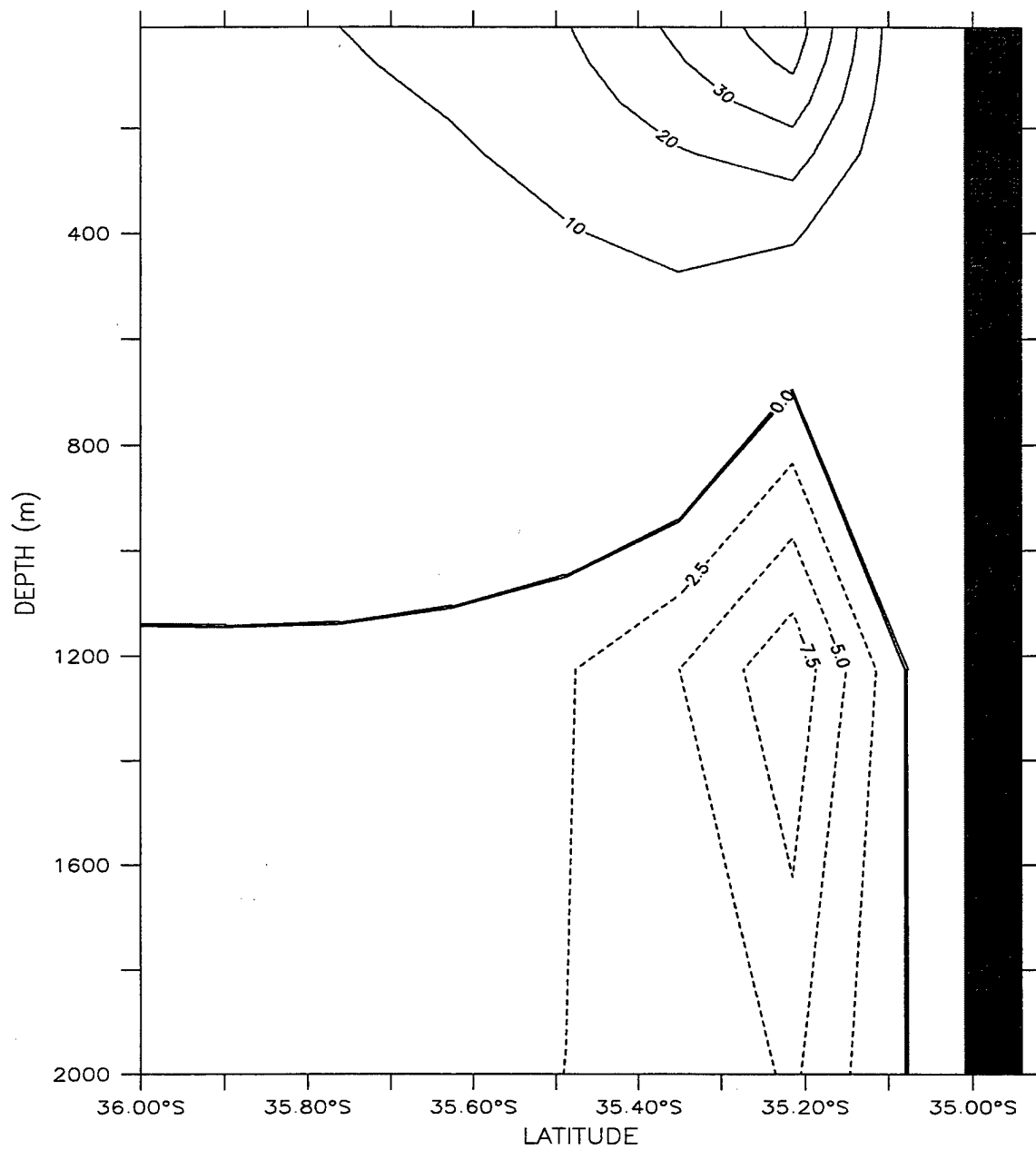
**Figure 13.** Cross-shore section of zonal velocity ( $u$ ) at (a and b)  $117^{\circ}\text{E}$  and (c)  $122^{\circ}\text{E}$  for (a) Experiment 3 and (b and c) Experiment 4 on day 15. The contour interval is (a and b) 5 cm/s and (c) 2.5 cm/s for westward flow (dashed lines) and 10 cm/s for eastward flow (solid lines).

LONGITUDE : 117E(117)  
T (DAY) : 15



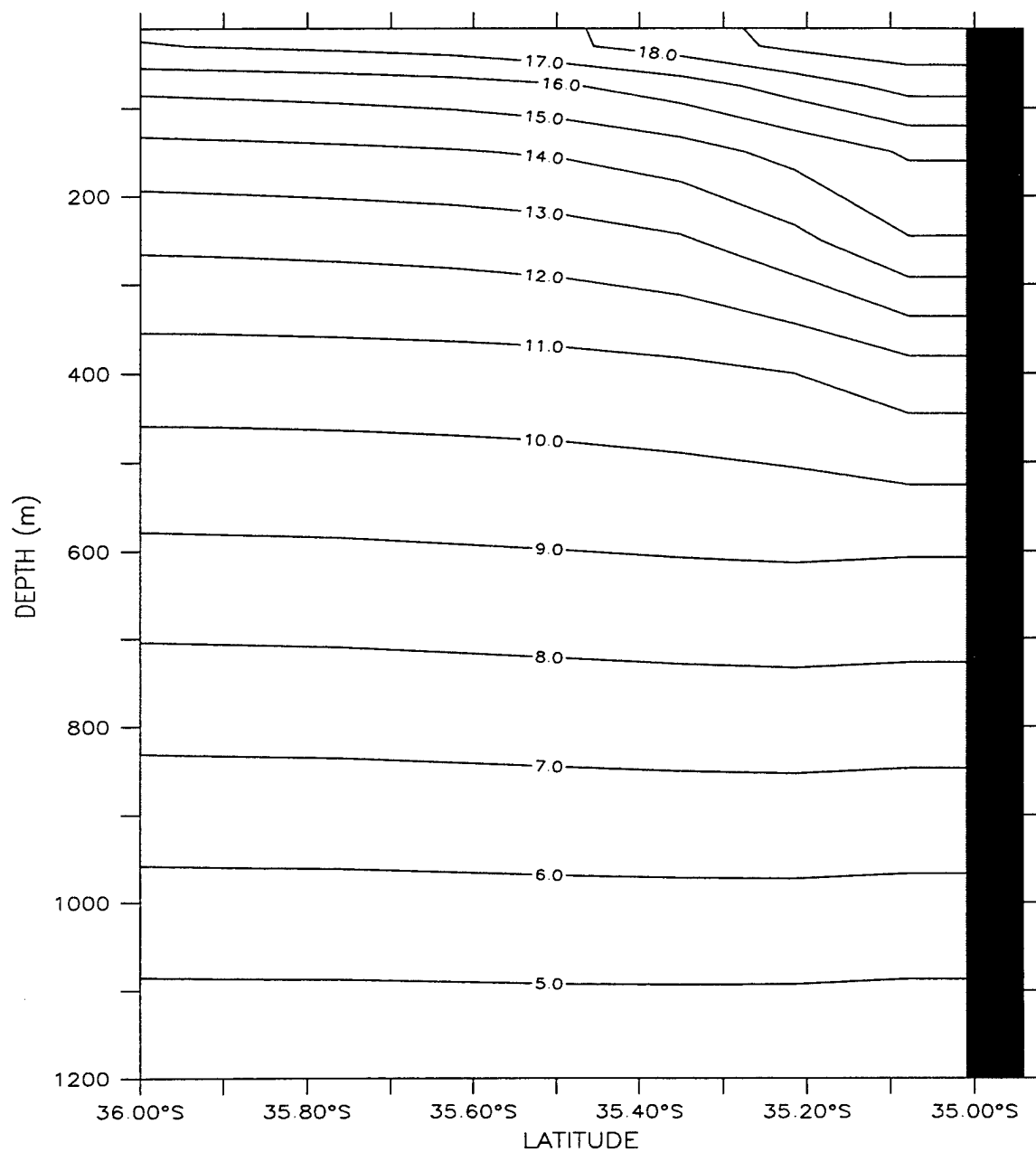
Zonal Velocity (cm/s)  
(b)

LONGITUDE : 122E(122)  
T (DAY) : 15



Zonal Velocity (cm/s)  
(c)

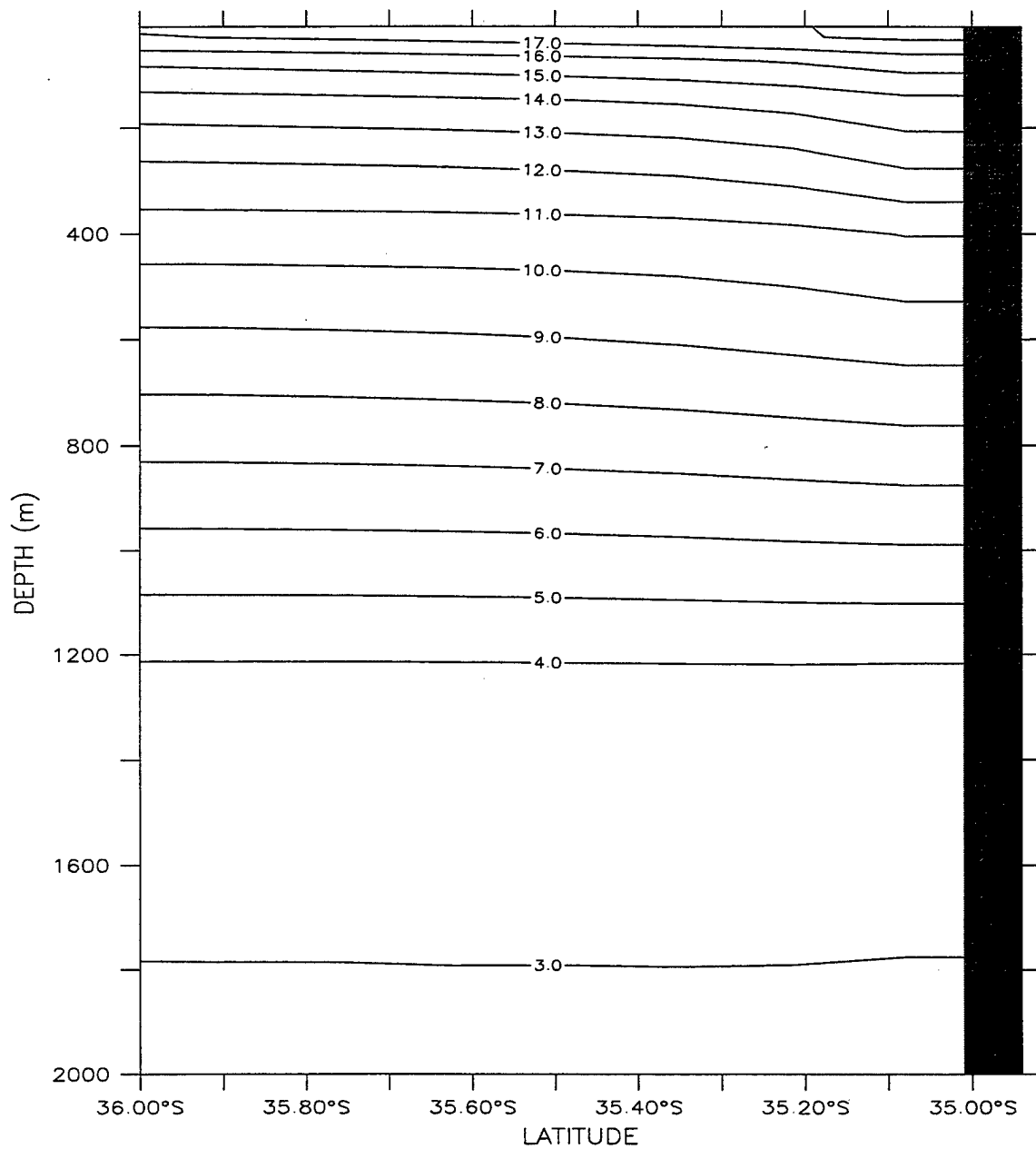
LONGITUDE : 117E(117)  
T (DAY) : 15



Temperature (deg C)  
(a)

**Figure 14.** Cross-shore section of temperature at (a) 117°E and (b) 122°E for Experiment 4 on day 15. The contour interval is 1°C.

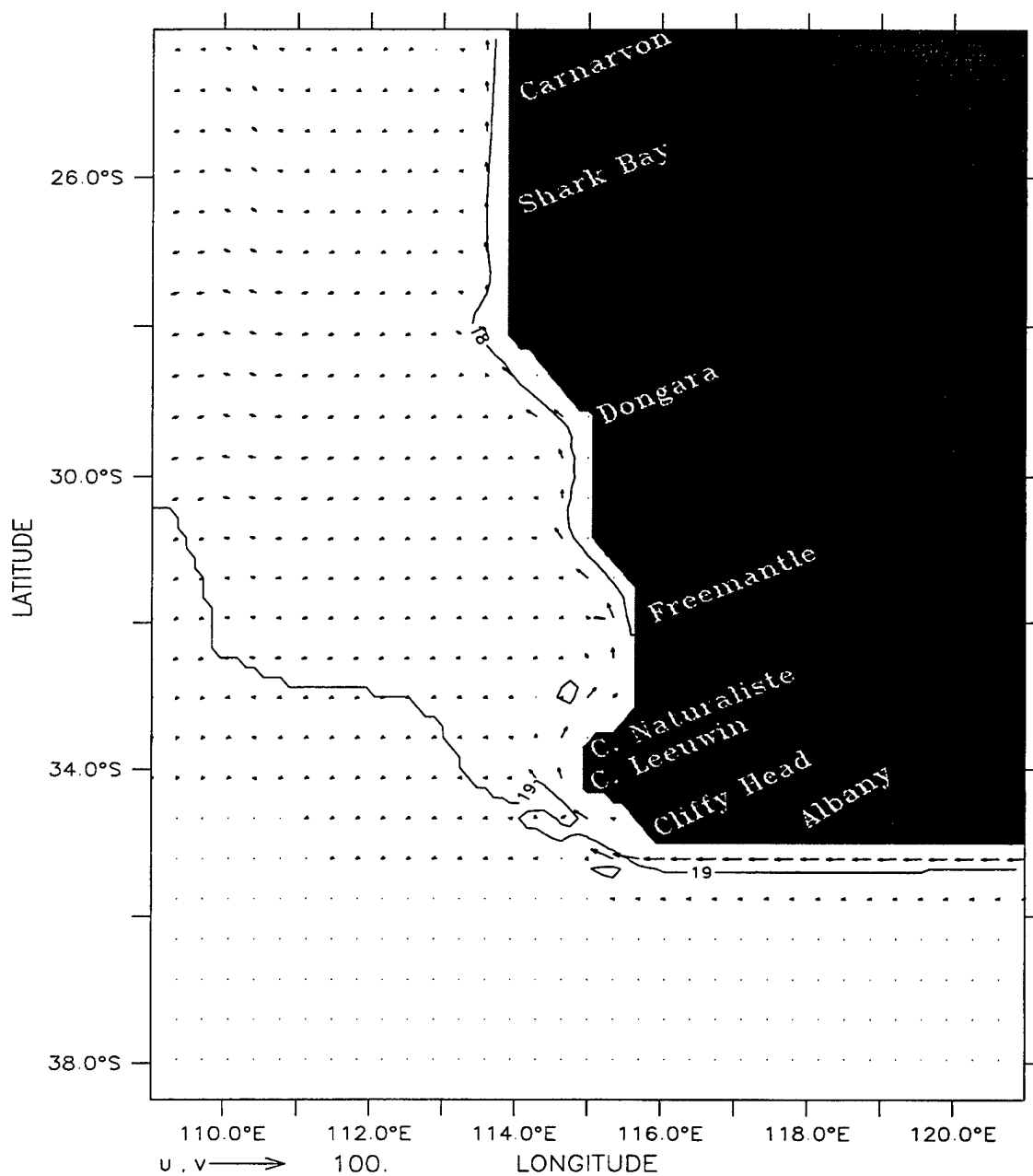
LONGITUDE : 122E(122)  
T (DAY) : 15



Temperature (deg C)  
(b)



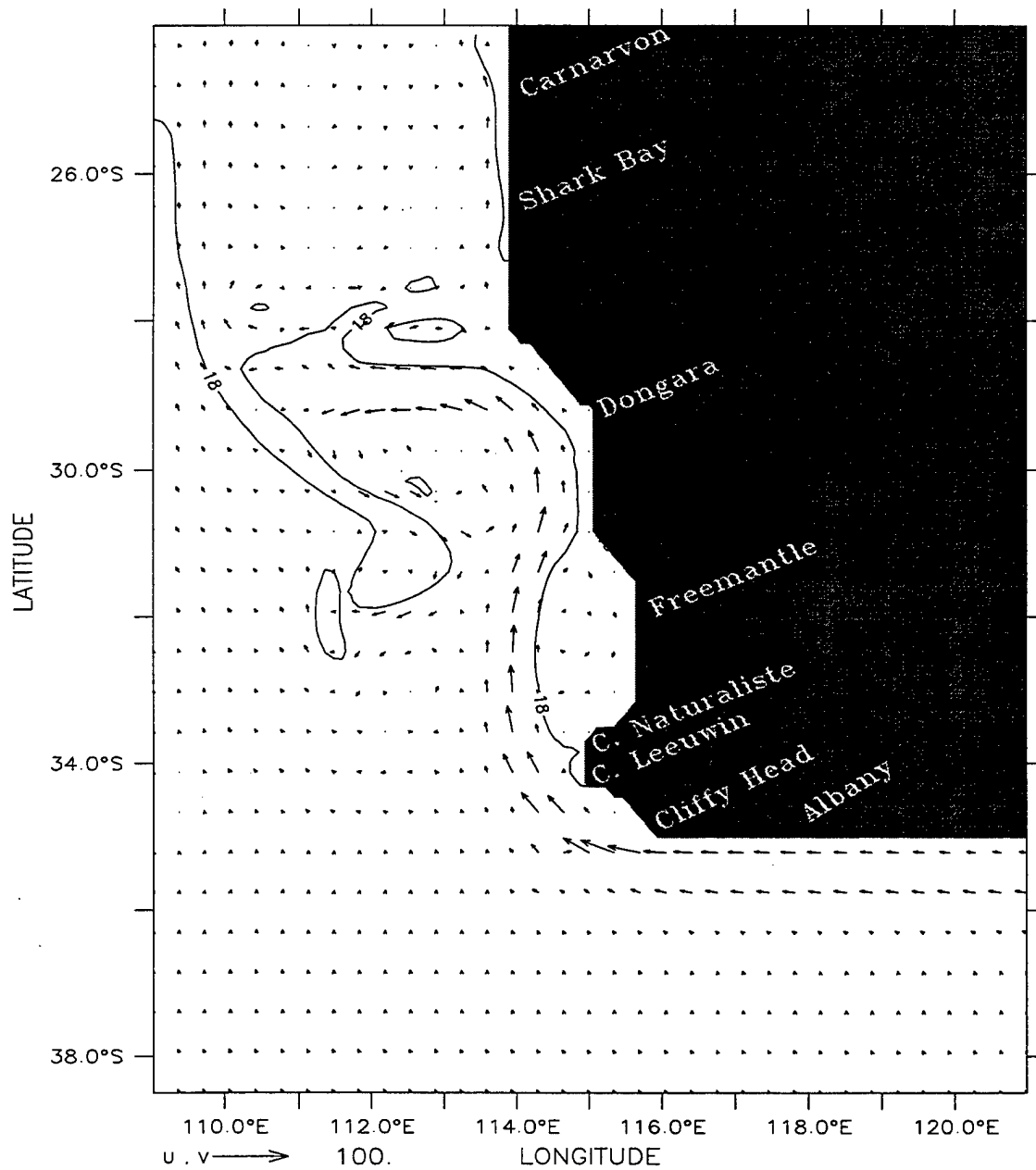
DEPTH (m) : 10  
T (DAY) : 33



Temperature (deg C) and Velocity (cm/s)  
(a)

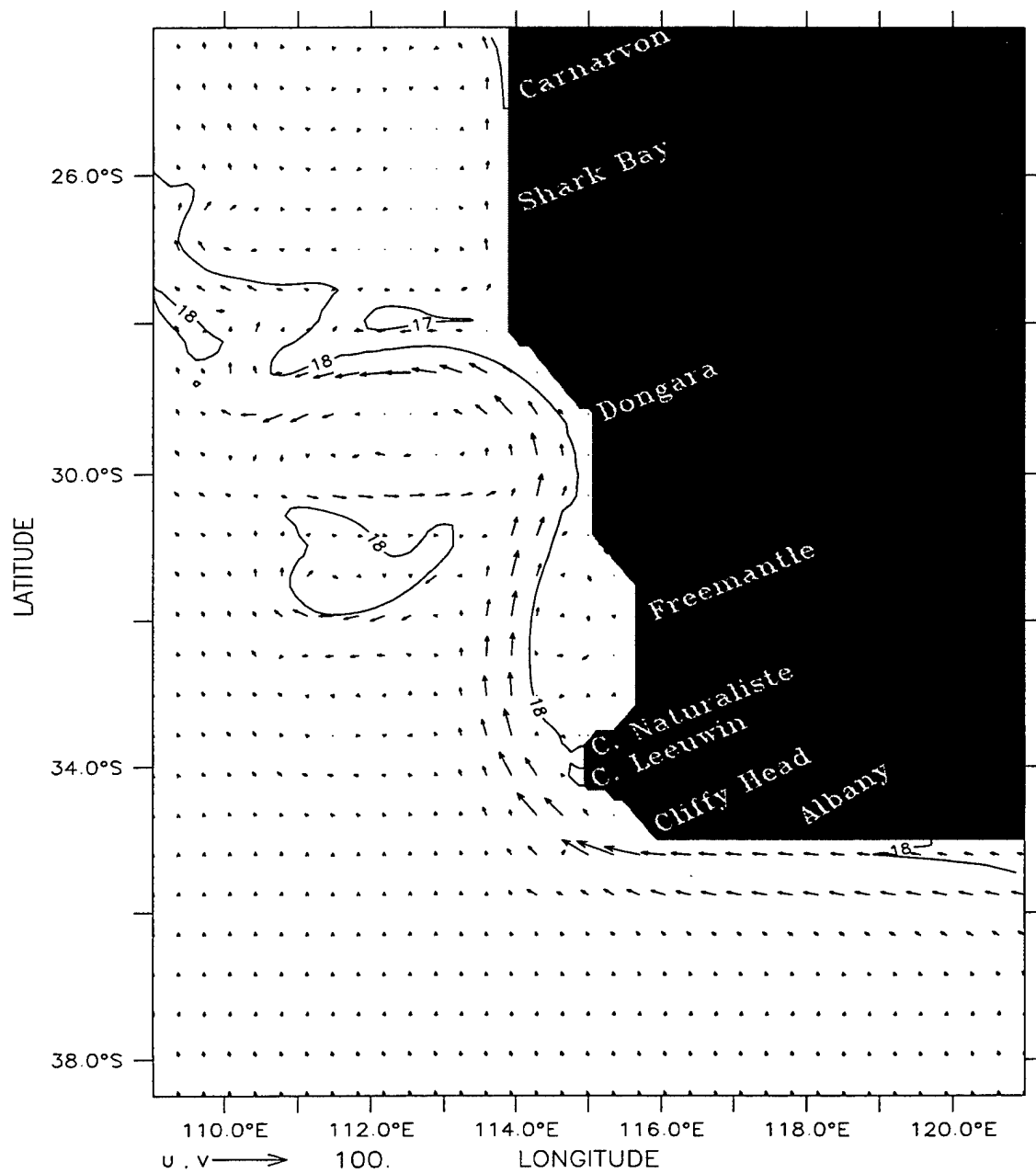
**Figure 15.** Temperature contours and velocity vectors at 10 m depth at days (a) 33, (b) 195, (c) 231, (d) 297, and (e) 363 of Experiment 5. The contour interval is 1°C. To avoid clutter, the velocity vectors are plotted every third grid point in the east-west direction and every fourth grid point in the north-south direction. Maximum velocity is 100 cm/s.

DEPTH (m) : 10  
T (DAY) : 195



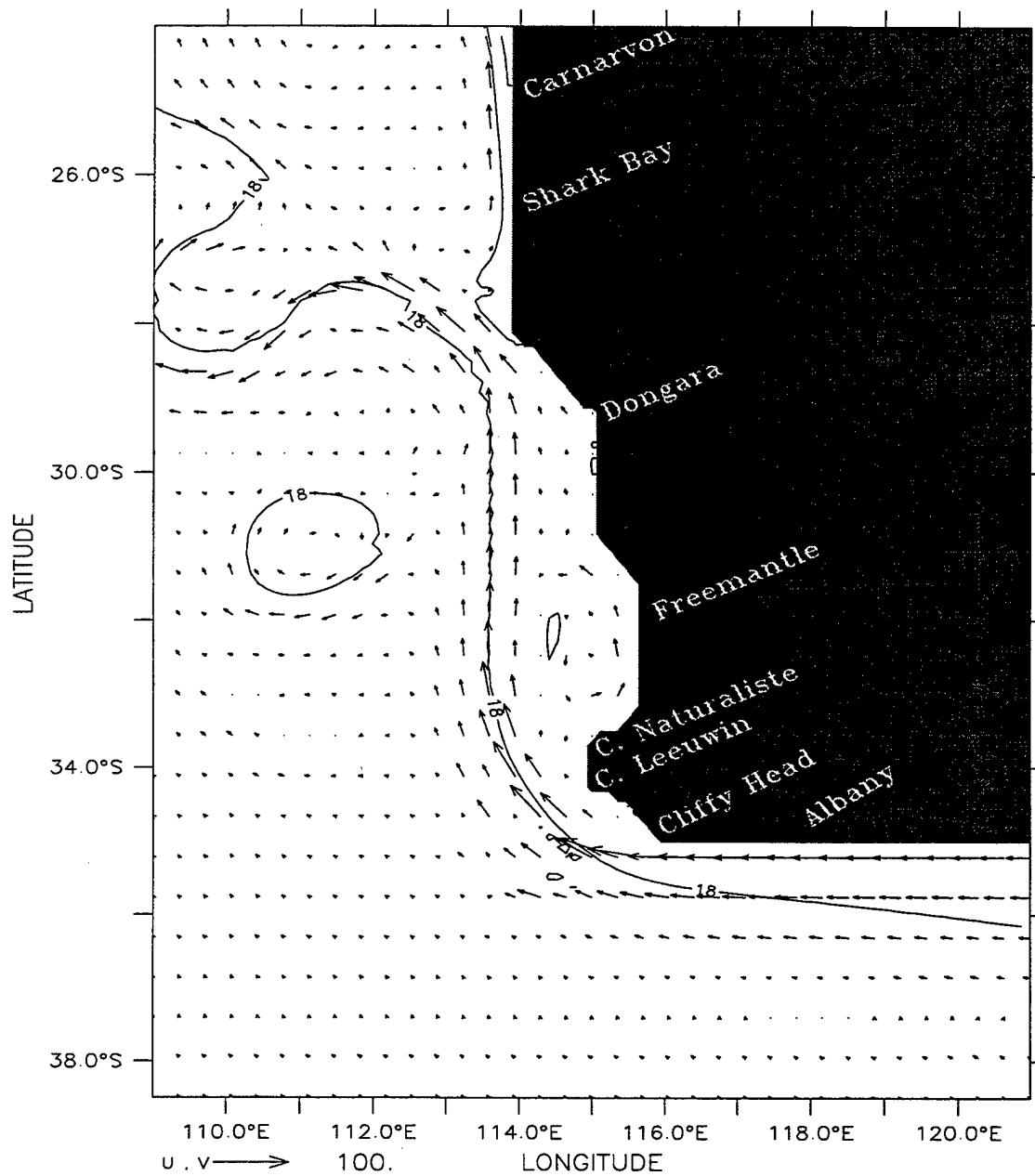
Temperature (deg C) and Velocity (cm/s)  
(b)

DEPTH (m) : 10  
T (DAY) : 231



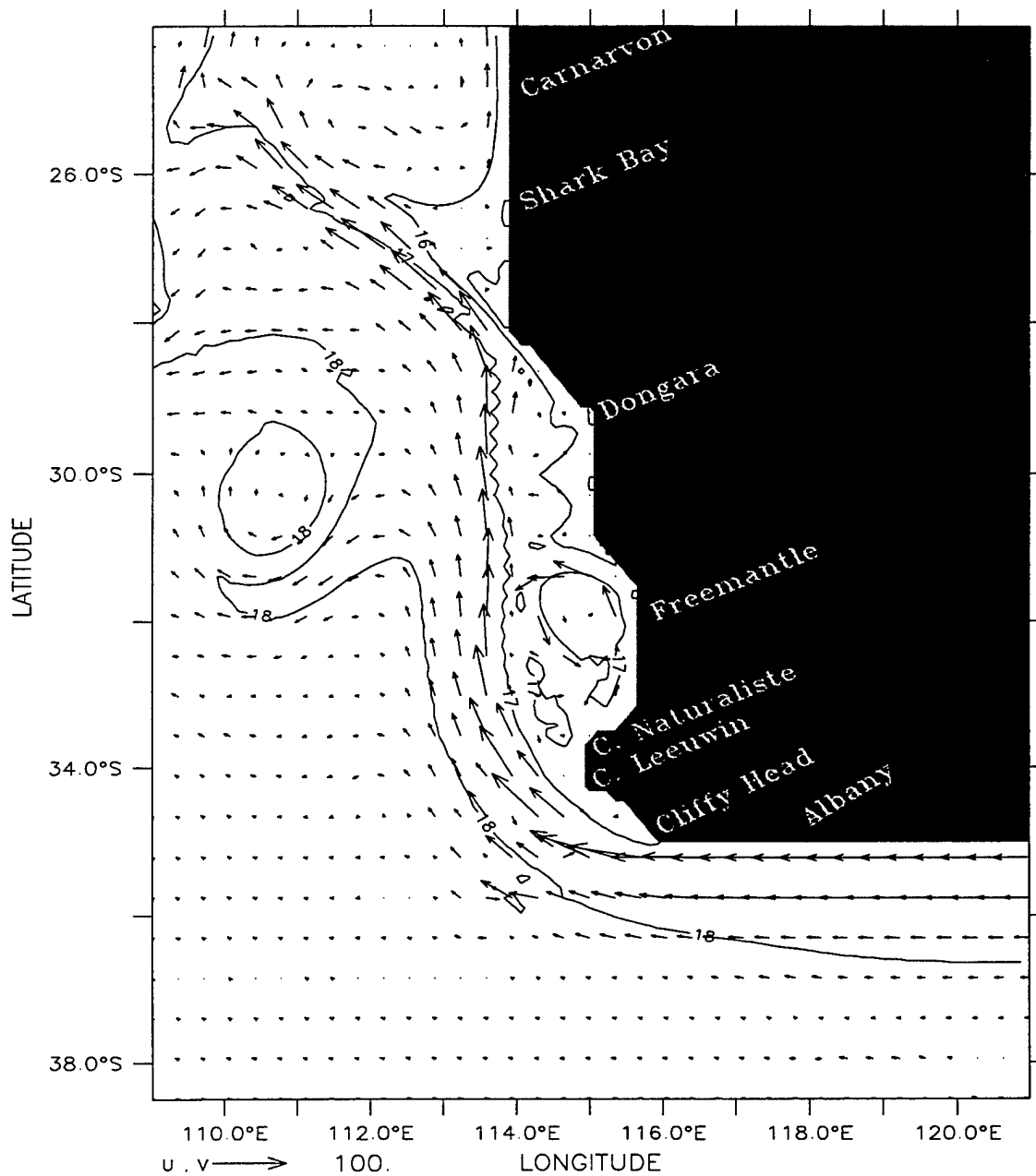
Temperature (deg C) and Velocity (cm/s)  
(c)

DEPTH (m) : 10  
T (DAY) : 297



Temperature (deg C) and Velocity (cm/s)  
(d)

DEPTH (m) : 10  
T (DAY) : 363



Temperature (deg C) and Velocity (cm/s)  
(e)

LATITUDE : 31.9S  
T (DAY) : 33

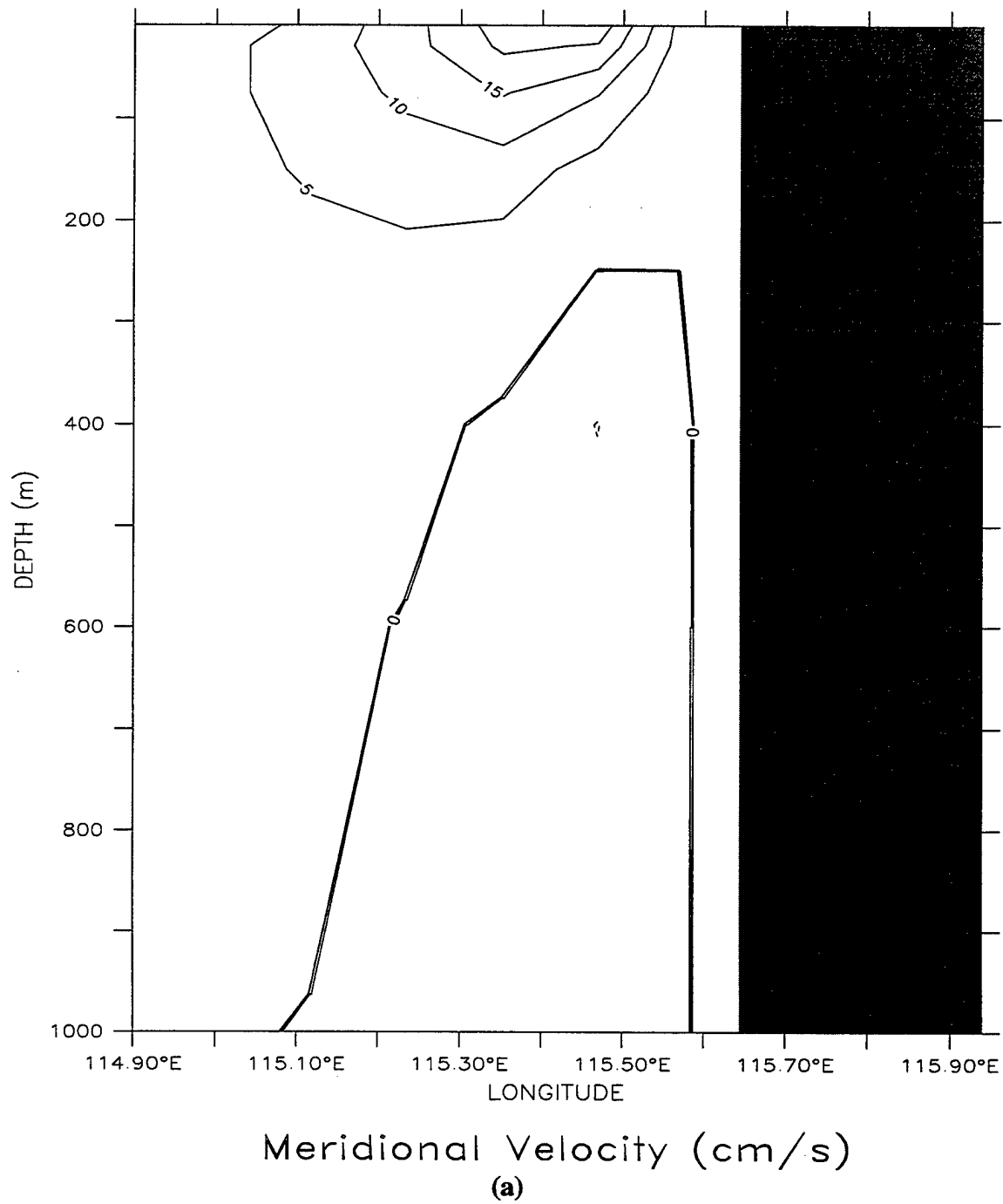
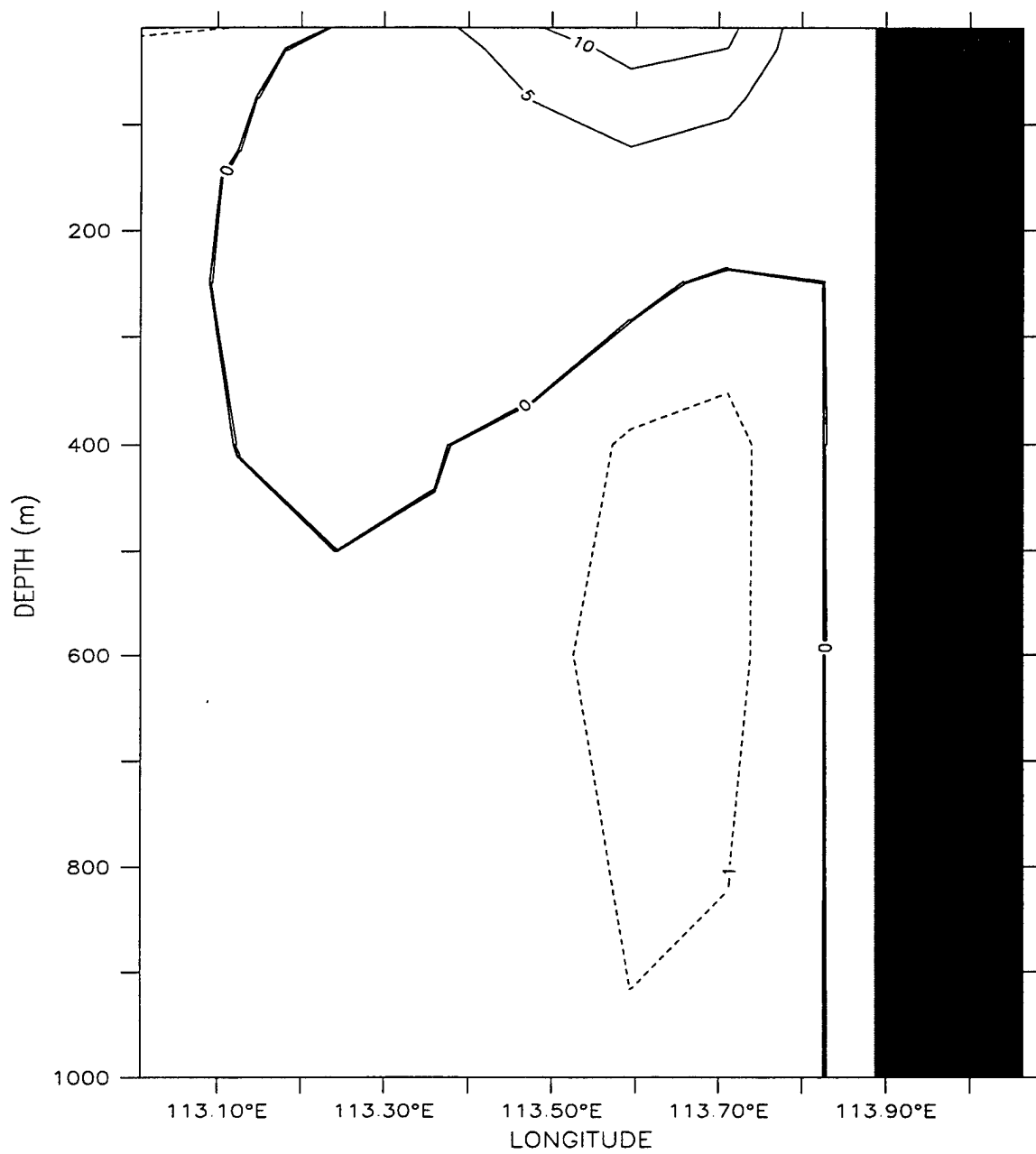


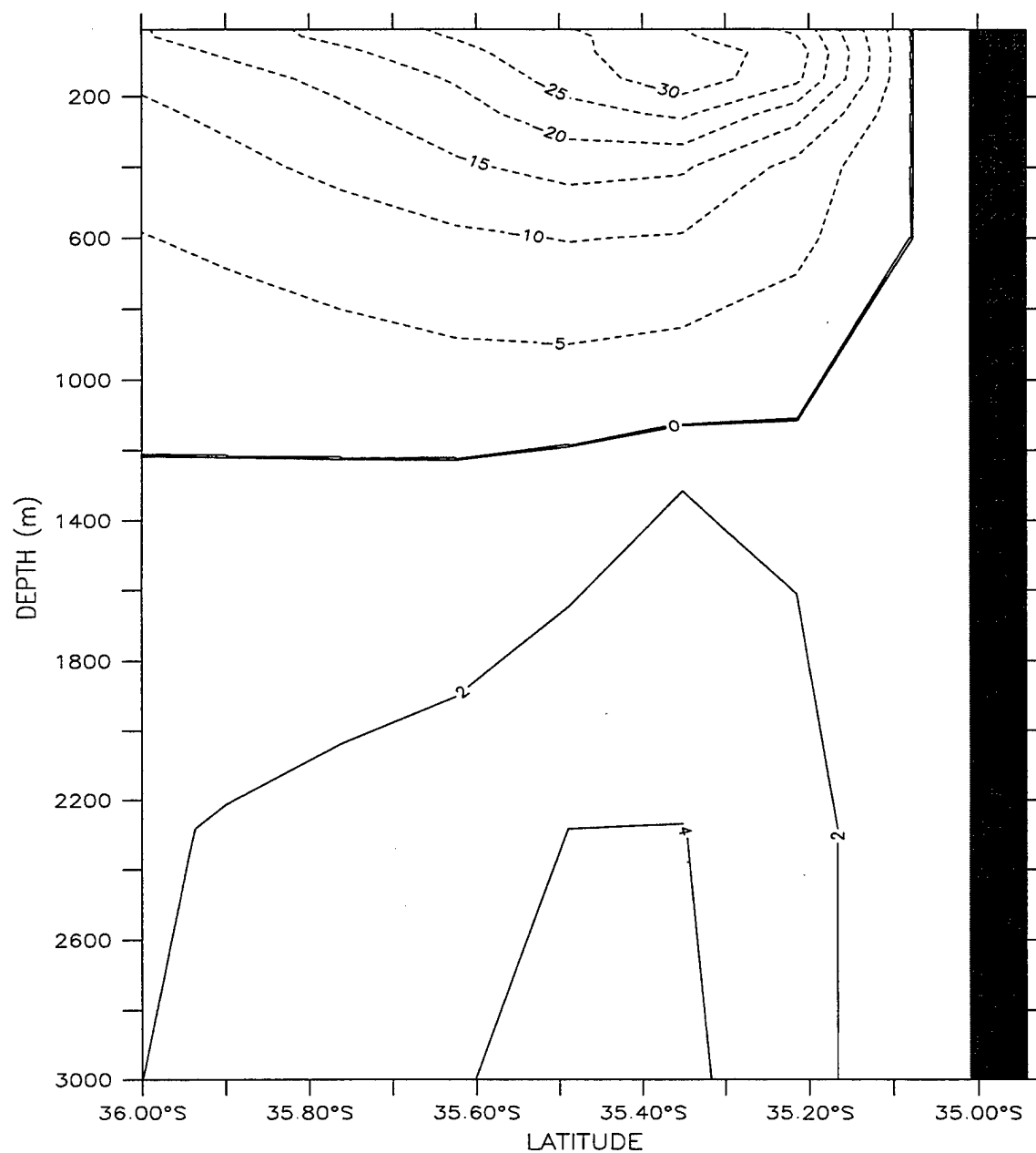
**Figure 16.** Cross-shore section of meridional velocity (v) at (a) ~32°S and (b) ~26°S for Experiment 5 on day 33. Contour interval is 1 cm/s for poleward flow (dashed lines) and 5 cm/s for equatorward flow (solid lines).

LATITUDE : 26.1S  
T (DAY) : 33



Meridional Velocity (cm/s)  
(b)

LONGITUDE : 117E(117)  
T (DAY) : 243



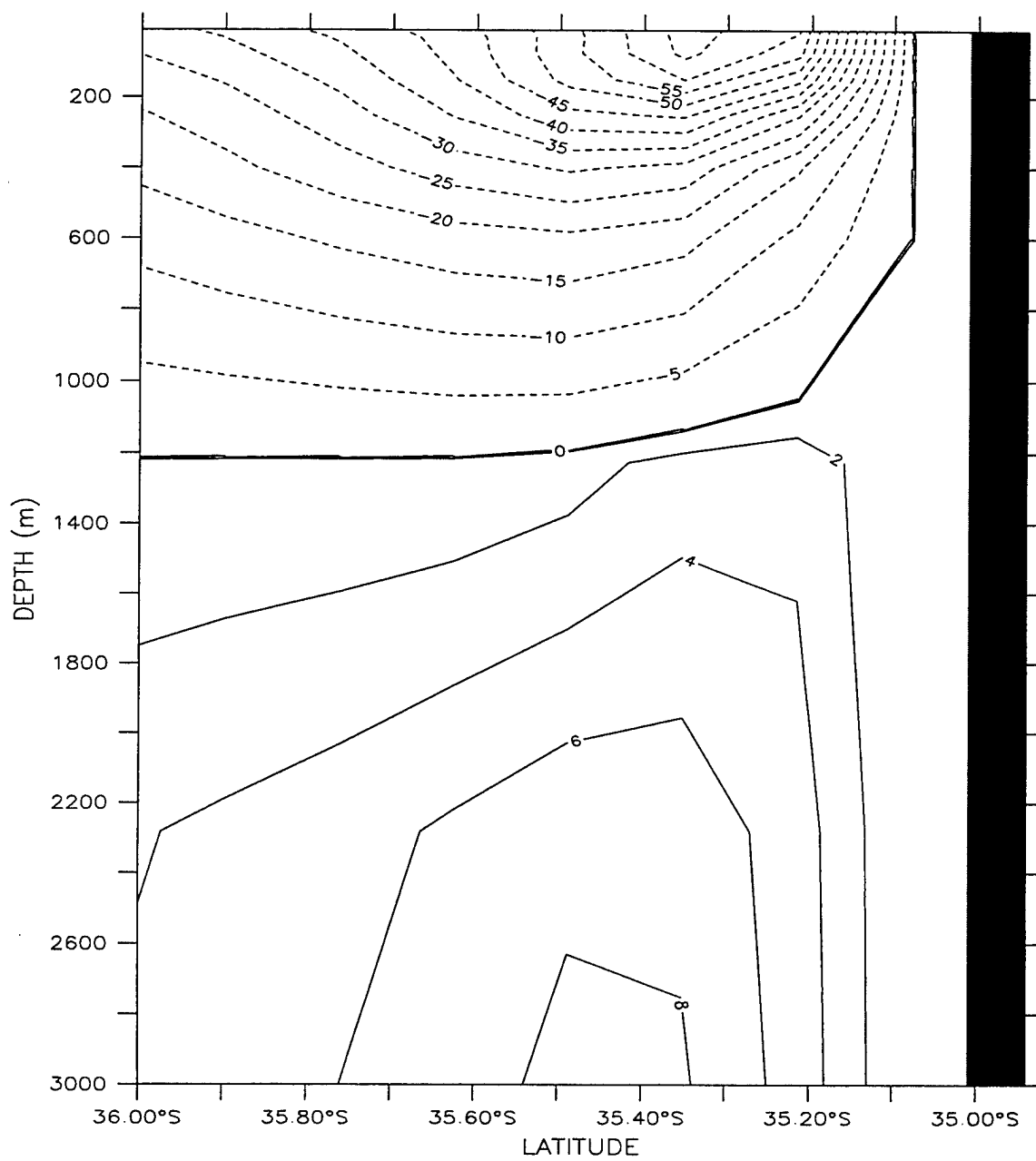
Zonal Velocity (cm/s)

(a)

**Figure 17.** Cross-shore section of zonal velocity ( $u$ ) at  $117^\circ\text{E}$  for Experiment 5 on days (a) 243 and (b) 363. Contour interval is 5 cm/s for westward flow (dashed lines) and 2 cm/s for eastward flow (solid lines).



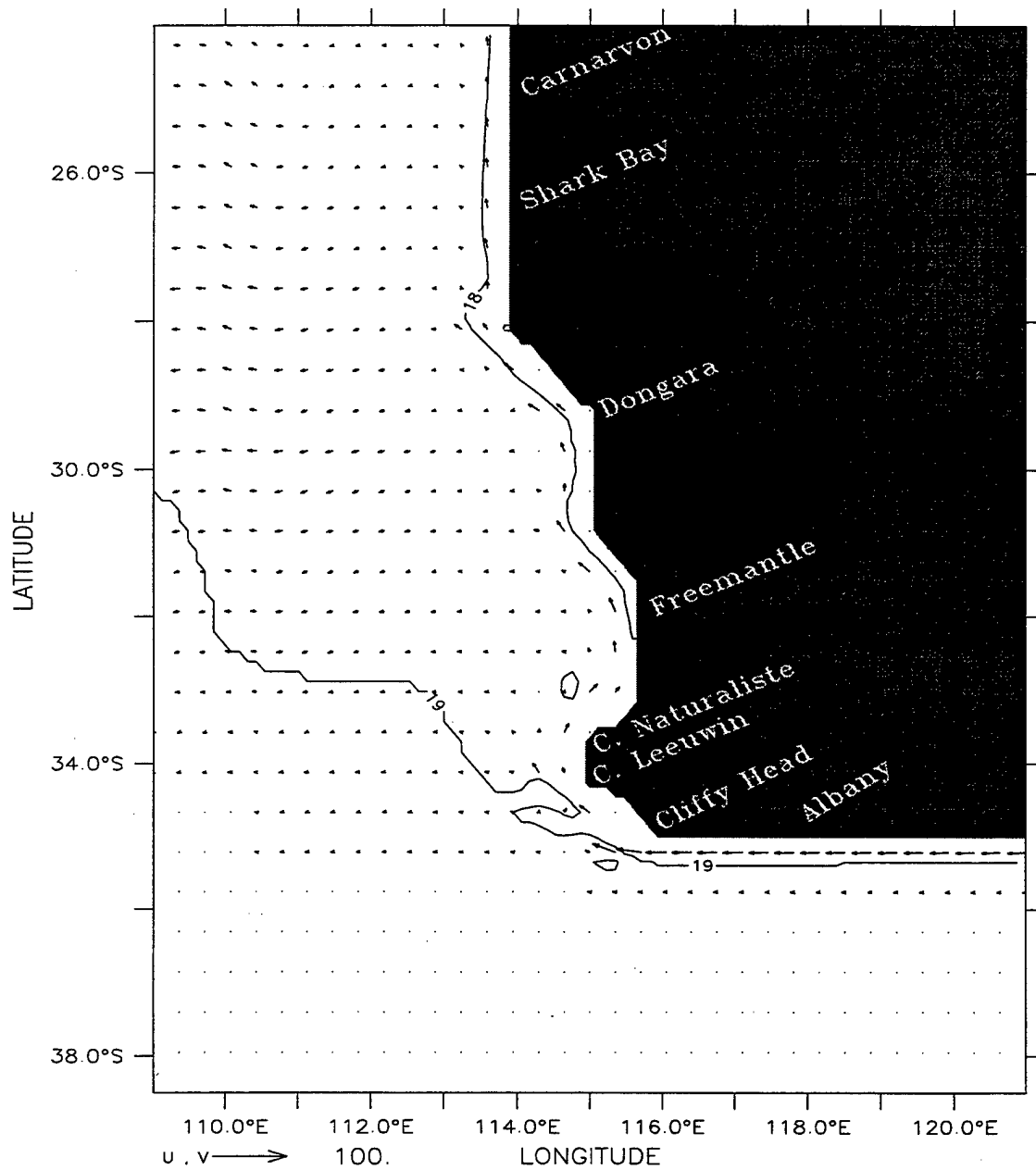
LONGITUDE : 117E(117)  
T (DAY) : 363



Zonal Velocity (cm/s)

(b)

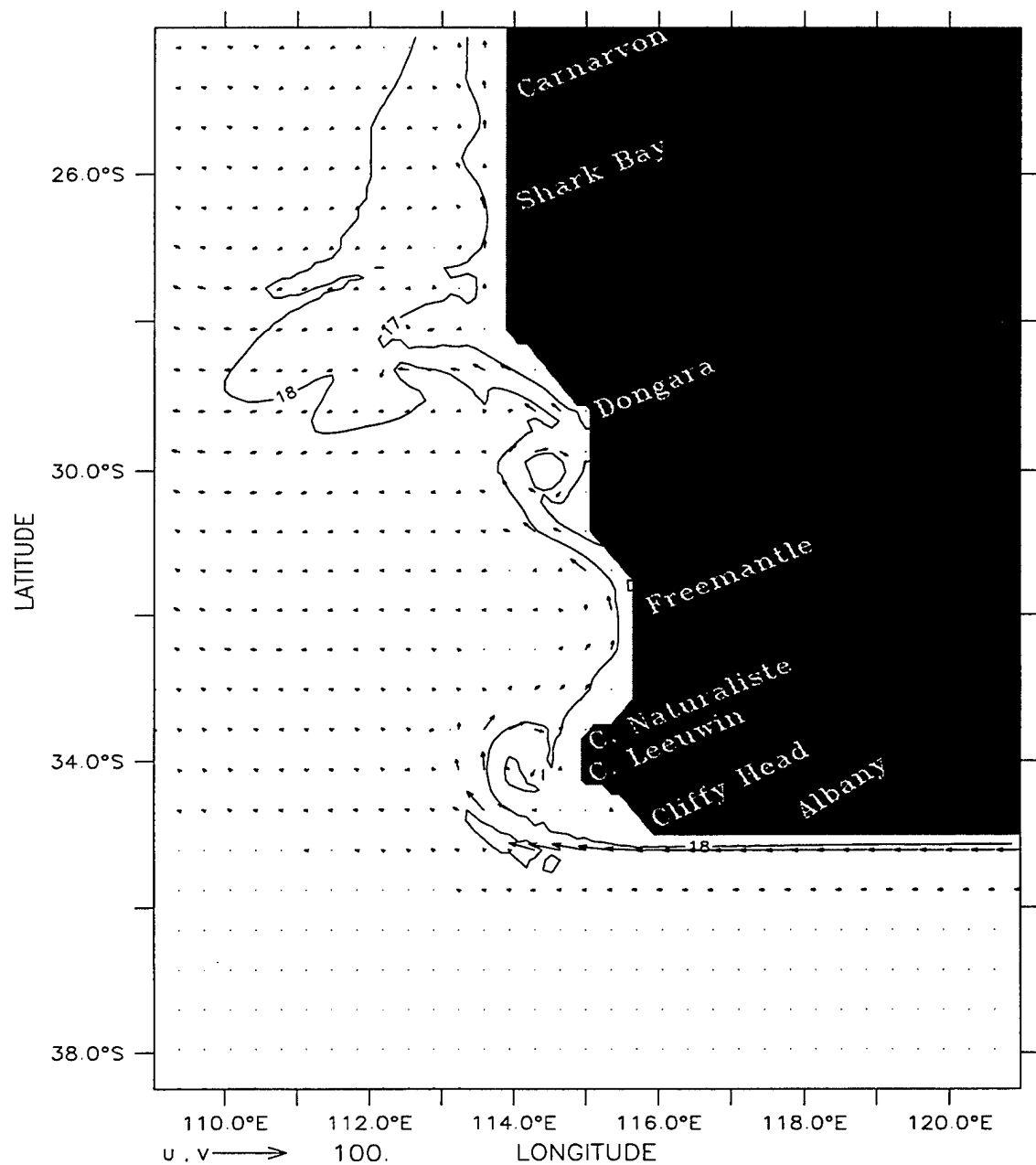
DEPTH (m) : 10  
T (DAY) : 33



Temperature (deg C) and Velocity (cm/s)  
(a)

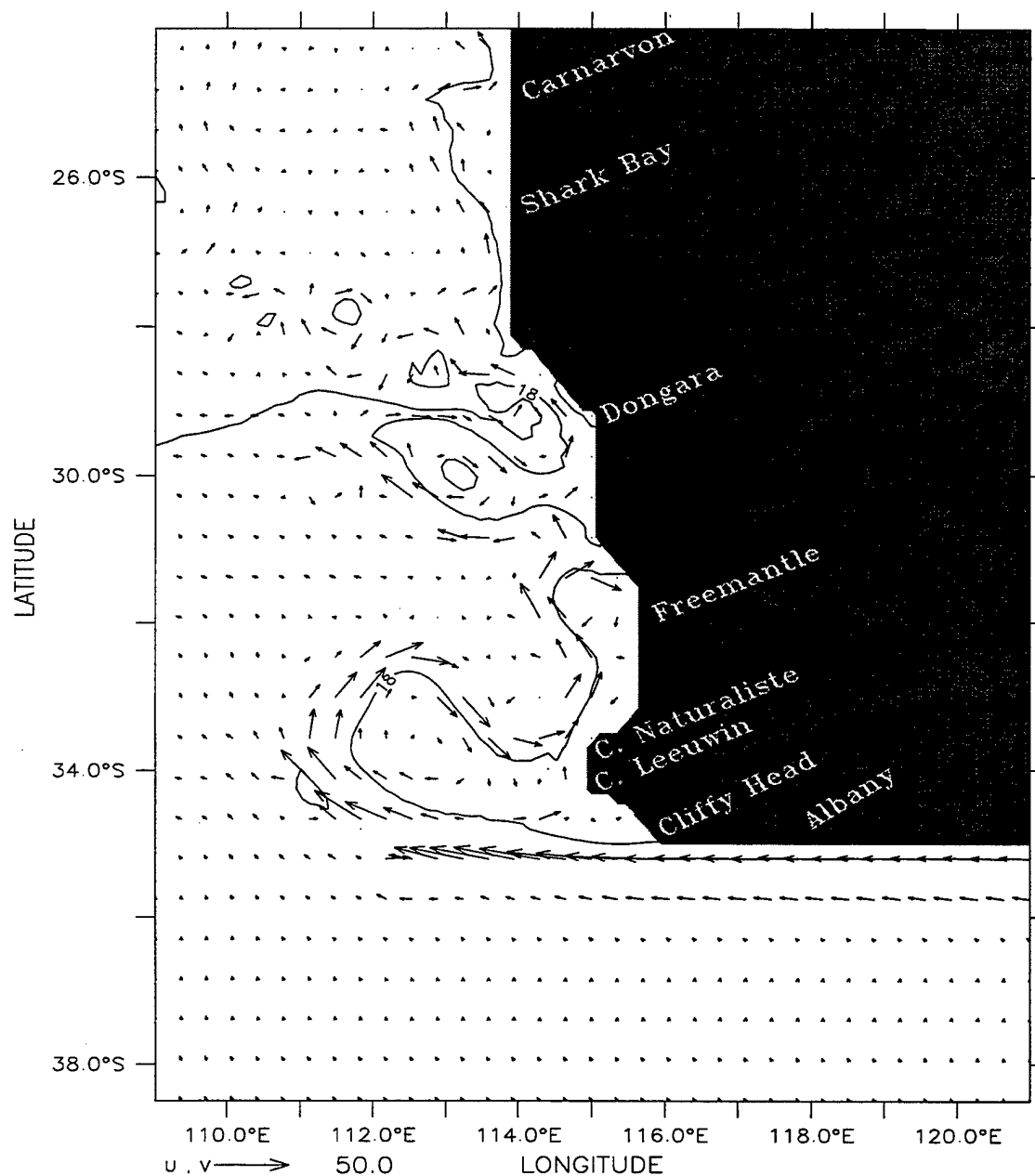
**Figure 18.** Temperature contours and velocity vectors at 10 m depth at days (a) 33, (b) 90, and (c) 165 of Experiment 6. The contour interval is 1°C. Maximum velocity for (a) and (b) is 100 cm/s and for (c) is 50 cm/s.

DEPTH (m) : 10  
T (DAY) : 90



Temperature (deg C) and Velocity (cm/s)  
(b)

DEPTH (m) : 10  
T (DAY) : 165



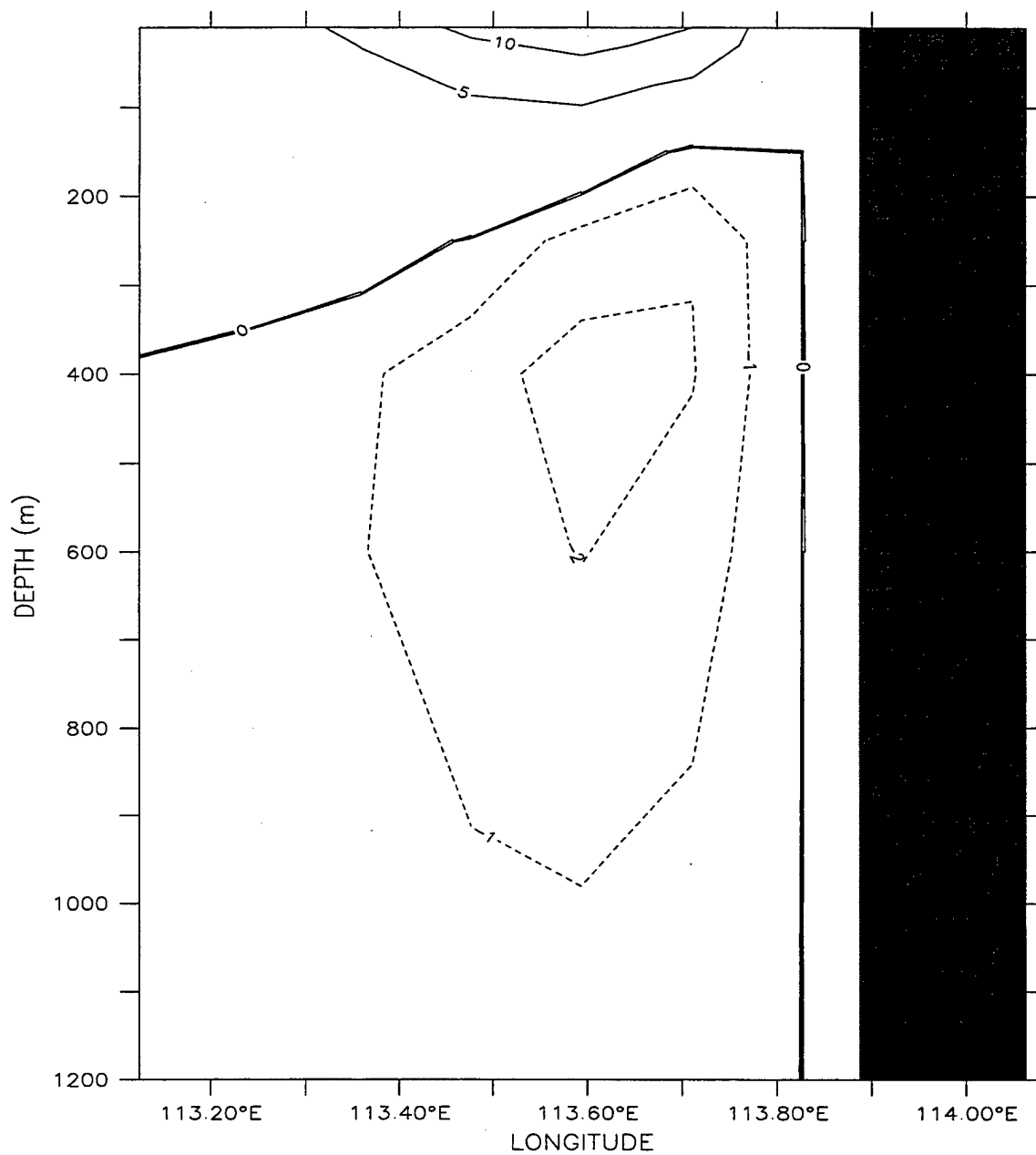
Temperature (deg C) and Velocity (cm/s)  
(c)

T (DAY) : 33



**Figure 19.** Cross-shore section of meridional velocity ( $v$ ) at (a)  $\sim 32^\circ\text{S}$  and (b)  $\sim 26^\circ\text{S}$  for Experiment 6 on day 33. Contour interval is 1 cm/s for poleward flow (dashed lines) and 5 cm/s for equatorward flow (solid lines).

LATITUDE : 26.1S  
T (DAY) : 33



Meridional Velocity (cm/s)

(b)

LATITUDE : 34S  
T (DAY) : 33

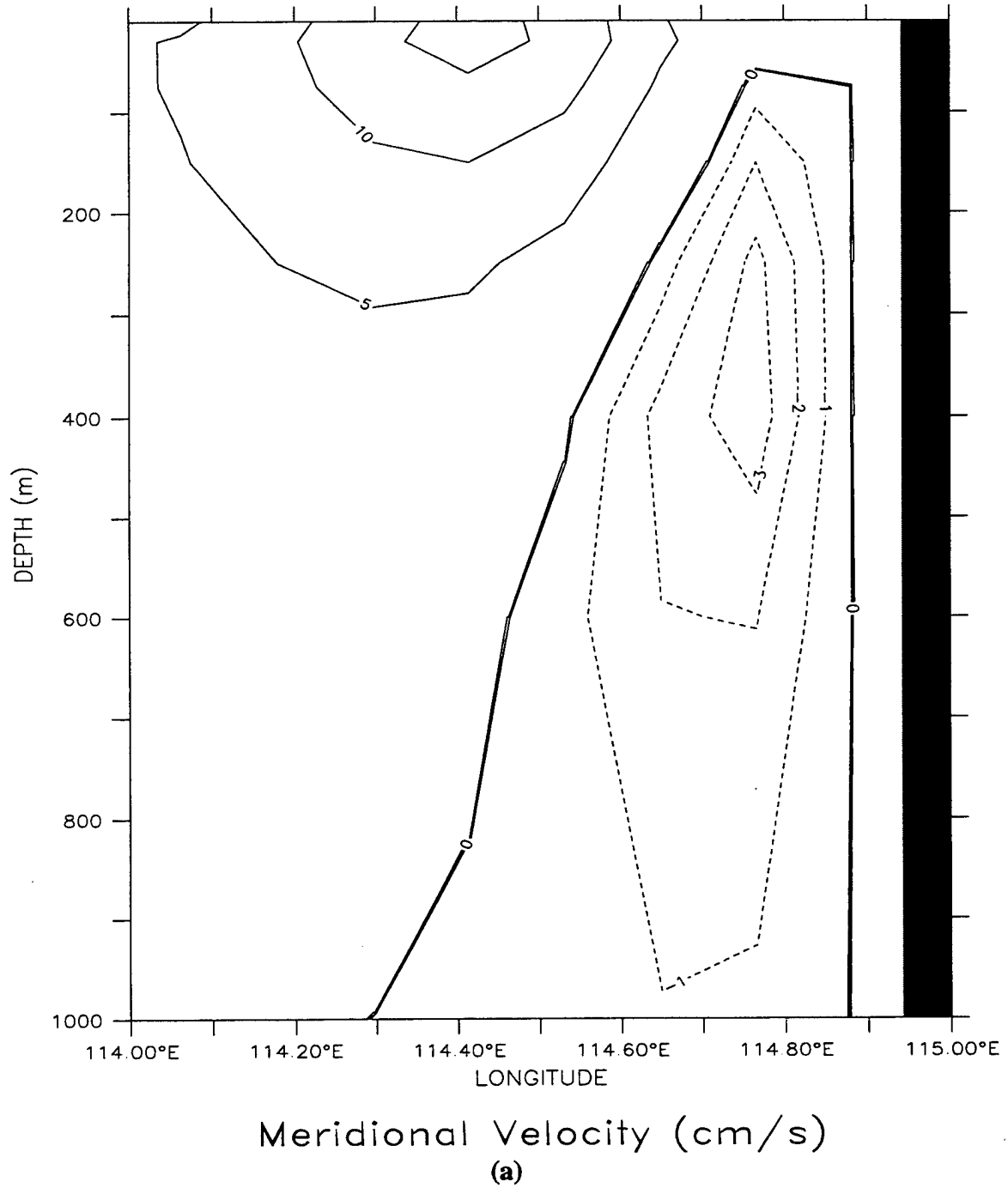
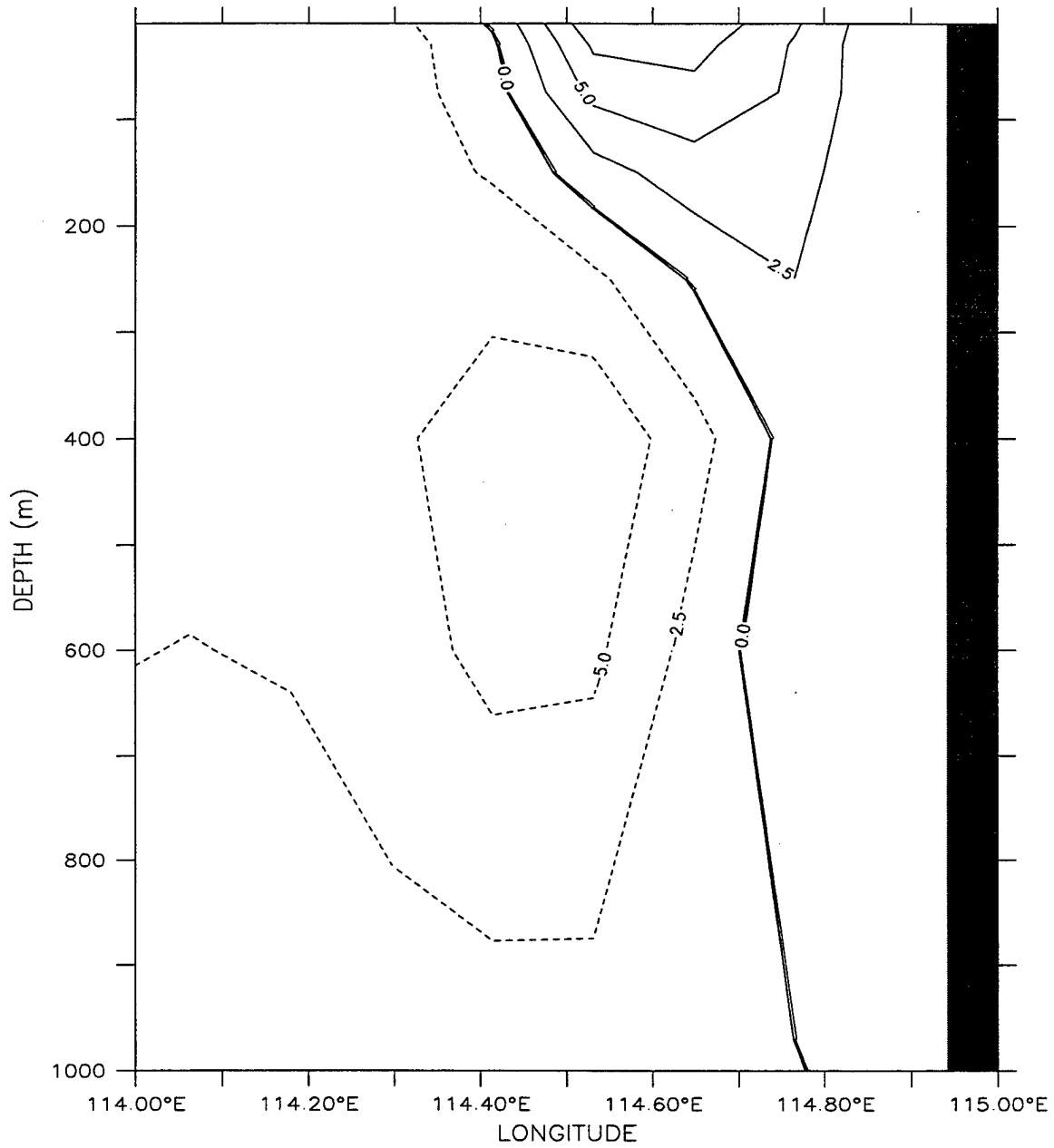


**Figure 20.** Cross-shore section of meridional velocity ( $v$ ) at  $34^\circ\text{S}$  at days (a) 33 and (b) 165 and at  $\sim 26^\circ\text{S}$  at day (c) 315 for Experiment 6. Contour interval is (a) 1 cm/s, (b) 2.5 cm/s, and (c) 5 cm/s for poleward flow (dashed lines) and (a and c) 5 cm/s and (b) 2.5 cm/s for equatorward flow (solid lines).

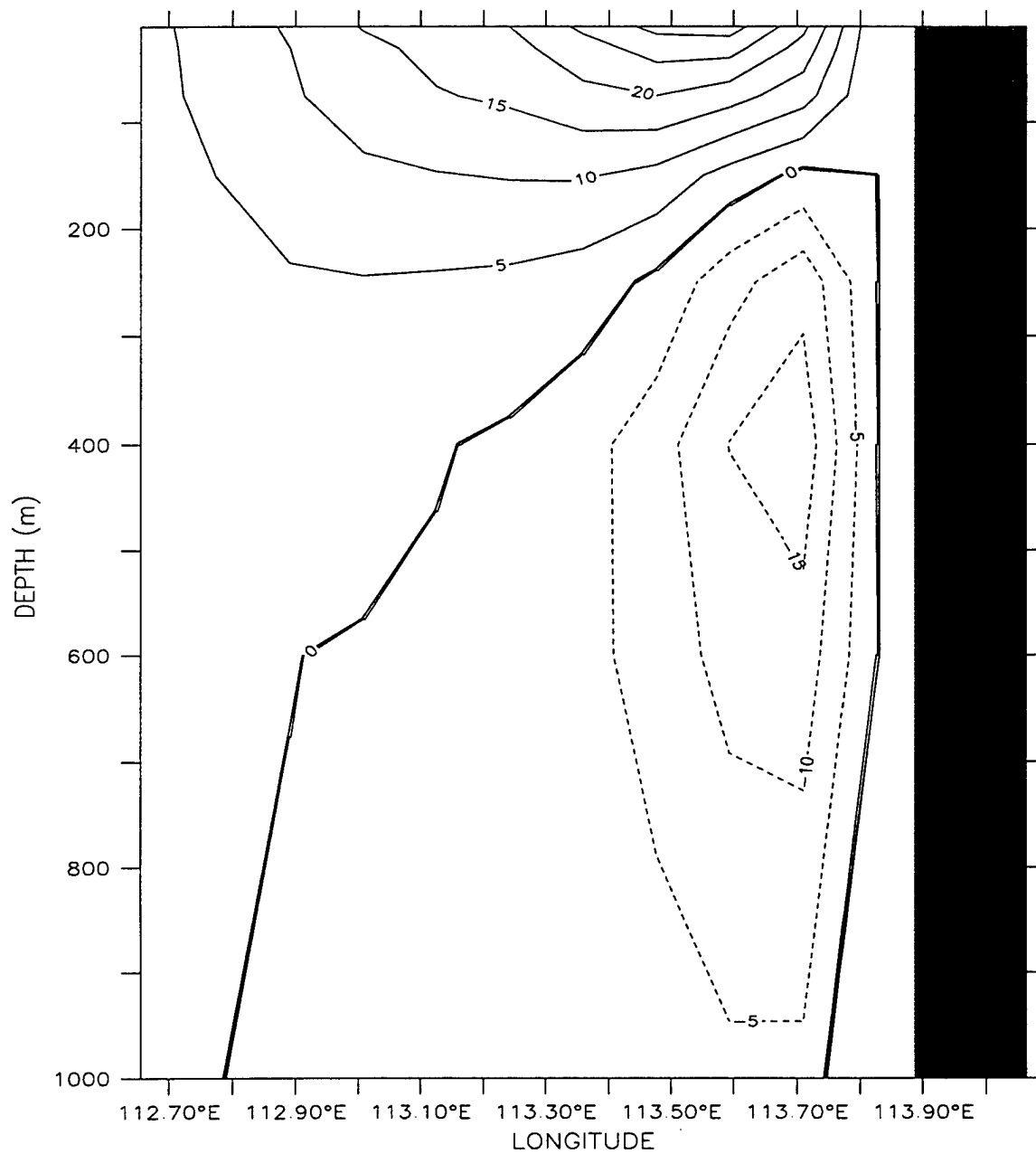
LATITUDE : 34S  
T (DAY) : 165



Meridional Velocity (cm/s)  
(b)



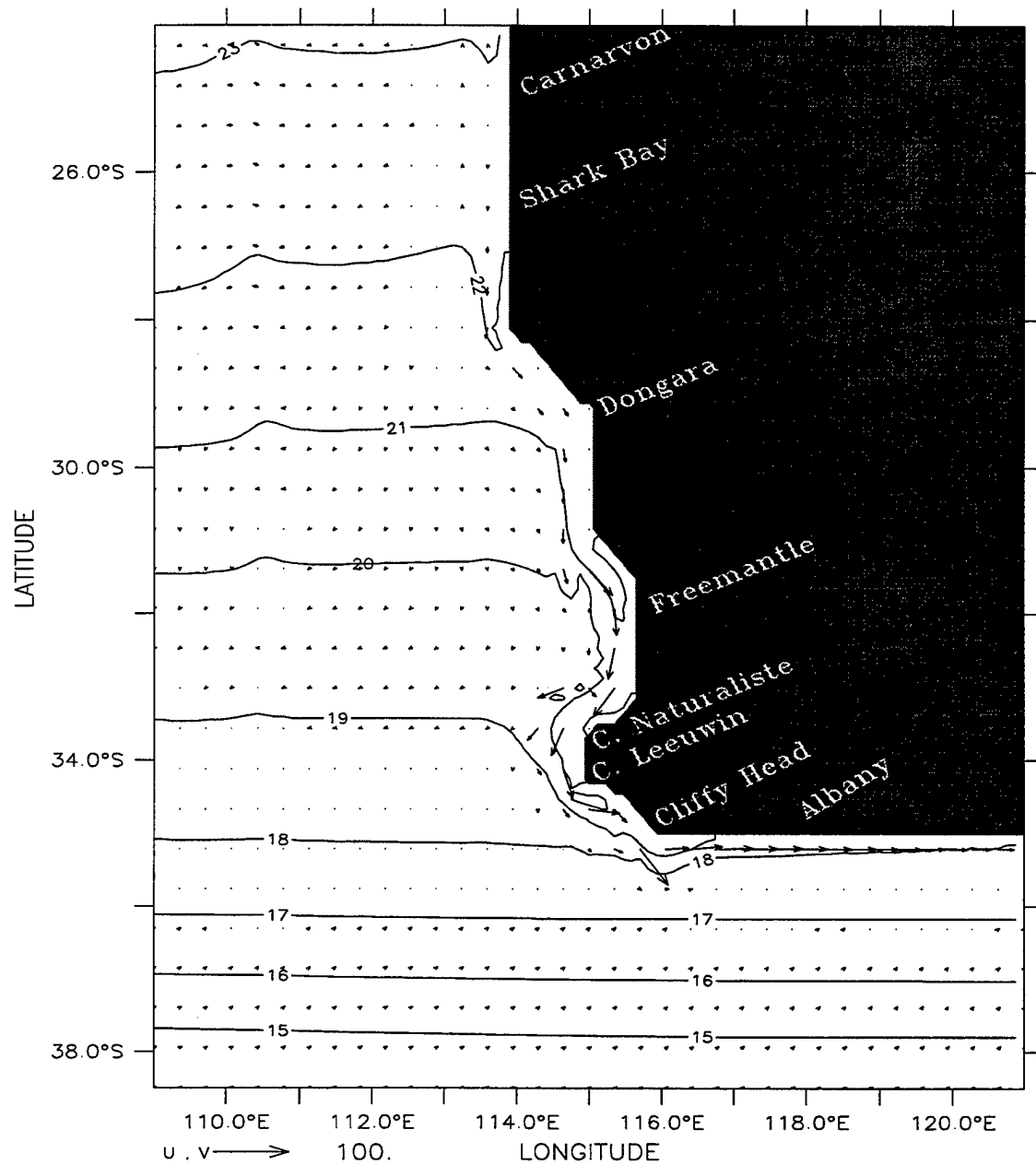
LATITUDE : 26.1S  
T (DAY) : 315



Meridional Velocity (cm/s)

(c)

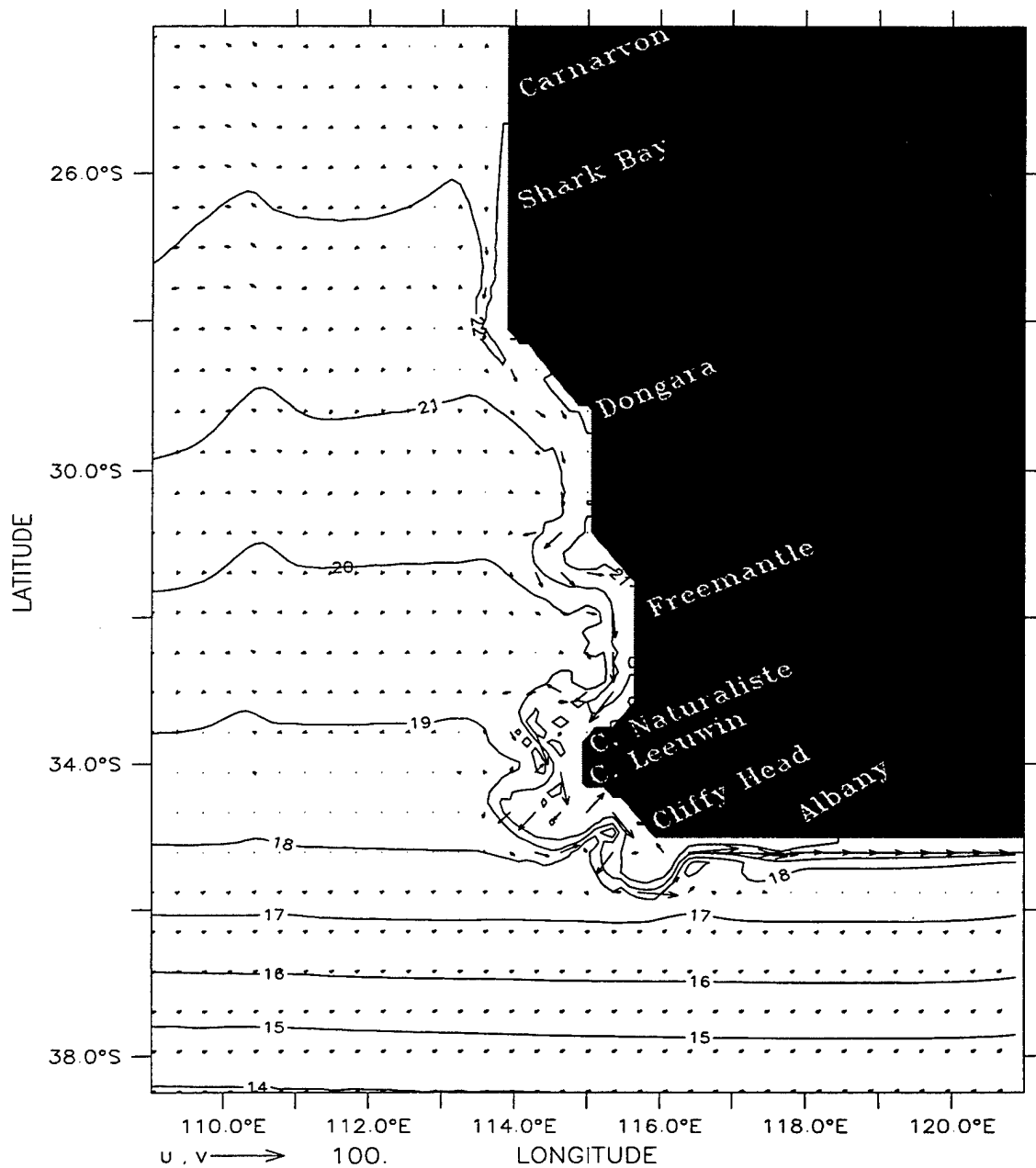
DEPTH (m) : 10  
T (DAY) : 15



Temperature (deg C) and Velocity (cm/s)  
(a)

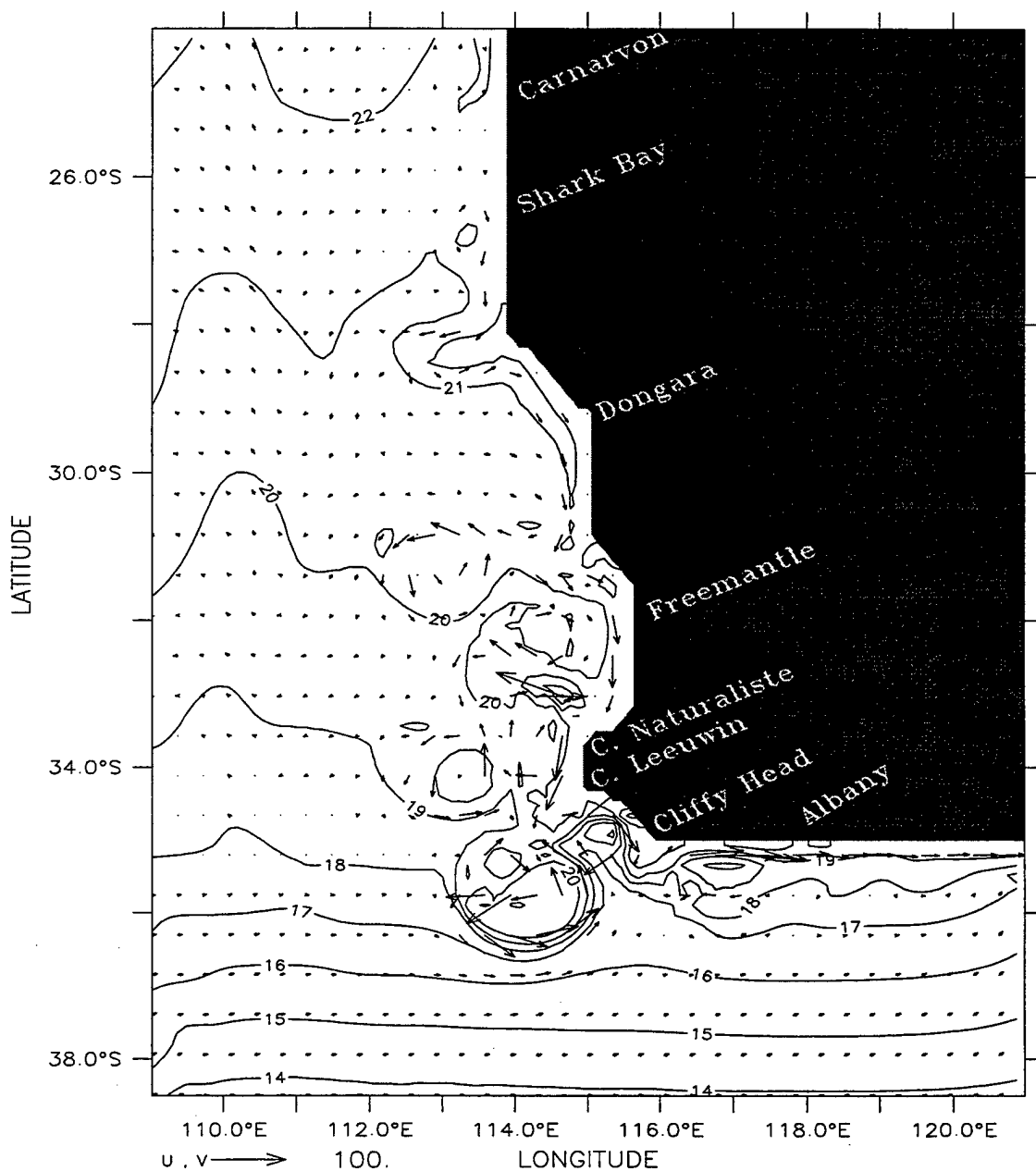
**Figure 21.** Temperature contours and velocity vectors at 10 m depth at days (a) 15, (b) 30, (c) 63, (d) 123, and (e) 363 of Experiment 7. The contour interval is 1°C for (a) – (d) and 2°C for (e). Maximum velocity is 100 cm/s.

DEPTH (m) : 10  
T (DAY) : 30



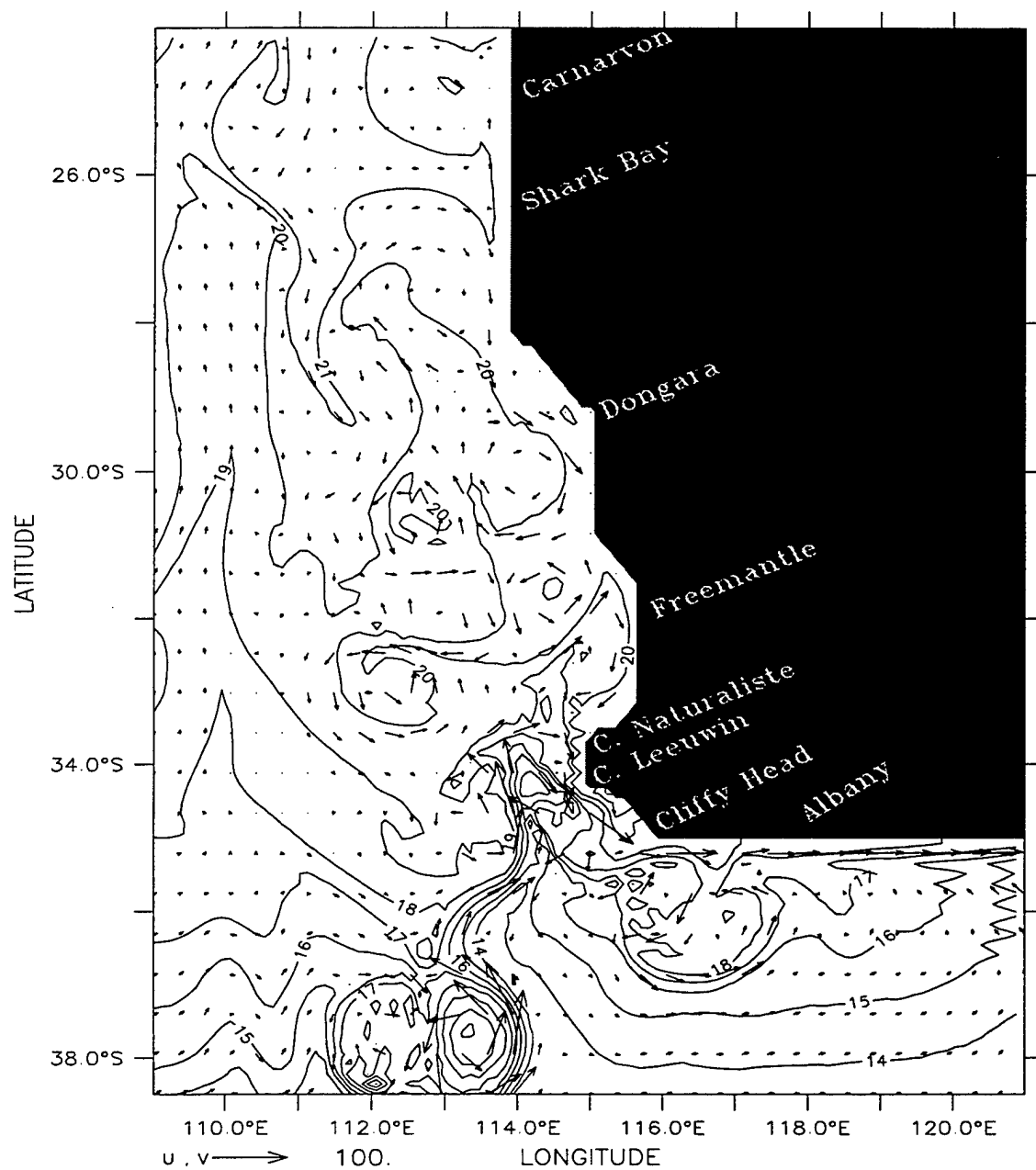
Temperature (deg C) and Velocity (cm/s)  
(b)

DEPTH (m) : 10  
T (DAY) : 63



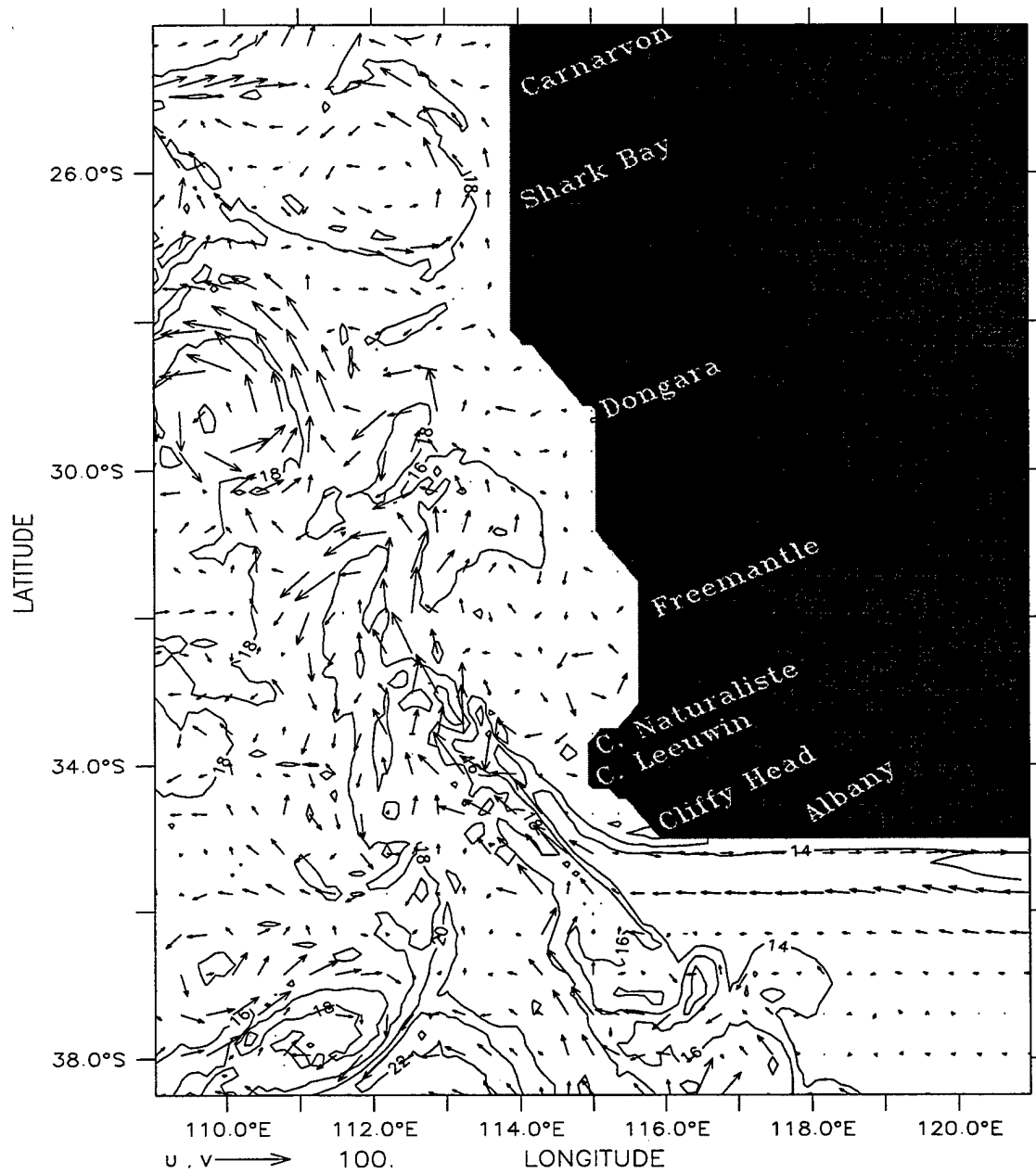
Temperature (deg C) and Velocity (cm/s)  
(c)

DEPTH (m) : 10  
T (DAY) : 123



Temperature (deg C) and Velocity (cm/s)  
(d)

DEPTH (m) : 10  
T (DAY) : 363



Temperature (deg C) and Velocity (cm/s)  
(e)

LATITUDE : 31.9S  
T (DAY) : 30

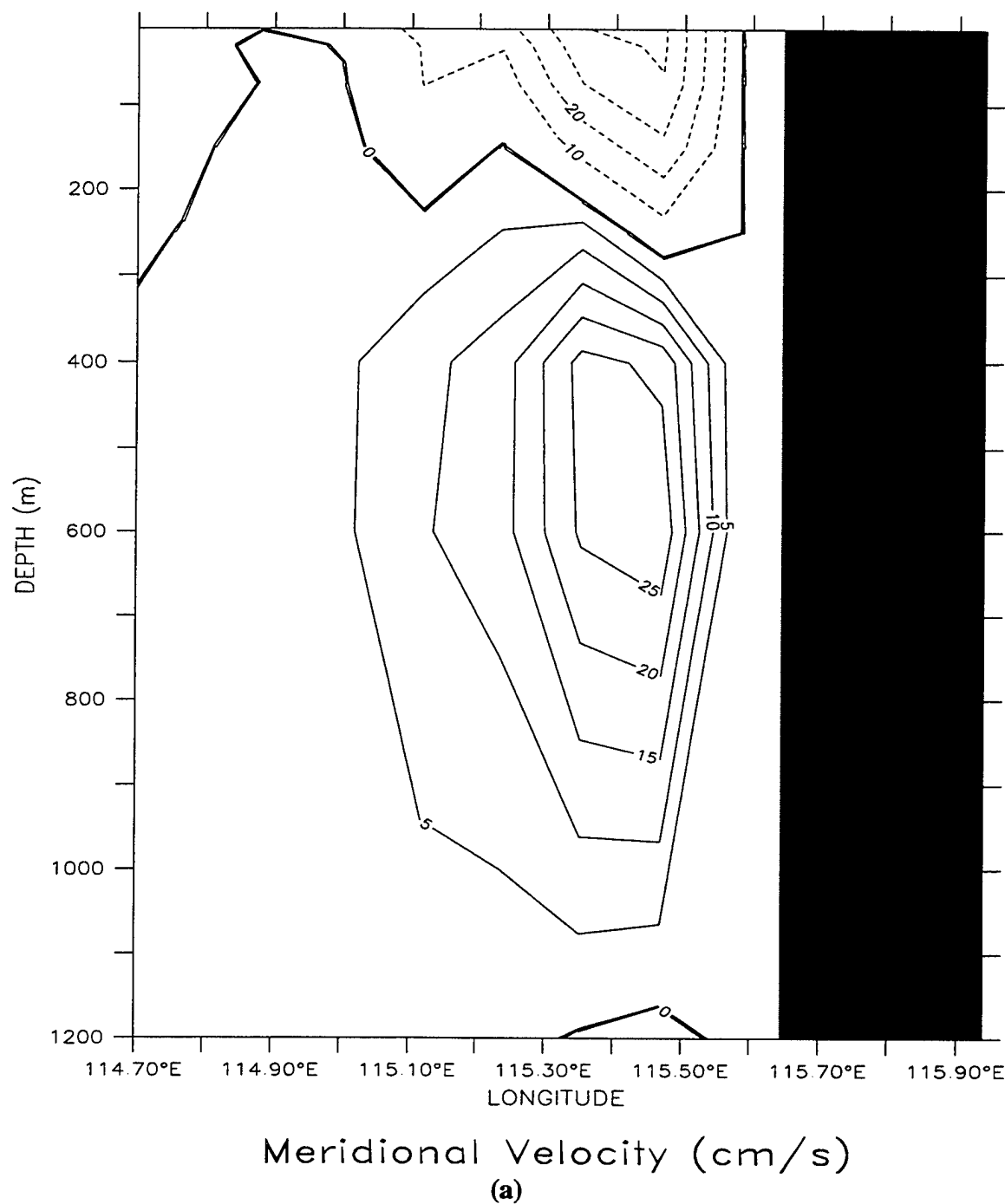
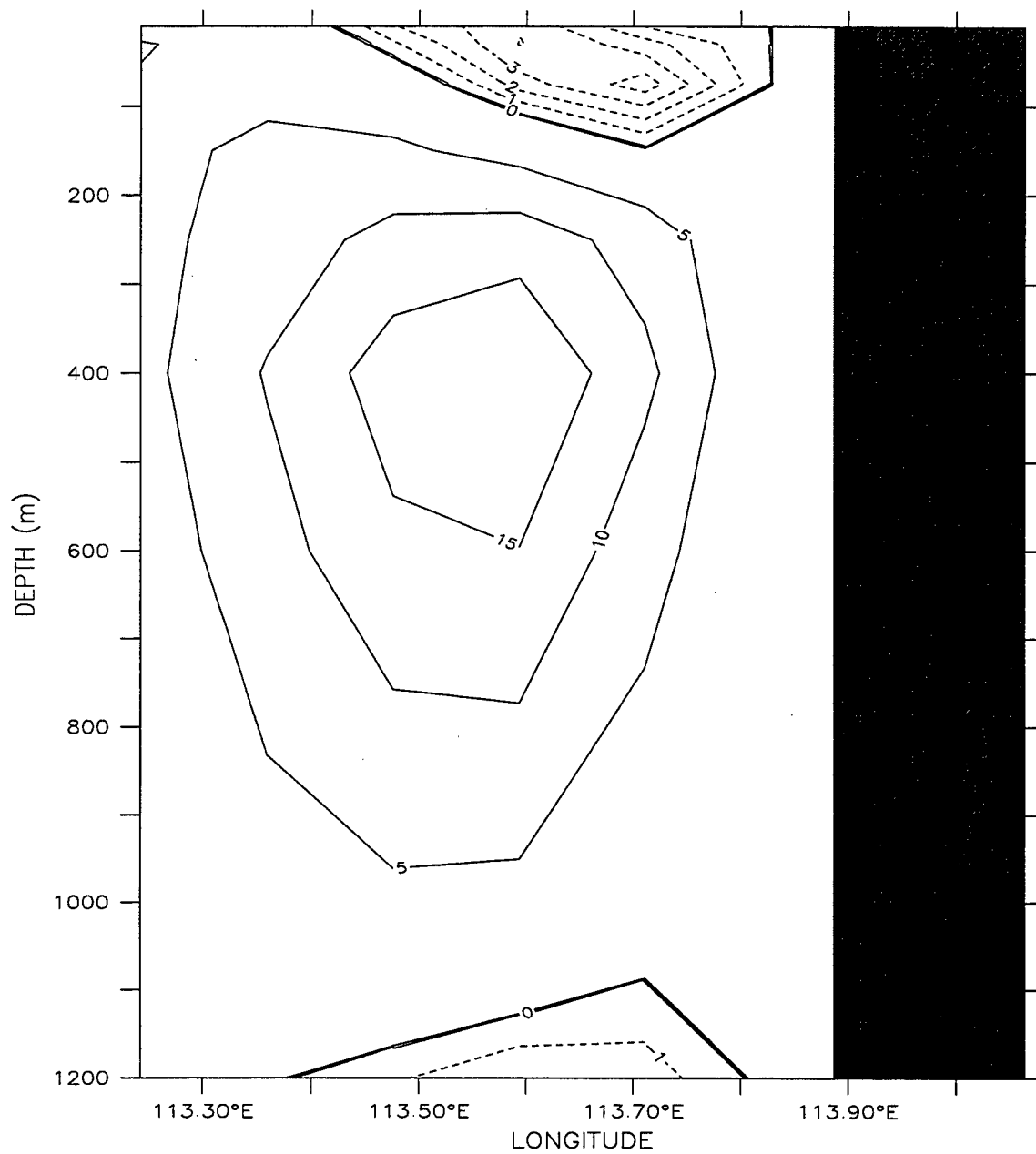


**Figure 22.** Cross-shore section of meridional velocity ( $v$ ) at (a)  $\sim 32^\circ\text{S}$  and (b)  $\sim 26^\circ\text{S}$  for Experiment 7 on day 30. Contour interval is (a) 10 cm/s and (b) 1 cm/s for poleward flow (dashed lines) and 5 cm/s for equatorward flow (solid lines).

LATITUDE : 26.1S  
T (DAY) : 30



Meridional Velocity (cm/s)  
(b)



LONGITUDE : 117E(117)  
T (DAY) : 30

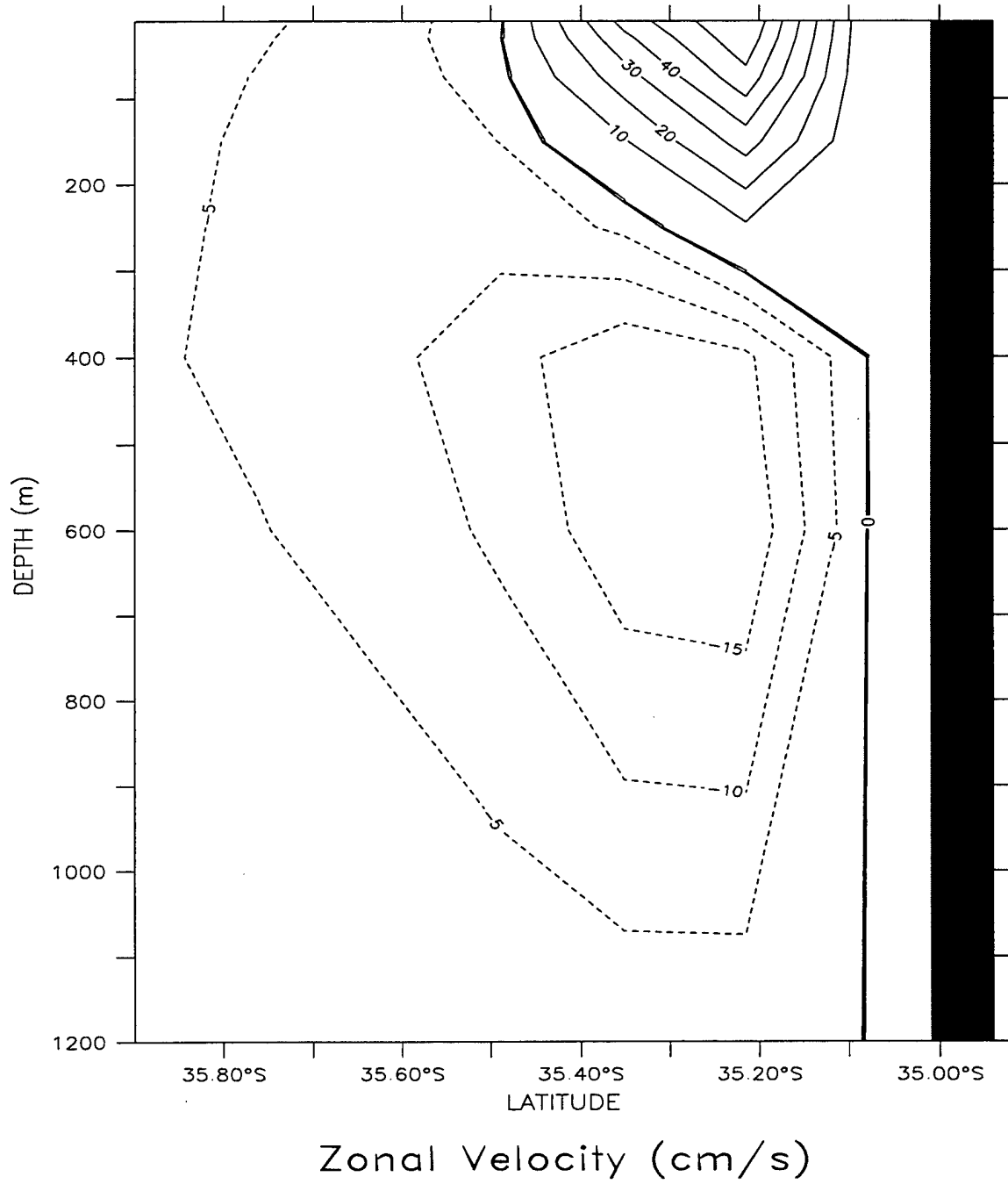


**Figure 23.** Cross-shore section of zonal velocity ( $u$ ) at 117°E for Experiment 7 on day 30. Contour interval is 5 cm/s for westward flow (dashed lines) and 10 cm/s for eastward flow (solid lines).

LATITUDE : 26.1S  
T (DAY) : 345

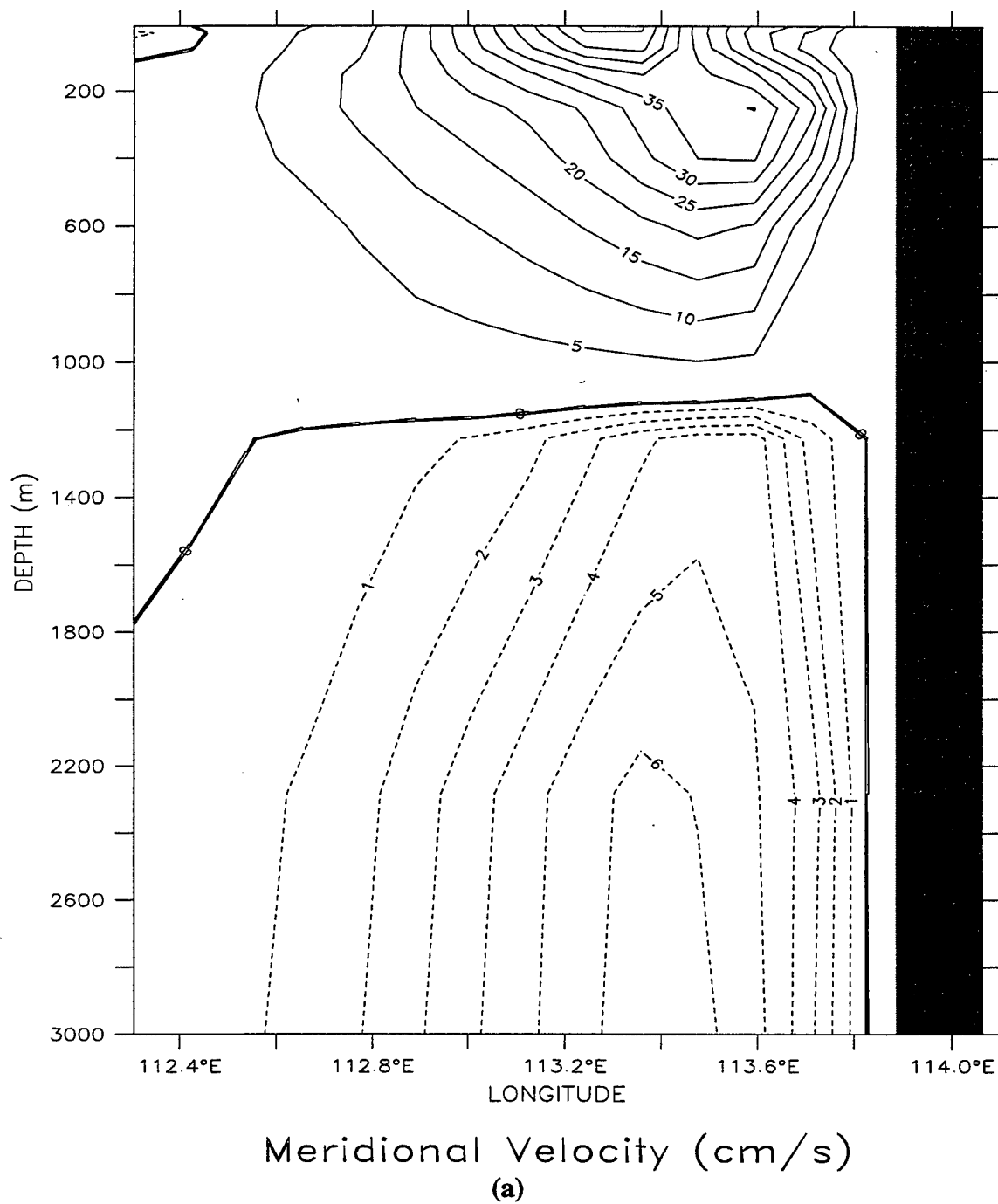
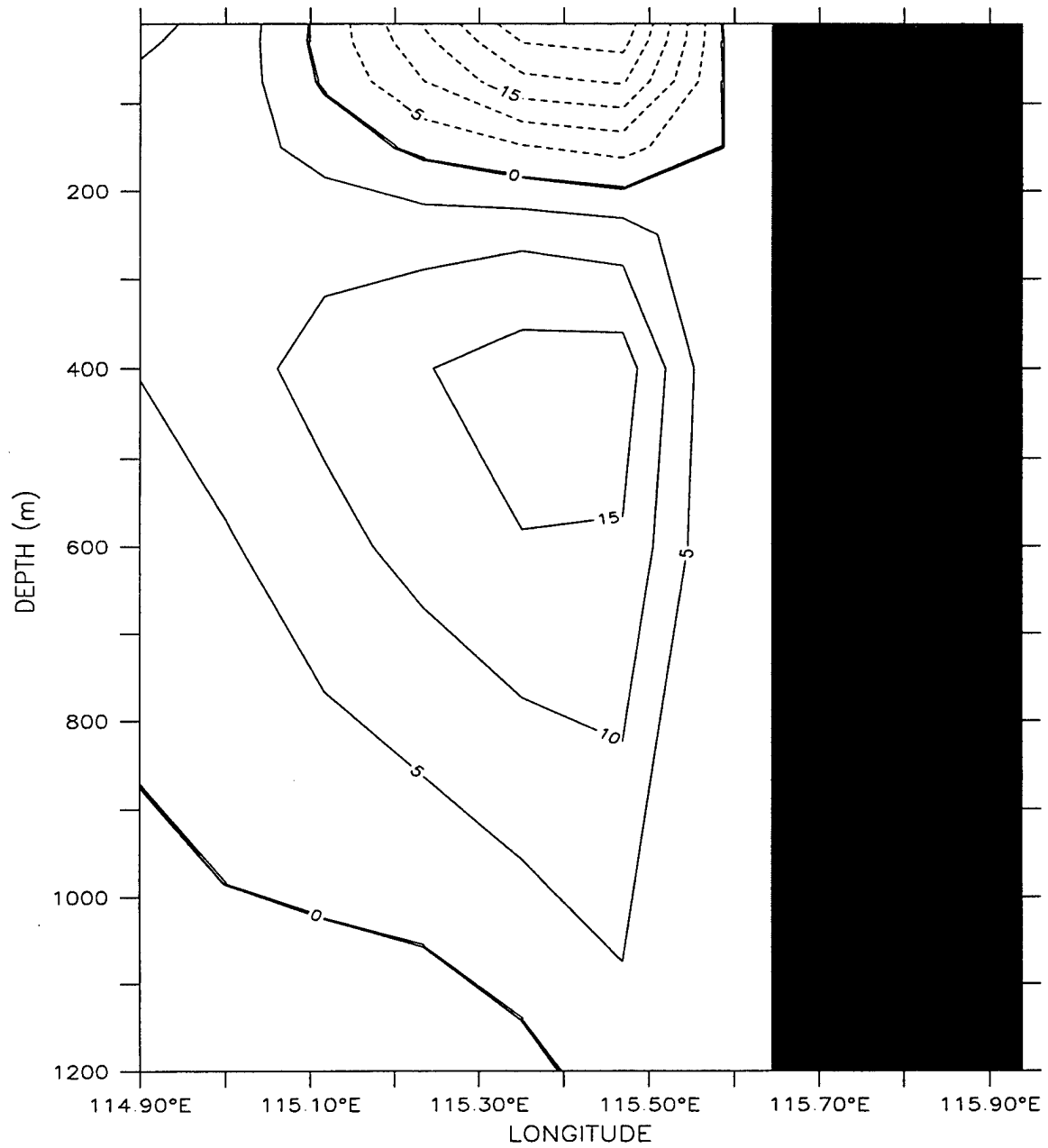


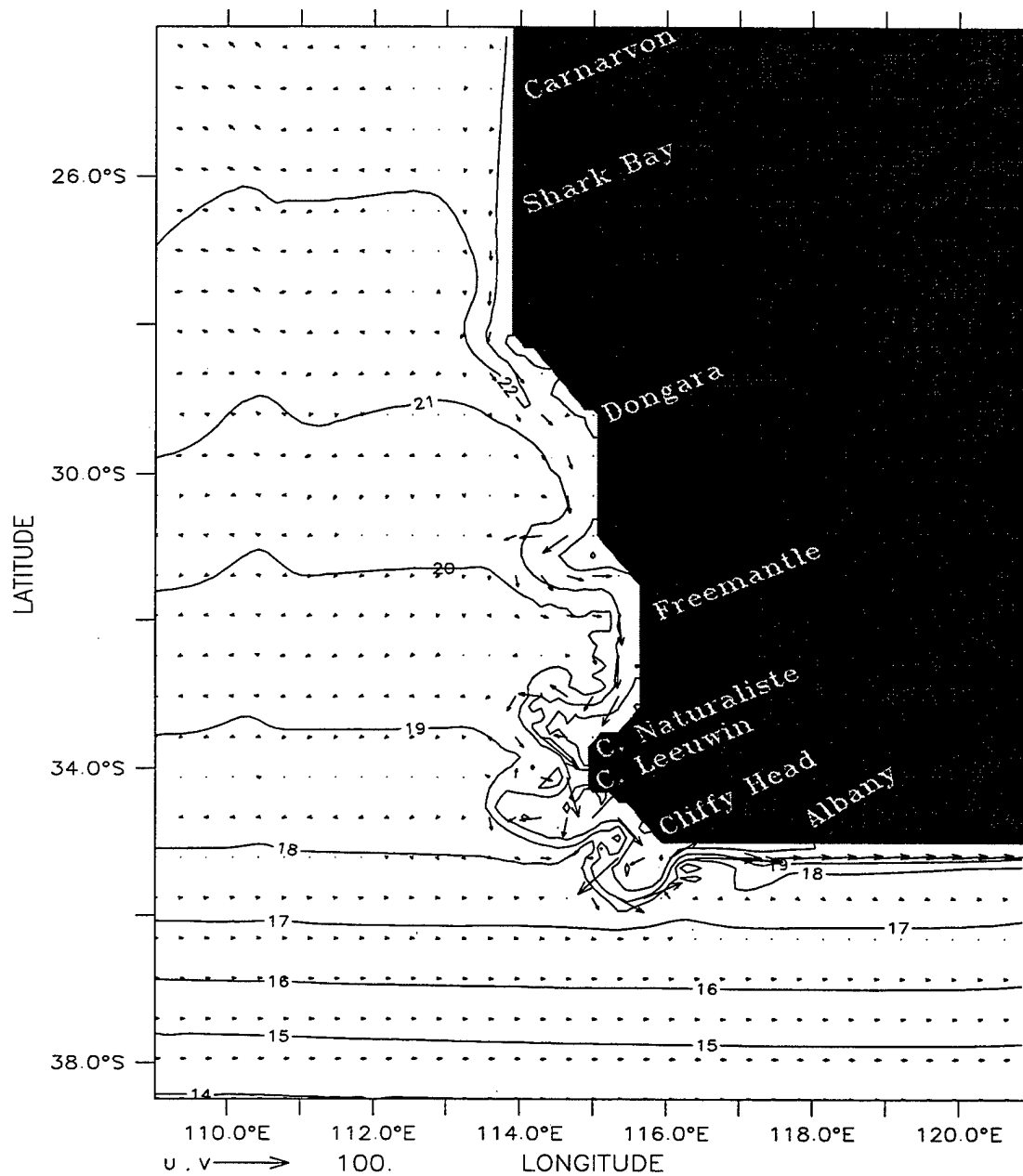
**Figure 24.** Cross-shore section of meridional velocity ( $v$ ) at (a)  $\sim 26^\circ\text{S}$  for Experiment 7 on day 345 and (b)  $\sim 32^\circ\text{S}$  for Experiment 8 on day 165. Contour interval is (a) 1 cm/s and (b) 5 cm/s for poleward flow (dashed lines) and 5 cm/s for equatorward flow (solid lines).

LATITUDE : 31.9S  
T (DAY) : 165



Meridional Velocity (cm/s)  
(b)

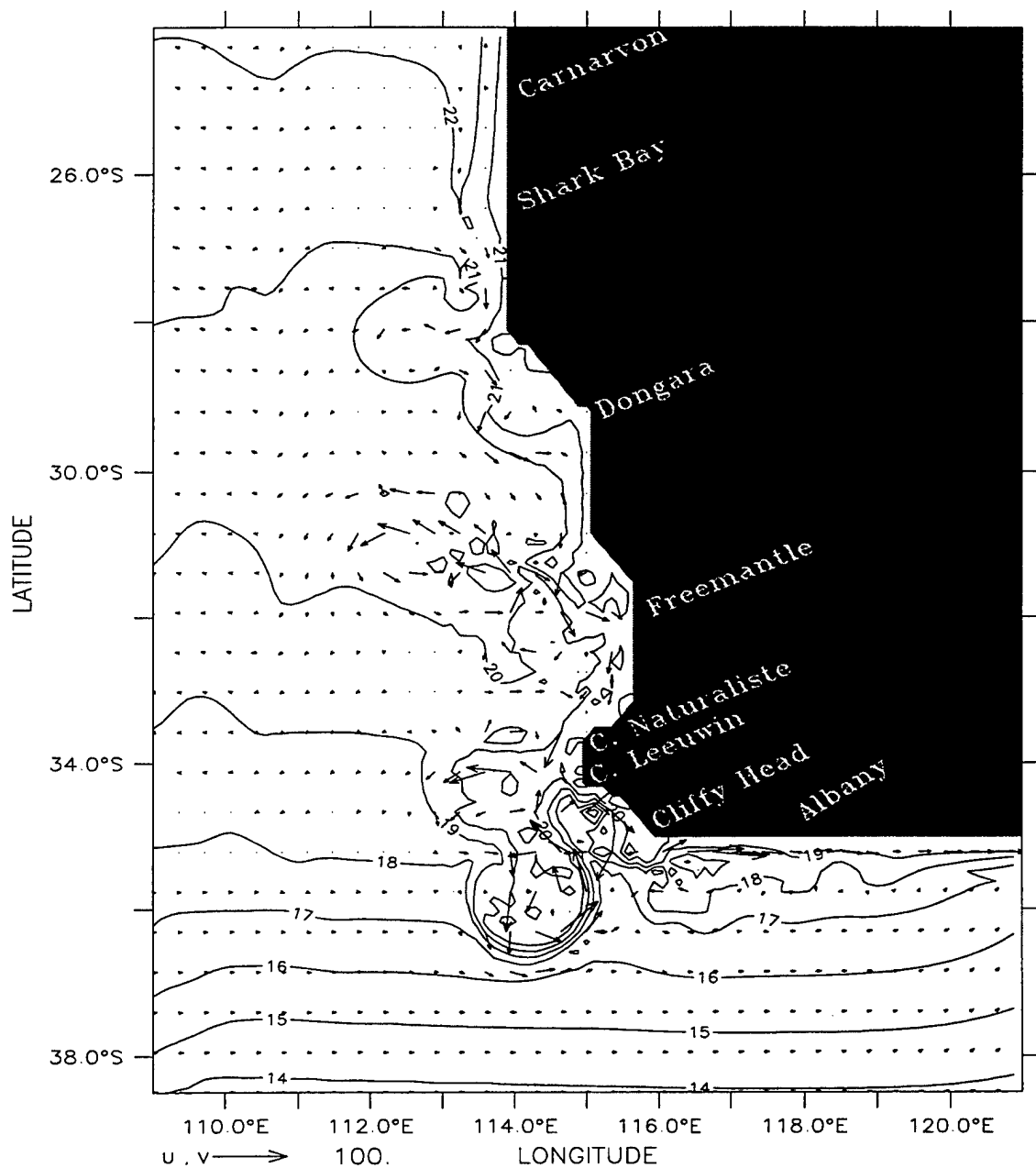
DEPTH (m) : 10  
T (DAY) : 30



Temperature (deg C) and Velocity (cm/s)  
(a)

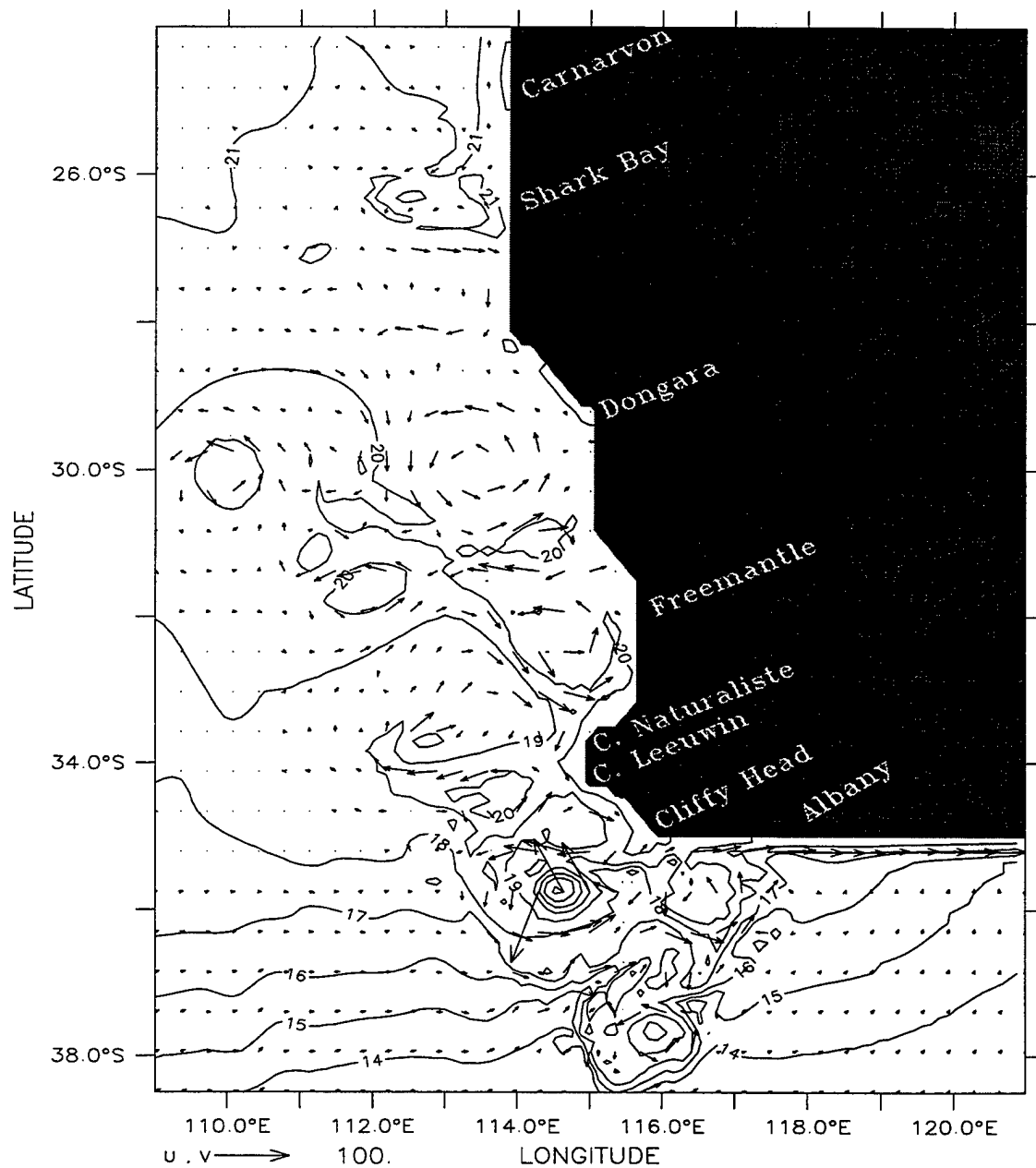
**Figure 25.** Temperature contours and velocity vectors at 10 m depth at days (a) 30, (b) 63, (c) 123, (d) 165, and (e) 363 of Experiment 8. The contour interval is  $1^{\circ}\text{C}$  for (a) – (d) and  $2^{\circ}\text{C}$  for (e). Maximum velocity is 100 cm/s. Note: In (e), temperature contours intersecting coast north of  $28^{\circ}\text{S}$  are  $16^{\circ}\text{C}$ .

DEPTH (m) : 10  
T (DAY) : 63



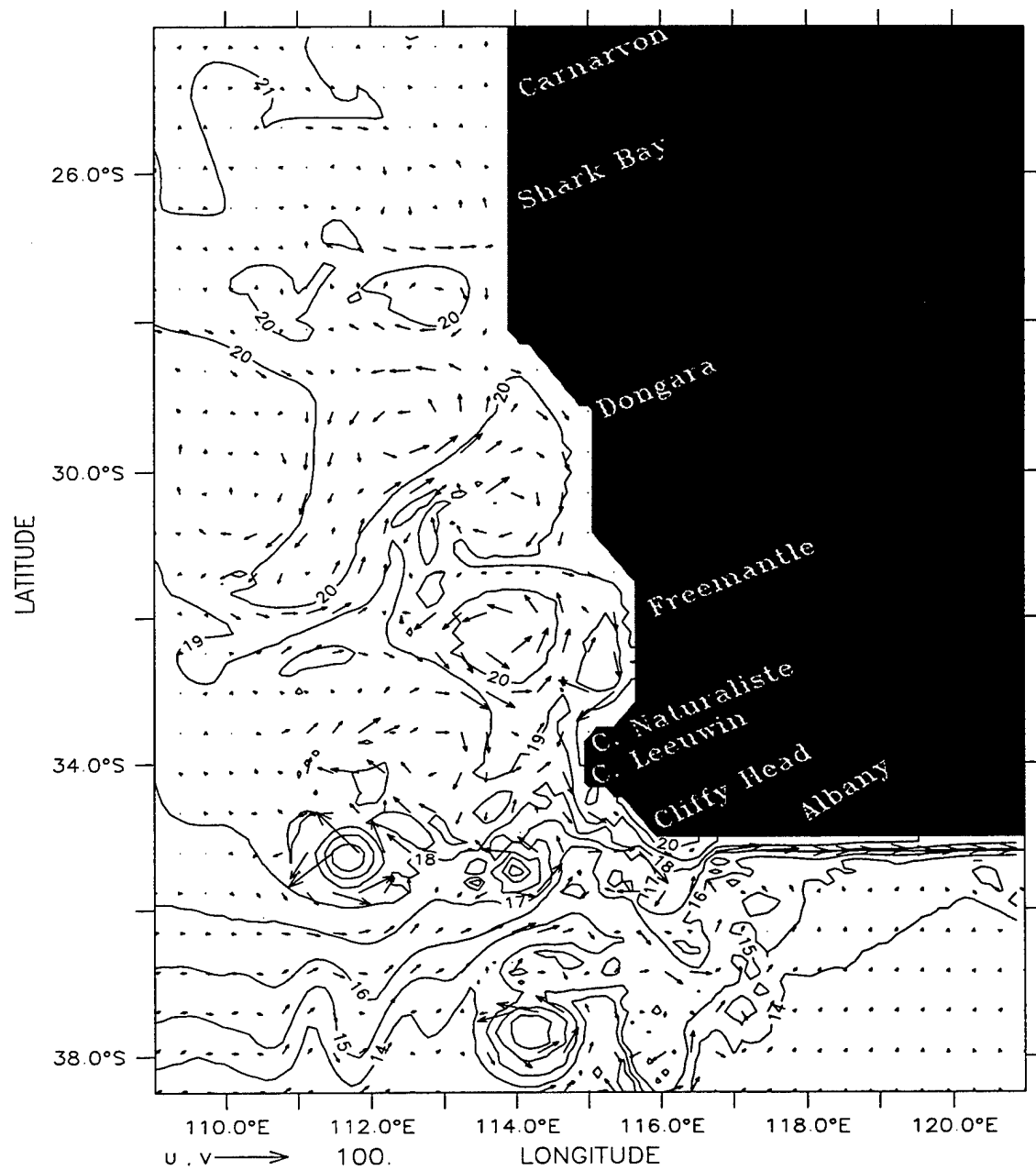
Temperature (deg C) and Velocity (cm/s)  
(b)

DEPTH (m) : 10  
T (DAY) : 123



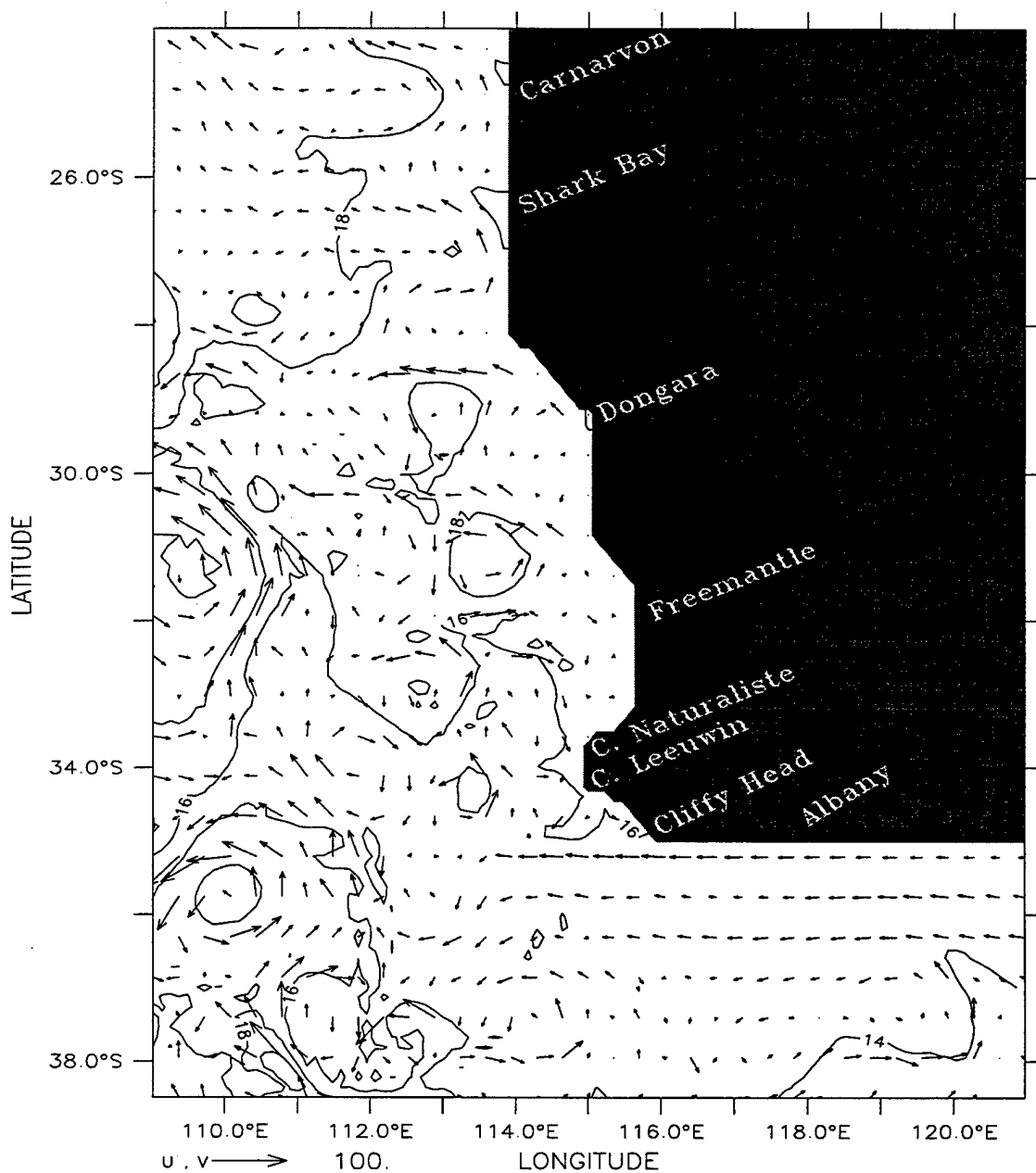
Temperature (deg C) and Velocity (cm/s)  
(c)

DEPTH (m) : 10  
T (DAY) : 165



Temperature (deg C) and Velocity (cm/s)  
(d)

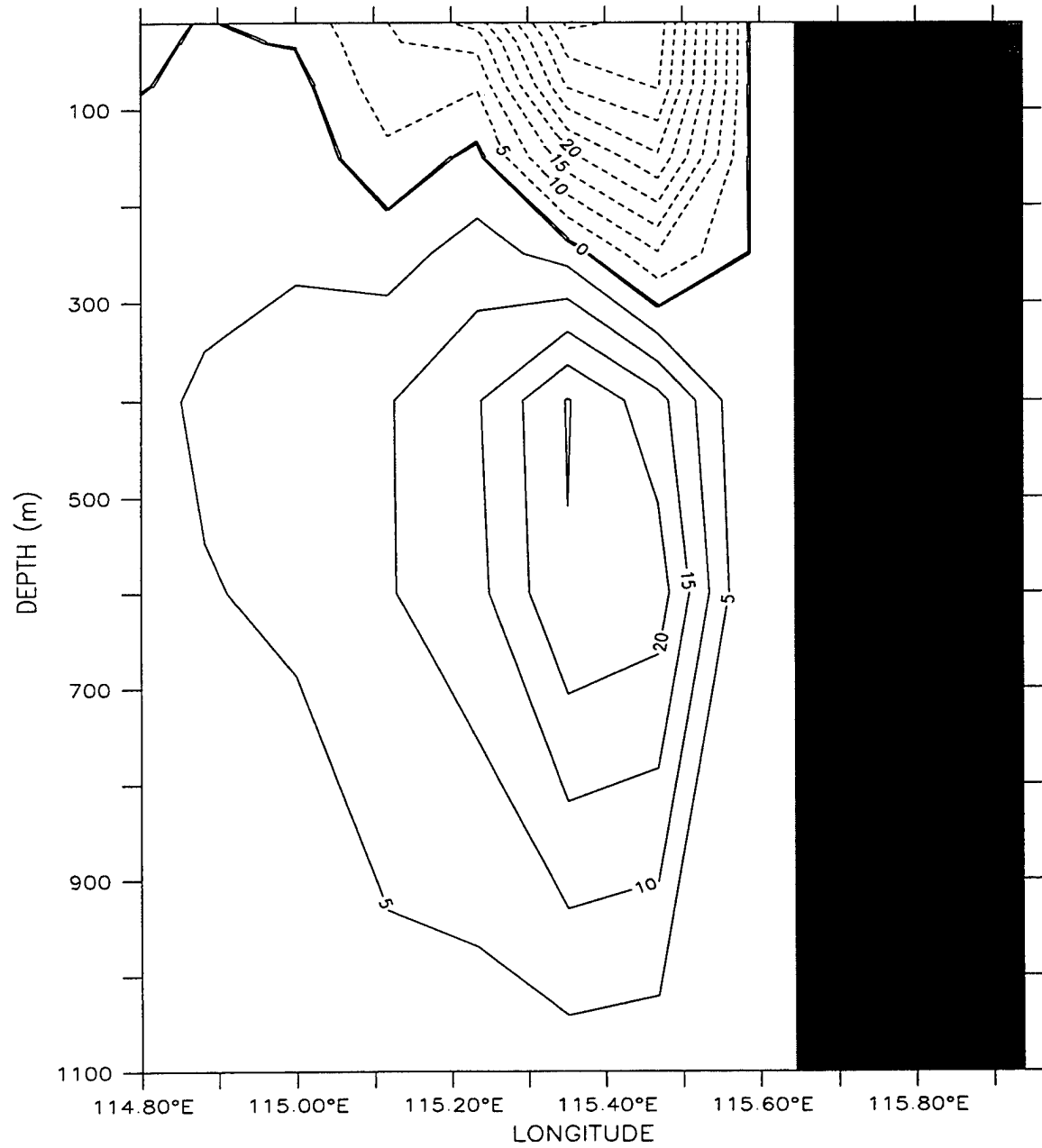
DEPTH (m) : 10  
T (DAY) : 363



Temperature (deg C) and Velocity (cm/s)  
(e)



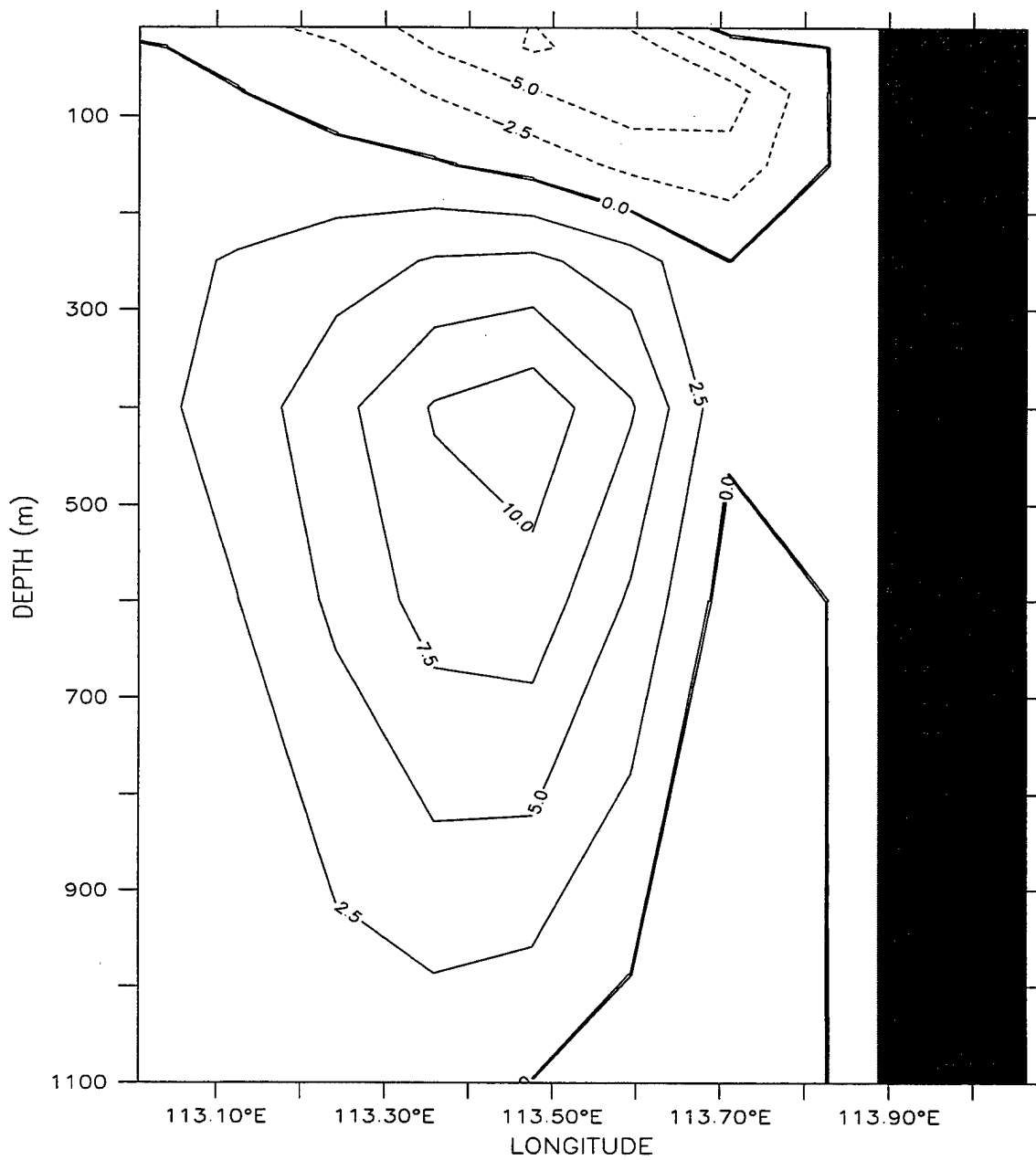
LATITUDE : 31.9S  
T (DAY) : 30



Meridional Velocity (cm/s)  
(a)

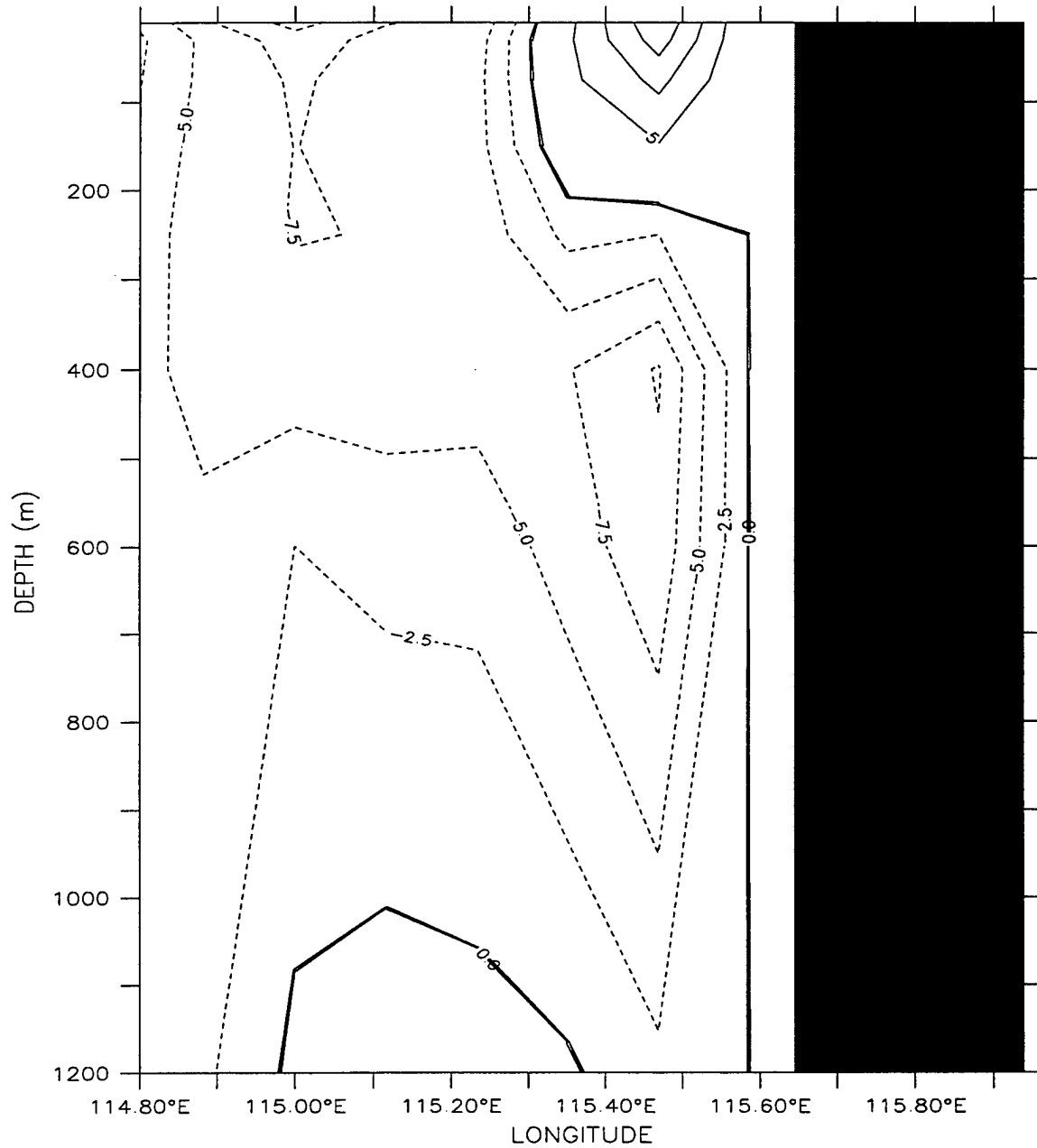
**Figure 26.** Cross-shore section of meridional velocity ( $v$ ) at (a)  $\sim 32^\circ\text{S}$  and (b)  $\sim 26^\circ\text{S}$  for Experiment 8 on day 30. Contour interval is (a) 5 cm/s and (b) 2.5 cm/s for poleward flow (dashed lines) and (a) 5 cm/s and (b) 2.5 cm/s for equatorward flow (solid lines).

LATITUDE : 26.1S  
T (DAY) : 30



Meridional Velocity (cm/s)  
(b)

LATITUDE : 31.9S  
T (DAY) : 363

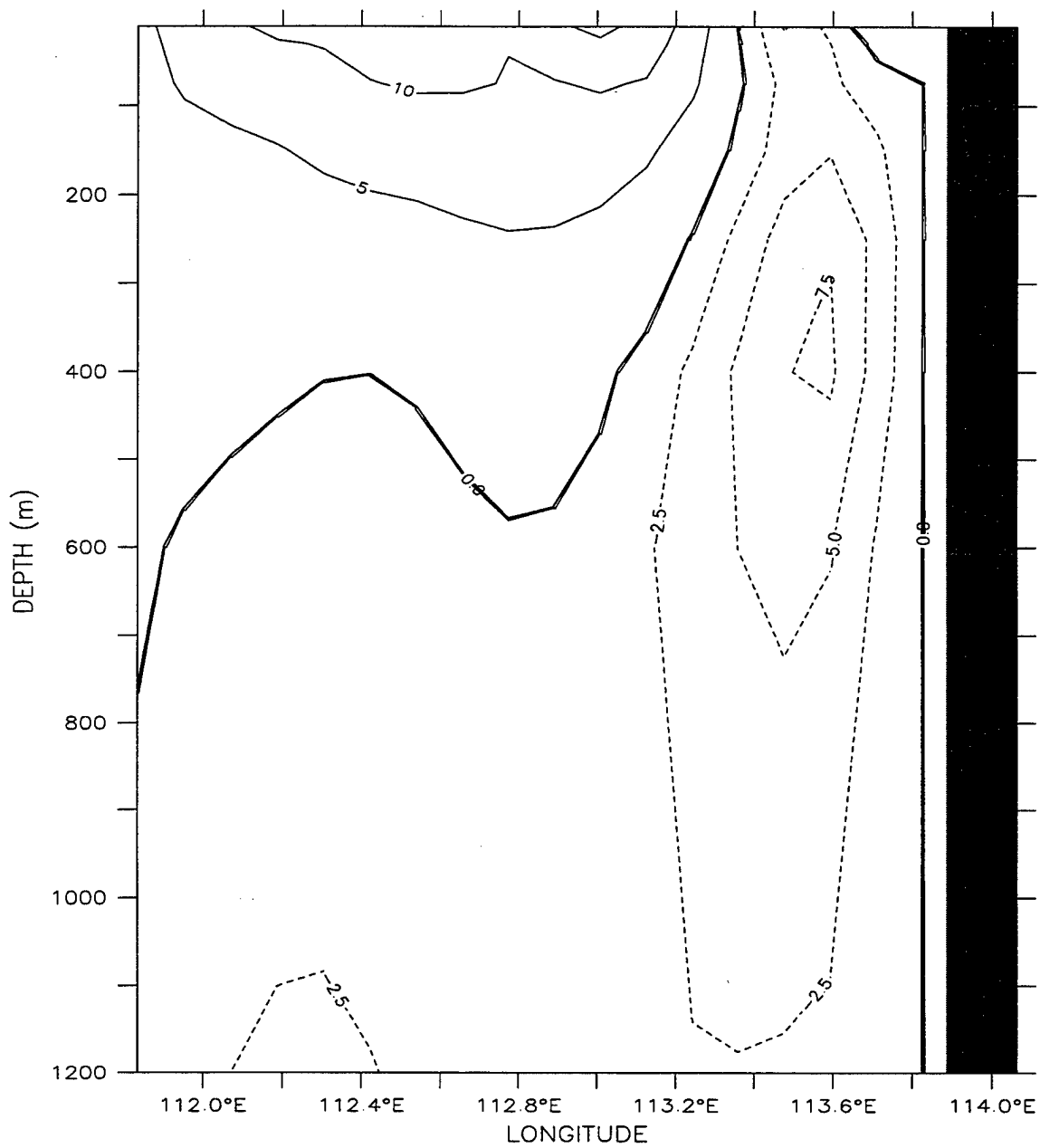


Meridional Velocity (cm/s)

(a)

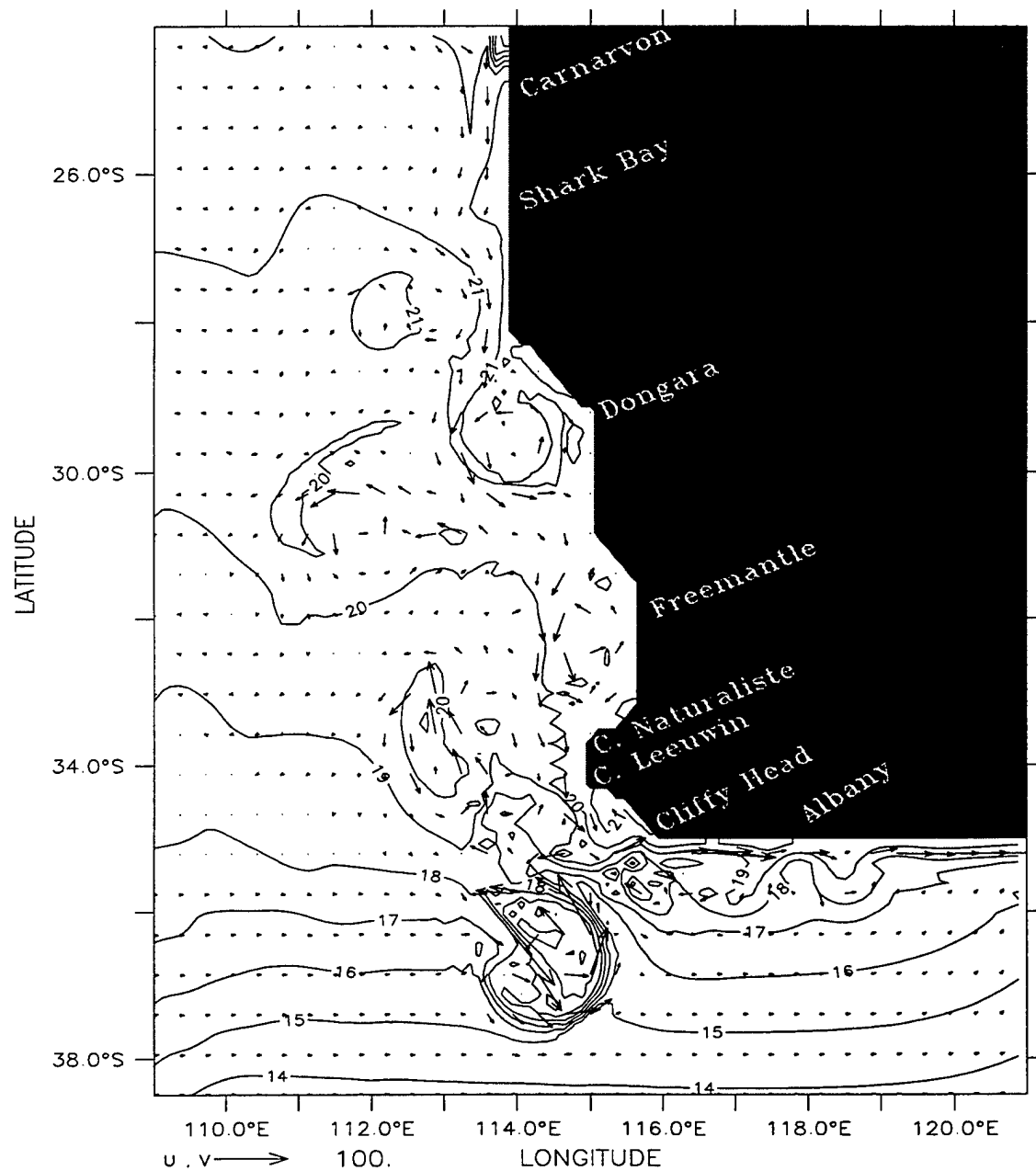
**Figure 27.** Cross-shore section of meridional velocity ( $v$ ) at (a)  $\sim 32^\circ\text{S}$  and (b)  $\sim 26^\circ\text{S}$  for Experiment 8 on day 363. Contour interval is 2.5 cm/s for poleward flow (dashed lines) and 5 cm/s for equatorward flow (solid lines).

LATITUDE : 26.1S  
T (DAY) : 363



Meridional Velocity (cm/s)  
(b)

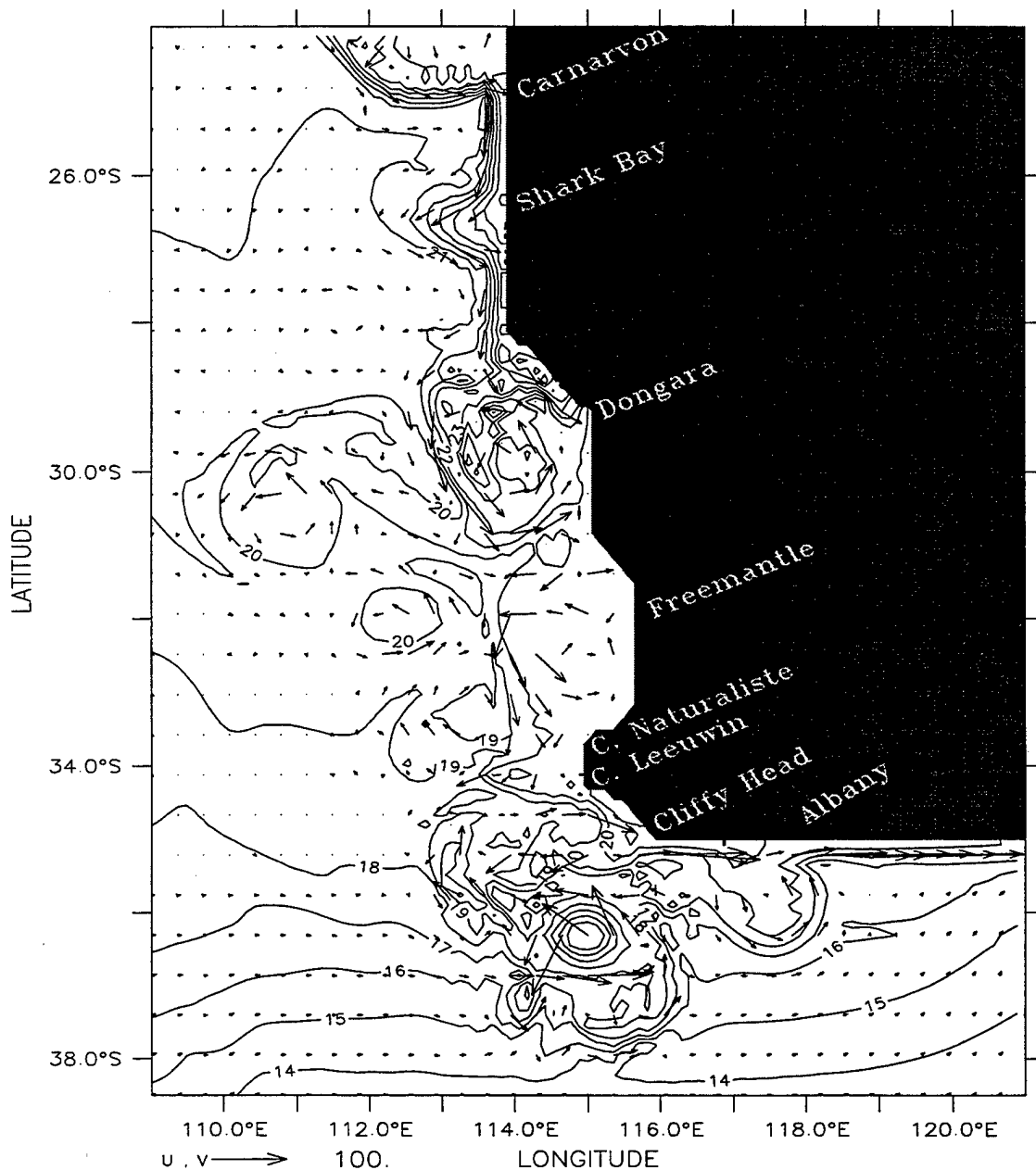
DEPTH (m) : 10  
T (DAY) : 78



Temperature (deg C) and Velocity (cm/s)  
(a)

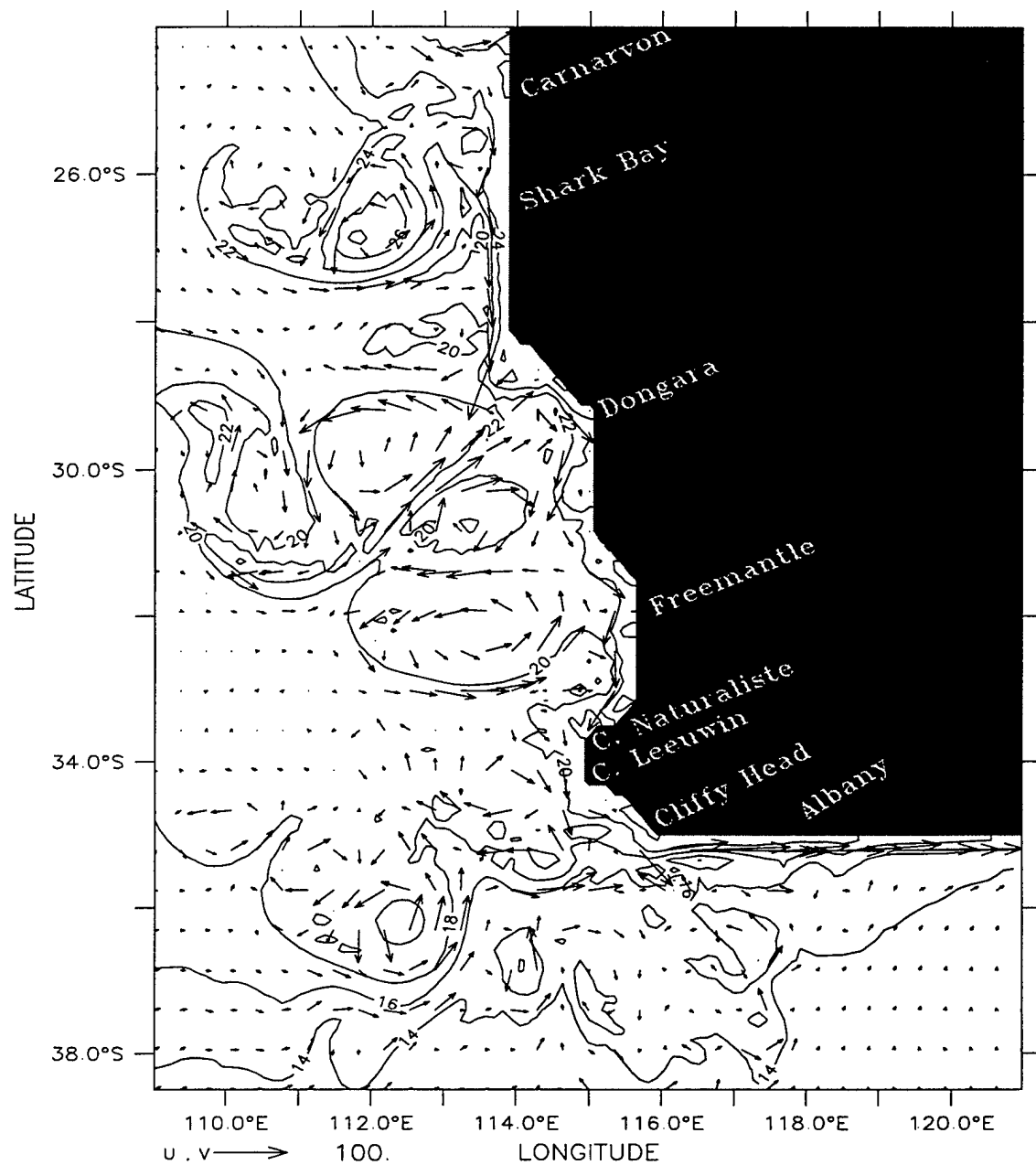
**Figure 28.** Temperature contours and velocity vectors at 10 m depth at days (a) 78, (b) 102, (c) 165, and (d) 363 of Experiment 9. The contour interval is 1°C for (a), (b), and (d) and 2°C for (c). Maximum velocity is 100 cm/s.

DEPTH (m) : 10  
T (DAY) : 102



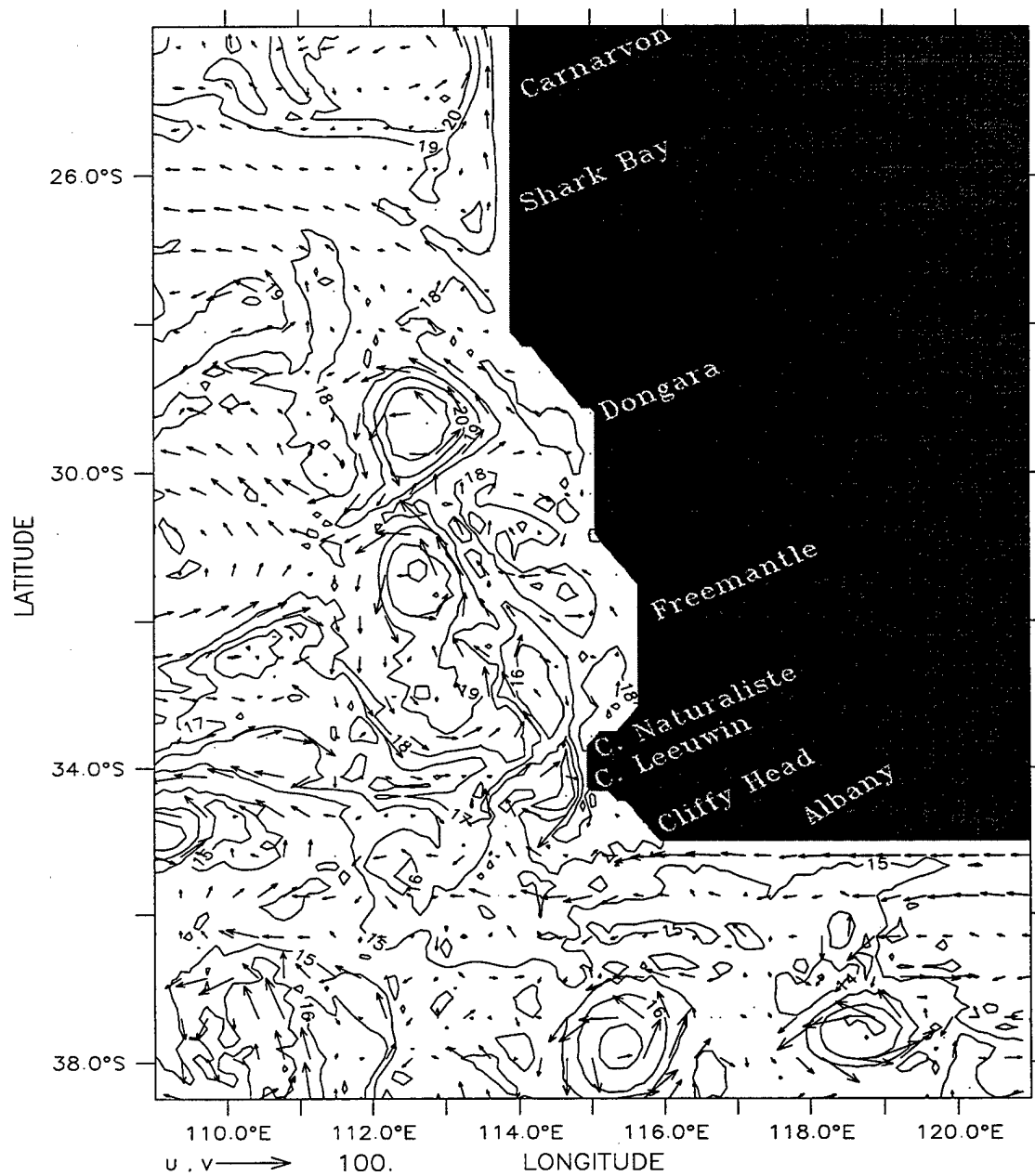
Temperature (deg C) and Velocity (cm/s)  
(b)

DEPTH (m) : 10  
T (DAY) : 165



Temperature (deg C) and Velocity (cm/s)  
(c)

DEPTH (m) : 10  
T (DAY) : 363



Temperature (deg C) and Velocity (cm/s)  
(d)



LATITUDE : 26.1S  
T (DAY) : 102

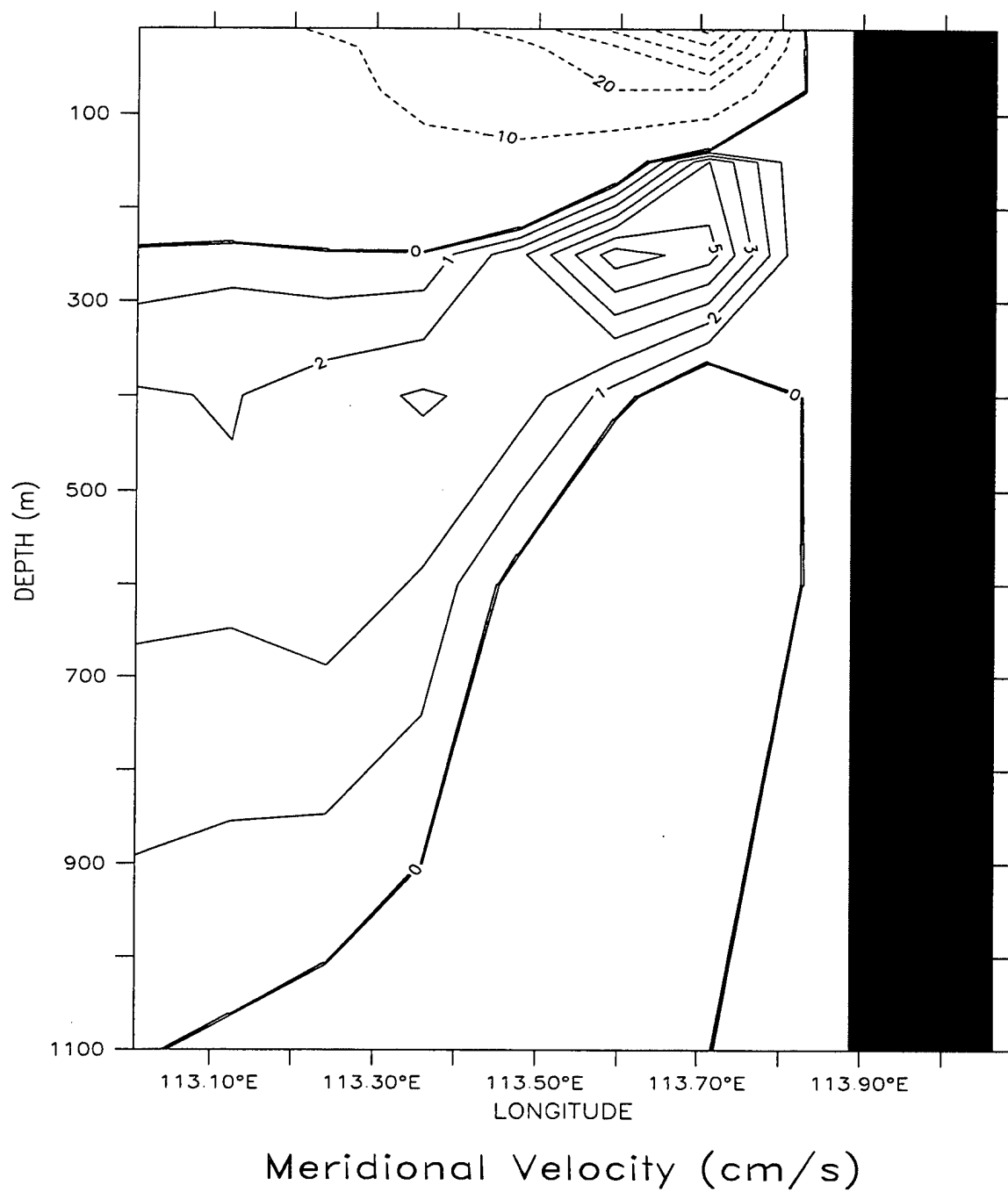


**Figure 29.** Cross-shore section of meridional velocity ( $v$ ) at  $\sim 26^\circ\text{S}$  for Experiment 9 on day 102. Contour interval is 10 cm/s for poleward flow (dashed lines) and 1 cm/s for equatorward flow (solid lines).

LATITUDE : 30S  
T (DAY) : 165

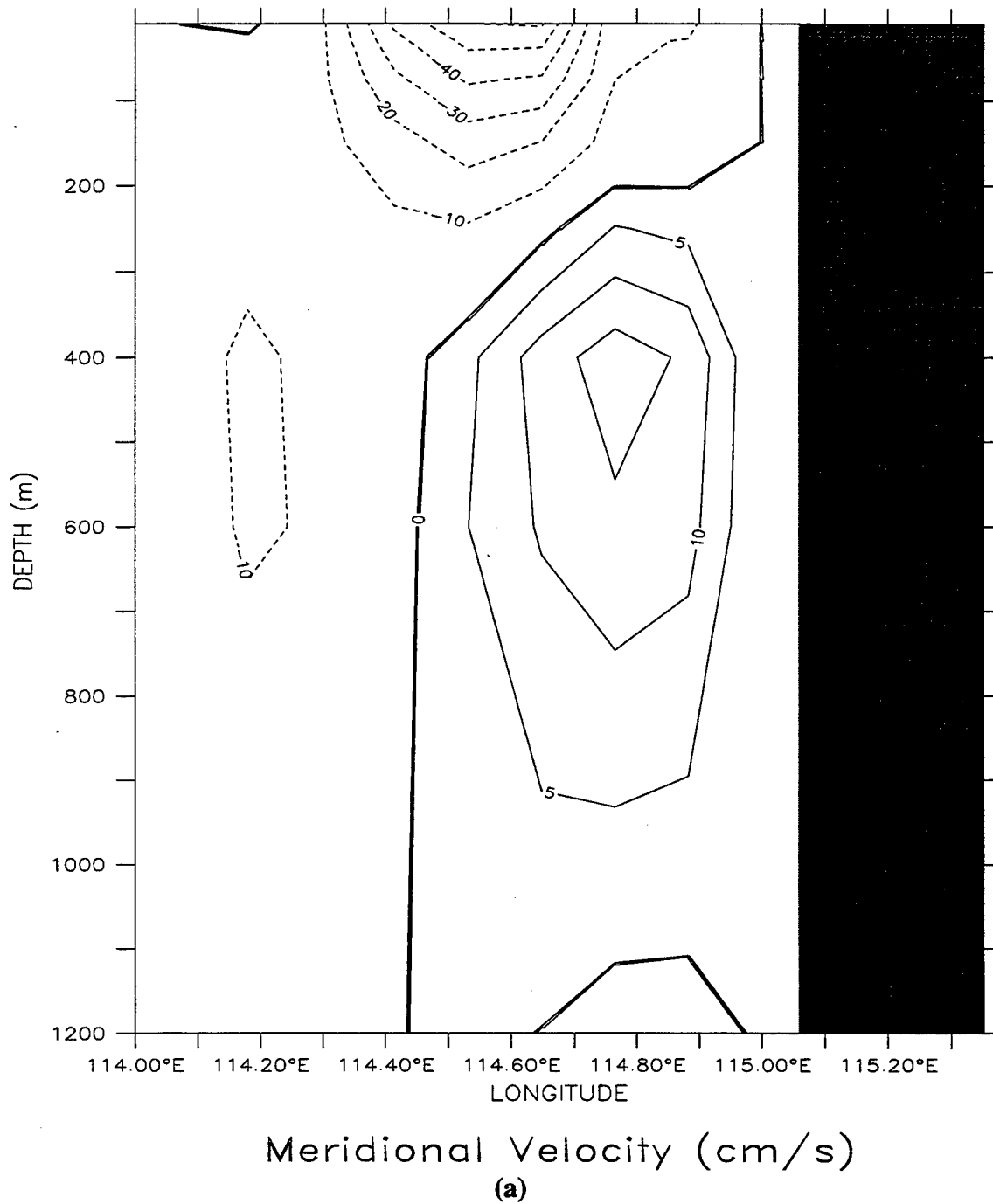
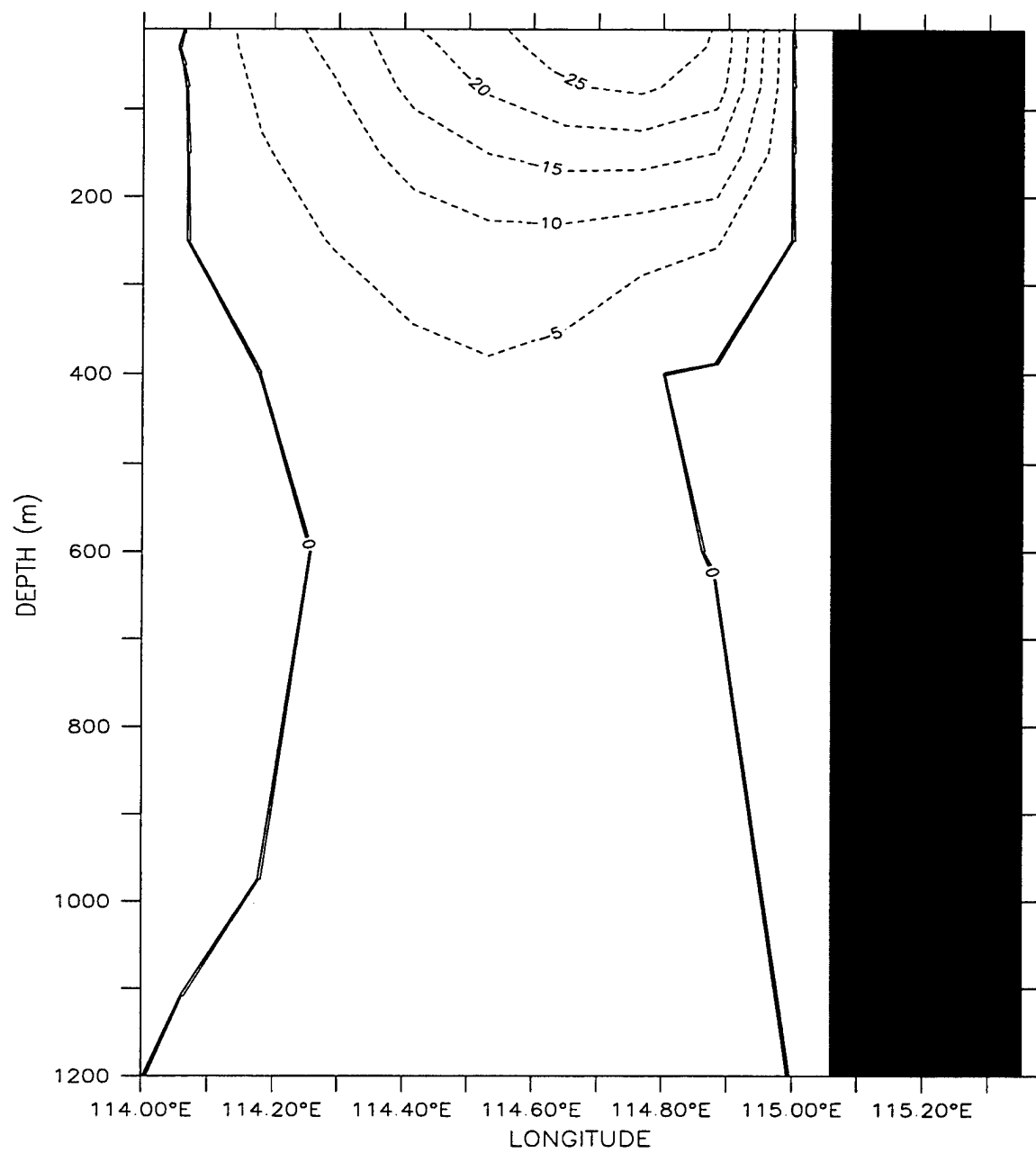


**Figure 30.** Cross-shore section of meridional velocity ( $v$ ) at 30°S for (a) Experiment 9 and (b) Experiment 8 at day 165. Contour interval is (a) 10 cm/s and (b) 5 cm/s for poleward flow (dashed lines) and 5 cm/s for equatorward flow (solid lines).

LATITUDE : 30S  
T (DAY) : 165



Meridional Velocity (cm/s)  
(b)

LONGITUDE : 117E(117)  
T (DAY) : 165

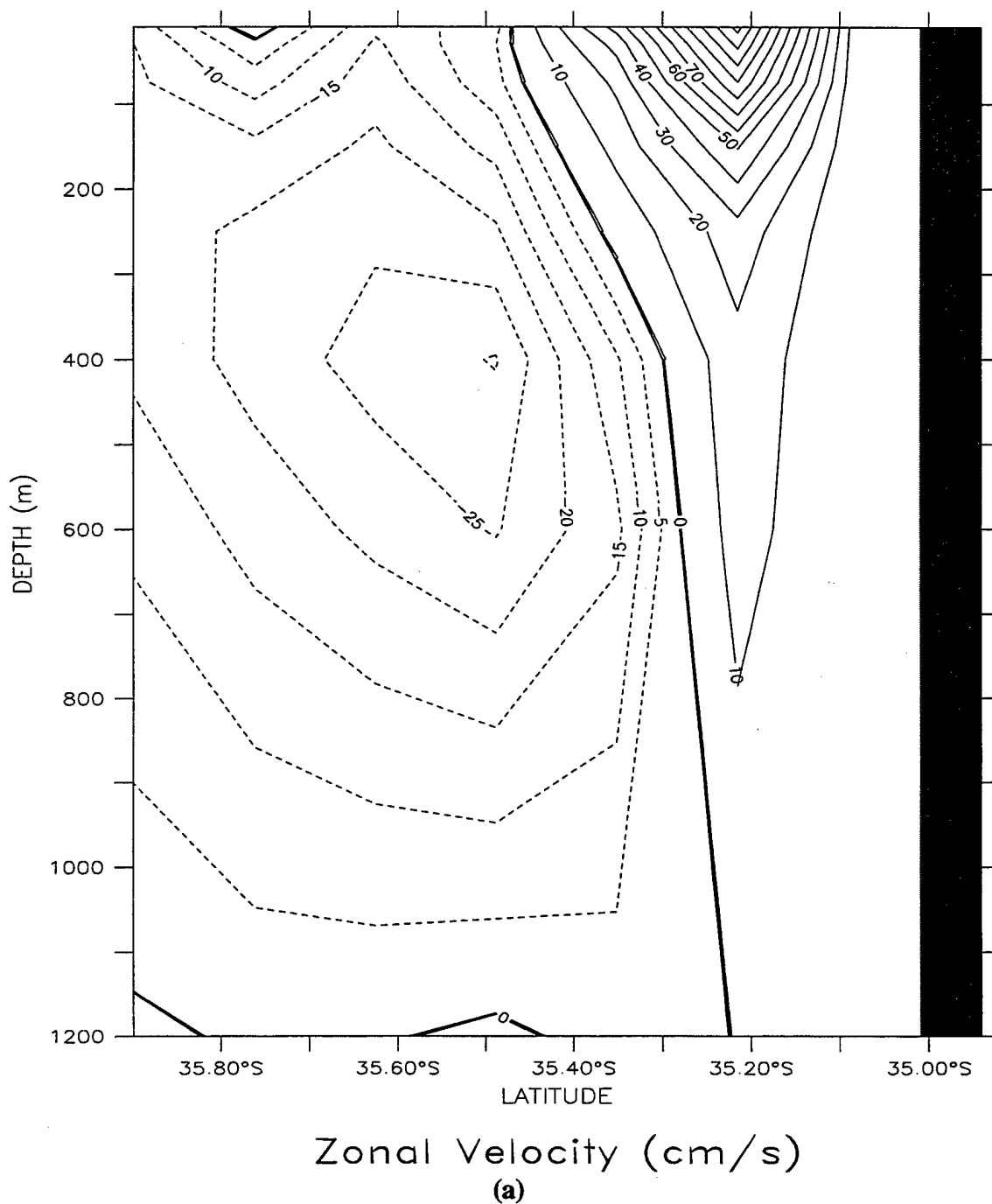
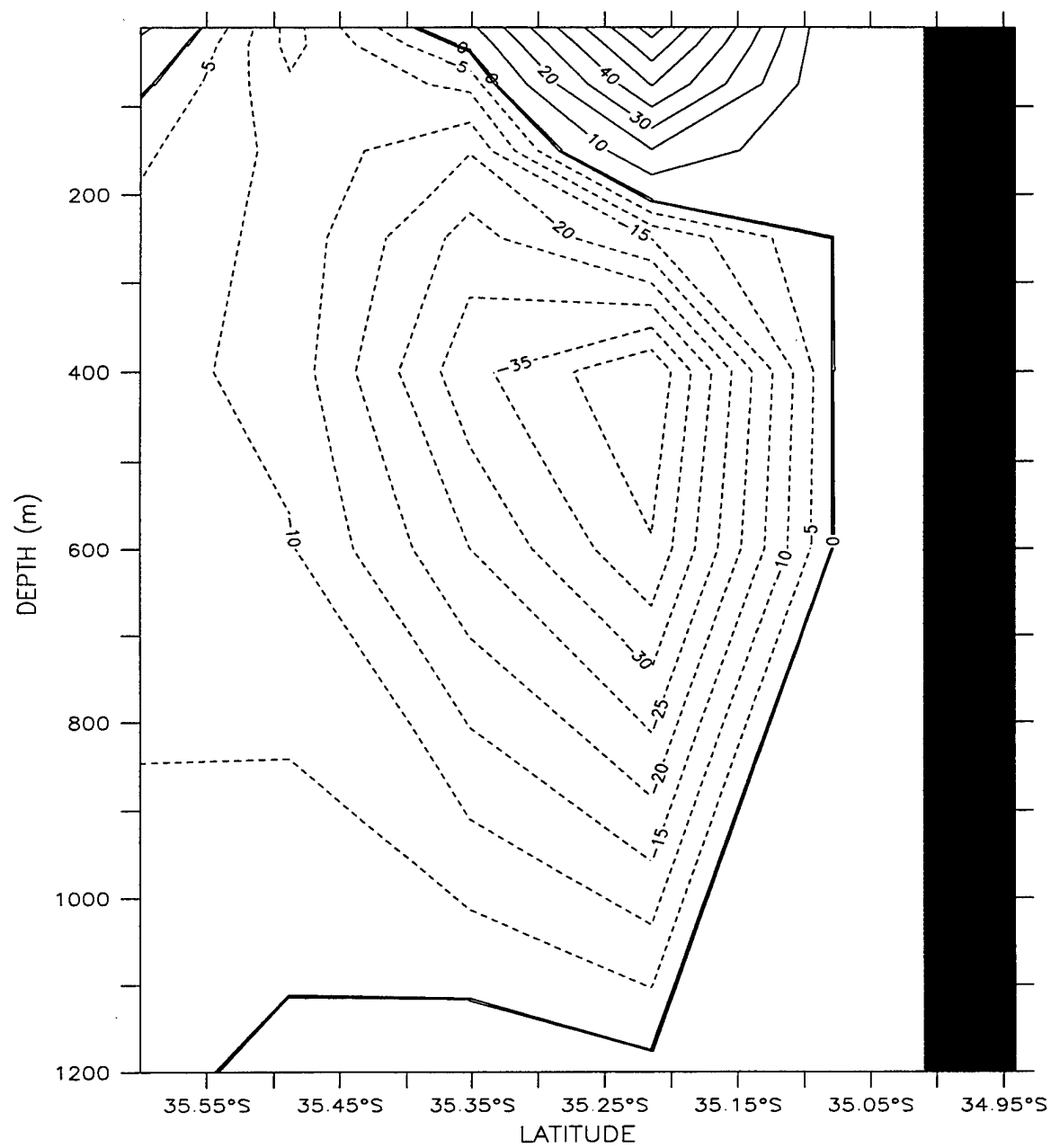


**Figure 31.** Cross-shore section of zonal velocity ( $u$ ) at 117°E for (a) Experiment 9 and (b) Experiment 8 at day 165. Contour interval is 5 cm/s for westward flow (dashed lines) and 10 cm/s for eastward flow (solid lines).

LONGITUDE : 117E(117)  
T (DAY) : 165



Zonal Velocity (cm/s)  
(b)

LATITUDE : 31.9S  
T (DAY) : 363

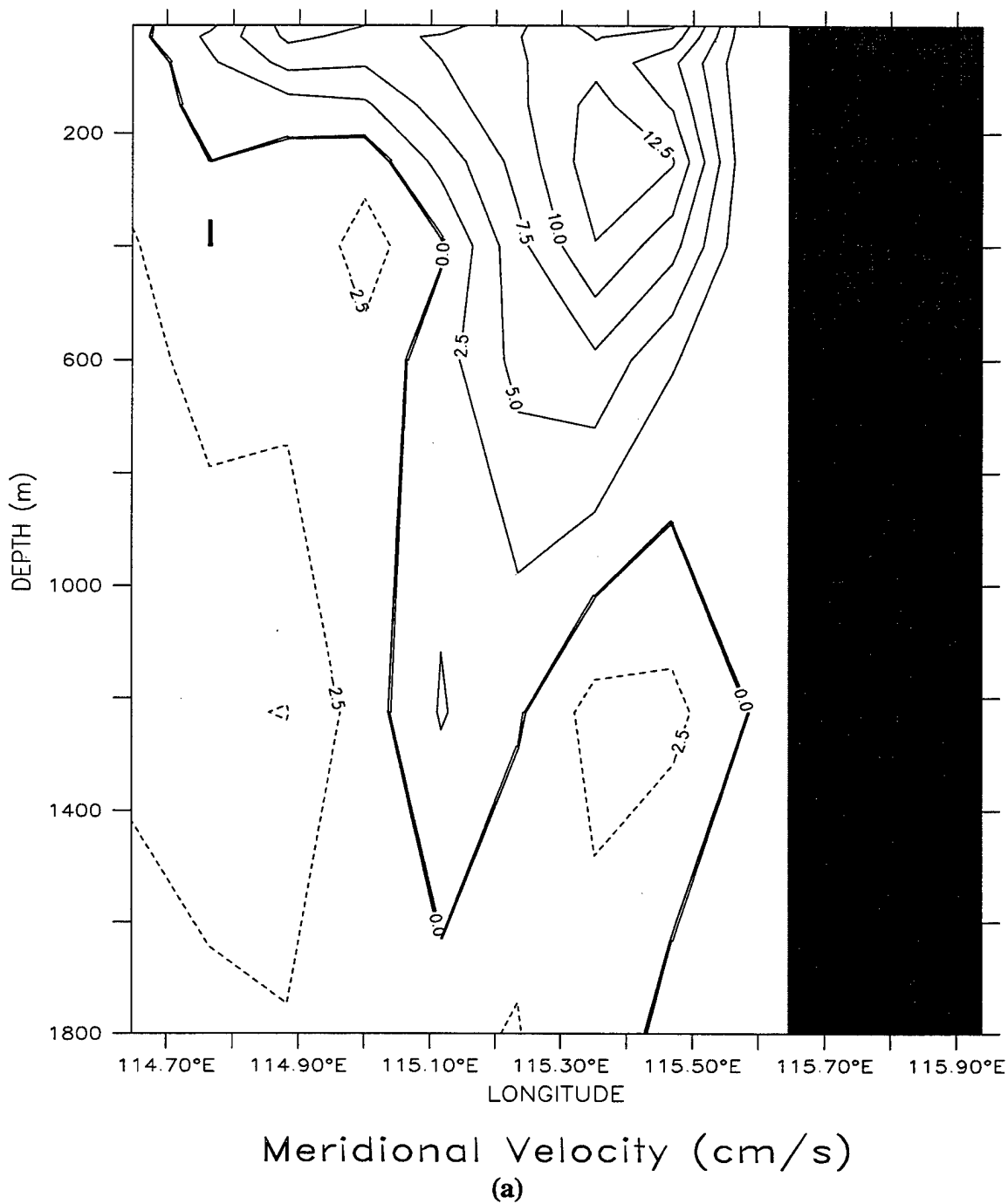
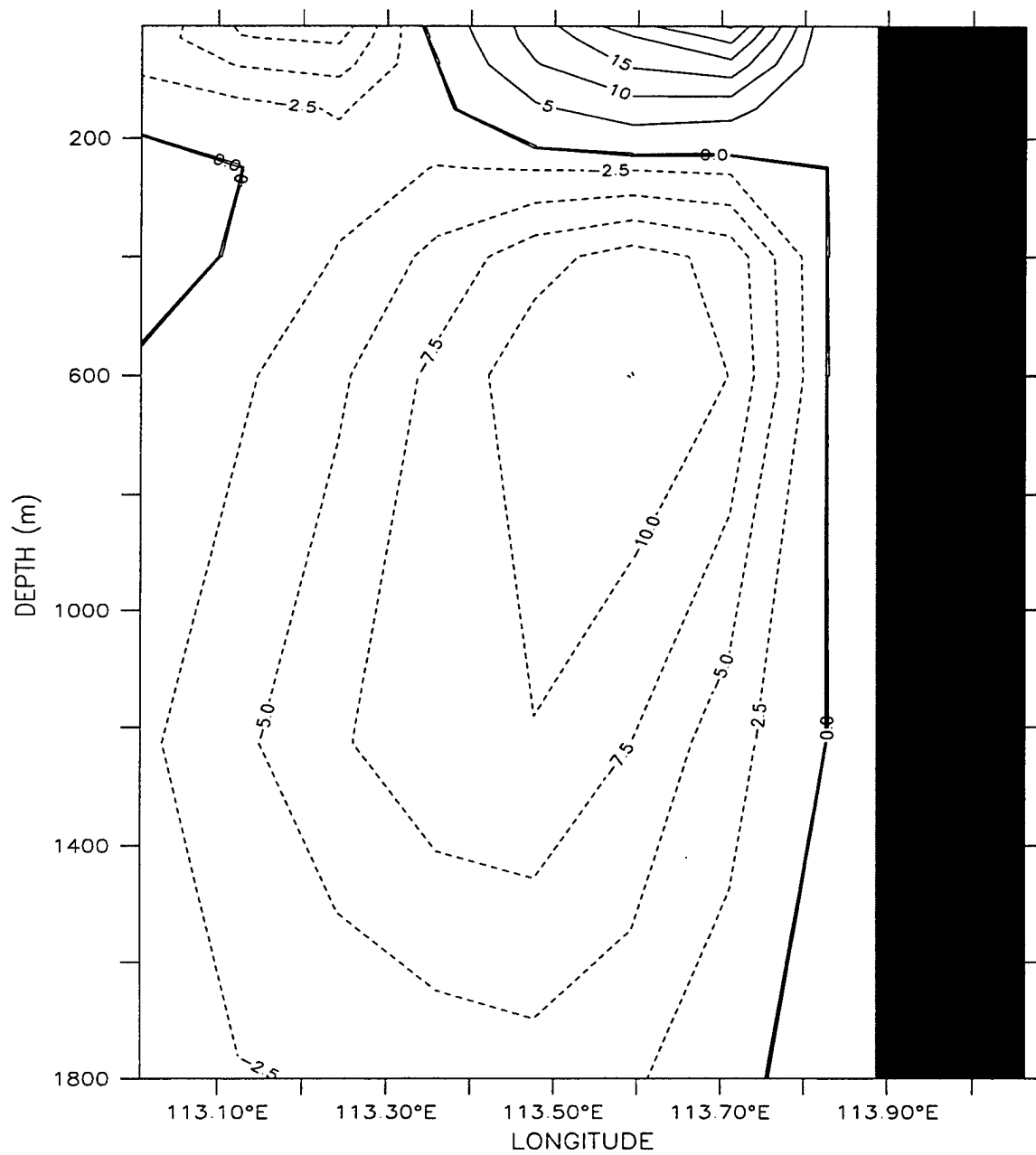


**Figure 32.** Cross-shore section of meridional velocity ( $v$ ) at (a)  $\sim 32^\circ\text{S}$  and (b)  $\sim 26^\circ\text{S}$  for Experiment 9 on day 363. Contour interval is 2.5 cm/s for poleward flow (dashed lines) and (a) 2.5 cm/s and (b) 5 cm/s for equatorward flow (solid lines).

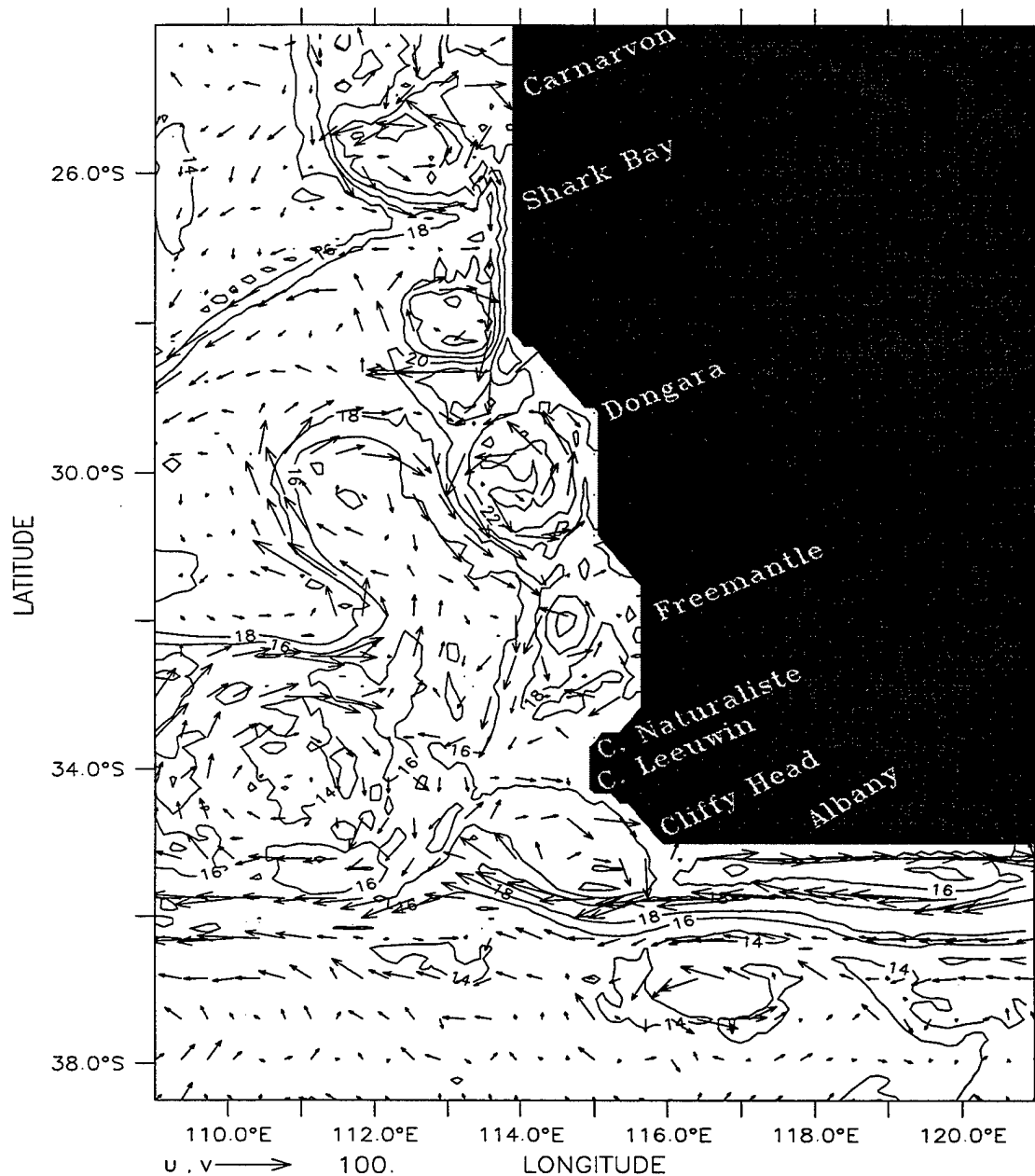
LATITUDE : 26.1S  
T (DAY) : 363



Meridional Velocity (cm/s)

(b)

DEPTH (m) : 10  
T (DAY) : 870

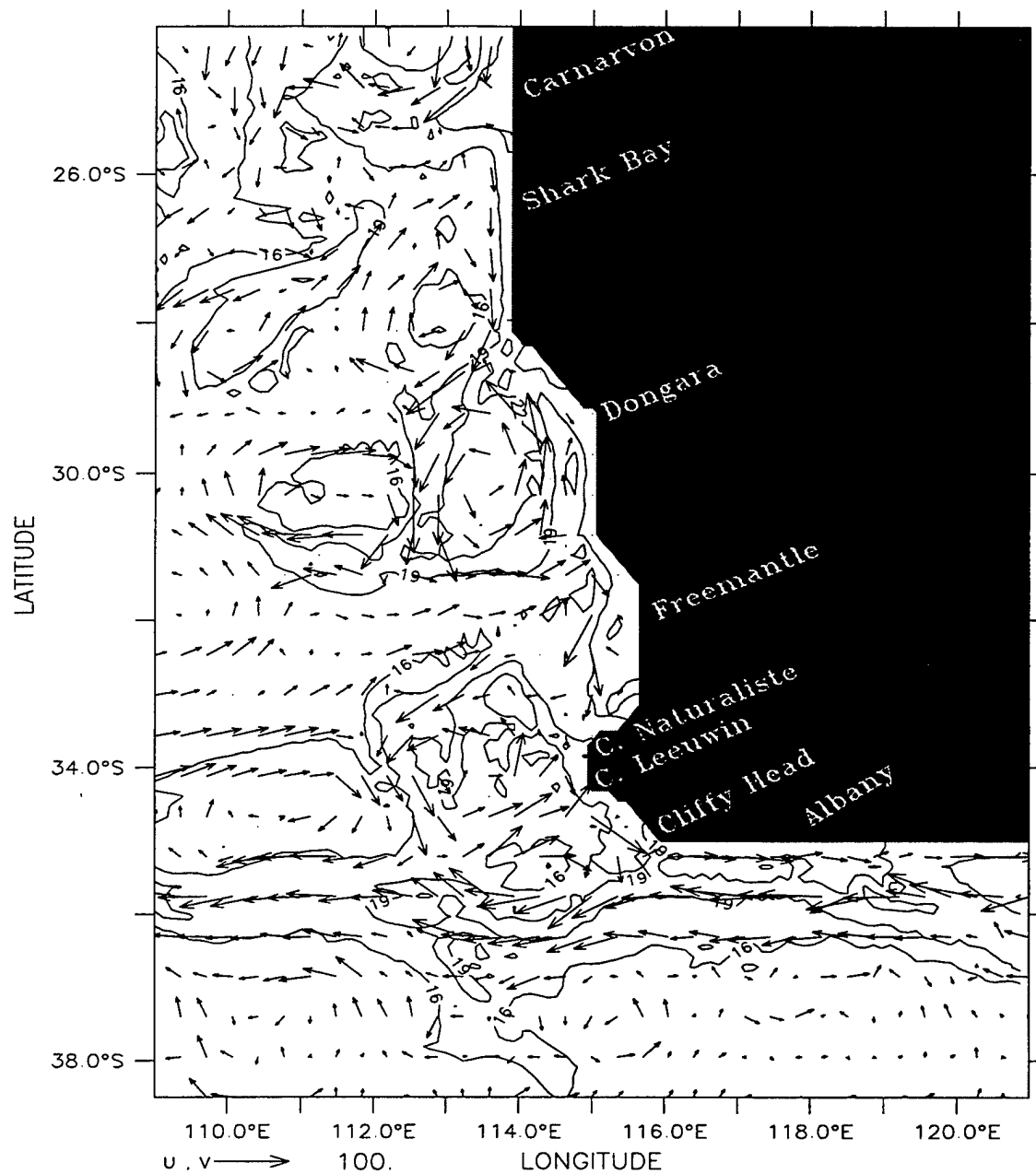


Temperature (deg C) and Velocity (cm/s)  
(a)

**Figure 33.** Temperature contours and velocity vectors at 10 m depth at days (a) 870, (b) 915, (c) 1026, and (d) 1092 of Experiment 9. The contour interval is 2°C for (a), 3°C for (b), and 1°C for (c) and (d). Maximum velocity is 100 cm/s.

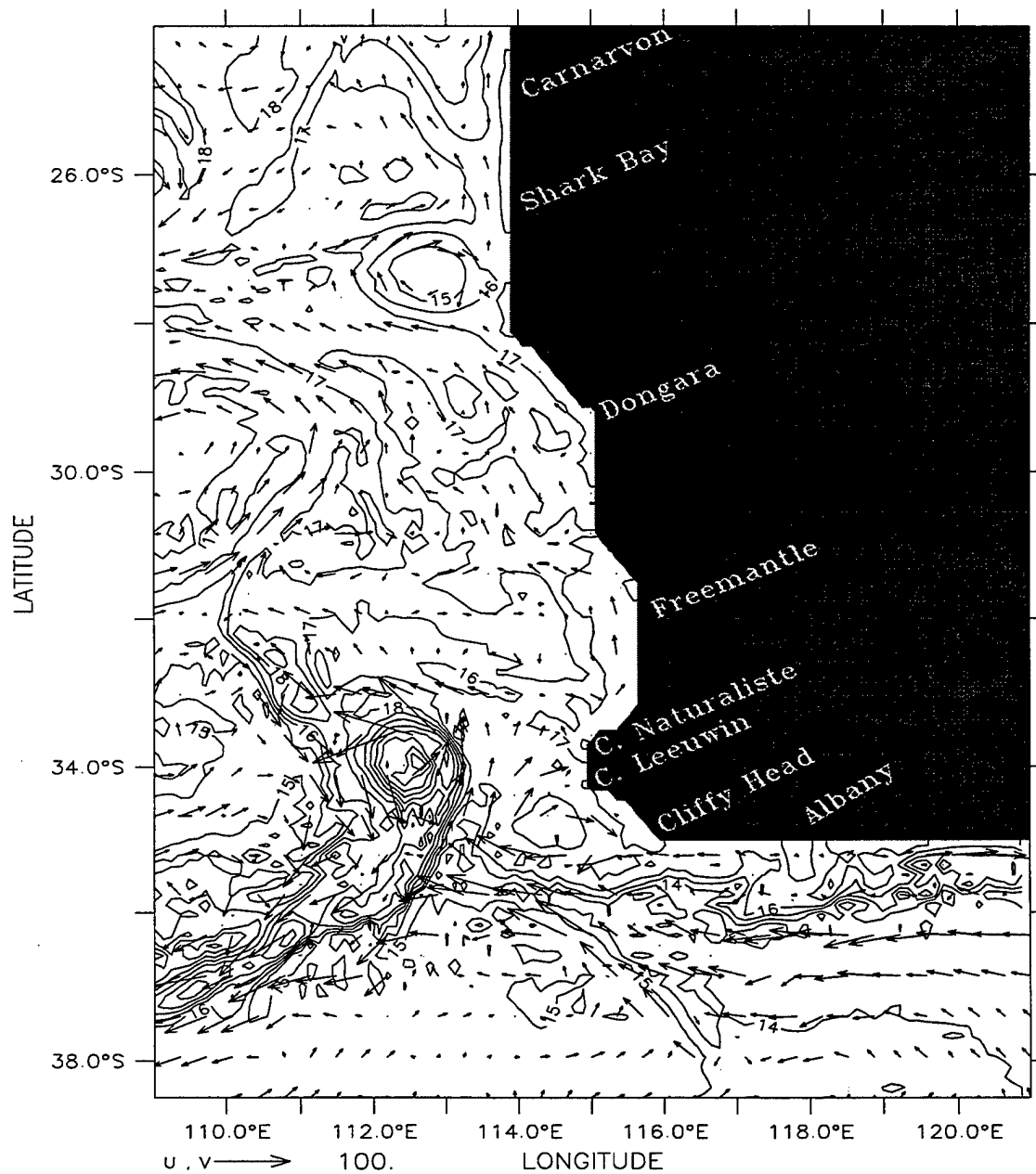


DEPTH (m) : 10  
T (DAY) : 915



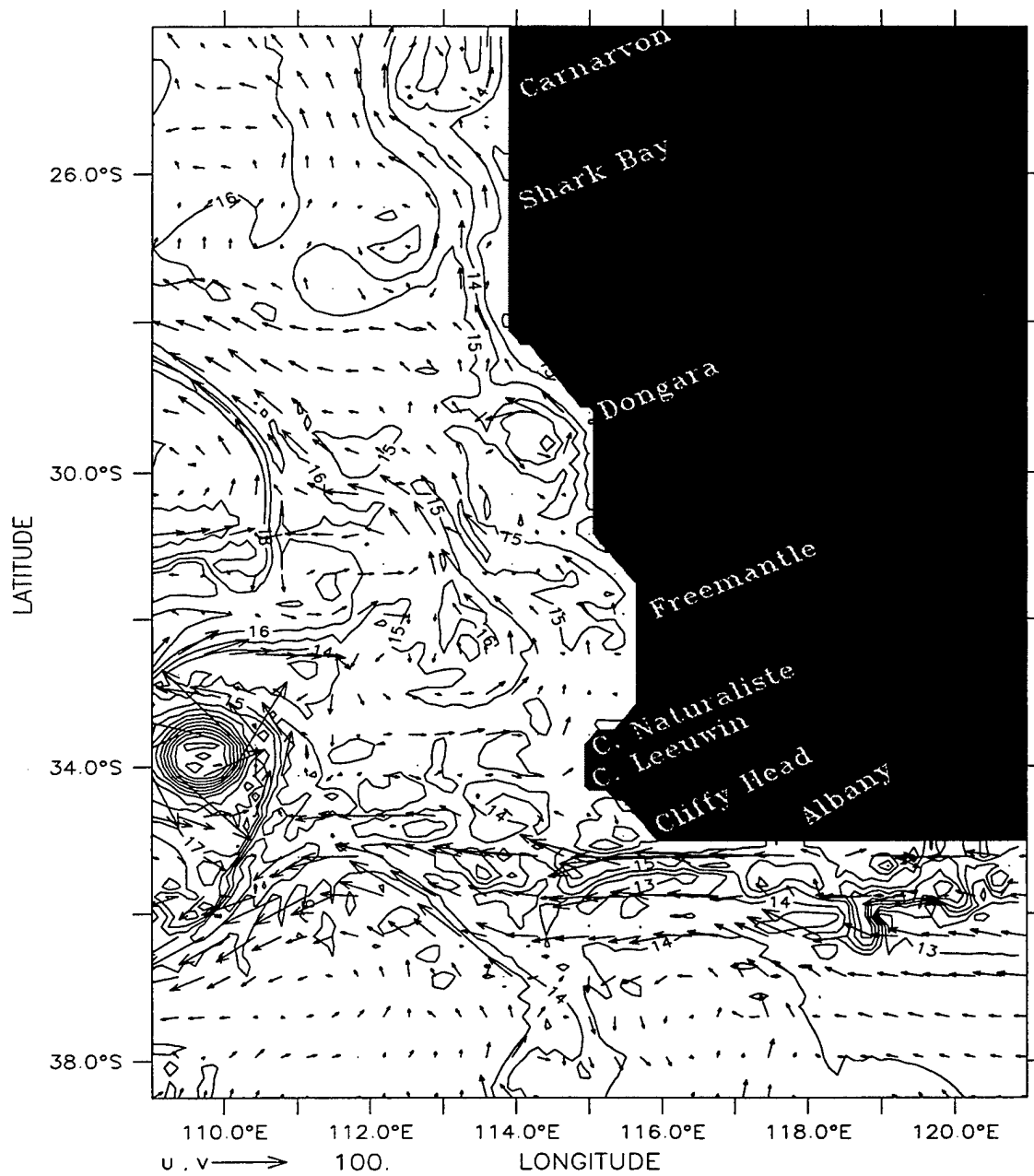
Temperature (deg C) and Velocity (cm/s)  
(b)

DEPTH (m) : 10  
T (DAY) : 1026



Temperature (deg C) and Velocity (cm/s)  
(c)

DEPTH (m) : 10  
T (DAY) : 1092



Temperature (deg C) and Velocity (cm/s)  
(d)

LATITUDE : 30S  
T (DAY) : 948

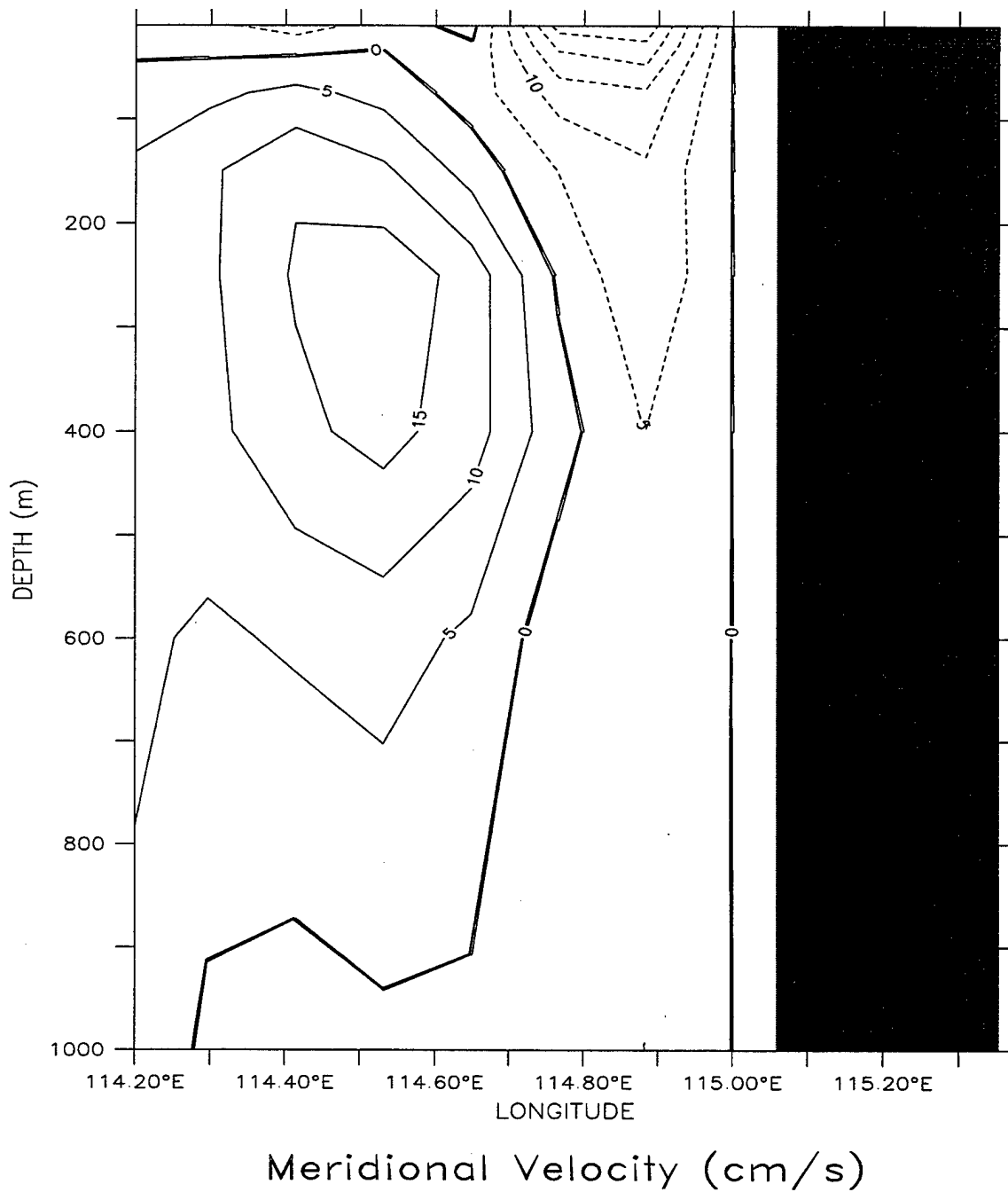


**Figure 34.** Cross-shore section of meridional velocity ( $v$ ) at 30°S on day 948 for Experiment 9. Contour interval is 5 cm/s for poleward flow (dashed lines) and 5 cm/s for equatorward flow (solid lines).

LONGITUDE : 117E(117)  
T (DAY) : 930

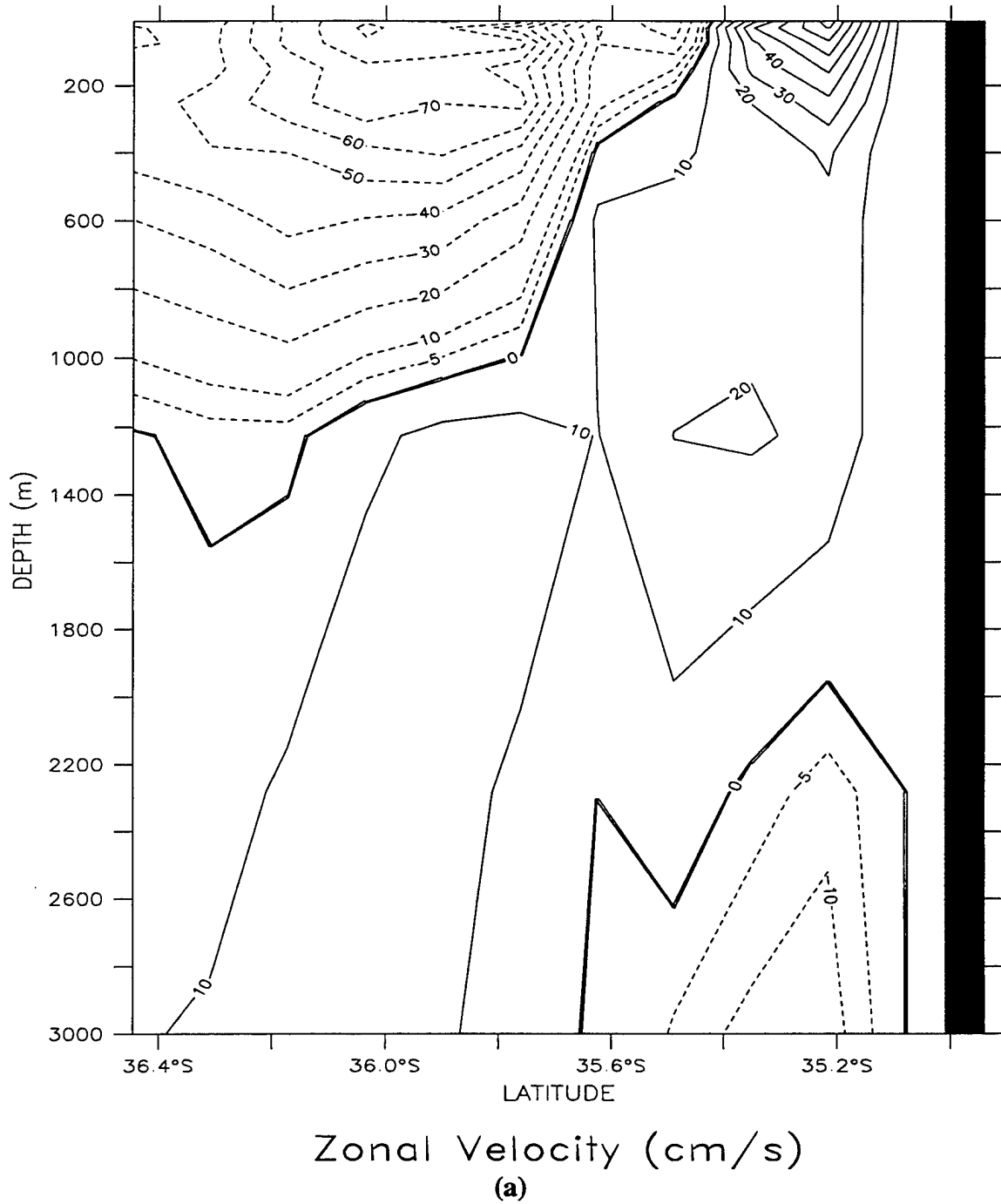
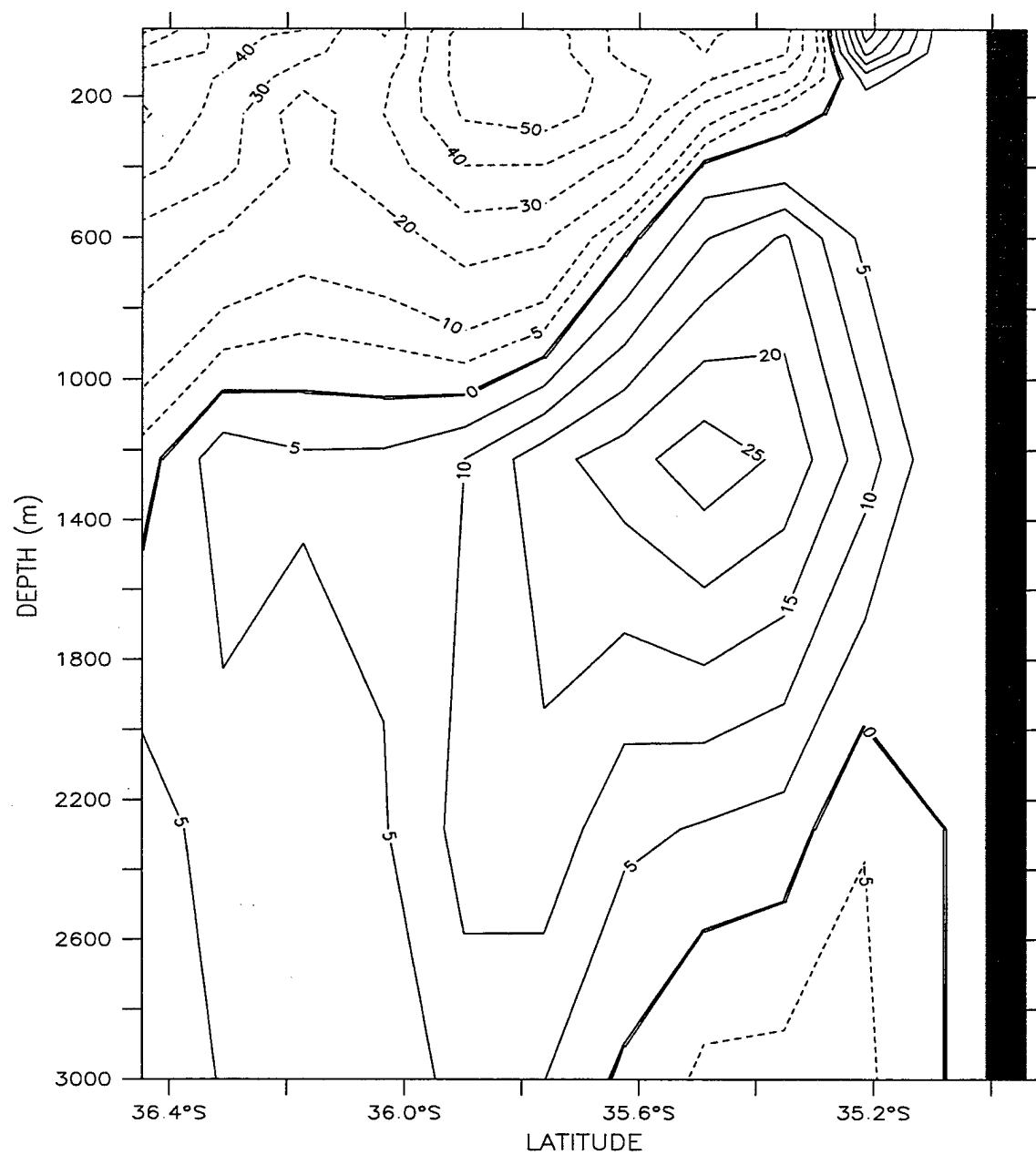


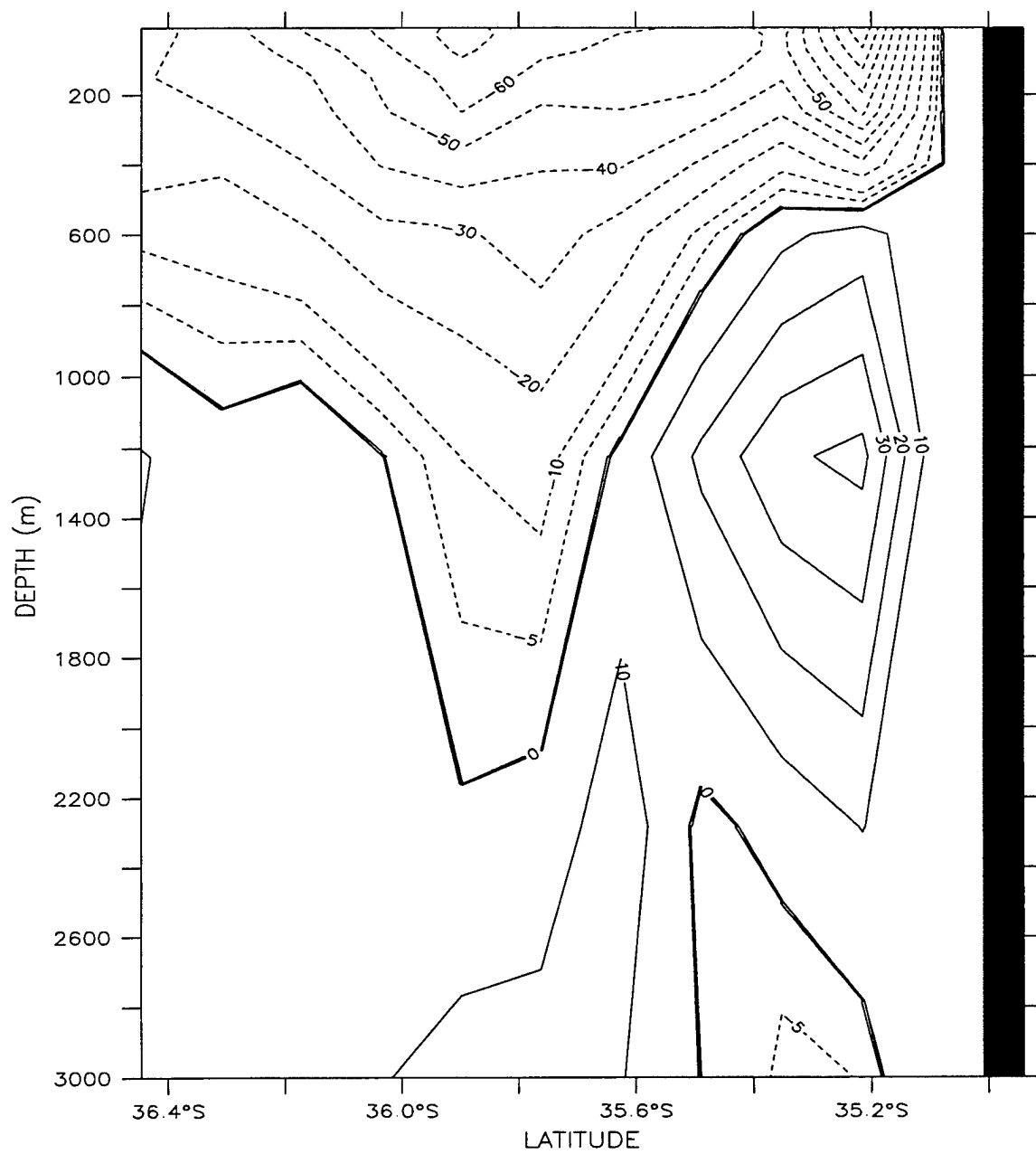
**Figure 35.** Cross-shore section of zonal velocity ( $u$ ) at  $\sim 117^\circ\text{E}$  for Experiment 9 on day (a) 930, (b) 990, and (c) 1074. Contour interval for velocities greater than (less than) 10 cm/s is 10 cm/s (5 cm/s) for westward flow (dashed lines). For eastward flow (solid lines), the contour interval is 10 cm/s in (a) and (c) and 5 cm/s in (b).

LONGITUDE : 117E(117)  
T (DAY) : 990



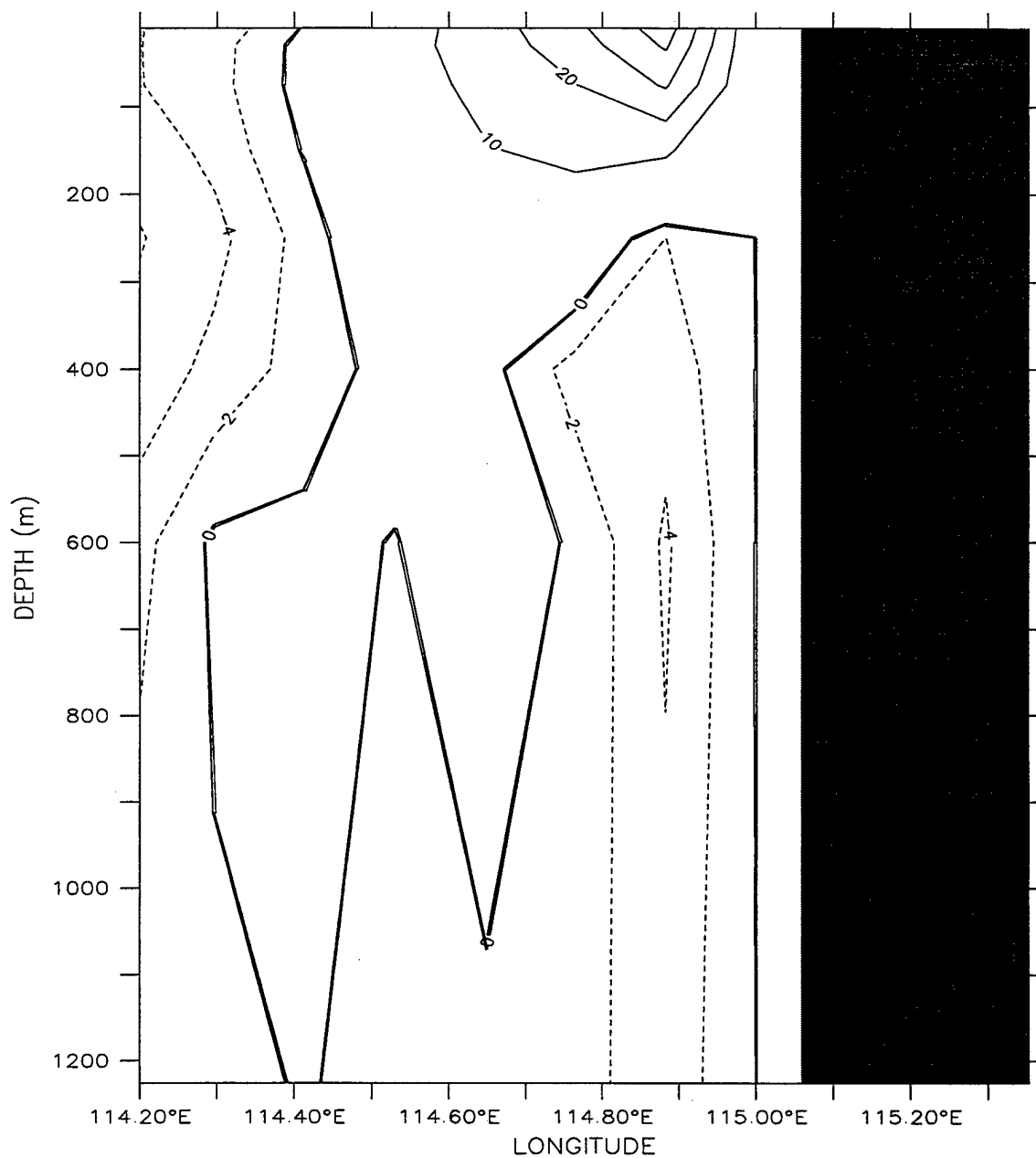
Zonal Velocity (cm/s)  
(b)

LONGITUDE : 117E(117)  
T (DAY) : 1074



Zonal Velocity (cm/s)  
(c)

LATITUDE : 30S  
T (DAY) : 1074



Meridional Velocity (cm/s)

(a)

**Figure 36.** Cross-shore section of meridional velocity (v) at 30°S for (a) Experiment 9 and (b) Experiment 6 at day 1074. Contour interval is (a) 2 cm/s and (b) 5 cm/s for poleward flow (dashed lines) and 10 cm/s for equatorward flow (solid lines).



LATITUDE : 30S  
T (DAY) : 1074



Meridional Velocity (cm/s)

(b)

LONGITUDE : 117E(117)  
T (DAY) : 1074

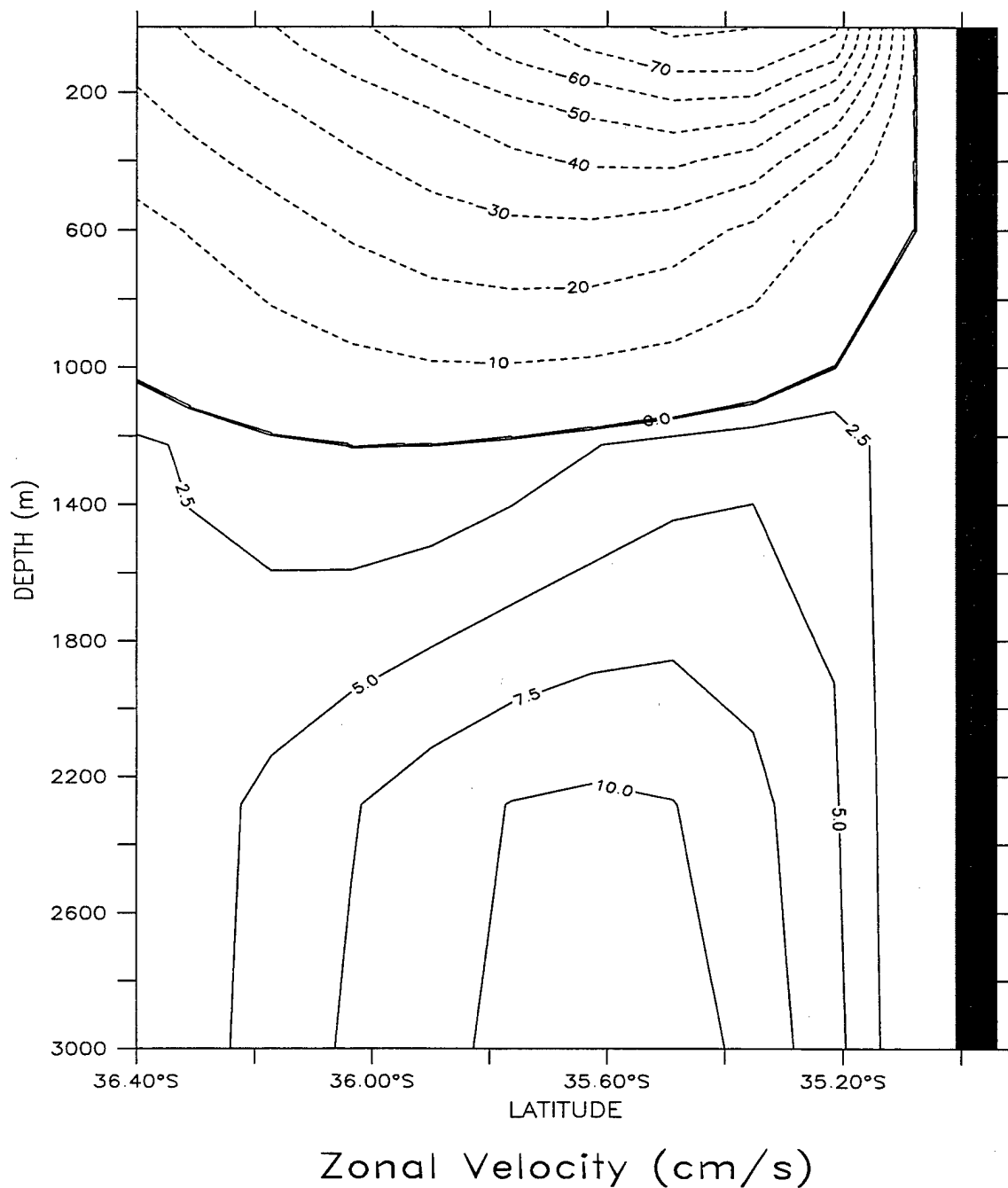


**Figure 37.** Cross-shore section of zonal velocity ( $u$ ) at 117°E on day 1074 for Experiment 6. Contour interval is 10 cm/s for westward flow (dashed lines) and 2.5 cm/s for eastward flow (solid lines).

DEPTH (m) : 10

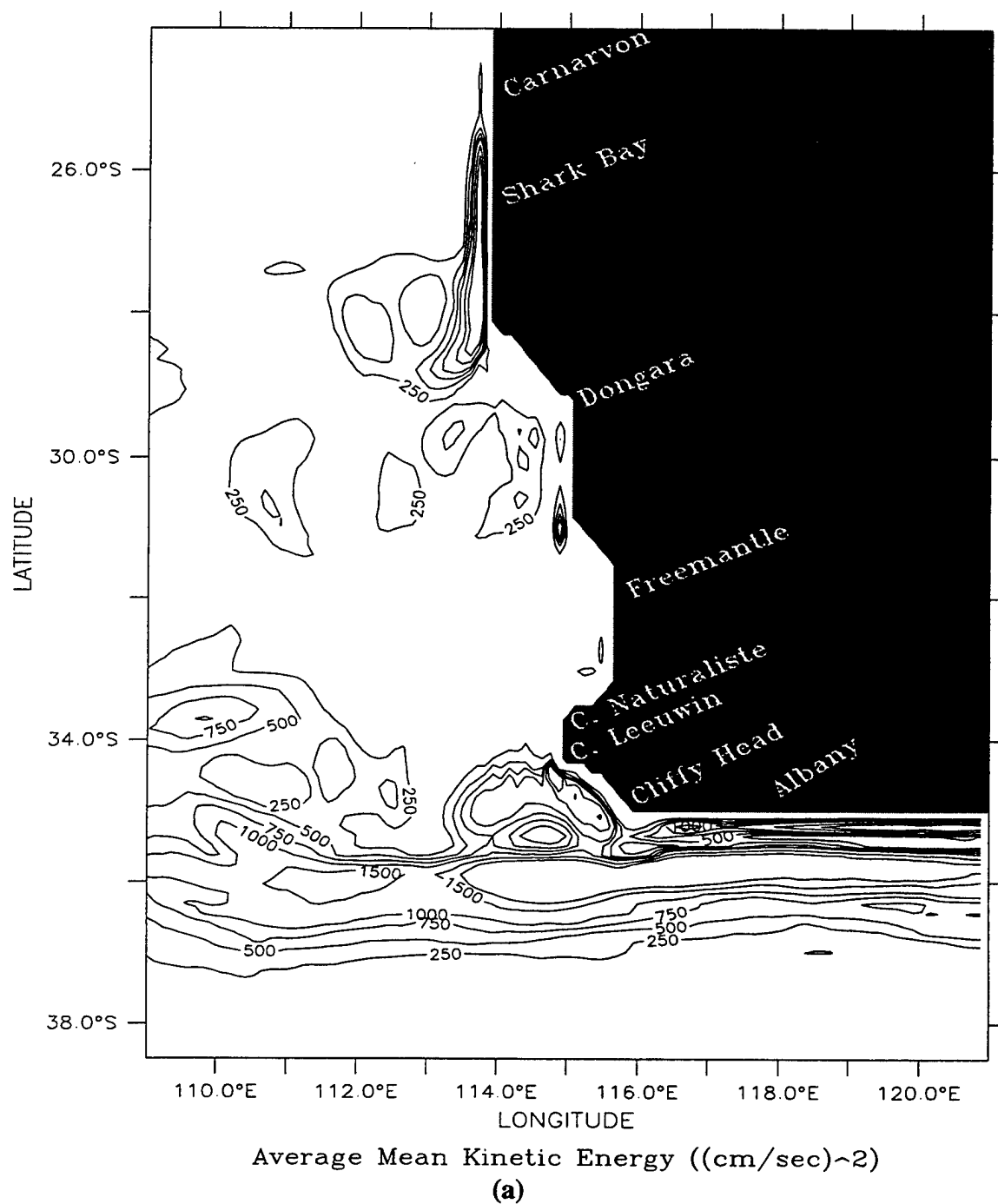
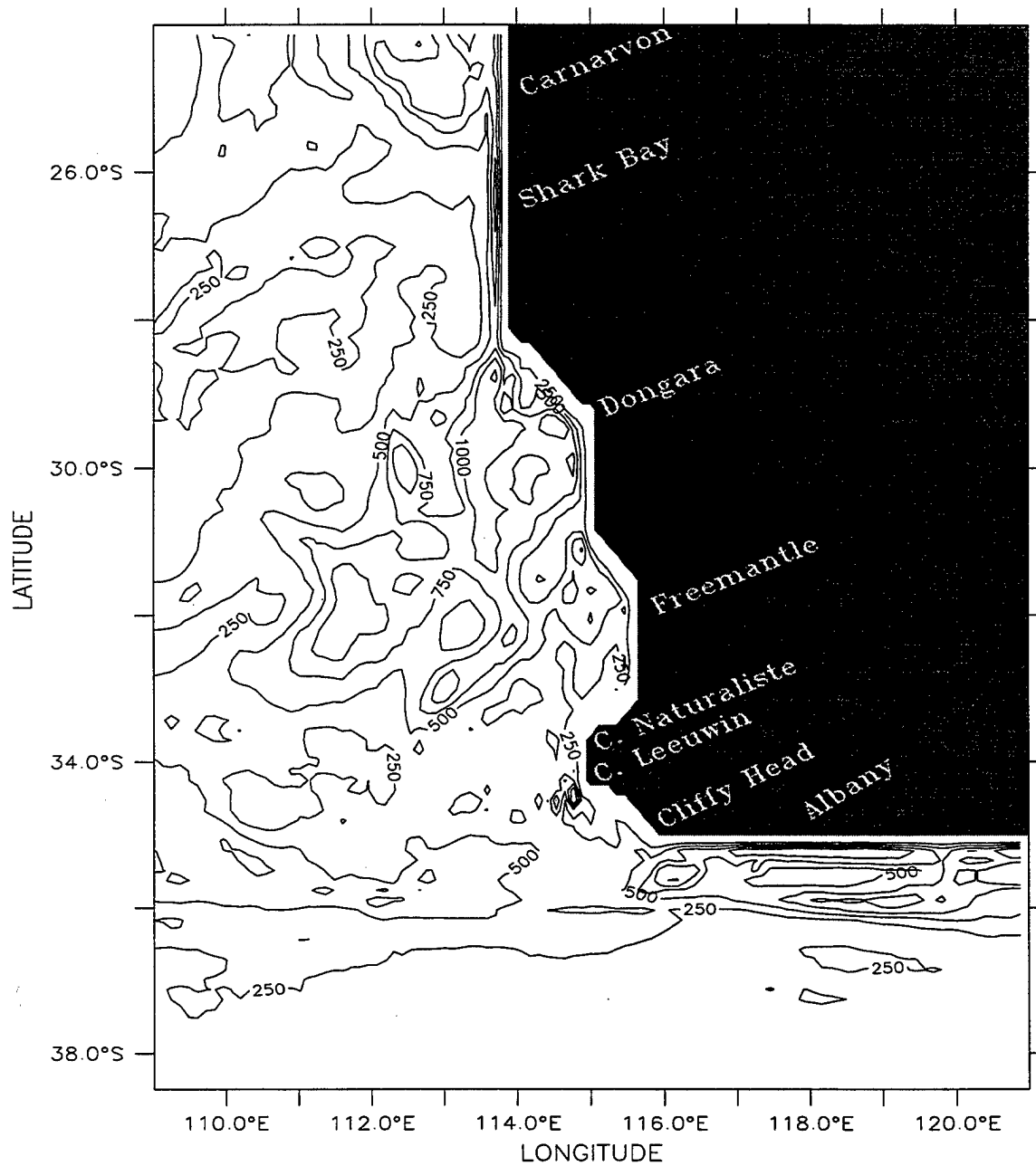


**Figure 38.** Horizontal map at 10 m depth of average (a) mean kinetic energy (MKE) and (b) eddy kinetic energy (EKE) for Experiment 9 in model year 3, time averaged for April through September, when the Leeuwin Current is strongest. Contour interval for kinetic energy ((cm/s)<sup>2</sup>) greater than 1000 is 500 and less than 1000 is 250.

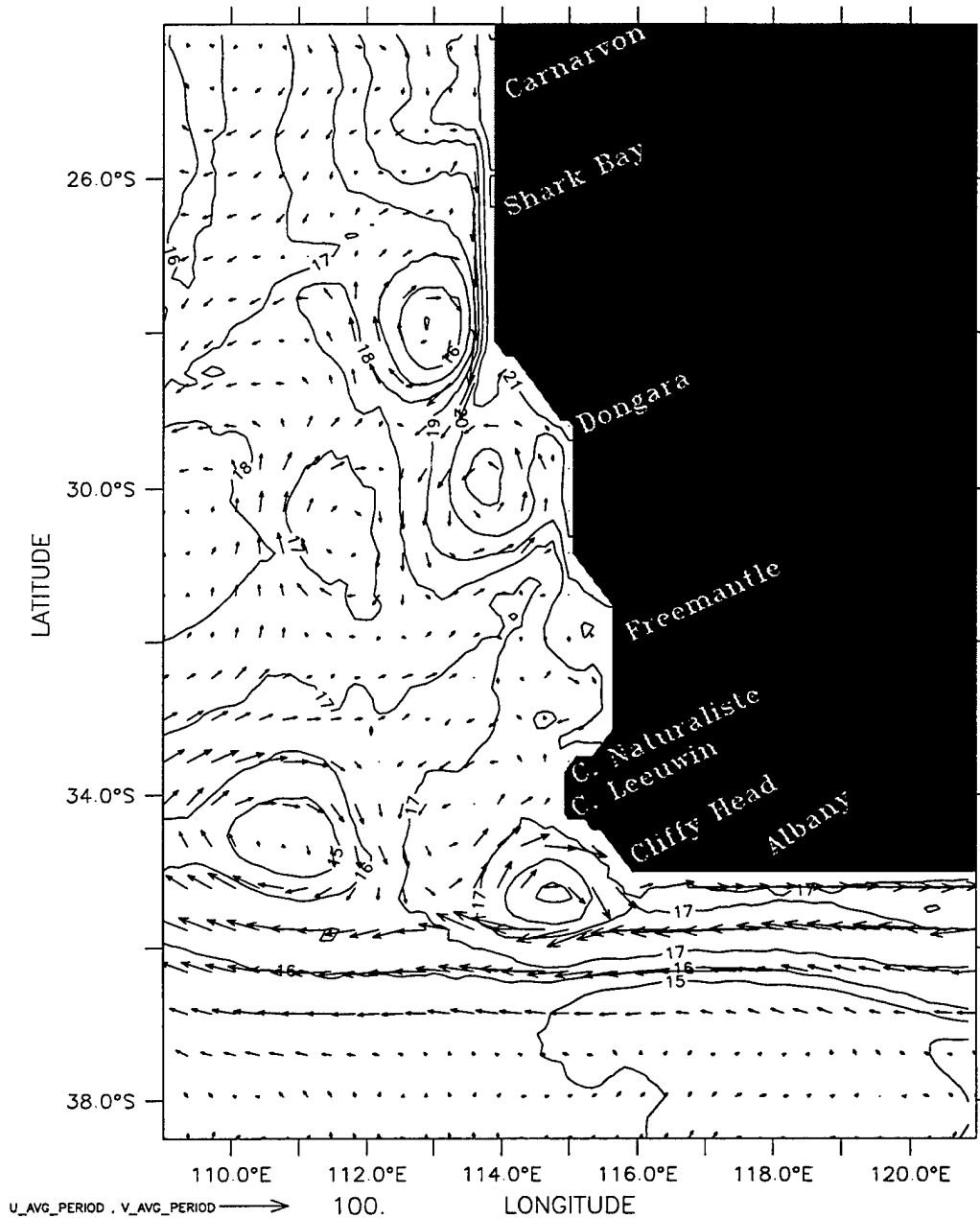
DEPTH (m) : 10



Average Eddy Kinetic Energy ((cm/sec)<sup>2</sup>)

(b)

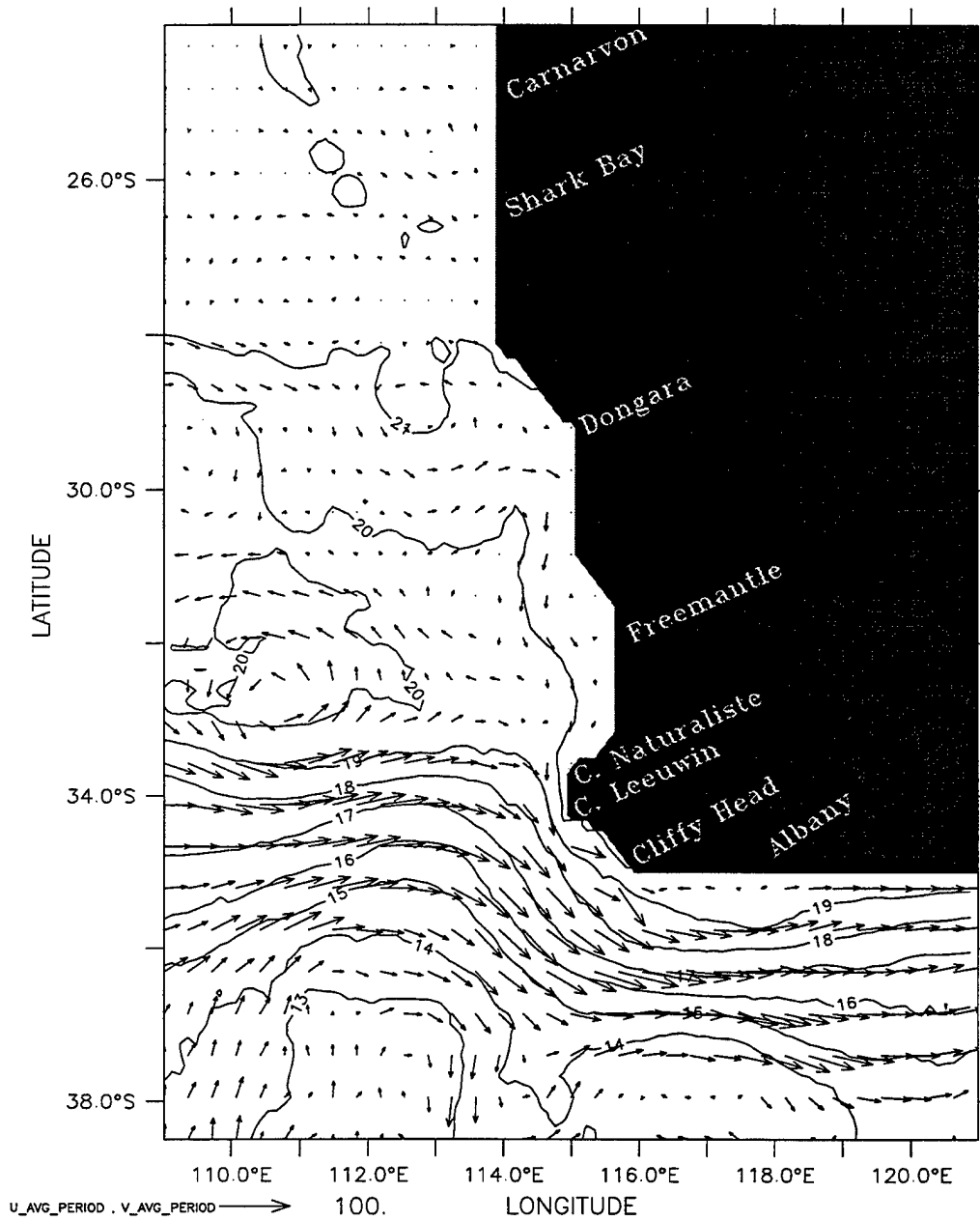
DEPTH (m) : 10



Average Temperature (deg C) and Velocity (cm/s)  
(a)

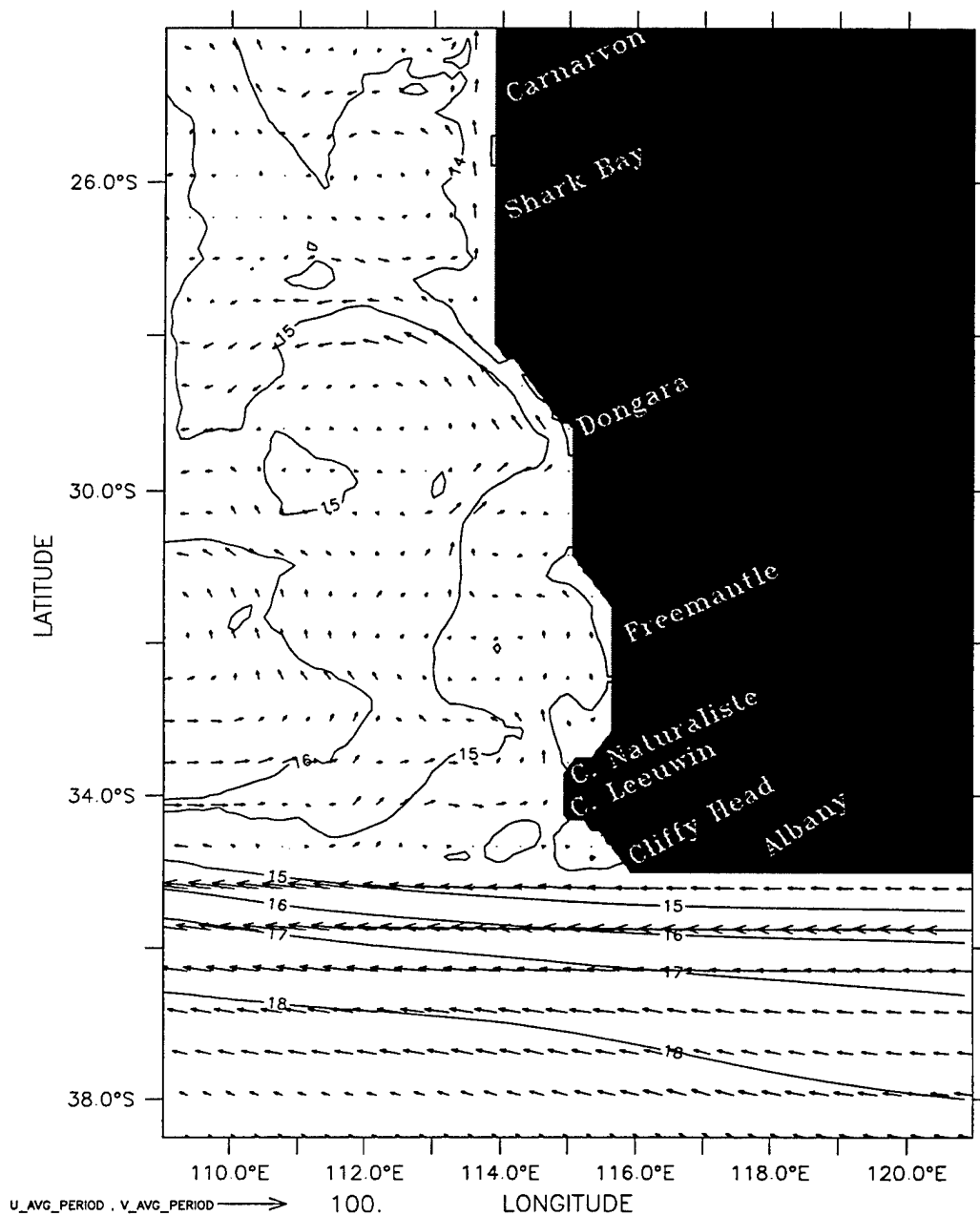
**Figure 39.** Temperature contours and velocity vectors at 10 m depth for Experiment (a) 9, (b) 3, (c) 6, and (d) 8 in model year 3, time averaged for April through September, when the Leeuwin Current is strongest. The contour interval is 1°C. Maximum velocity is 100 cm/s.

DEPTH (m) : 10



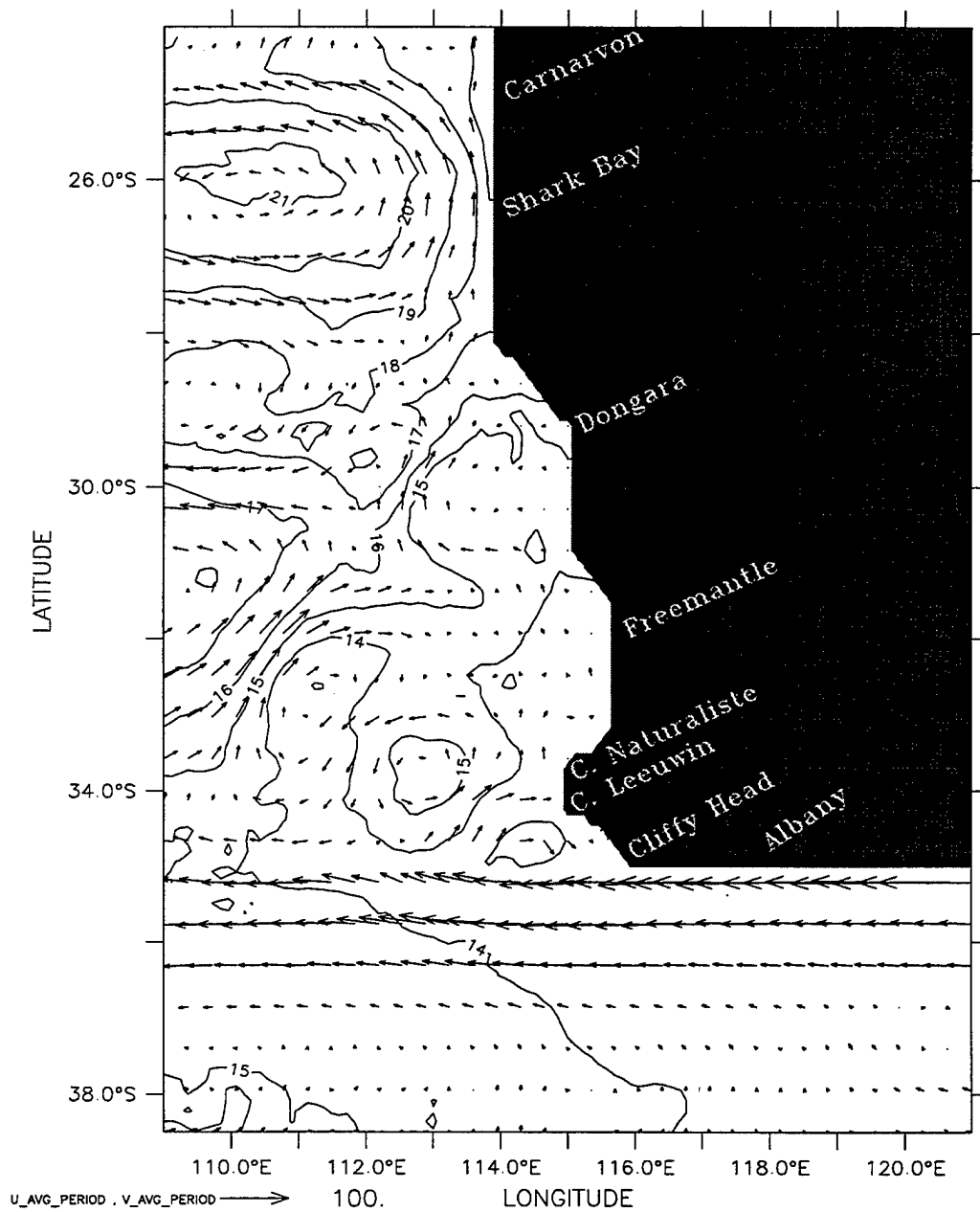
Average Temperature (deg C) and Velocity (cm/s)  
(b)

DEPTH (m) : 10



Average Temperature (deg C) and Velocity (cm/s)  
(c)

DEPTH (m) : 10



Average Temperature (deg C) and Velocity (cm/s)  
(d)



LATITUDE : 30S  
T (DAY) : 930

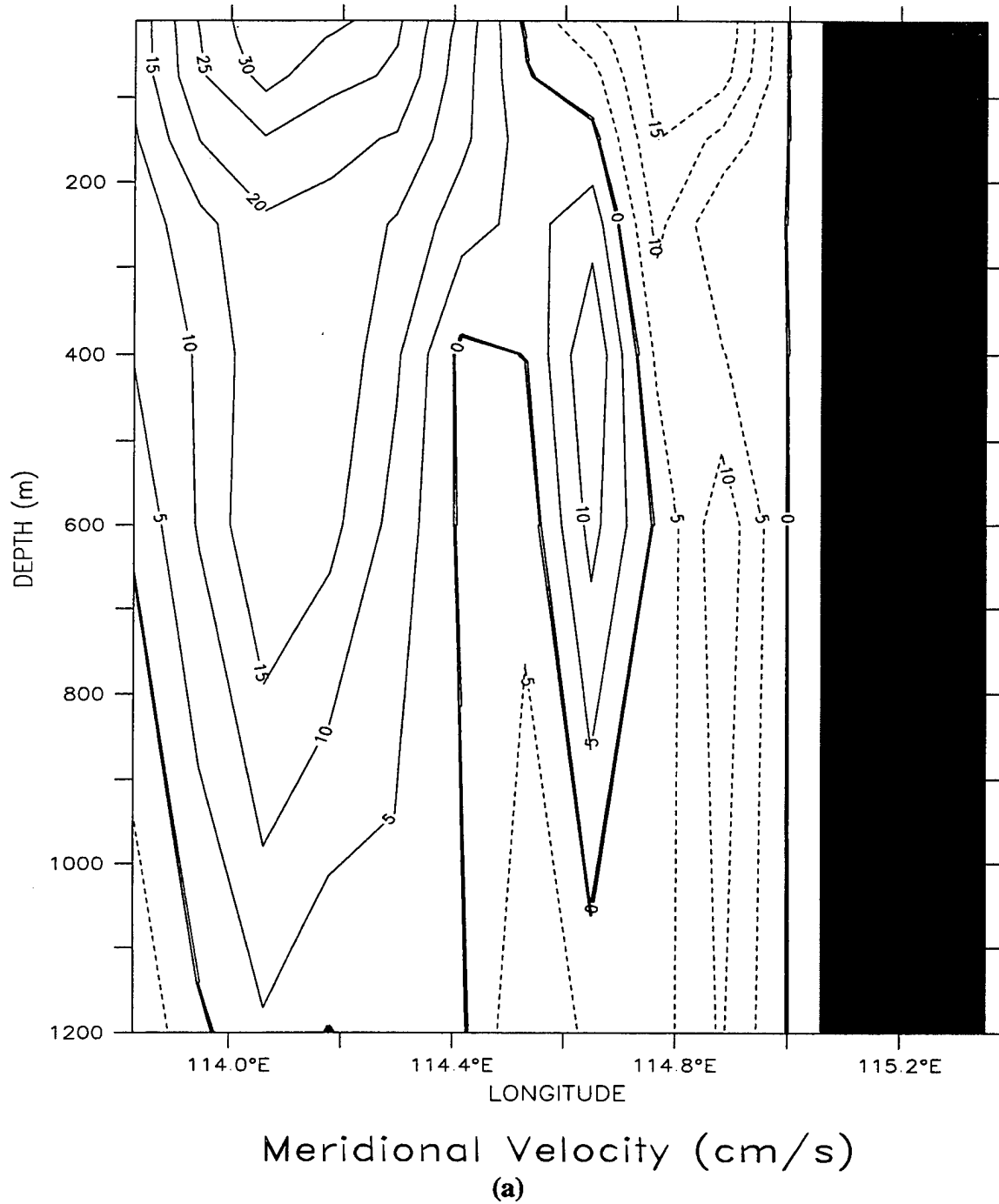
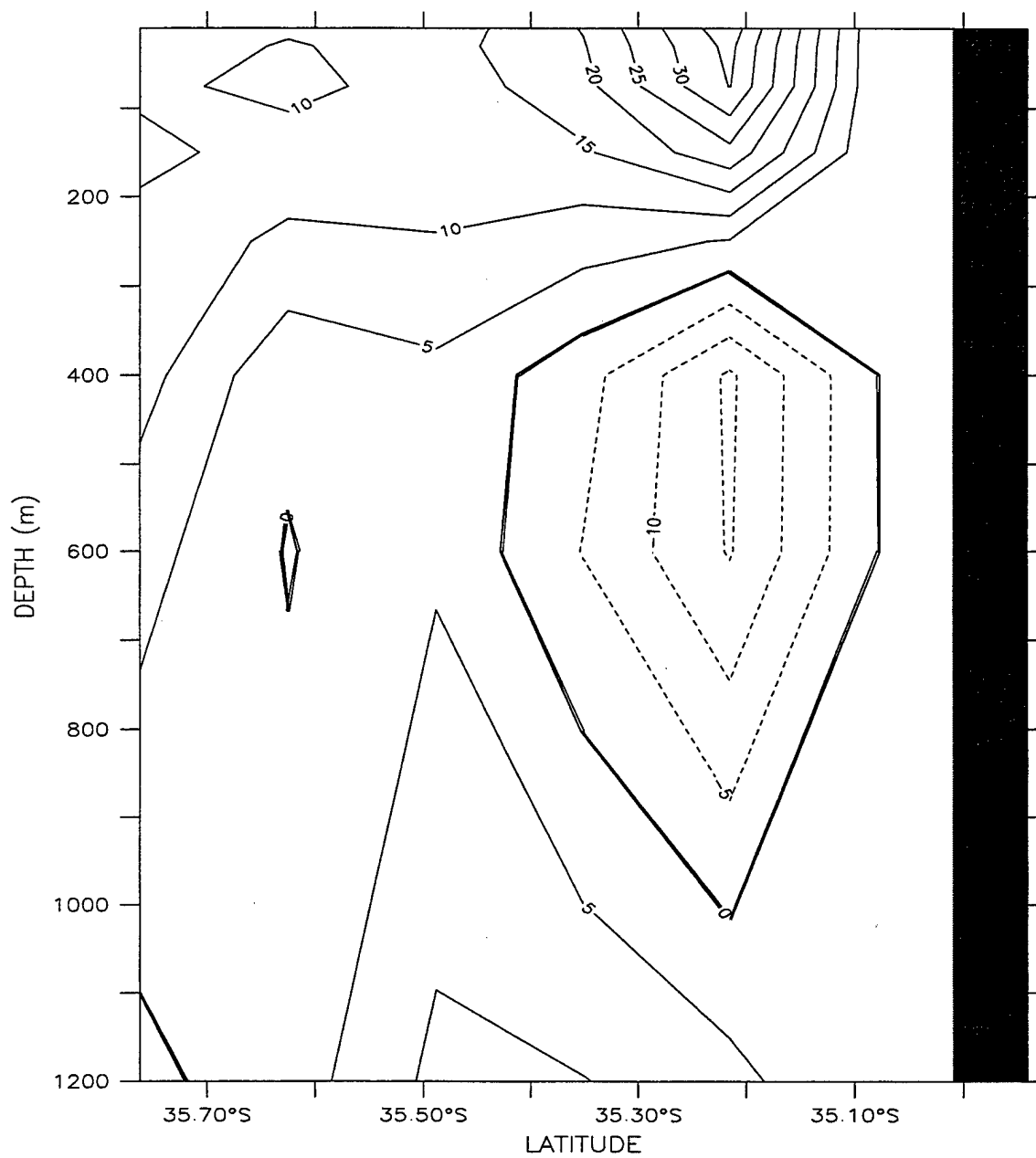


**Figure 40.** Cross-shore section of (a) meridional velocity ( $v$ ) at  $30^\circ\text{S}$  on day 930 and (b) zonal velocity ( $u$ ) at  $117^\circ\text{E}$  on day 918 for Experiment 3. Contour interval is 5 cm/s for (a) poleward and (b) westward flow (dashed lines) and 5 cm/s for (a) equatorward and (b) eastward flow (solid lines).

LONGITUDE : 117E(117)  
T (DAY) : 918



Zonal Velocity (cm/s)  
(b)

DEPTH (m) : 10

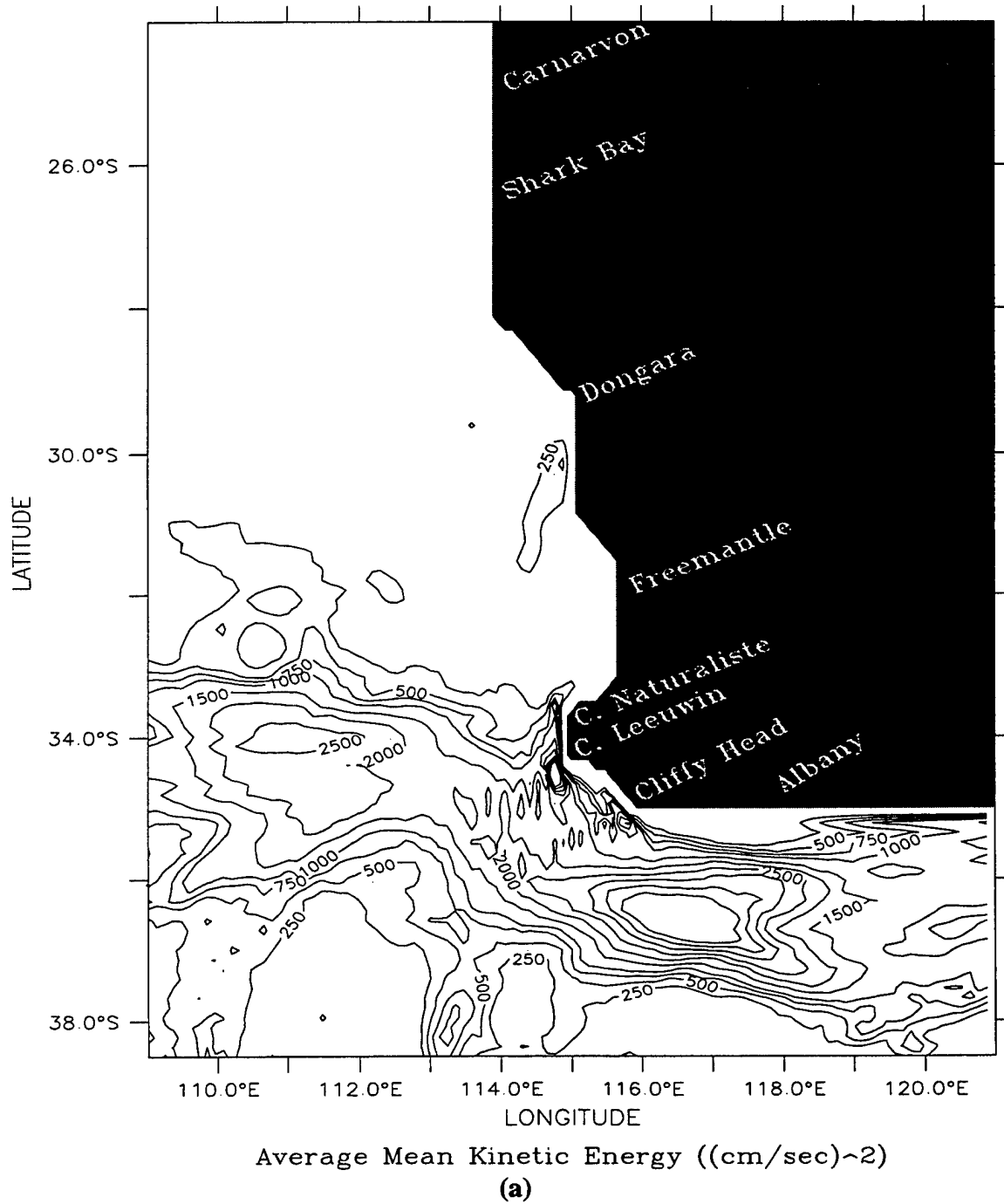
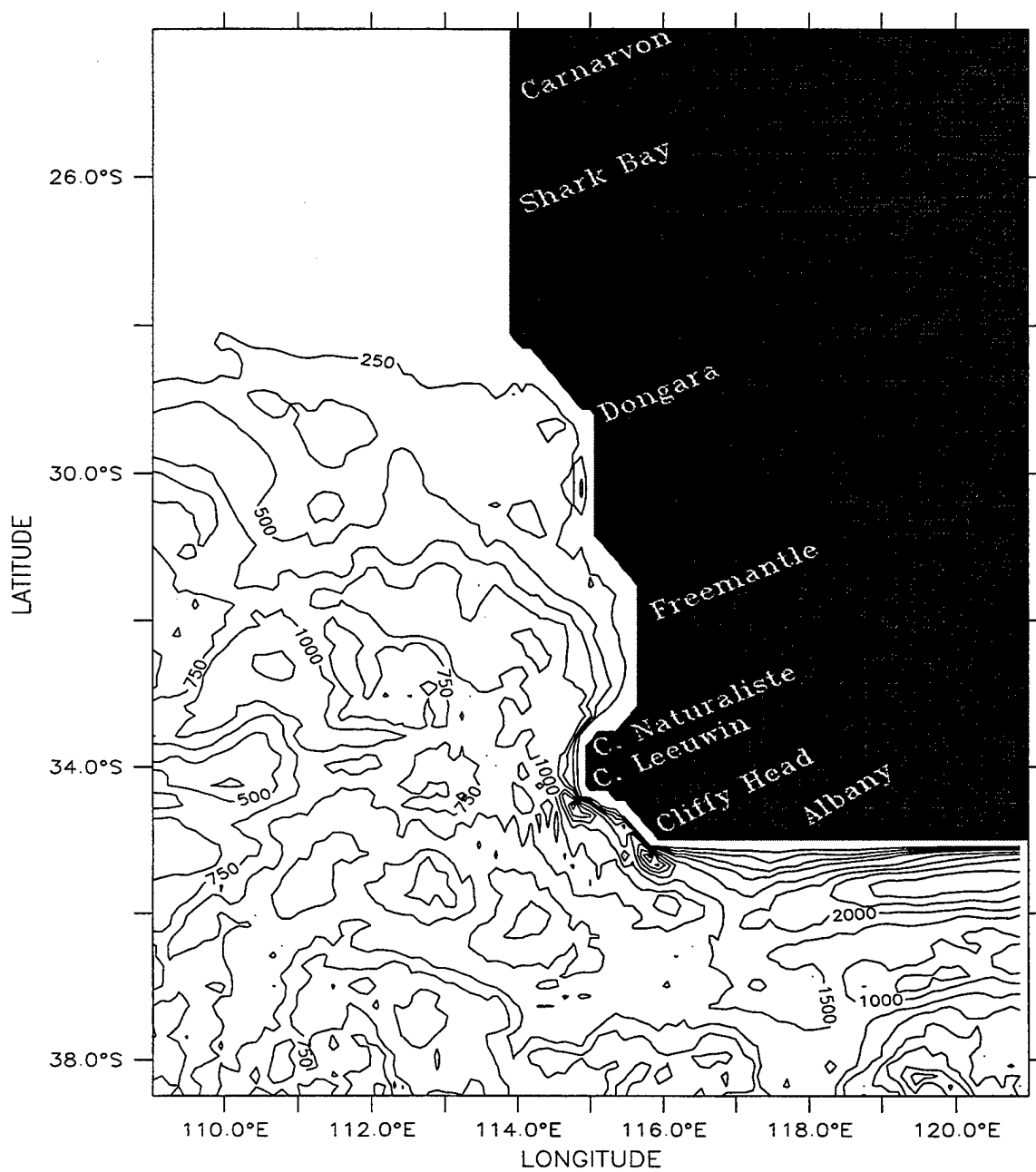


**Figure 41.** Horizontal map at 10 m depth of average (a) mean kinetic energy (MKE) and (b) eddy kinetic energy (EKE) for Experiment 3 in model year 3, time averaged for April through September, when the Leeuwin Current is strongest. Contour interval for kinetic energy ((cm/s)<sup>2</sup>) greater than 1000 is 500 and less than 1000 is 250.

DEPTH (m) : 10



Average Eddy Kinetic Energy ((cm/sec)<sup>2</sup>)

(b)

LATITUDE : 30S  
T (DAY) : 912

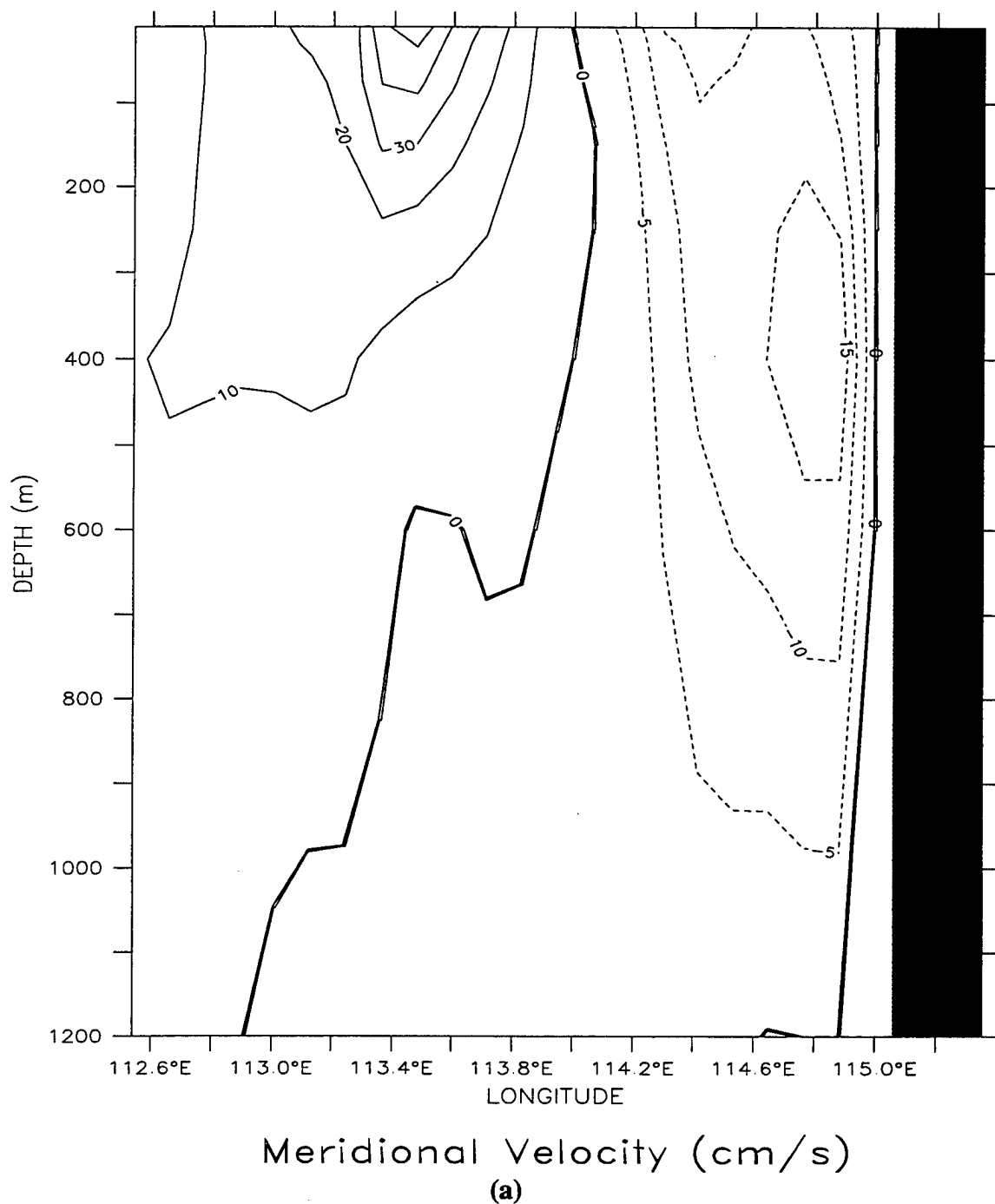
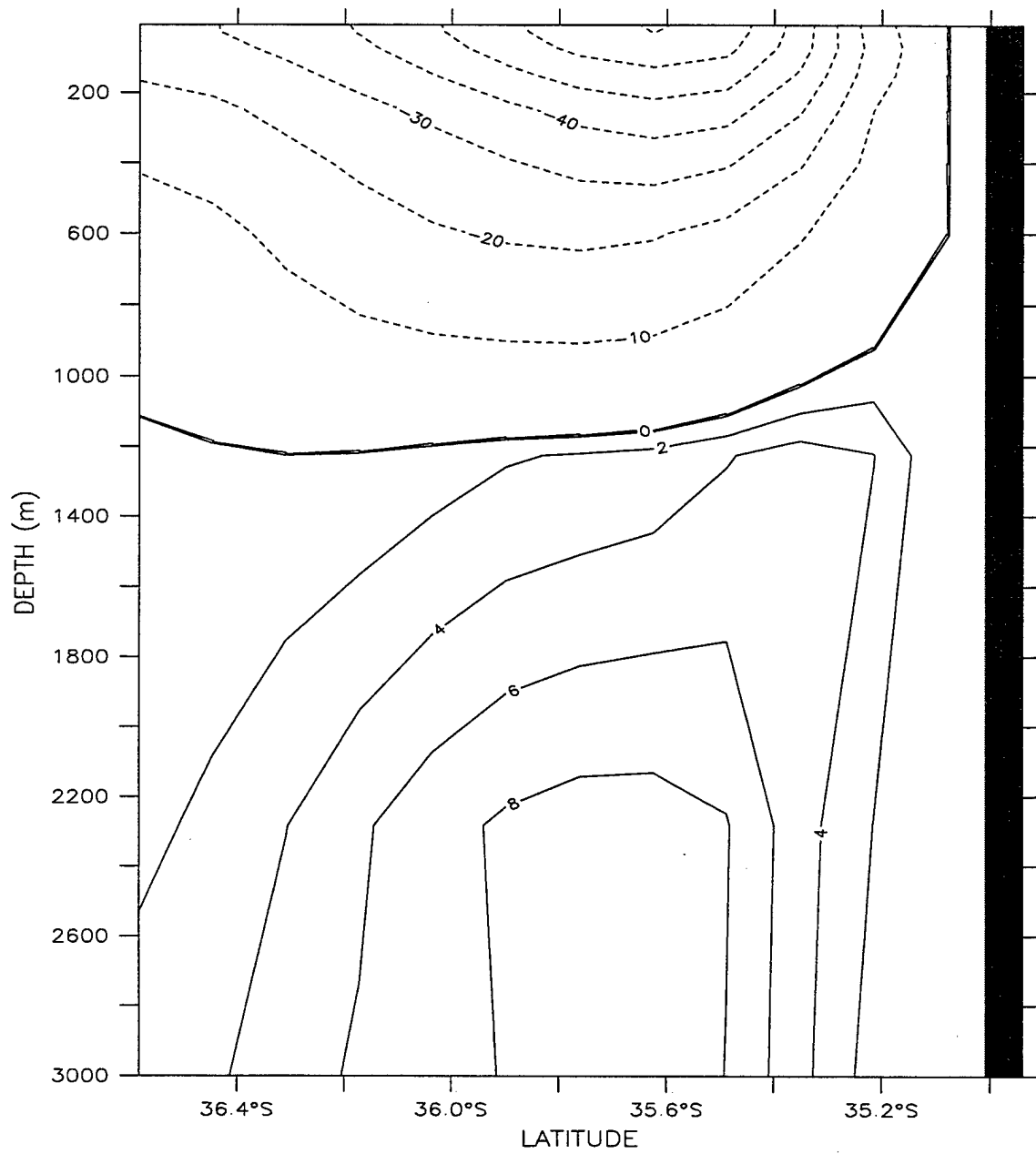


**Figure 42.** Cross-shore section of (a) meridional velocity ( $v$ ) at  $30^\circ\text{S}$  on day 912 and (b) zonal velocity ( $u$ ) at  $117^\circ\text{E}$  on day 924 for Experiment 6. Contour interval is (a) 5 cm/s and (b) 10 cm/s for (a) poleward and (b) westward flow (dashed lines) and (a) 10 cm/s and (b) 2 cm/s for (a) equatorward and (b) eastward flow (solid lines).

LONGITUDE : 117E(117)  
T (DAY) : 924



Zonal Velocity (cm/s)  
(b)

DEPTH (m) : 10

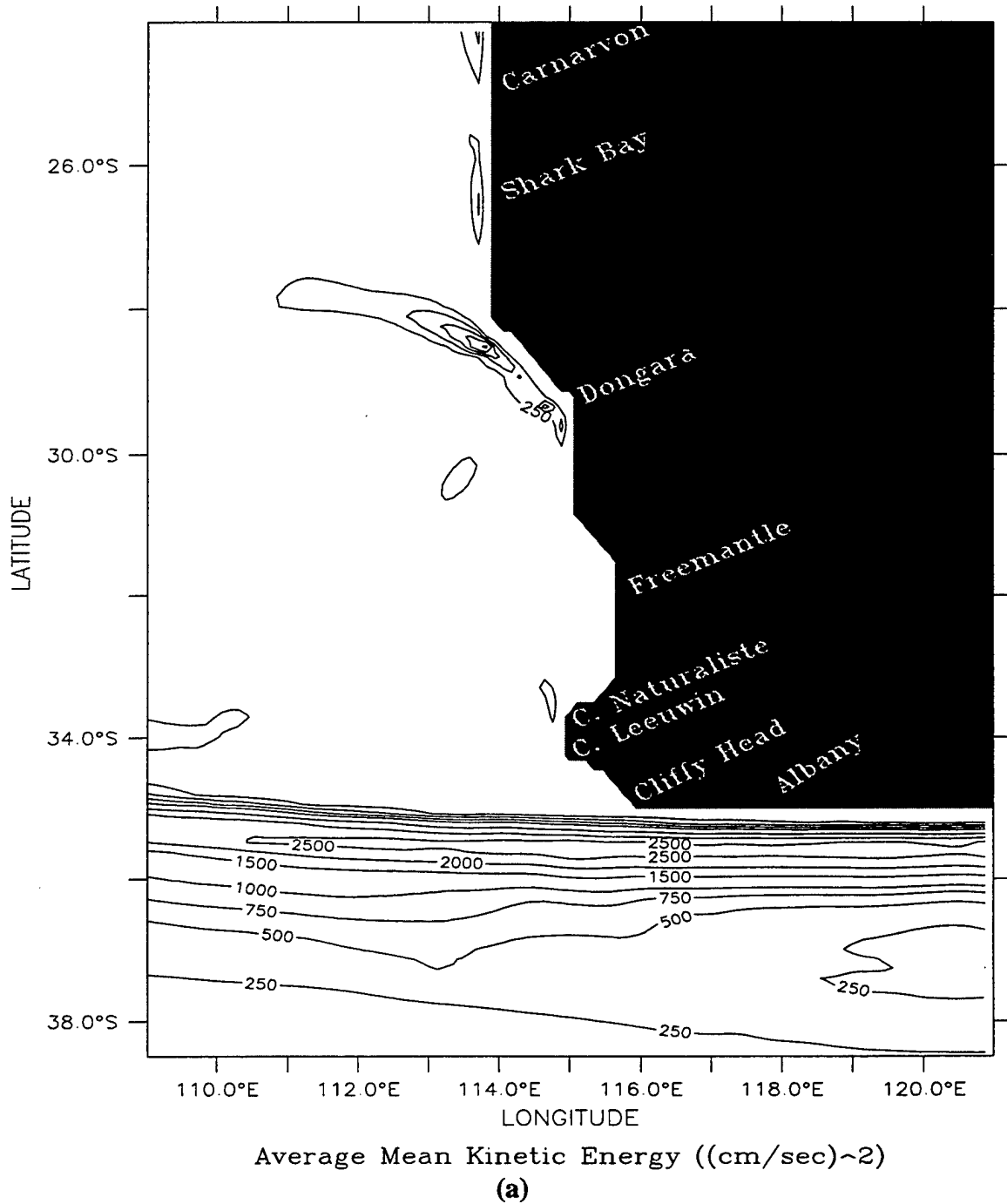
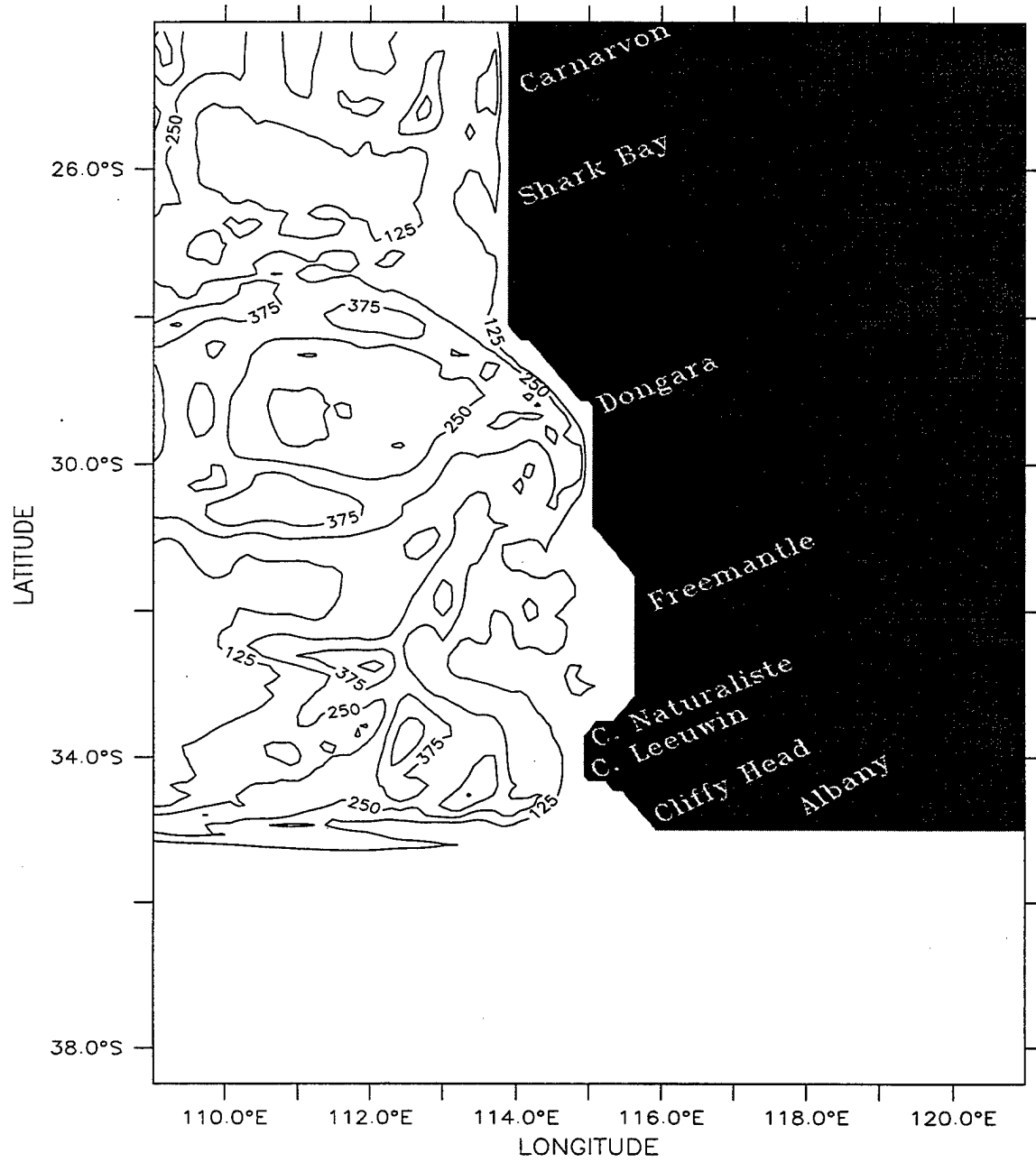


**Figure 43.** Horizontal map at 10 m depth of average (a) mean kinetic energy (MKE) and (b) eddie kinetic energy (EKE) for Experiment 6 in model year 3, time averaged for April through September, when the Leeuwin Current is strongest. Contour interval for kinetic energy ((cm/s)<sup>2</sup>) greater than 1000 is 500 and less than 1000 is (a) 250 and (b) 125.

DEPTH (m) : 10

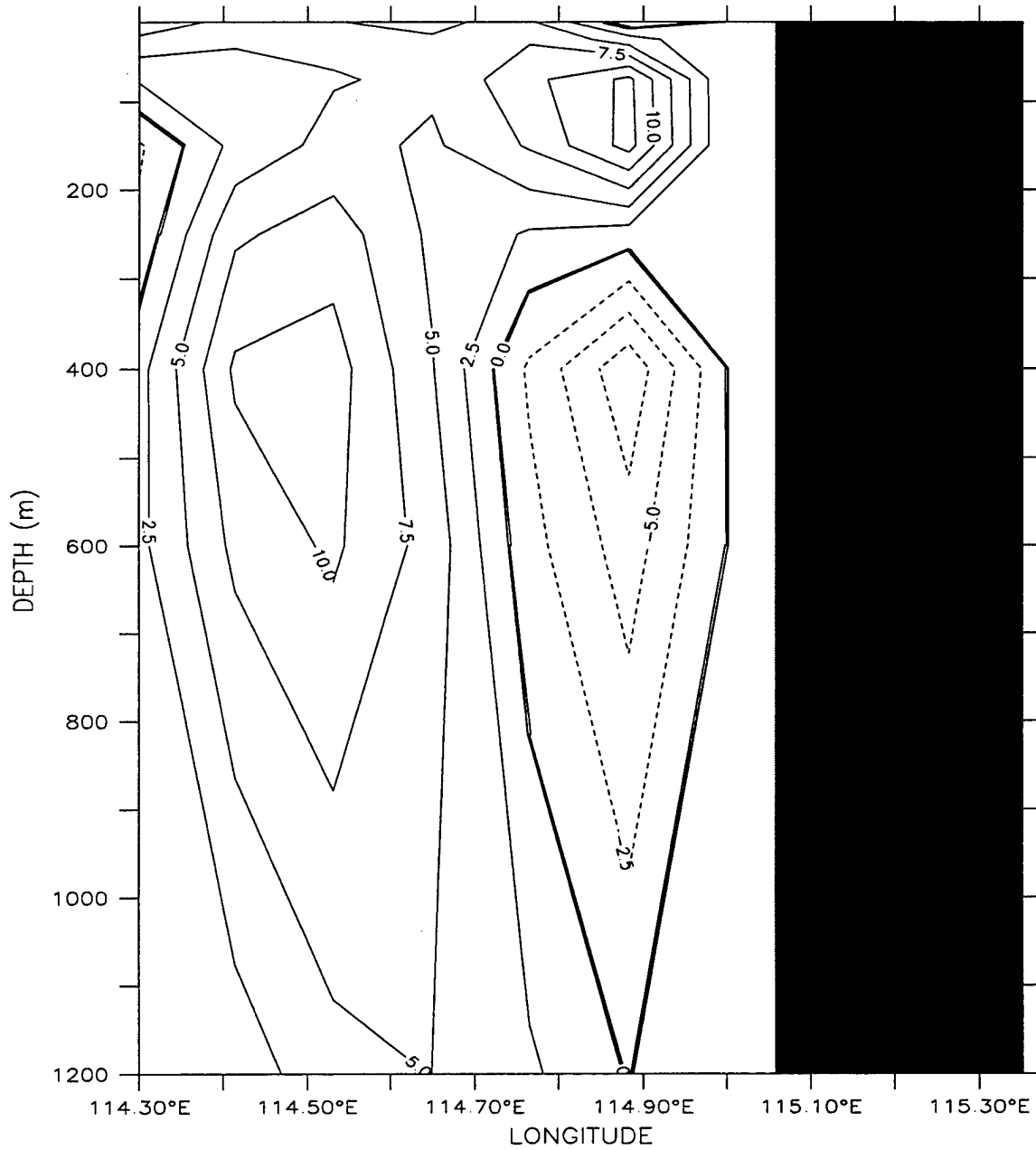


Average Eddy Kinetic Energy ((cm/sec)<sup>2</sup>)

(b)



LATITUDE : 30S  
T (DAY) : 915

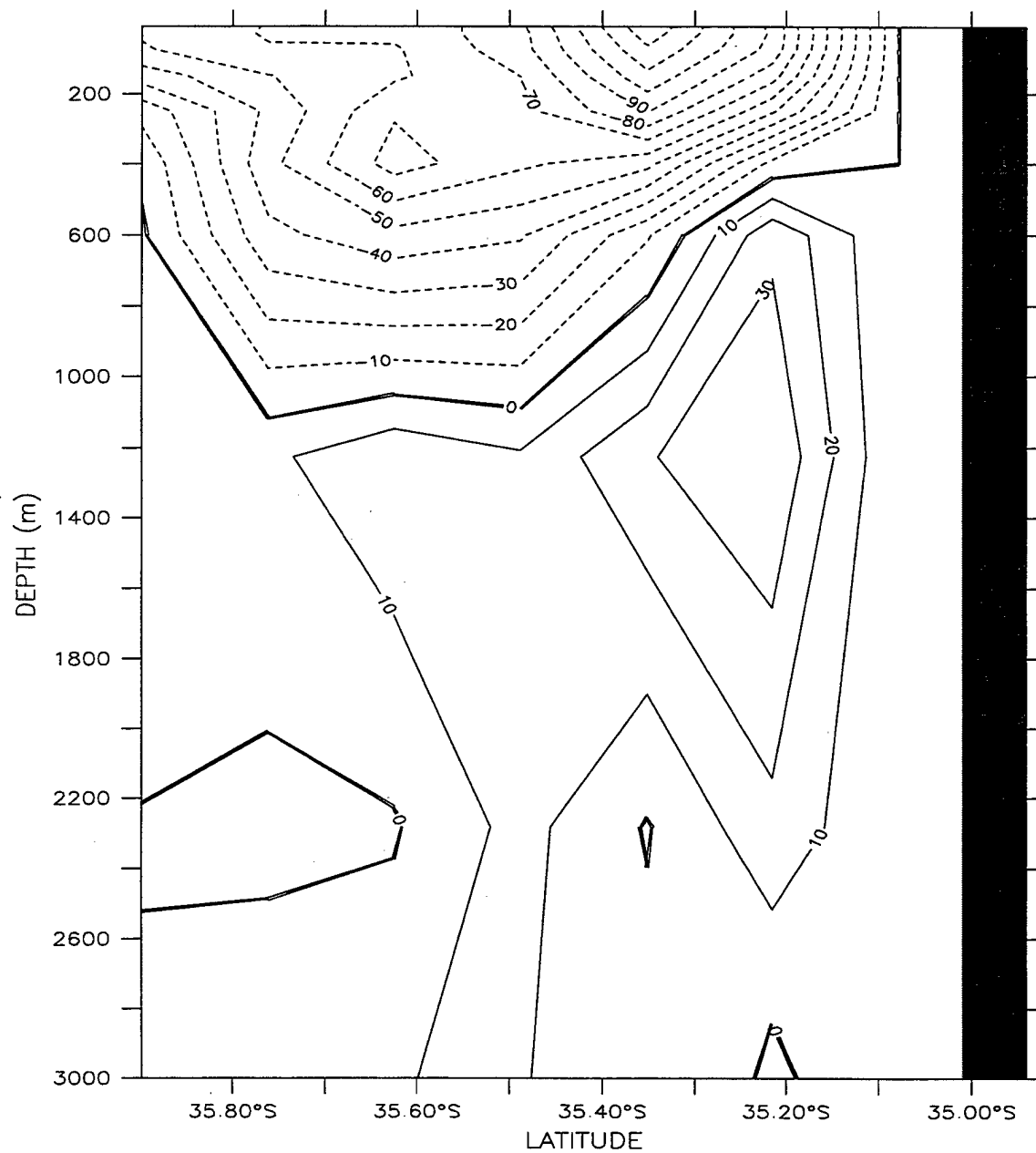


Meridional Velocity (cm/s)

(a)

**Figure 44.** Cross-shore section of (a) meridional velocity ( $v$ ) at  $30^\circ\text{S}$  on day 915 and (b) zonal velocity ( $u$ ) at  $117^\circ\text{E}$  on day 930 for Experiment 8. Contour interval is (a) 2.5 cm/s and (b) 10 cm/s for (a) poleward and (b) westward flow (dashed lines) and (a) 2.5 cm/s and (b) 10 cm/s for (a) equatorward and (b) eastward flow (solid lines).

LONGITUDE : 117E(117)  
T (DAY) : 930



Zonal Velocity (cm/s)  
(b)

DEPTH (m) : 10

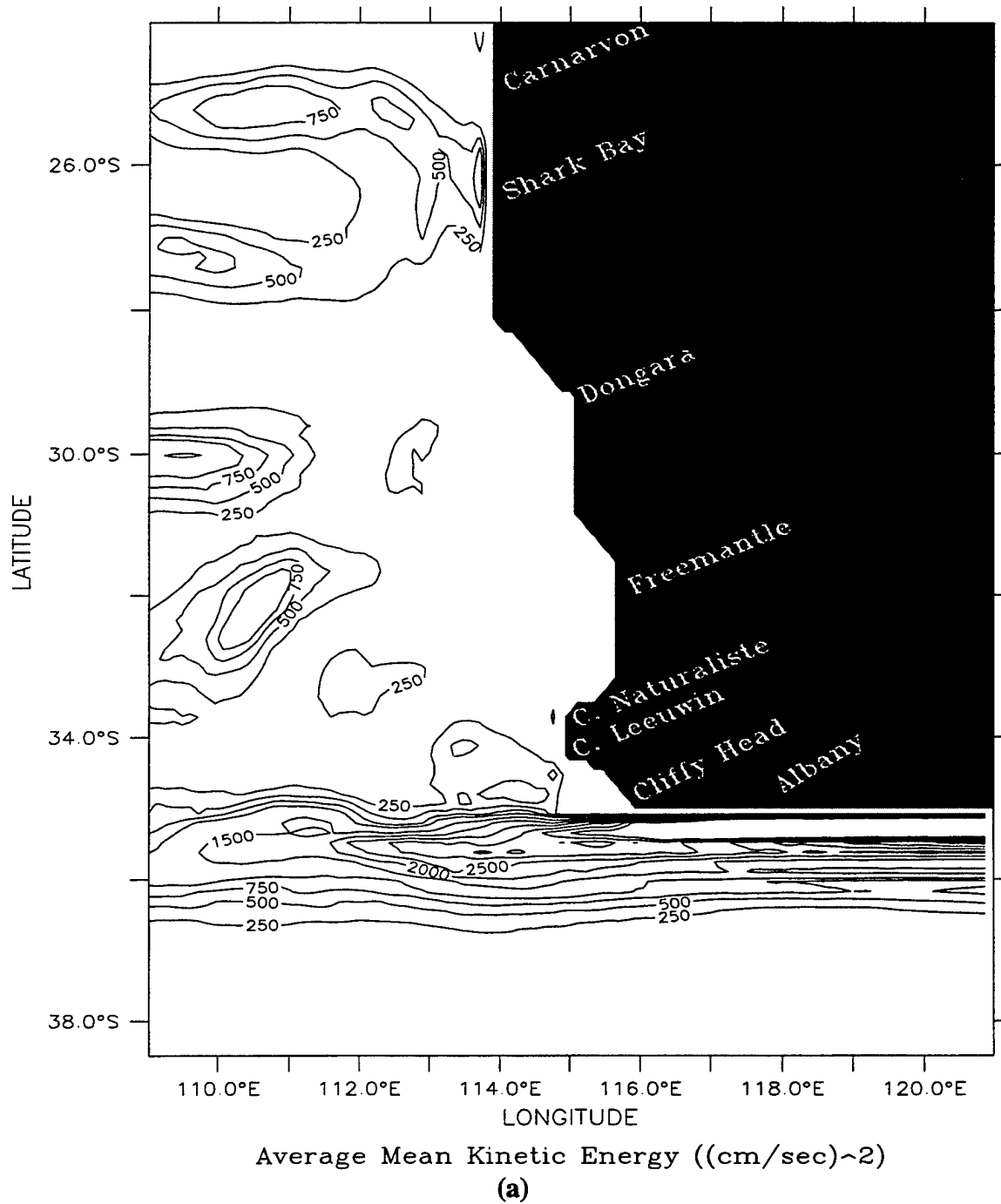
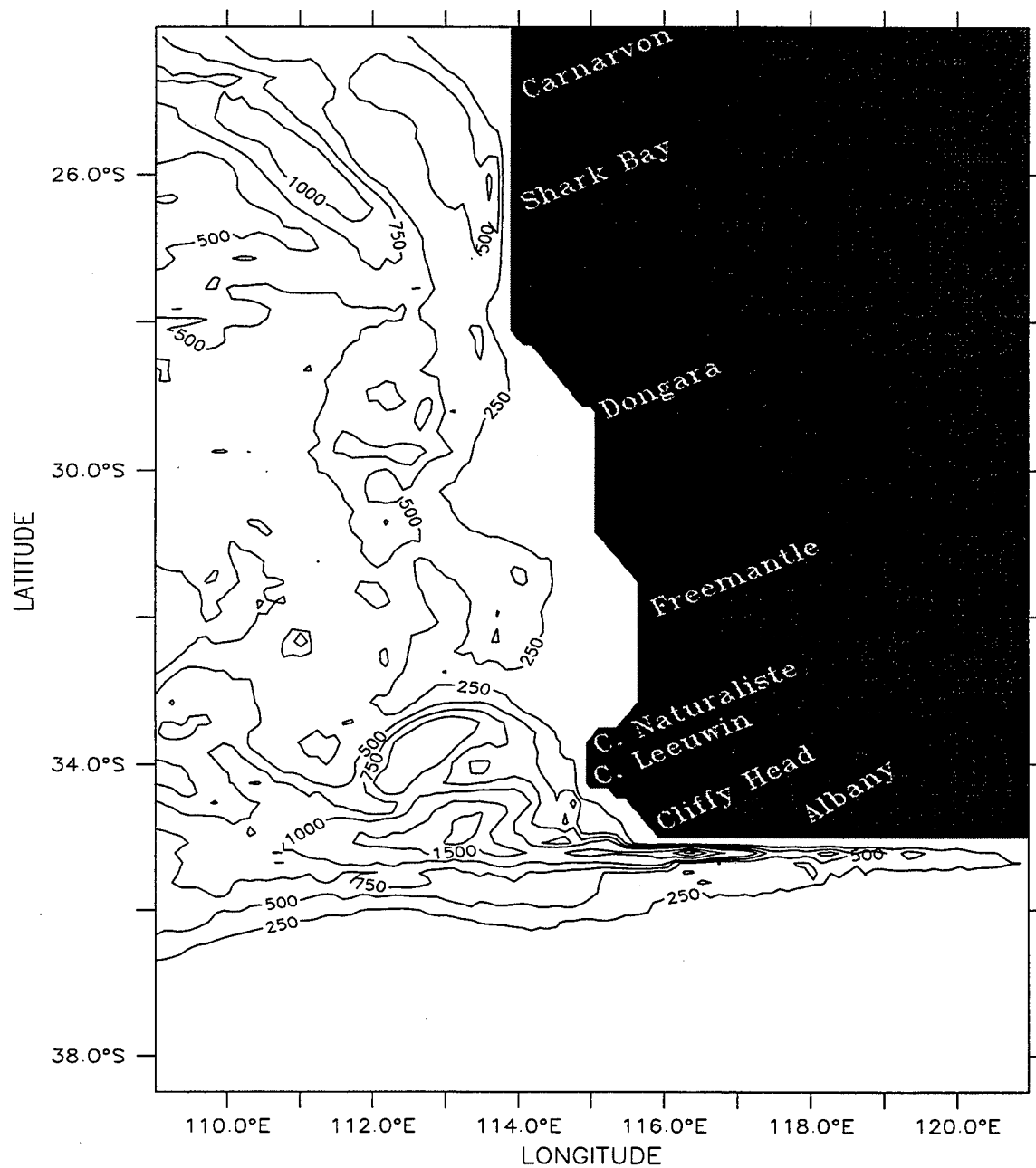


**Figure 45.** Horizontal map at 10 m depth of average (a) mean kinetic energy (MKE) and (b) eddy kinetic energy (EKE) for Experiment 8 in model year 3, time averaged for April through September, when the Leeuwin Current is strongest. Contour interval for kinetic energy ((cm/s)<sup>2</sup>) greater than 1000 is 500 and greater than 1000 is 250.

DEPTH (m) : 10



Average Eddy Kinetic Energy ((cm/sec)<sup>2</sup>)

(b)

**THIS PAGE INTENTIONALLY LEFT BLANK**

**Table 1. Values of constants used in the model**

Constant	Value	Definition
$T_0$	278.2°K	Constant Reference Temperature
$S_0$	34.7	Constant Reference Salinity
$\rho_0$	1.0276 gm cm <sup>3</sup>	Density of Sea Water At $T_0$ and $S_0$
$\alpha$	$2.4 \times 10^{-4} (\text{°K})^{-1}$	Thermal Expansion Coefficient
$\beta$	$7.5 \times 10^{-4}$	Saline Expansion Coefficient
$K$	10	Number of Levels In Vertical
$\Delta x$	$1.1 \times 10^5$ cm	Cross-Shore Grid Spacing
$\Delta y$	$1.4 \times 10^6$ cm	Alongshore Grid Spacing
$H$	$4.5 \times 10^5$ cm	Total Ocean Depth
$\Delta t$	800 s	Time Step
$f_0$	$-0.76 \times 10^{-4} \text{ s}^{-1}$	Mean Coriolis Parameter
$g$	980 cm s <sup>2</sup>	Acceleration of Gravity
$A_M$	$2 \times 10^{17} \text{ cm}^4 \text{ s}^{-1}$	Biharmonic Momentum Diffusion Coefficient
$A_H$	$2 \times 10^{17} \text{ cm}^4 \text{ s}^{-1}$	Biharmonic Heat Diffusion Coefficient
$K_M$	$0.5 \text{ cm}^2 \text{ s}^{-1}$	Vertical Eddy Viscosity
$K_H$	$0.5 \text{ cm}^2 \text{ s}^{-1}$	Vertical Eddy Conductivity

**Table 2. Temperature profile for North West Shelf Waters**

<b>Layer</b>	<b>(Depth in meters)</b>	<b>Temperature (°C)</b>
1	10	29.5
2	30	28.5
3	75	26.5
4	150	21

**Table 3. Summary of specific experimental design**

<b>Exp #</b>	<b>Coriolis Parameterization</b>	<b>Thermohaline Gradient</b>	<b>Wind Forcing</b>	<b>Ideal (Straight) Coastline</b>	<b>North West Shelf Water</b>
<b>1</b>	<i>f</i> -plane	YES	NO	NO	NO
<b>2</b>	<i>f</i> -plane	YES	NO	YES	NO
<b>3</b>	$\beta$ -plane	YES	NO	NO	NO
<b>4</b>	$\beta$ -plane	YES (top 5 layers)	NO	NO	NO
<b>5</b>	<i>f</i> -plane	NO	YES	NO	NO
<b>6</b>	$\beta$ -plane	NO	YES	NO	NO
<b>7</b>	<i>f</i> -plane	YES	YES	NO	NO
<b>8</b>	$\beta$ -plane	YES	YES	NO	NO
<b>9</b>	$\beta$ -plane	YES	YES	NO	YES



**THIS PAGE INTENTIONALLY LEFT BLANK**

## LIST OF REFERENCES

- Arakawa, A. and V. R. Lamb, Computational design of the basic dynamical processes of the UCLA general circulation model, *Methods Comput. Phys.*, 17, 173-265, 1977.
- Batteen, M. L., Wind-forced modeling studies of currents, meanders, and eddies in the California Current System, *J. Geophys. Res.*, 102, 985-1009, 1997.
- Batteen, M. L. and C. L. Butler, Modeling studies of the Leeuwin Current off Western and Southern Australia, *J. Phys. Oceanogr.*, 28, 2199-2221, 1998.
- Batteen, M. L. and Y. -J. Han, On the computational noise of finite difference schemes used in ocean models, *Tellus*, 33, 387-396, 1981.
- Batteen, M. L. and P. J. Murray, The role of the planetary beta effect on currents and meddies in the Northern Canary Current System, *J. Geophys. Res.*, To be submitted, 2000.
- Batteen, M. L., M. J. Rutherford, and E. J. Bayler, A numerical study of wind and thermal forcing effects on the ocean circulation off Western Australia, *J. Phys. Oceanogr.*, 22, 1406-1433, 1992.
- Boland, F. M., J. A. Church, A. M. G. Forbes, J. S. Godfrey, A. Huyer, R. L. Smith, and N. J. White, Current-meter data from the Leeuwin Current Interdisciplinary Experiment, *CSIRO Marine Laboratories*, Report 198, 31pp., 1988.
- Camerlengo, A. L. and J. J. O'Brien, Open boundary conditions in rotating fluids, *J. Comput. Phys.*, 89, 12-35, 1980.
- Church, J. A., G. R. Cresswell, and J. S. Godfrey, The Leeuwin Current. In: *Poleward Flows along Eastern Ocean Boundaries*, S. Neshhyba, C. N. K. Moorers, R. I. Smith, and R. T. Barber, Eds, Springer-Verlag, 230-252, 1989.
- Cresswell, G. R. and T. J. Golding, Observations of a south-flowing current in the southeastern Indian Ocean, *Deep-Sea Res.*, 27A, 449-466, 1980.
- Cresswell, G. R. and J. L. Peterson, The Leeuwin Current south of Western Australia, *Aust. J. Mar. Freshwater Res.*, 44, 285-303, 1993.
- Feliks, Y., On the Rossby radius of deformation in the ocean, *J. Phys. Oceanogr.*, 15, 1607-1685, 1985.
- Gentili, J., Thermal anomalies in the Eastern Indian Ocean, *Nature (London) Phys. Sci.*, 238, 93-95, 1972.

- Godfrey, J. S. and K. R. Ridgway, The large-scale environment of the poleward-flowing Leeuwin Current, Western Australia: Longshore steric height gradients, wind stresses and geostrophic flow, *J. Phys. Oceanogr.*, 15, 481-495, 1985.
- Godfrey, J. S., D. J. Vaudrey, and S. D. Hahn, Observations of the shelf-edge current south of Australia winter 1982, *J. Phys. Oceanogr.*, 16, 668-679, 1986.
- Hirst, A. C., and J. S. Godfrey, The role of Indonesian Throughflow in a global ocean GCM, *J. Phys. Oceanogr.*, 23, 1057-1086, 1993.
- Holland, W. R., The role of mesoscale eddies in the general circulation of the ocean-Numerical experiments using a wind-driven quasi-geostrophic model, *J. Phys. Oceanogr.*, 8, 363-392, 1978.
- Holland, W. R. and M. L. Batteen, The parameterization of subgrid scale heat diffusion in eddy-resolved ocean circulation models, *J. Phys. Oceanogr.*, 16, 200-206, 1986.
- Levitus, S., and T. P. Boyer, World ocean atlas 1994, Vol. 4: Temperature, *NOAA Atlas NESDI 4*, 117 pp., U. S. Dept. of Commerce, Washington, D.C., 1994.
- McCreary, J. P., S. R. Shetye, and P. K. Kundu, Thermohaline forcing of eastern boundary currents: With application to the circulation off the west coast of Australia, *J. Mar. Res.*, 44, 71-92, 1986.
- Parrish, R. H., A. Bakun, D. M. Husby, and C. S. Nelson, Comparative climatology of selected environmental processes in relation to eastern boundary current pelagic fish reproduction. In: *Proc. Expert Consultation to Examine Changes in Abundance and Species of Neritic Fish Resources*, G. D. Sharp and J. Csirke, Eds., San Jose, Costa Rica, FAO Fish Rep. 291, Vol. 3, 731-778, 1983.
- Smith, R. L., A. Huyer, J. S. Godfrey, and J. A. Church, The Leeuwin Current off Western Australia, 1986-1987, *J. Phys. Oceanogr.*, 21, 323-345, 1991.
- Thompson, R. O. R. Y., Observations of the Leeuwin Current off Western Australia, *J. Phys. Oceanogr.*, 14, 623-628, 1984.
- Thompson, R. O. R. Y., Continental-shelf scale model of the Leeuwin Current, *J. Mar. Res.*, 45, 813-827, 1987.
- Trenberth, K. E., W. G. Large, J. G. Olsen, The mean annual cycle in global ocean wind stress, *J. Phys. Oceanogr.*, 20, 1742-1760, 1990.
- Weatherly, G. L., A study of the bottom boundary layer of the Florida Current, *J. Phys. Oceanogr.*, 2, 54-72, 1972.

Weaver, A. J. and J. H. Middleton, On the Dynamics of the Leeuwin Current, *J. Phys. Oceanogr.*, 19, 626-648, 1988.

**THIS PAGE INTENTIONALLY LEFT BLANK**

## INITIAL DISTRIBUTION LIST

	No. Copies
1. Defense Technical Information Center.....2 8725 John J. Kingman Rd, STE 0944 Ft. Belvoir, VA 22060-6218	
2. Dudley Knox Library.....2 Naval Postgraduate School 411 Dyer Rd Monterey, CA 93943-5101	
3. Chairman (Code OC/Gd).....1 Department of Oceanography Naval Postgraduate School Monterey, CA 93943-5122	
4. Chairman (Code MR/Wx).....1 Department of Meteorology Naval Postgraduate School Monterey, CA 93943-5114	
5. Dr. Mary L. Batteen, (Code OC/Bv).....5 Department of Oceanography Naval Postgraduate School Monterey, CA 93943-5122	
6. Dr. Curtis A. Collins, (Code OC/Co) .....1 Department of Oceanography Naval Postgraduate School Monterey, CA 93943-5122	
7. LCDR Troy J. Tworek.....3 1229 Alamoot Drive Chesapeake, VA 93322-7078	